Instability and Transition of Swept-Wing Flow

Mechanisms of interaction between crossflow instabilities and forward-facing steps

Casacuberta Puig, J.

DOI
10.4233/uuid:aaca54c8-ffe0-4e05-9302-17c3ff290a52

Publication date
2025

Document Version
Final published version

Citation (APA)
Casacuberta Puig, J. (2025). *Instability and Transition of Swept-Wing Flow: Mechanisms of interaction between crossflow instabilities and forward-facing steps*. [Dissertation (TU Delft), Delft University of Technology]. https://doi.org/10.4233/uuid:aaca54c8-ffe0-4e05-9302-17c3ff290a52

Instability and Transition of Swept-Wing Flow

Jordi Casacuberta Puig

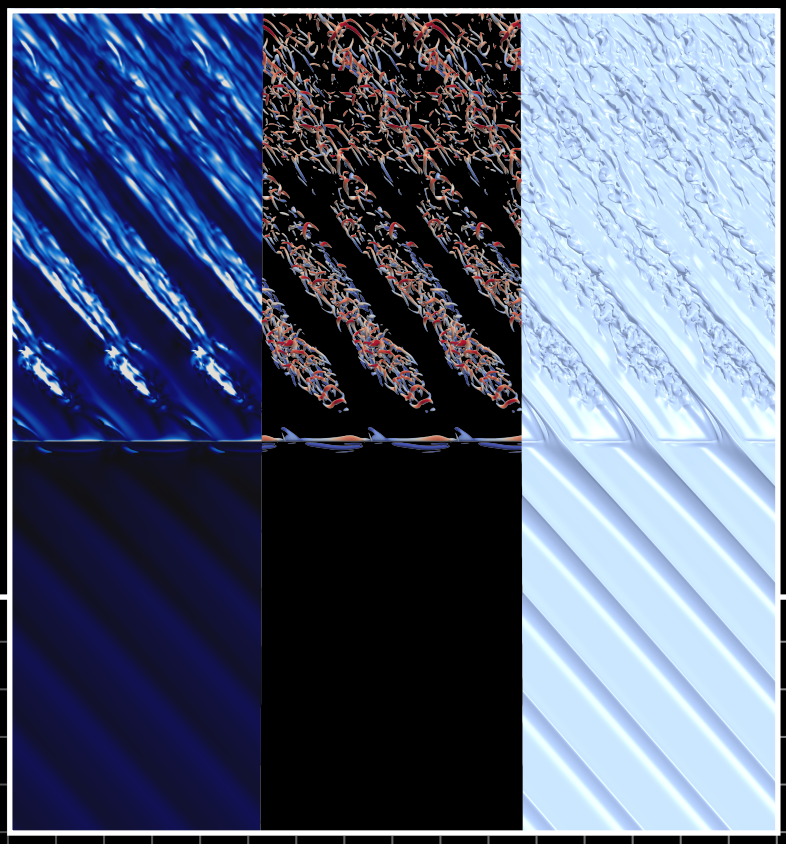

Instability and Transition of Swept-Wing Flow

Mechanisms of interaction between crossflow instabilities and forward-facing steps

Dissertation

for the purpose of obtaining the degree of doctor
at Delft University of Technology
by the authority of the Rector Magnificus prof. dr. ir. T.H.J.J. van der Hagen,
chair of the Board of Doctorates,
to be defended publicly on
Thursday 11 December 2025 at 15:00 hours

by

Jordi CASACUBERTA PUIG

Master of Science in Aerospace Engineering,
Delft University of Technology, the Netherlands,
born in Barcelona, Spain

This dissertation has been approved by

promotor: Prof. dr. M. Kotsonis
promotor: Prof. dr.-ing. habil. S. Hickel

Composition of the doctoral committee:

Rector Magnificus,	chairperson
Prof. dr. M. Kotsonis,	Delft University of Technology, promotor
Prof. dr.-ing. habil. S. Hickel,	Delft University of Technology, promotor

Independent members:

Dr.-Ing. M. J. Kloker,	University of Stuttgart, Germany
Dr. J. Eppink,	NASA Langley Research Center, USA
Dr. O. Marxen,	University of Surrey, UK
Prof. dr. P. J. Schmid,	King Abdullah University of Science and Technology, SA
Prof. dr. D. A. von Terzi,	Delft University of Technology, The Netherlands

Reserve member:

Prof. dr. ir. L.L.M. Veldhuis,	Delft University of Technology, The Netherlands

This thesis has received HPC resources from the Dutch national e-infrastructure with the support of SURF Cooperative. The author acknowledges the support of the European Research Council through Starting Grant no. 803082 GloWing.

Keywords: aerodynamics, instability, transition, boundary layer, DNS, cross-flow, step, flow control

Printed by: Koninklijke Rijnja – The Netherlands

Front & Back: Design by J. Casacuberta Puig with DALL-E. Front: laminar-turbulent transition induced by a step from DNS, depicted through velocity isosurface (right), Q-criterion isosurface (centre), and wall shear (left). Back: the metaphysical representation of transition, expressed through the tension between the Greek gods Apollo (reason and order) and Dionysus (passion and chaos).

ISBN 978-94-6384-882-4

An electronic version of this dissertation is available at
`http://repository.tudelft.nl/`.

What is done out of love always takes place beyond good and evil.

Friedrich Nietzsche

This thesis is dedicated to those who live with passion through their *art*, for they understand that *creating* and *discovering* are life's deepest affirmations.

Contents

Summary

This thesis presents a theoretical and numerical investigation of how a surface forward-facing step alters the stability and transition mechanisms of a laminar incompressible swept-wing boundary layer dominated by stationary crossflow instabilities (CFI). The results elucidate the processes that cause significant transition advancement due to the step and, in turn, challenge the classic paradigm in fluid mechanics that rapid, localised surface-geometry variations are universally detrimental to laminar flow. Through Direct Numerical Simulations (DNS) and new theoretical modelling, this thesis shows that, under specific conditions, a forward-facing step stabilises pre-existing stationary crossflow vortices and thereby delays laminar-turbulent transition.

Steady-state DNS are conducted first to examine the interaction mechanisms between CFI of varying amplitude and steps of different heights, corresponding to roughness Reynolds numbers (Re_{hh}) from 368 to 832.

Three methodological innovations underpin the analysis of stationary-perturbation effects. First, a perturbation-projection framework is introduced, decomposing the perturbation field relative to the local base-flow orientation rather than the wall. This enables the identification of modal and non-modal growth mechanisms and reveals that the lift-up effect governs the behaviour of the fundamental CFI as it passes over the step. The formulation uncovers a previously unreported reverse (i.e., stabilising) lift-up effect, capable of inducing a rapid local decay of kinetic perturbation energy. Whether this *reverse* (stabilising) or the *classic* (destabilising) lift-up effect occurs at the step depends, at least, on step height and free-stream evolution. Secondly, the analysis elucidates how non-modal stationary perturbation streaks emerge as inherent features of swept step flows; it also shows that an inflectional instability of the step-flow profiles amplifies high-order harmonic (i.e., smaller-wavelength) CFI modes downstream of the step, as confirmed experimentally. Finally, an extended Reynolds-Orr energy framework quantifies the amplitude-dependent mechanisms of energy exchange underlying these effects. The resulting deformation of the near-wall shear layer downstream of the step –beneath the crest of the pre-existing crossflow vortex– plays a central role in transition advancement.

Complementary unsteady DNS and linear stability analyses reveal that early transition induced by the step (under both critical and supercritical conditions) is not driven by classic secondary crossflow instabilities. Instead, a new shear-layer instability developing downstream of the step is identified as the key transition-promotion mechanism. Overall, these findings establish a new physical and modelling basis for understanding, predicting, and ultimately controlling laminar flow over relief-shaped swept wings, offering a promising new direction towards robust passive laminar-flow-control strategies for future aircraft.

Samenvatting

Dit proefschrift onderzoekt theoretisch en numeriek hoe een voorwaarts gerichte trede de stabiliteits- en transitismechanismen beïnvloedt van een laminaire, onsamendrukbare grenslaag over een gepijlde vleugel die wordt gedomineerd door stationaire kruisstromingsinstabiliteiten (crossflow instabilities, CFI). De resultaten verduidelijken de processen die leiden tot een significante vervroeging van de transitie door de aanwezigheid van de trede en dagen het klassieke paradigma uit dat lokale hoogtevariaties per definitie nadelig zijn voor laminaire stroming. Directe Numerieke Simulaties (DNS) en nieuwe theoretische modellering tonen daarentegen aan dat een voorwaarts gerichte trede, onder specifieke omstandigheden, bestaande kruisstromingswervelingen kan stabiliseren en zo de laminair-turbulente transitie kan vertragen.

Stationaire DNS zijn uitgevoerd om de interactiemechanismen te onderzoeken tussen CFI's met verschillende amplitudes en tredes met uiteenlopende hoogten, overeenkomend met ruigheid-Reynoldsgetallen (Re_{hh}) van 368 tot 832.

Drie methodologische vernieuwingen vormen de kern van de analyse. Ten eerste wordt een projectiekader geïntroduceerd waarin het verstoringsveld wordt ontbonden ten opzichte van de lokale basisstroomoriëntatie in plaats van de wand. Deze aanpak maakt het mogelijk modale en niet-modale groeimechanismen te onderscheiden en onthult een omgekeerd (stabiliserend) lift-up-effect, dat lokaal een snelle afname van de kinetische verstoringsenergie veroorzaakt. Of dit omgekeerde of klassieke (destabiliserende) lift-up-effect optreedt, hangt af van de tredehoogte en de ontwikkeling van de vrije stroming. Ten tweede blijken niet-modale verstoringsstrepen intrinsieke kenmerken van stromingen over gepijlde tredes, terwijl een inflectionele instabiliteit hogere-orde CFI-modi stroomafwaarts versterkt. Ten slotte kwantificeert een uitgebreide Reynolds–Orr-energiebalans de amplitude-afhankelijke energie-uitwisseling. De vervorming van de schuiflaag onder de kam van de kruisstromingswerveling speelt daarbij een centrale rol in de transitie.

Tijdafhankelijke DNS en lineaire stabiliteitsanalyses tonen aan dat de vervroeging van transitie door de trede –zowel onder kritische als superkritische omstandigheden– niet wordt veroorzaakt door klassieke secundaire kruisstromingsinstabiliteiten, maar door een nieuwe schuiflaaginstabiliteit stroomafwaarts van de trede. Deze bevindingen vormen een nieuw kader voor het begrijpen en beheersen van laminaire stroming over oppervlakken met reliëf en wijzen de weg naar robuuste passieve laminar-flow-controlstrategieën voor toekomstige vliegtuigen.

I

Background, scope, and methods

1

Introduction

Abstract: *This chapter introduces the engineering context, fundamental fluid dynamics concepts, the theoretical foundation, and prior work assessing the effects of two-dimensional surface features on boundary-layer instability. It concludes by articulating the research objective and questions addressed in this thesis.*

1

1.1. Motivation

On February 28th, 2019, Airbus Operations S.A.S., Toulouse (FR) and Airbus SAS, Blagnac (FR) patented a new method for manufacturing a wing leading edge (Kierbel et al., 2019). The manufacturing method is claimed to reduce surface irregularities with respect to the prior art and therefore to improve the laminar flow quality. But why has the aeronautics industry patented a method to attain wing surface irregularities (Ra and Rt) as low as 0.2 μm (Kierbel et al., 2019)?

To minimise wing drag and thereby reduce aircraft fuel consumption, the boundary layer over the wings and fuselage ought to remain laminar over the largest possible spatial extent. A laminar boundary layer is characterised by ordered, smooth flow but is inherently prone to transition to turbulence, a state characterised by disorganised and seemingly unpredictable flow. Figure 1.1 illustrates this laminar-turbulent transition in flat-plate flow. The wall shear stress is larger when the boundary layer is in turbulent state, as opposed to laminar state.

Kierbel et al. (2019) indicate that to "extend the laminar flow towards the rear of the wing has a tendency to reduce drag by the order of 8% at cruising speed and aviation-fuel consumption by the order of 4 to 5%", see their claim [0107]. This proposition is linked to a conventional aircraft morphology (see their claim [0044]), i.e., "which comprises a fuselage, wings, nacelles positioned under the wings, and a tail assembly". The German (DLR) and French (ONERA) Aerospace Centres report that delaying laminar-turbulent transition past 50% of the wing chord length decreases drag by 5 to 8%. This leads to improved aircraft-fuel efficiency in the order of 4 to 7%; or, equivalently, 2 to 5 tons of fuel saved in a typical flight from Frankfurt to Los Angeles (HLFC–WIN consortium, 2023). Gibson et al. (2021) from the Airbus Group indicate that a 5% reduction of fuel consumption may be achieved if transition is shifted past 60% of the wing chord length on the wing upper surface. See also the reports by Rossow (2010), Allison et al. (2010), or Wicke et al. (2012) for a discussion on the topic. It is to be noted that significant benefits in terms of fuel saving are achieved as well if large portions of laminar flow are maintained over the fin, horizontal tail, and nacelles (Schrauf, 2005).

However, in a practical scenario involving operational conditions, the laminar-turbulent transition typically develops very close to the wing leading edge (Joslin, 1998b; Hepperle, 2008; Rossow, 2010; Wicke et al., 2012; Gibson et al., 2021). By way of example, for an Airbus A320 aircraft type flying at an altitude of 10,000 m and cruise Mach number $M = 0.8$, transition is reported at 15% of chord length (Rossow, 2010) and it shifts towards a higher percentage of the chord length as one moves towards the wing tip due to wing taper. Currently, aircraft manufacturers assume essentially turbulent boundary-layer flow over most wetted surfaces (Gibson et al., 2021) and to revert this is a major quest in the field of aerodynamics. The National Aeronautics and Space Administration (NASA) refers to it as aviation's Holy Grail, since "conquering laminar flow [...] would mean dramatic improvements in fuel efficiency" (NASA social media, 2011; NASA Blog, 2011). In 2018, Airbus was awarded the Aviation Week Networks Laureate Award for BLADE. The Breakthrough Laminar Aircraft Demonstrator in Europe (BLADE) is a multi-partner EU-sponsored initiative aimed at assessing the feasibility of laminar-flow wings in commercial avi-

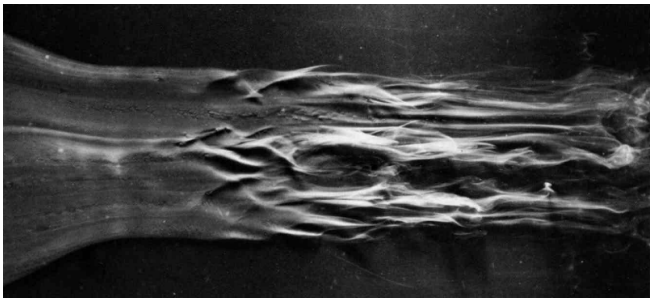

Figure 1.1: Visualisation (top view) of natural laminar-turbulent transition over an unswept flat plate at an angle of attack of 1°, with flow from left to right. The Reynolds number is $Re = 10^5$. Laminar flow is visible on the left. © ONERA 1980, photo by H. Werlé.

ation. For example, figure 1.2 (*b*) shows a laminar outer-wing section used in a BLADE flight-test demonstrator.

At the start of the BLADE project, Airbus' former head of central research and technology, Axel Flaig, explained that it had not been possible to manufacture sufficiently smooth *industrial wings* to achieve and maintain laminar flow during regular airline operations (Gubisch, 2017). As early as year 1938, it has been reported that "very small imperfections of surface are sufficient to move transition points forward and so increase drag" (Jones, 1938). More specifically, it is well-established that if early transition is promoted by a surface feature, the transition-front location is bounded between the feature itself and the transition-front location in reference (i.e., no-feature) conditions (Fage and Preston, 1941; Dryden, 1953; Tani, 1969). So, what is meant by surface features or irregularities in this context?

Flaig notes that sharp two-dimensional (i.e., invariant in one spatial direction) steps and gaps near the leading edge of transport aircraft wings, such as those arising at panel junctions or around slats, can inhibit laminar flow (Gubisch, 2017). Considering business jets, it is typical to find a spanwise joint between skin panels forming the leading edge part and the main wing part, which are a source of laminar flow deterioration (Drake et al., 1996). Daniel Kierbel, project leader of BLADE, explains that laminar flow may typically be disrupted as well by insect debris, icing-related features, scratches, grease, surface waviness, and deformation of fastener heads (Goold, 2018). Daniel Kierbel is in fact co-inventor of the patent publication cited at the beginning of this section. The background of the invention by Kierbel et al. (2019) considers a wing structure composed of two spars joined by ribs, see figure 1.2 (*a*) and their claim [0002]. The *skin* of the wing is formed by top and bottom panels (parts **28**, **30**, **38**, and **40** in figure 1.2 (*a*)) that are attached to the structure. These panels are typically machined metal plates (see their claim [0003]). According to Kierbel et al. (2019), reducing their geometrical tolerances (i.e., two-dimensional steps and gaps at the junction) carries great increase in manufacturing cost and complexity. However, these geometrical tolerances must be as small as possible to broaden the extent of laminar flow (Kierbel et al., 2019).

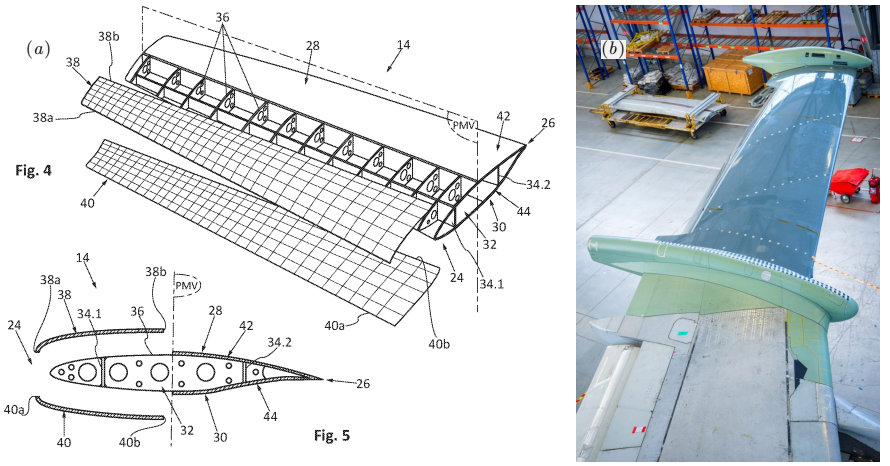

Figure 1.2: (*a*) Figures 4 and 5 from the patent publication by Kierbel et al. (2019), which describes a method for manufacturing an aircraft leading edge panel. Figure 4 presents a perspective view of a wing, while Figure 5 shows its cross-sectional view. As stated in the source, "panels **38** and **40** are connected to the structure **32** [...] before or after the vertical mid plane PMV". (*b*) Laminar outer-wing section of the Airbus A340 used in the BLADE test demonstrator flight (A340-300 MSN001) employed to assess, among other aspects, the influence of step-like manufacturing tolerances on laminarity (Fendt, 2017; Appel, 2021). © Airbus 2017, photo by P. Pigeyre.

This thesis provides a theoretical and numerical investigation into the impact of surface features on transition promotion in laminar swept-wing flows, with a particular focus on the associated instability mechanisms. The scope is placed specifically on forward-facing steps. Theoretical and numerical approaches are combined to develop physical understanding at a fundamental level and generate modelling frameworks. At the same time, the conclusions of this thesis challenge the major claims outlined earlier: numerical and theoretical evidence is presented showing that this surface feature is not universally detrimental to laminar swept-wing flow. That is, under certain conditions, a forward-facing step stabilises pre-existing stationary crossflow instability and potentially delays transition as a consequence. The latter can be further exploited to design and optimise passive laminar flow control strategies.

1.2. Theoretical background

This section introduces the theoretical background supporting the analysis of results in this thesis. It begins by establishing key concepts from instability theory, followed by a description of the pertinent base flows, relevant transition routes and mechanisms, and characteristic features of forward-facing-step flow. Finally, an overview of traditional methods for instability modelling is presented, and the novel modelling frameworks developed in this thesis are introduced.

1.2.1. Introductory concepts: flow (in)stability

Perhaps one of the most thought-provoking questions posed to a researcher in flow instability is: *what is a flow instability?* This phenomenon is the precursor to laminar-turbulent transition in a wide range of flow scenarios and therefore it warrants formalisation.

Flow instability may be understood as the tendency of a fluid flow to depart from a reference base state. This tendency can be characterised by the increase in kinetic energy of a perturbation field in the flow, which is the deviation of a new (evolving) state from a reference base state. Above a certain threshold of kinetic energy increase, an initially laminar fluid flow may transition towards a new state, see Schmid and Henningson (2001, section 1.3), for instance a turbulent state. From the perspective of classic stability theory, the base state represents an equilibrium condition that may be either stable or unstable to a perturbation, as determined by its ability to return to equilibrium (Schmid and Brandt, 2014).

Flow instabilities can be characterised through stability analysis (Gregory et al., 1955; Mack, 1984; Arnal, 1994; Huerre and Monkewitz, 1990; Reed and Saric, 1996; Schmid and Henningson, 2001; Theofilis, 2003). Letting $\mathbb{NS}$ be the non-linear Navier-Stokes operator applied to a state-variable $\boldsymbol{q}$ vector, with suitable boundary and initial conditions, the incompressible Navier-Stokes equations can be expressed as

$$\dot{\boldsymbol{q}} = \mathbb{NS}(\boldsymbol{q}), \tag{1.1}$$

where the overdot denotes the time derivative. The laminar base state, hereafter referred to as the unperturbed base flow, is the steady state of equation (1.1) satisfying $\dot{\boldsymbol{q}}_{\mathrm{B}} = \mathbb{NS}(\boldsymbol{q}_{\mathrm{B}}) = 0$. The stability approach decomposes the state vector $\boldsymbol{q} = [\boldsymbol{v}\ p]^{\mathrm{T}}$ as

$$\boldsymbol{q}(x, y, z, t) = \boldsymbol{q}_{\mathrm{B}}(x, y, z) + \boldsymbol{q}'(x, y, z, t), \tag{1.2}$$

where $\boldsymbol{q}' = [\boldsymbol{v}'\ p']^{\mathrm{T}}$ is the perturbation field, $\boldsymbol{q}_{\mathrm{B}} = [\boldsymbol{v}_{\mathrm{B}}\ p_{\mathrm{B}}]^{\mathrm{T}}$, $\boldsymbol{v} = [u\ v\ w]^{\mathrm{T}}$ is the velocity field, p indicates the static pressure, and t is the time. A Cartesian coordinate system is here considered, that is fixed and oriented relative to the wing; that is, x and z respectively denote the directions orthogonal and parallel to the leading edge (see § 2.1.1), and y denotes the wall-normal coordinate. The perturbation components in the x-, y-, and z-directions are denoted by u', v', and w', respectively.

A major instability mechanism that manifests in the field $\boldsymbol{q}'$ of swept-leading-edge flow is the stationary crossflow instability (CFI); see the detailed description of the corresponding base-flow topology (§ 1.2.2) and the mechanisms of CFI growth (§ 1.2.3) below. This phenomenon was first observed in flight experiments on a F-86 aircraft (Gray, 1952). The amplification of this *primary* instability along the leading-edge-orthogonal direction spatially deforms the flow. This effectively gives rise to a new stationary (base) state, known as the steady perturbed flow, susceptible to *secondary* unsteady instabilities that are harbingers of turbulence. To ascertain how a surface step promotes transition, this thesis first characterises the stationary step-flow mechanisms that modify the incoming CFI; i.e., the topology of the steady perturbed flow. This forms the basis to, secondly, assess the unsteady mechanisms ultimately leading to turbulence.

In this thesis, the spatial evolution of CFI is fully resolved by means of Direct Numerical Simulations of the *total flow field*, i.e., $\boldsymbol{q}$ (1.2). Physical insight into the perturbation behaviour is gained *a posteriori* through inspection of the governing equations and analysing the DNS data. This is elaborated as follows: introducing decomposition (1.2) into the non-dimensional form of the stationary incompressible Navier-Stokes equations for a fluid with constant density and constant viscosity (1.1) and subtracting the base-flow condition identically yields

$$(\underline{\boldsymbol{v}}' \cdot \boldsymbol{\nabla})\,\underline{\boldsymbol{v}}_{\mathrm{B}} + (\underline{\boldsymbol{v}}_{\mathrm{B}} \cdot \boldsymbol{\nabla})\,\underline{\boldsymbol{v}}' = -\boldsymbol{\nabla}\underline{p}' + \frac{1}{Re}\boldsymbol{\nabla}^2\underline{\boldsymbol{v}}' - (\underline{\boldsymbol{v}}' \cdot \boldsymbol{\nabla})\,\underline{\boldsymbol{v}}'. \tag{1.3}$$

The underbar here denotes non-dimensional variables, and Re is the Reynolds number. Similarly, the continuity condition expressed in perturbation form reads as

$$\boldsymbol{\nabla} \cdot \underline{\boldsymbol{v}}' = 0. \tag{1.4}$$

Equations (1.3) and (1.4), which are commonly referred to as the perturbation equations, govern the evolution of any generic stationary perturbation. The establishment of CFI in the first place is initially governed by receptivity (Morkovin, 1969), that is, the process by which disturbances in the free stream –such as vorticity and sound– generate boundary-layer perturbations. In this thesis, the receptivity stage is not explicitly resolved in the numerical simulations but is instead modelled.

1.2.2. The laminar swept-wing boundary layer

The stability of laminar swept-wing flow is analysed by considering an idealised representation of the wing geometry. Swept-wing flow refers to the flow over a wing whose leading edge is angled relative to the fuselage. As is common practice in the literature, the physical model in this thesis assumes that the chord is constant along the span, the twist is virtually zero, and that the wing has effectively infinite spanwise extent, i.e., root and tip effects are disregarded. By virtue of this set of assumptions, collectively referred to as *infinite wingspan*, the unperturbed base flow is conceived as a three-dimensional spanwise-invariant flow field, i.e., $\partial \boldsymbol{q}_{\mathrm{B}}/\partial z = 0$.

In this model of swept-wing flow, the free-stream velocity vector may be conveniently decomposed into components parallel (spanwise) and orthogonal (chordwise) to the leading-edge direction (see figure 1.3). As the flow approaches the wing body, the leading-edge-orthogonal component decelerates, whereas the leading-edge-parallel component remains essentially unchanged in inviscid flow. Consequently, a dividing streamline exists in the potential-flow region that is parallel to the leading-edge axis and virtually separates the upper and lower sides of the wing. This so-called attachment line at the leading edge (Pfenninger, 1965; Gaster, 1967; Cumpsty and Head, 1969; Hall et al., 1984) is the isoline of maximum static pressure on symmetric bodies (Arnal, 1994). The attachment line is accompanied by an attachment-line boundary layer by virtue of no-slip at the wall. Leveraging the assumption of infinite wingspan, the attachment-line boundary layer exhibits constant properties, i.e., thickness and wall friction, as dictated by the balance between the incoming free-stream flow and outflow cause by flow divergence at the attachment line (Poll, 1977).

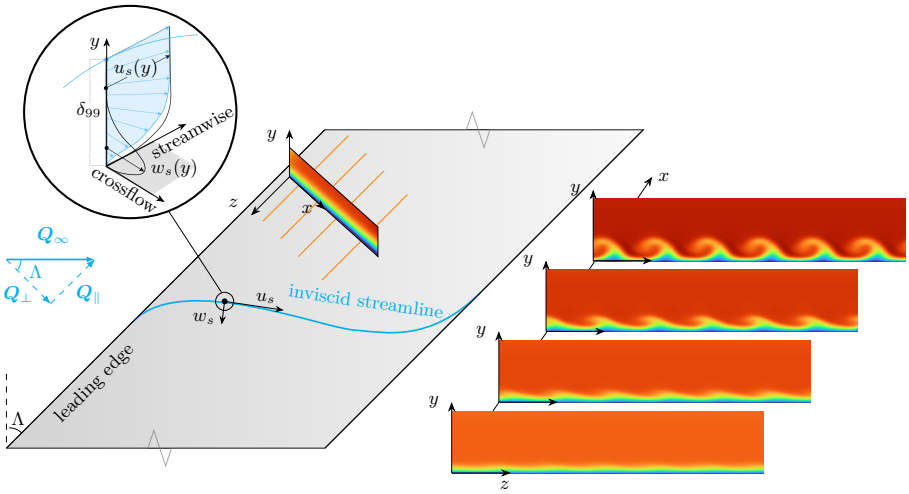

Figure 1.3: Sketch of swept-wing flow with stationary CFI. The wing is swept at angle Λ and the incoming freestream velocity vector Q_∞ is decomposed into components parallel ($Q_\parallel$) and orthogonal ($Q_\perp$) to the leading edge. The cyan curve shows the trajectory of an inviscid streamline along the wing, and the local coordinate system $\{x, y, z\}$ is oriented relative to the wing, where x is orthogonal to the leading edge, y is the wall-normal direction, and z is parallel to the leading edge. The z-y planes of streamwise velocity on the right, which are distributed along x (see orange lines on the wing for reference), show the modulation of the boundary layer due to the growth of the stationary CFI: blue and green (*low* velocity), orange (*moderate* velocity), red (*large* velocity). The free-stream velocity increases in x, as exemplified by the transition between orange and red colours in the planes. The top circular inset (adapted from Rius-Vidales (2022)) shows the boundary-layer organisation: the crossflow velocity profile, $w_s(y)$ in black, points normal to the inviscid-streamline direction, and the streamwise velocity profile, $u_s(y)$ in black, points tangent to it. The three-dimensional composite (blue) follows w_s near the wall and bends to match u_s farther from the wall. The marker δ_{99} expresses the 99% boundary-layer thickness.

A crossflow boundary layer (see figure 1.3) forms immediately downstream of the attachment line (Arnal, 1994), driven by the combined effect of sweep angle and chordwise pressure gradient. This process can be described as follows: the free-stream flow accelerates in the chordwise direction, as imposed by the aerofoil geometry, hence the inviscid streamline[1] in the potential-flow region bends inboard, that is, towards the wing root. In contrast, the velocity vectors in the boundary layer do not align with the direction of the edge velocity (figure 1.3); centrifugal and static pressure forces form an equilibrium in the potential-flow region. However, the reduced momentum of near-wall flow, in conjunction with essentially invariant static pressure along the wall-normal direction, shall be balanced by the viscous shear stress. This balance is

[1]The literature (see, for instance, (Haynes and Reed, 2000)) generally defines the local direction of the inviscid streamline as being tangent to the boundary-layer-edge velocity. This is customary in analyses carried out through the boundary-layer equations. However, this definition poses a problem for Navier-Stokes systems due to the non-uniformity of accelerated free-stream flow in the wall-normal direction. The reader is referred to § 2.1.1, where the definition of *inviscid streamline* is unequivocally established in this thesis.

maintained through a secondary-flow that develops towards the concave side of the inviscid streamline, as dictated by the direction and sense of pressure-force excess.

The convoluted organisation of the crossflow boundary layer may be represented by decomposing the velocity profiles into components orthogonal, called the crossflow profile, and parallel, called the streamwise profile, to the inviscid streamline (figure 1.3). Along the spatial region ranging from the attachment line to the x-location of maximum free-stream velocity, the inviscid streamline maintains its inboard curvature and the crossflow profile points inboard. The crossflow velocity is zero at the wall and approaches zero in the limit as it tends toward the boundary-layer edge. It peaks in between, with a strength of typically 5 to 10% of the free-stream velocity (Arnal, 1994). Past the peak in the wall-normal direction, the crossflow velocity decreases monotonically towards the free-stream, hence the crossflow velocity profile is inflectional (Arnal, 1994; Bippes, 1999; Saric et al., 2003).

At the chordwise location of maximum free-stream velocity, the inviscid streamline begins to bend outboard, i.e., towards the wing tip. Consequently, in the wing-aligned coordinate system, the in-plane trajectory of the inviscid streamline exhibits an inflection point. Downstream of this point in x, the near-wall portion of the crossflow profile reverses, i.e., it points towards the outboard direction, as driven by the adverse pressure gradient. The upper portion of the crossflow velocity profile maintains an inboard orientation, hence the profile as a whole develops an S-shape, but it may be completely reversed for a sufficiently strong adverse pressure gradient (Arnal, 1994).

1.2.3. Transition due to modal crossflow instability

Primary instability

Three-dimensional incompressible or subsonic laminar flow over a reference (i.e., without a step) swept wing supports four main instability mechanisms: attachment line, Tollmien-Schlichting (TS), Görtler, and crossflow (Saric et al., 2003). Considering a low-disturbance background, representative of free-flight environments, laminar-turbulent transition is typically initiated by the *exponential* growth of a primary instability eigenmode. The focus of this thesis is restricted to boundary layers dominated by the stationary crossflow instability (CFI).

Strong CFI growth typically occurs near the leading edge of highly swept wings, where the favourable pressure gradient is large (Arnal, 1994). The associated crossflow velocity profile is inflectional (§ 1.2.2), thus it is inviscidly unstable and prone to primary eigenmode growth (Mack, 1984; Saric et al., 2003). The associated instability, namely CFI, can manifest in the form of either travelling (i.e., non-zero temporal frequency) or stationary (i.e., zero temporal frequency) perturbations, with the dominant mode determined by receptivity conditions. On smooth surfaces and high-turbulence environments, the travelling CFI tends to dominate (Deyhle and Bippes, 1996), whereas stationary CFI is favoured in low-turbulence conditions with distributed surface roughness. Crossflow instabilities exhibit low receptivity to acoustic disturbances (Radeztsky et al., 1999). This thesis focuses on stationary CFI, given its greater relevance in low-turbulence free-flight environments (Saric et al., 2003).

The stationary CFI manifests in the boundary layer as a periodic array of co-

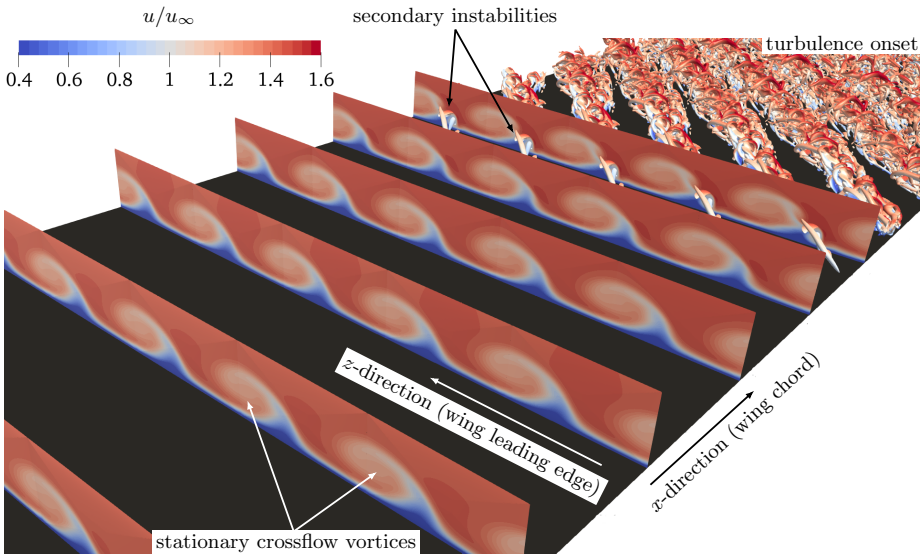

Figure 1.4: Elements of CFI-driven transition: stationary crossflow vortices are depicted in planes of instantaneous velocity u and secondary crossflow instabilities visualised as Q-criterion isosurfaces colour-coded by u. The velocity planes are oriented parallel to the wing's leading edge and u_∞ expresses the free-stream velocity.

rotating vortices that grow in strength along the direction orthogonal to the wing's leading edge (see figures 1.3 and 1.4). In addition to the crossflow velocity profile (§ 1.2.2), a set of velocity profiles approximately aligned with the direction orthoghonal to the inviscid streamline also exhibit inflectional behaviour (Bippes, 1999). According to Linear Stability Theory (LST) (§ 1.2.6), the wave perturbation associated with the CFI is oblique, i.e., it possesses a non-zero spanwise wavenumber. The wavenumber vector (§ 1.2.6) of the stationary CFI is nearly, though not exactly, orthogonal to the local inviscid streamline (Arnal, 1994). In contrast, the wavenumber vector of the travelling CFI points in different directions, forming an angle of about 85° to 89° with the inviscid streamline (Arnal, 1994), depending on the temporal frequency under consideration (Deyhle and Bippes, 1996).

A stage of non-linear growth and saturation of the stationary CFI follows the initial phase of *exponential* eigenmode growth; in turn, the non-linear growth phase typically precedes the stage of secondary-instability amplification and ultimately laminar breakdown. Early experiments showed that measured perturbation growth rates differ from those predicted by LST when sufficiently large perturbation amplitudes are attained (Müller, 1990; Kachanov and Tararykin, 1990; Bippes, 1991). To mildly relax the condition of boundary-layer homogeneity in x supporting LST (see § 1.2.6) effectively enables the use of the Parabolised Stability Equations (PSE) approach (Bertolotti et al., 1992; Herbert, 1997). The PSE is nowadays a popular method to assess the linear (LPSE) and non-linear (NPSE) stability of slowly varying shear

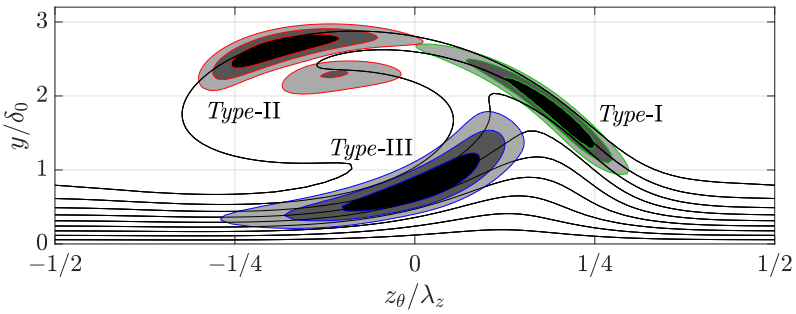

Figure 1.5: Sketch of classic secondary crossflow instabilities. Isocontours of stability eigenmode shapes at 40%, 60%, and 80% of their maximum value corresponding to *type*-I (green), *type*-II (red), and *type*-III (blue). Solid black lines in the background indicate the stationary crossflow vortex.

flows. The NPSE approach was proven capable of modelling the stages of strong non-linear crossflow-perturbation evolution (e.g., Bertolotti, 1996; Haynes and Reed, 2000; Casacuberta et al., 2022b), thereby confirming that the primary cause of the discrepancies between experimental observations and linear theory is the nonlinear saturation of the crossflow vortices.

Secondary instability

The steady perturbed flow, i.e., the base state deformed by the amplification of the stationary CFI, is prone to secondary instability mechanisms (see figure 1.4), ultimately responsible for laminar breakdown.

Secondary perturbations with high-frequency content (i.e., significantly higher than the primary travelling CFI) were initially identified in swept-Hiemenz (Poll, 1985; Malik et al., 1994) and swept-wing (Kohama et al., 1991; Deyhle and Bippes, 1996) flow configurations. Considering a swept-wing boundary layer, Malik et al. (1999) report two families of secondary instability eigenmodes (see figure 1.5) using Secondary Linear Stability Theory (SLST). The *type*-I (or z-)mode is produced most strongly by the spanwise shear in the outer part of the upwelling region of the primary crossflow vortex (i.e., "on its shoulder"). The *type*-II (or y-)mode, on the other hand, gains its energy primarily from the wall-normal shear and is located on top of the crossflow vortex. Theoretical results of Fischer and Dallmann (1991) identify a low-frequency eigenmode dominant in the near-wall shear layer of the crossflow vortex, which is nowadays referred to as *type*-III (Koch et al., 2000), see figure 1.5. The *type*-III is commonly interpreted as the primary travelling crossflow mechanism distorted by the stationary crossflow mechanism. A main difference between the primary travelling and secondary *type*-III perturbations is that the latter modifies the eigenmode topology and attains a local maximum at the shear layer underneath the crossflow vortex (Högberg and Henningson, 1998).

The DNS of Högberg and Henningson (1998) for a Falkner-Skan-Cooke boundary layer revealed *type*-I and *type*-III structures; however, manifestations of the *type*-II eigenmode are not observed. Consistent with findings of Högberg and Henningson

(1998), Wassermann and Kloker (2002) identify in their DNS the high-frequency *type*-I and low-frequency *type*-III instability mechanisms. *Type*-II perturbations are argued to arise only in *less physically relevant* cases, as for instance, when the primary crossflow vortex has a subcritical spanwise wavelength. In such cases, the narrow spacing between the stationary crossflow vortices potentially weakens the *type*-I amplification, which may facilitate the development of *type*-II perturbations (Wassermann and Kloker, 2002). Nonetheless, manifestations of the *type*-II mechanism in numerical simulations have been recently reported (Li et al., 2016, 2017).

In this thesis, transition under smooth-wall reference conditions is driven by the amplification of the *type*-I secondary crossflow instability. Figure 1.4 illustrates this scenario. The growth of the *type*-I instability gives rise to large-scale, finger-like structures. Similar to the eigenmode shape itself (figure 1.5), these finger-like structures develop along the laterally inclined shear layer of the stationary crossflow vortex and are tilted relative to the vortex axis (Janke and Balakumar, 2000; Wassermann and Kloker, 2002; Bonfigli and Kloker, 2007; Serpieri and Kotsonis, 2016).

Högberg and Henningson (1998) observe that high-frequency instabilities display larger growth rates than the low-frequency ones, but the onset of low-frequency instabilities is placed at a more upstream location than the high-frequency ones. The *type*-I,-II,-III mechanisms have been identified experimentally as well; see for instance Serpieri and Kotsonis (2016) for a detailed characterization of the secondary instabilities using Particle Image Velocimetry (PIV). Groot et al. (2018) investigate the validity and limitations of two-dimensional spanwise stability analysis, hereafter referred to as BiGlobal, applied to experimentally-measured base flows.

Bonfigli and Kloker (2007) conduct an extensive comparison between DNS and two-dimensional stability analysis of a stationary-crossflow-dominated boundary layer. Significant disagreement is reported in some cases in terms of spatial growth rates: the stability results are found to be very sensitive to the representation of the steady perturbed flow in the stability problem (Bonfigli and Kloker, 2007). In their study, they define three alternative extraction procedures, which ensure satisfaction of the continuity equation for the steady perturbed flow in three different *orthogonal* coordinate systems, while adhering to the slow-evolution hypotheses underlying the stability analysis. With the advent of the approach of Li and Choudhari (2011) employing a non-orthogonal coordinate system, the conditions of periodicity in the spanwise direction and flow quasi-invariance in the direction of the crossflow-vortex axis can be accounted for simultaneously. Casacuberta et al. (2022a) solve the two-dimensional stability problem using a non-orthogonal coordinate system, similar to the approach presented by Li and Choudhari (2011); the corresponding analysis is presented in chapter 8 of this thesis. A good agreement is reported between DNS and stability analysis in terms of amplification factors and perturbation shape of the *type*-I and *type*-III mechanisms (Casacuberta et al., 2022a).

Notwithstanding the fact that this thesis focuses on CFI-dominated flows, a forward-facing step induces localised regions of adverse pressure gradient (Tufts et al., 2017). Consequently, potential effects on transition stemming from a TS instability mechanism are not to be discarded *a priori*. In a reference scenario, when the crossflow velocity profile becomes S-shaped (§ 1.2.2) in the region of decelerated free-

stream flow (i.e., under an adverse pressure gradient), the unperturbed base flow becomes unstable to the TS mechanism (Arnal, 1994). It is an instability of the streamwise velocity profile (see § 1.2.2 and figure 1.3), thus the wavenumber vector points approximately in the direction of the inviscid streamline. Wassermann and Kloker (2005) numerically investigate the interaction between incoming crossflow vortices and TS instability. They conclude that the TS instability acts mainly as a source of low-frequency secondary instabilities and exhibits little influence on the final breakdown stage.

1.2.4. Alternative transition routes: non-modal growth

The lift-up effect

Morkovin (1969) introduced the notion that a primary instability mechanism, such as crossflow, could be *bypassed* by "another strongly amplifying mechanism". Over the years, the idea of *bypass transition* has been subject to considerable debate, particularly in relation to the influence of surface features[2]. Nonetheless, the existence of routes towards turbulence beyond the primary modal one is now well established, see the well-known diagram by Morkovin et al. (1994) in figure 8.9 (§ 8.1.1).

To explore the possibility of an alternative transition scenario, Lord Rayleigh's Inflection Point Theorem (Rayleigh, 1880) is invoked, which represents one of the foundational results in the development of flow stability theory. Namely, a necessary condition for *instability* (i.e., exponential growth of wave-like perturbations in the sense described in § 1.2.6) of parallel, incompressible, inviscid, two-dimensional flow is that the mean-velocity profile possesses an inflection point. Despite the significance and utility of this theorem, extensive experimental evidence has repeatedly demonstrated that perturbation growth can occur also in the absence of inflectional mean-flow profiles and that laminar-turbulent transition takes place in scenarios where linear modal stability analysis predicts stable flow, such as pipe flow.

The discovery of the so-called lift-up effect (Moffatt, 1967; Ellingsen and Palm, 1975; Landahl, 1975, 1980) aided to address this apparent contradiction. *Localised* streaky perturbations, which initially form linearly due to the lift-up effect, may subsequently experience stages of nonlinear growth and eventual breakdown. The breakdown of a localised *finite*-amplitude perturbation produces a turbulent spot (Henningson et al., 1990; Breuer and Landahl, 1990; Henningson et al., 1993). As an example, the lift-up effect has been linked to the premature transition of boundary-layer flow exposed to high levels of free-stream turbulence or distorted by surface features (Klebanoff, 1971; Kendall, 1985; Westin et al., 1994; Andersson et al., 2001; Matsubara and Alfredsson, 2001; Jacobs and Durbin, 2001; Reshotko, 2001; Brandt et al., 2003, 2004; Zaki and Durbin, 2005; White et al., 2005; Brandt, 2007).

The work of Ellingsen and Palm (1975) and Landahl (1975, 1980), on what later came to be known as the lift-up effect, essentially establishes that from the viewpoint of perturbation kinetic energy, any parallel inviscid shear flow is unstable to a large set of initial three-dimensional perturbations. This holds irrespective of the exponential

[2] In this thesis, the term *surface feature* refers to either a protrusion or a depression relative to the reference wall, characterised by a rapid variation in wall geometry. Specifically, the forward-facing step investigated here represents a sharp surface feature.

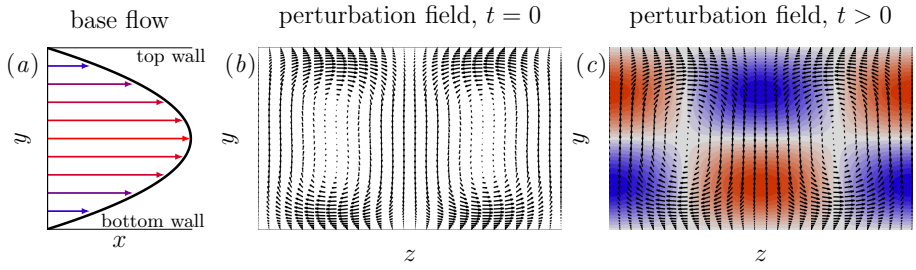

Figure 1.6: Sketch of the lift-up effect in channel flow: at $t = 0$, cross-stream perturbation rolls (b) interact with the base parabolic profile (a), inducing streamwise streaks of alternating low (blue) and high (red) momentum (c) that develop over time in accordance with the underlying velocity distribution in (a). Here, z denotes the channel-width direction and y is the inhomogeneous (wall-normal) direction along which the base-flow profile varies. The perturbation rolls in (b) were computed using the code OptimalDisturbance.m provided by Schmid and Brandt (2014).

(or, asymptotic modal) stability of the flow. The physical principle of the lift-up effect is illustrated typically as follows: a cross-stream perturbation of wave-like form superimposed on a shear layer, for instance a pair of counter-rotating vortical structures, *lifts up* low-momentum fluid and pushes down high-momentum fluid in adjacent regions of the flow field following the wave-like distribution. By retaining their original streamwise momentum, the displaced fluid particles introduce regions of streamwise-momentum deficit and excess and therefore induce inherently streamwise *perturbation* streaks that can attain very large amplitude over a short spatial or temporal extent. Figure 1.6 exemplifies this mechanism in channel flow.

The foundational studies by Ellingsen and Palm (1975) and Landahl (1975, 1980) were conducted under the assumption of inviscid flow, and the underlying concepts were extended by Hultgren and Gustavsson (1981) accounting for the effect of viscosity. By its principle, the lift-up effect is associated with the mechanism of *optimal* (Andersson et al., 1999; Luchini, 2000) streamwise vortices (i.e., the initial perturbation yielding the largest possible *transient growth* of kinetic perturbation energy) relaxing into streamwise streaks following a non-modal (or, *algebraic*, as opposed to *exponential*) growth (Butler and Farrell, 1992; Reddy and Henningson, 1993; Schmid and Henningson, 2001; Schmid, 2007).

Non-modal stability theory

Non-modal perturbation growth arises from the non-normality of the linear operator governing the evolution of perturbations in some cases, i.e., from the non-orthogonality of its associated eigenfunctions (Butler and Farrell, 1992; Trefethen et al., 1993; Reddy and Henningson, 1993; Schmid and Henningson, 2001; Schmid, 2007). Although this thesis addresses the non-modal growth of perturbations in space, it is instructive to introduce the underlying concept through a canonical example, such as the temporal initial-value problem (Schmid and Henningson, 2001).

Consider unswept, parallel flow, i.e., $\boldsymbol{v}_{\mathrm{B}} = [u_{\mathrm{B}}(y)\ 0\ 0]^{\mathrm{T}}$, and the linearised form of the perturbation equations (1.3) expressed using a velocity-vorticity formulation.

1

Solutions are sought in the form:

$$\begin{aligned} v'(x,y,z,t) &= \tilde{v}(y,t)\ \mathrm{e}^{\mathrm{i}(\alpha x+\beta z)} + \mathrm{c.c.},\\ \eta'(x,y,z,t) &= \tilde{\eta}(y,t)\ \mathrm{e}^{\mathrm{i}(\alpha x+\beta z)} + \mathrm{c.c.}, \end{aligned} \tag{1.5}$$

where $\eta' = \partial u'/\partial z - \partial w'/\partial x$ is the wall-normal perturbation vorticity and α and β indicate the chordwise and spanwise wavenumbers, respectively. In this scenario, the (linear) equations governing the evolution of the wall-normal perturbation velocity, v', and the wall-normal perturbation vorticity are

$$\left[\left(\frac{\partial}{\partial t} + \mathrm{i}\alpha u_\mathrm{B}\right)(\mathbb{D}^2 - ||\boldsymbol{k}||^2) - \mathrm{i}\alpha\frac{\mathrm{d}^2 u_\mathrm{B}}{\mathrm{d}y^2} - \frac{1}{Re}(\mathbb{D}^2 - ||\boldsymbol{k}||^2)^2\right]\tilde{v} = 0, \tag{1.6a}$$

$$\left[\left(\frac{\partial}{\partial t} + \mathrm{i}\alpha u_\mathrm{B}\right) - \frac{1}{Re}(\mathbb{D}^2 - ||\boldsymbol{k}||^2)\right]\tilde{\eta} = -\mathrm{i}\beta\frac{\mathrm{d}u_\mathrm{B}}{\mathrm{d}y}\ \tilde{v}. \tag{1.6b}$$

The boundary conditions read $\tilde{v} = \mathbb{D}\tilde{v} = \tilde{\eta} = 0$ at the wall and freestream. In (1.6), $\mathbb{D}$ denotes $\partial/\partial y$ and $\boldsymbol{k} = [\alpha\ \beta]^\mathrm{T}$ expresses the wavenumber vector (see § 1.2.6 for further details). Equations (1.6a) and (1.6b) are respectively the Orr-Sommerfeld and Squire equations, which may be expressed in matrix form as

$$\frac{\partial}{\partial t}\begin{bmatrix} ||\boldsymbol{k}||^2 - \mathbb{D}^2 & 0 \\ 0 & 1 \end{bmatrix}\begin{bmatrix}\tilde{v}\\ \tilde{\eta}\end{bmatrix} + \underbrace{\begin{bmatrix} \mathbb{L}_\mathrm{OS} & 0 \\ \mathrm{i}\beta(\frac{\mathrm{d}u_\mathrm{B}}{\mathrm{d}y}) & \mathbb{L}_\mathrm{SQ}\end{bmatrix}}_{\mathbb{L}_\mathrm{L}}\begin{bmatrix}\tilde{v}\\ \tilde{\eta}\end{bmatrix} = 0, \tag{1.7}$$

with $\mathbb{L}_\mathrm{OS}$ and $\mathbb{L}_\mathrm{SQ}$ indicating the Orr-Sommerfeld and Squire operators, respectively; see Brandt (2014) for reference. The eigenvalues of a non-normal matrix system such as (1.7) govern the dynamics in the long term, but not necessarily over a finite time (or finite spatial) horizon (Reddy and Henningson, 1993; Schmid and Brandt, 2014).

At the core of the present ideas lies the realisation that the wall-normal perturbation vorticity is linearly forced by the wall-normal perturbation velocity when $\beta \neq 0$ (Reddy and Henningson, 1993). This coupling arises primarily from the off-diagonal term in the operator $\mathbb{L}_\mathrm{L}$ (1.7), namely $\mathrm{i}\beta(\mathrm{d}u_\mathrm{B}/\mathrm{d}y)$, through which the solution of the Orr-Sommerfeld equation (1.6a) drives the solution to the Squire equation (1.6b) (Brandt, 2014; Zaki and Durbin, 2005).

This process typically manifests as the rapid, *transient* development of a streaky perturbation (Zaki and Durbin, 2005), i.e., growth of the horizontal velocity components, followed by a stage of viscous damping (Hultgren and Gustavsson, 1981). In contrast, a modal perturbation mechanism governs the evolution of perturbations that evolve like the background base flow and experience amplification of all velocity components by a common growth rate (Marxen et al., 2009) in the limit of parallel-flow approximation. Overall, applying these concepts –originally developed for parallel flows with well-defined wall-normal and wall-parallel components– to the highly deformed three-dimensional flow over the step presents a significant challenge and, in doing so, validates the approach introduced in the conclusion of § 1.2.6 where novel frameworks for instability modelling are proposed.

As described above in § 1.2.3, the amplification of stationary crossflow vortices is essentially a modal perturbation phenomenon. However, it is also well established that swept-wing flow supports significant non-modal growth of localised perturbations over a finite spatial extent (Breuer and Kuraishi, 1994; Corbett and Bottaro, 2001; Tempelmann et al., 2010). The crossflow-type perturbation wave exhibits the largest transient amplification among all wave types (Breuer and Kuraishi, 1994). Such non-modal growth can initiate the formation of modal crossflow vortices, for instance, in the presence of localised roughness elements (Zoppini et al., 2023), which subsequently evolve through the classic Orr-Sommerfeld-type mechanism. In other words, modal and non-modal growth mechanisms are complementary in swept-wing flow, as both excite similar perturbation structures (Corbett and Bottaro, 2001; Tempelmann et al., 2010), namely alternating streaks of high- and low-momentum fluid (Breuer and Kuraishi, 1994; Saric et al., 2003).

The secondary instability of localised perturbations

Sufficiently amplified streaky structures can sustain secondary instabilities (Andersson et al., 2001; Asai et al., 2002; Brandt et al., 2003; Konishi and Asai, 2004; Brandt, 2007; Ricco et al., 2011), eventually leading to premature breakdown and transition, even if the streaks are predicted to decay asymptotically. This scenario typically arises in the wake of a critical three-dimensional surface feature in unswept-flow conditions (De Tullio et al., 2013; Loiseau et al., 2014; Casacuberta et al., 2020) or during what is most commonly understood as *bypass transition*, where so-called Klebanoff modes (Kendall, 1985) develop in two-dimensional flow subjected to moderate-to-high levels of free-stream turbulence (Klebanoff, 1971; Westin et al., 1994; Matsubara and Alfredsson, 2001; Jacobs and Durbin, 2001; Brandt et al., 2004; Zaki and Durbin, 2005). Analogous to the instability mechanisms associated with Görtler vortices (Swearingen and Blackwelder, 1987), secondary instabilities of streaks are typically classified as either symmetric (called varicose) or anti-symmetric (called sinuous) based on their eigenmode shape relative to the streak shape. The spatial growth of sinuous and varicose instabilities leads to the shedding of quasi-streamwise-oriented vortices and hairpin-like vortices, respectively (Asai et al., 2002; Brandt and Henningson, 2002; Konishi and Asai, 2004).

1.2.5. Streaks in forward-facing steps: modal and non-modal effects

This thesis investigates the influence of sharp surface features, such as forward-facing steps, on the promotion of boundary-layer transition. Forward-facing steps are ubiquitous in a broad range of engineering applications, and consequently, extensive prior work has examined the topology and behaviour of the flow over such features. In most studies, the step is embedded in two-dimensional (i.e., unswept) boundary-layer flow, where streaks have been reported as characteristic flow structure associated with the step (e.g., figure 1.7 (*a*)).

The computational analysis by Wilhelm et al. (2003) shows that the two-dimensional unperturbed base flow around a forward-facing step can exhibit regions of flow recirculation both upstream (e.g., figure 1.7 (*b*)) and downstream of the step. Their

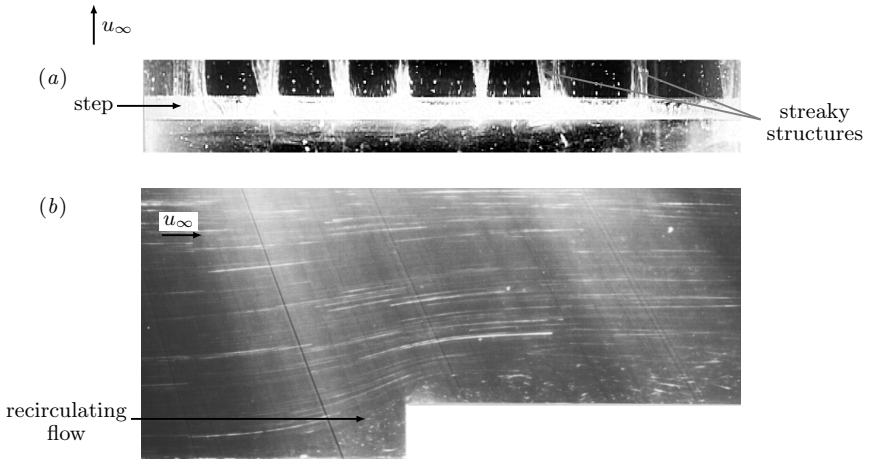

Figure 1.7: Elements of forward-facing-step flow in a channel: (a) top view (flow from bottom to top) showing streaky structures at the upper step corner via hydrogen bubble visualisation (Stüer et al., 1999) and (b) side view (flow from left to right) illustrating streamline deflection and the upstream recirculation region forming ahead of the step, visualised using a tracer method (Ando and Shakouchi, 2004).

study emphasises the mechanisms through which the initially two-dimensional base flow evolves into a strongly three-dimensional one. Wilhelm et al. (2003), and later Marino and Luchini (2009), attribute this transition of the step-flow topology to a sensitive response to disturbances present in the incoming flow. It is noted that, in this context, "transition" refers exclusively to changes in the laminar-flow topology.

Specifically, in three-dimensional swept-wing flow, the recirculating-flow regions at the step are not a closed system, but an open helical one, due to the presence of spanwise velocity (Tufts et al., 2017). The chordwise pressure gradient changes significantly in a very short spatial region: it switches from adverse immediately upstream of the step, to favourable around the step apex, and back to adverse immediately downstream of the step (Tufts et al., 2017). This rapid pressure-gradient changeover induces a pronounced spanwise modulation of the flow at the step (Eppink, 2020) and of the CFI in particular (Rius-Vidales and Kotsonis, 2021).

For unswept conditions, both experimental (Stüer et al., 1999) (figure 1.7 (a)) and numerical (Lanzerstorfer and Kuhlmann, 2012) studies have reported the existence of streaky structures close downstream of the step. The mechanisms of streak formation and growth around forward-facing steps have been subject of discussion. This feature has been associated with the lift-up effect (Lanzerstorfer and Kuhlmann, 2012), as well as with a Görtler-type instability mechanism (Chiba et al., 1995; Pollard et al., 1996). However, Stüer et al. (1999) indicate that their experiments do not support the latter in that the instability at the step must be of a type stronger than the Görtler instability. Wilhelm et al. (2003) and Marino and Luchini (2009) further argue that the streaks cannot originate from an absolute instability of the recirculating flow at

the step, at least for the parameter choices considered in their studies. The streaks are argued to be a linear perturbation effect, inasmuch as the intensity of streaks changes proportionally to that of incoming disturbances (Wilhelm et al., 2003).

Marxen et al. (2009) analyse the two-dimensional separating boundary layer over a flat plate and describe the development of three-dimensional streaky structures. Arguing that the amplification of the perturbation streaks in such flow environments may result from a modal mechanism, a non-modal mechanism, or a mixture of both, Marxen et al. (2009) employ a set of diagnostic metrics to distinguish between these possibilities. The flow environment studied by Marxen et al. (2009) is similar to the present swept-step flow: in both scenarios, the boundary layer is subject to a favourable-to-adverse pressure gradient and a recirculating-flow region develops (Marxen et al., 2009; Tufts et al., 2017; Eppink, 2020).

Marxen et al. (2009) conclude that non-modal growth ascribed to the lift-up effect governs the perturbation response initially. Further downstream, within the adverse-pressure-gradient region, a modal instability of Görtler type sets in as dominant perturbation mechanism. To segregate between essentially modal- and non-modal-growth regimes, Marxen et al. (2009) decompose the perturbation vector into components tangential and normal to the *local* base-flow orientation (i.e., the local base-flow vector) instead of tangential and normal to the wall. While non-modal growth by the lift-up effect favors the amplification of the flow-aligned perturbation component, in the case of a modal instability, all perturbation components ought to exhibit a similar growth rate (Marxen et al., 2009), within the limit of parallel-flow approximation.

A similar decomposition of the perturbation vector is employed by Lanzerstorfer and Kuhlmann (2012) to scrutinise the mechanisms of energy transfer between stationary perturbations and the unperturbed base flow in unswept forward-facing-step flow. Specifically, following the methodology of Albensoeder et al. (2001), Lanzerstorfer and Kuhlmann (2012) decompose the production term of the Reynolds-Orr equation (§ 1.2.6) by expressing the perturbation vector into components tangential and normal to the local base-flow orientation. A principal term emerging from this decomposition characterises the lift-up effect (Lanzerstorfer and Kuhlmann, 2011, 2012; Loiseau et al., 2016; Picella et al., 2018), that is, the kinetic-energy transfer rate between unperturbed base flow and streamwise (i.e., flow aligned) perturbations by the action of the cross-stream (i.e., flow orthogonal) perturbations. The term provides the dominant contribution around the step, thus Lanzerstorfer and Kuhlmann (2012) argue that the lift-up effect contributes mainly to the amplification of streaks in unswept step flow. Similar analysis and interpretation have been used in studies of cavity flow (Albensoeder et al., 2001; Picella et al., 2018).

1.2.6. Instability modelling: classic and novel approaches

As mentioned above, Direct Numerical Simulations (DNS) of the three-dimensional incompressible Navier-Stokes equations are carried out in this thesis to investigate instability and transition mechanisms. The DNS setup is guided by wind-tunnel experiments (Rius-Vidales and Kotsonis, 2021), in which a monochromatic stationary CFI is enforced through Discrete Roughness Elements (DRE) distributed along the

1

wing span (Zoppini et al., 2023). This is common practice in academic investigations to avoid flow non-uniformity (Reibert et al., 1996), given to the high receptivity of CFI to surface micro-roughness (Deyhle and Bippes, 1996).

By virtue of the periodicity of perturbations in the leading-edge-parallel (spanwise) direction, the stationary content of the perturbation field $\boldsymbol{q}'$ (1.2) can be decomposed into Fourier modes. Accordingly, the stationary velocity-perturbation field from steady-state DNS computations is expressed as

$$\boldsymbol{v}'(x,y,z) = \sum_{j=-N}^{N} \underbrace{\tilde{\boldsymbol{v}}_{(0,j)}(x,y)\ \mathrm{e}^{\mathrm{i}j\beta_0 z}}_{\boldsymbol{v}'_{(0,j)}}, \tag{1.8}$$

where $\tilde{\boldsymbol{v}}_{(0,j)} \in \mathbb{C}^3$ are the Fourier coefficients[3], N is (one half of) the number of modes, and $\mathrm{i}^2 = -1$. The symmetric term $\boldsymbol{v}'_{(0,-j)}$ is the complex conjugate of $\boldsymbol{v}'_{(0,j)}$, which is hereafter denoted by $\{\cdot\}^\dagger$ or c.c., $\boldsymbol{v}'_{(0,0)}$ is the mean-flow distortion, and $\beta_0 \in \mathbb{R}$ is the fundamental perturbation wavenumber in z. The moduli of the components of $\tilde{\boldsymbol{v}}_{(0,j)}$ read $|\tilde{u}|_{(0,j)}$, $|\tilde{v}|_{(0,j)}$, and $|\tilde{w}|_{(0,j)}$ and the associated phases are denoted by $\varphi^u_{(0,j)}$, $\varphi^v_{(0,j)}$, and $\varphi^w_{(0,j)}$.

Given a stationary mode with $\beta = j\beta_0$, where $j = 1, \ldots, N$, the norm of the perturbation vector at every point in space reads

$$||\boldsymbol{v}'_{(0,j)}|| \equiv |\tilde{\psi}|_{(0,j)} = \sqrt{|\tilde{u}|^2_{(0,j)} + |\tilde{v}|^2_{(0,j)} + |\tilde{w}|^2_{(0,j)}}. \tag{1.9}$$

In turn, $|\tilde{\psi}|_{(0,j)}$ relates to the kinetic energy of mode $j\beta_0$ at a given x-location as

$$E_{j\beta_0} = \frac{1}{2}\int_0^\infty |\tilde{\psi}|^2_{(0,j)}\ \mathrm{d}y. \tag{1.10}$$

The most energetic wave component (1.8) of the stationary CFI, the so-called fundamental or primary CFI mode, appears in the mode $|j| = 1$ of decomposition (1.8). As it will be elaborated upon in this thesis, when a surface step is present, the fundamental CFI is contained within, but it is not exclusively the, mode $|j| = 1$.

The present DNS make no assumptions about the perturbation growth character or the spatial evolution of the unperturbed base flow. In contrast, classic boundary-layer instability theory is built on a framework constrained by a set of relatively restrictive assumptions. First, the unperturbed base flow is taken as a *parallel* flow, i.e., it is a one-dimensional solution of the Navier-Stokes equations. The reader is referred to Mack (1984), Saric (1994), and Arnal (1994) for completeness in the definition of parallel flow; particularly, regarding a consistent measure of the perturbation amplification factor, which is a central concept for empirical transition-prediction methods (Van Ingen, 1956; Smith and Gamberoni, 1956). Second, the perturbations are assumed to be of *small*-amplitude sufficiently upstream of the transition region; that is, they are the solution to the perturbation equations (1.3-1.4) linearised about the unperturbed base flow.

[3]In this thesis, the nomenclature $\{\cdot\}_{(0,j)}$ denotes perturbation quantities of spanwise wavenumber $j\beta_0$ and of stationary nature.

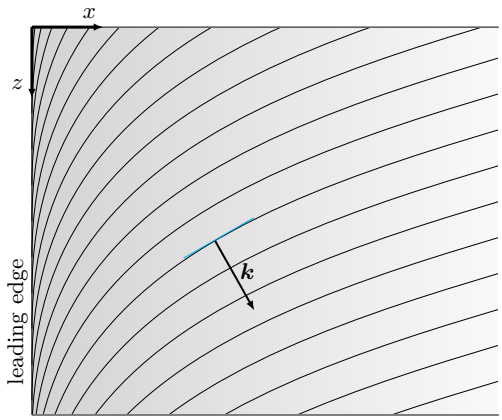

Figure 1.8: Illustration of perturbation organisation near the leading-edge region: lines of constant phase (solid black) and the direction of the wavenumber vector $\boldsymbol{k}$.

Leveraging the two above-mentioned assumptions transforms the perturbation equations (§ 1.2.1) into a system of partial differential equations with coefficients that are a function of y only. This suggests solutions to be sought in *wave* form, i.e.,

$$\boldsymbol{q}'(x,y,z,t) = \tilde{\boldsymbol{q}}(y)\, \mathrm{e}^{\mathrm{i}(\alpha x+\beta_0 z-\omega t)} + \text{c.c.}, \tag{1.11}$$

$\tilde{\boldsymbol{q}} = \tilde{\boldsymbol{q}}_r + \mathrm{i}\tilde{\boldsymbol{q}}_i$, to reduce the system to a set of ordinary differential equations (Saric, 1994). Here, $\tilde{\boldsymbol{q}}$ denotes the shape function, $\alpha = \alpha_r + \mathrm{i}\alpha_i$ under the so-called spatial approach, and the temporal angular frequency, ω, is set to zero when perturbations are assumed to be stationary, as in the case for CFI. Correspondingly, α_i is the perturbation growth rate and α_r expresses the perturbation wavenumber in x. By expressing $\tilde{\boldsymbol{q}} = |\tilde{\boldsymbol{q}}|\mathrm{e}^{\mathrm{i}\varphi}$, $\varphi \in \mathbb{R}$, and recalling that (1.11) is real-valued, the magnitude of ansatz (1.11), denoted by A, satisfies

$$\frac{1}{A}\frac{\mathrm{d}A}{\mathrm{d}x} = -\alpha_i. \tag{1.12}$$

Mack (1977) notes that "obviously, A could have been chosen at any y and [(1.12)] would be the same. It is this property that enables us to talk about the *amplitude* of an instability wave in the same manner as the amplitude of a water wave, even though this amplitude is a function of y." By analogy with other wave phenomena, a wavenumber vector, $\boldsymbol{k}$, may be defined (figure 1.8) to characterise wave propagation, with magnitude $||\boldsymbol{k}|| = \sqrt{\alpha_r^2 + \beta_0^2}$, forming an angle with the x-direction equal to $\psi_k = \arctan(\beta_0/\alpha_r)$.

On considering the solution ansatz (1.11) and formulating suitable boundary conditions, the perturbation equations constitute an eigenvalue problem (see also § 1.2.4), known as the Orr-Sommerfeld (OS) equation. For an unbounded fluid system such

1

as boundary-layer flow, the eigenvalue problem generally comprises a finite set of discrete eigenvalues and a continuous spectrum (Grosch and Salwen, 1978; Mack, 1984; Schmid and Henningson, 2001). Central to Linear Stability Theory (LST) is the idea that, within the present framework and for a specified base flow, Reynolds number, and input stability parameters, the fundamental CFI can be traced back to a *mode*, i.e., an eigenfunction associated with a discrete complex eigenvalue (α_r, α_i).

For the specified Reynolds number and wave parameters, whether this *crossflow mode* displays a tendency to exponentially grow (i.e., the base flow is destabilised and $\alpha_i < 0$), decay (i.e., the base flow is stabilised and $\alpha_i > 0$), or remain neutral (i.e., $\alpha_i = 0$), is dictated solely by the evolution of the pertinent local base-flow profile in y. In this context of *local* stability analysis, i.e., inherent to the local parallel-flow profile, a crossflow instability is classified as convective, meaning it amplifies as it convects away from the source of instability. In contrast, an absolute instability grows in both upstream and downstream directions from the source (Huerre and Monkewitz, 1990). It should be noted that the terms *global*, which refers to the flow field as a whole (Huerre and Monkewitz, 1990), and *local* are sometimes used differently across the literature (Theofilis, 2003).

The description of stationary CFI as a single *mode* or *wave* subject to *asymptotic exponential growth* (1.11) will be shown to be untenable near sharp surface features, such as the forward-facing step investigated in this thesis. Building upon insights obtained from the unrestricted DNS, this thesis examines perturbation behaviour from a viewpoint different than the classic analysis of eigensolutions of a linear response equation. Specifically, the discussion of stationary perturbation effects at the step centres on three main directions of novelty that set their foundations on classic stability concepts, which are introduced next:

(*i*) Projection of the perturbation field onto the local base flow: the perturbation field is decomposed relative to the local orientation of the base-flow streamlines rather than relative to the wall. Under the classic wall-based decomposition, the perturbation field of a stationary Fourier mode j (1.8) reads

$$\boldsymbol{v}'_{(0,j)}(x,y,z) = u'_{(0,j)}(x,y,z)\hat{\boldsymbol{\imath}} + v'_{(0,j)}(x,y,z)\hat{\boldsymbol{\jmath}} + w'_{(0,j)}(x,y,z)\hat{\boldsymbol{k}}, \qquad (1.13)$$

where $\hat{\boldsymbol{\imath}} = [1\ 0\ 0]^{\mathrm{T}}, \hat{\boldsymbol{\jmath}} = [0\ 1\ 0]^{\mathrm{T}}, \hat{\boldsymbol{k}} = [0\ 0\ 1]^{\mathrm{T}}$ and $u'_{(0,j)}$, $v'_{(0,j)}$, $w'_{(0,j)}$ are complex-valued scalar fields. Following the ideas of Albensoeder et al. (2001) and Lanzerstorfer and Kuhlmann (2012), the perturbation field is alternatively decomposed into a component $\boldsymbol{v}'_{t,(0,j)}(x,y,z) : \mathbb{R}^3 \to \mathbb{C}^3$ characterising the perturbation acting tangent to (i.e., in the local direction of) the base-flow streamlines and a complementary vector component $\boldsymbol{v}'_{n,(0,j)}(x,y,z) : \mathbb{R}^3 \to \mathbb{C}^3$. The latter characterises the perturbation acting normal to the base-flow streamlines, i.e., in the cross-stream direction, such that $\boldsymbol{v}'_{(0,j)} = \boldsymbol{v}'_{t,(0,j)} + \boldsymbol{v}'_{n,(0,j)}$. Details of the decomposition are provided in § 3.2, and chapters 4, 5, and 6 further develop the rationale for this approach.

(*ii*) Structural identification: $\boldsymbol{v}'_t$ and $\boldsymbol{v}'_n$ carry information on the main structural elements composing the CFI. Although the growth of CFI generates co-rotating vortices modulating the boundary layer (see figures 1.3 and 1.9 (*a*)),

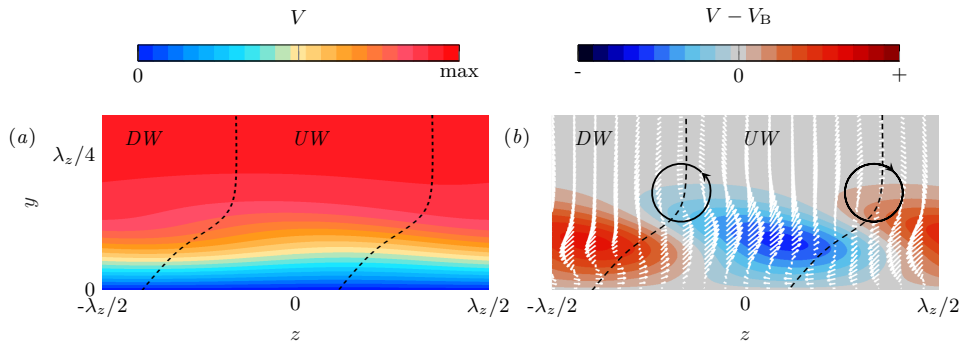

Figure 1.9: (*a*) Manifestation of the CFI in the *total* flow field (i.e., base flow plus perturbation) and (*b*) at a perturbation level (i.e., when isolated from the base flow). In (*b*), the CFI is represented following the decomposition proposed in this thesis (§ 3.2): regions of streamwise momentum deficit (blue contour) and excess (red contour) accompanied by cross-stream rolls (white arrows in the plane). Dashed lines segregate cross-stream perturbation upwash (UW) and downwash (DW) and circular black arrows indicate the sense of rotation of the rolls. Here, V denotes streamwise velocity (see §§ 3.2 and 6.2.1 for details) and the subscript "B" indicates base-flow quantity. The CFI wavelength is denoted by λ_z.

when isolated from the unperturbed base flow, the CFI appears as a set of perturbation rolls. That is, streamwise-vortical structures described by $\boldsymbol{v}'_n$, that counter-rotate with respect to each other (see white arrows in figure 1.9 (*b*)). Despite the motion by $\boldsymbol{v}'_n$ having a small amplitude relative to $\boldsymbol{v}'_t$, it is efficient in redistributing streamwise momentum. This produces a *scar* or distortion in the flow that appears as regions of streamwise-velocity excess and deficit (i.e., $\boldsymbol{v}'_t$), see colour contours in figure 1.9 (*b*), as similarly reported for the Görtler instability (Floryan, 1986). In swept-wing flow, Saric et al. (2003) correspondingly describe that "the weak motion of the [stationary crossflow] wave convects $\mathcal{O}(1)$ streamwise momentum producing a strong distortion in the streamwise boundary-layer profile".

Accordingly, a key advantage of the proposed perturbation projection is its ability to identify and trace coherent perturbation structures within the complex step flow, characterised by strong streamline curvature (Eppink, 2020; Rius-Vidales and Kotsonis, 2021) and intense shear. The effectiveness of this approach is demonstrated and analysed in chapters 4, 5, and 6.

(***iii***) **Characterisation of the mechanisms of energy exchange:** energy-balance equations of the stationary harmonic perturbation modes (1.8) are formulated in this thesis (§ 3.1). These are used towards characterising linear and nonlinear mechanisms of energy exchange between relevant perturbation structures and with the base flow. To that end, an extended formulation of the well-known Reynolds-Orr equation is proposed, considering each perturbation mode (1.8), individually. The Reynolds-Orr equation governs the temporal change of the

perturbation kinetic energy in a volume V, here denoted by E_V, so that

$$\frac{\mathrm{d}E_V}{\mathrm{d}t} = P + D. \tag{1.14}$$

The $D < 0$ expresses viscous dissipation and P indicates production, that is, the kinetic-energy transfer rate between the unperturbed base flow and the perturbation field as a whole. Equation (1.14) is specific to the case of a localised or spatially-periodic perturbation. In this scenario, the integration of (1.3) leads to the vanishing of boundary terms, including the non-linear mechanism or perturbation advection, see Schmid and Henningson (2001).

1.3. Effects of two-dimensional surface features on instability and transition

This section reviews the state of the art on the effects of two-dimensional surface features in promoting instability growth and laminar-turbulent transition in boundary-layer flows. It also discusses recent experimental and numerical studies that highlight mechanisms of transition delay induced by a surface forward-facing step.

1.3.1. Mechanisms of transition advancement

The understanding of interactions between boundary-layer instabilities and surface features is pivotal to laminar-turbulent transition research. Early flight experiments on smooth wings (Jones, 1938) showed that even very small surface features can drastically shift the transition front upstream. For decades, the aerodynamics community has devoted considerable efforts to characterising the mechanisms by which surface features alter the transition route. With few exceptions (Fransson et al., 2006; Fujii, 2006; Saric et al., 2011), general consensus holds that rapid spatial variations in surface geometry promote upstream movement of the transition front.

As such, the published literature on the effects of spanwise-invariant surface features on transition elaborates mainly on how transition is promoted. From early experiments on two-dimensional (i.e., unswept) flow, it was established that the transition-front location is bounded between the surface feature and the transition-front location in reference (i.e., feature-free) conditions (Fage and Preston, 1941; Dryden, 1953; Tani, 1969). Tests performed on a flat surface (i.e., zero-pressure-gradient flow) with a two-dimensional wire mounted on it showed that increasing either the wire height or the free-stream velocity caused a forward shift of the transition front (Fage and Preston, 1941; Tani, 1969). Much of the empirical knowledge available at the time materialised essentially in a so-called roughness Reynolds number (or roughness-equivalent Reynolds number), which became a popular transition-correlation parameter (Smith and Clutter, 1959; Braslow, 1960). It is defined as

$$Re_{hh} = \frac{u_h h}{\nu}, \tag{1.15}$$

where h is the roughness height, ν is the kinematic viscosity, and u_h is the velocity of the undisturbed boundary layer at the element height. The roughness Reynolds

number, Re_{hh}, was for instance reported as a successful correlation parameter for tests performed with two-dimensional wires (Smith and Clutter, 1959). However, this thesis (see chapters 7 and 8) shows that the transition regimes resulting from the interaction between a pre-existing CFI and a forward-facing step are influenced by the amplitude of the incoming perturbation. Therefore, they cannot be categorised exclusively based on Reynolds number and wavelength, as also reported by Eppink (2020) and Rius-Vidales and Kotsonis (2020, 2021).

Historically, two essential agents have been debated regarding the mechanisms by which a surface feature promotes transition. On the one hand, the destabilising influence of the mean-flow profiles in the wake of the surface feature. In particular, Klebanoff and Tidstrom (1972) argue that the effect of two-dimensional roughness is a "stability-governed phenomenon" in that the roughness "does not introduce disturbances that add to the disturbance level in the boundary layer". On the other hand, perturbations introduced by the surface feature itself. In this regard, the work of Goldstein (1985) is highlighted, as it investigates the coupling between an incoming TS instability and acoustic disturbances scattered by the surface feature (Saric et al., 2002). Similarly, Fasel et al. (1977) argue that a backward-facing step influences transition by acting as a source of perturbations through vortex shedding in the separated flow downstream of the step.

At present, the effect of a two-dimensional surface feature on two-dimensional boundary layers is primarily attributed to the generation of TS perturbations (Ergin and White, 2006), and, with few exceptions (Radeztsky et al., 1991), the presence of the feature promotes transition (Nayfeh, 1992; Perraud and Séraudie, 2000). In a three-dimensional boundary layer, a surface strip acts mainly by producing stationary crossflow vortices (Saric, 1994). The scope of this thesis, however, lies in assessing the influence of a two-dimensional surface feature on a pre-existing instability.

For a TS perturbation interacting with a localised surface feature, Wu and Hogg (2006) report that the incoming TS wave is scattered at the feature. It thereby experiences a change in amplitude, quantified by a transmission coefficient (Wu and Hogg, 2006), which expresses the relative change in amplitude of the TS perturbation before and after scattering. When evaluated for the separated flow over a two-dimensional hump, Xu et al. (2016) find a strong increase in the transmission coefficient, as compared with that of a smaller element. For an analogous scenario encompassing an incoming TS perturbation and a hump, Park and Park (2013) conclude that their interaction is governed by both viscous and inviscid instability mechanisms. The former is associated with the original TS mechanism, whereas the latter is linked to the inflectional nature of the base-flow profiles in the vicinity of the hump. Furthermore, Park and Park (2013) report significant discrepancies in the predicted perturbation growth rates when comparing PSE (§ 2.2.3) and LST (§ 1.2.6).

For the case of a swept laminar separation bubble interacting with an incoming oblique TS perturbation or a crossflow perturbation, Hetsch and Rist (2009) highlight the superior accuracy of PSE over LST. Edelmann and Rist (2014) report good agreement between DNS and LST in terms of the perturbation amplification factor in two-dimensional forward-facing-step flows. Following the work of Perraud et al. (2004) and Crouch et al. (2006), Edelmann and Rist (2014) quantify the influence of

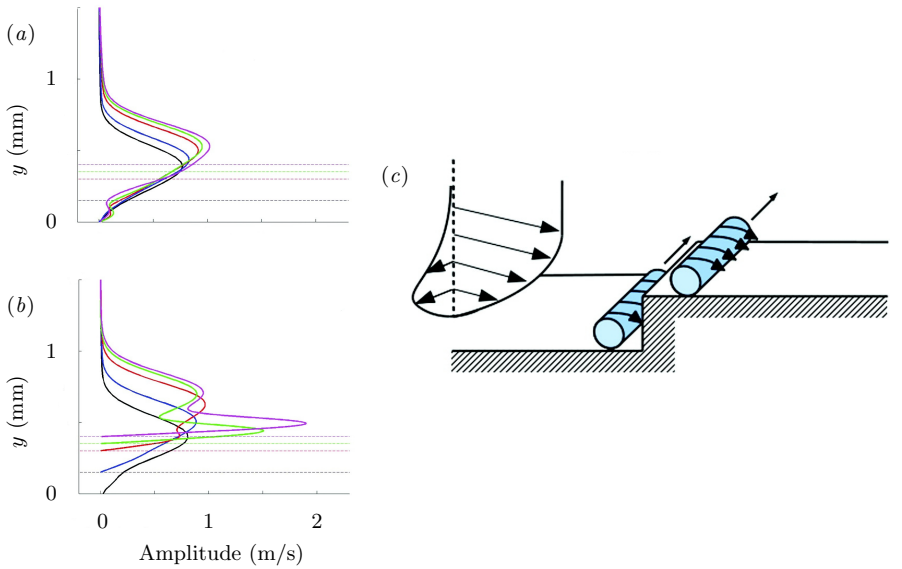

Figure 1.10: Step-CFI interaction model proposed by Tufts et al. (2017). (c) Schematic of step-induced helical flow. (*a*,*b*) Stationary CFI perturbation profiles immediately upstream (*a*) and immediately downstream (*b*) of *small* (blue), *moderate* (red), and *large* (green and magenta) steps, with the no-step case shown in black, reproduced from Tufts et al. (2017, cf. figures A4 and A6).

a forward-facing step by comparing the modified perturbation amplification factor with that of the reference no-step case. Among the vast literature on the effect of two-dimensional surface features on the laminar-turbulent transition, pressure-gradient effects have historically received little attention. The sparse literature on this topic motivated a series of experiments involving forward-facing steps mounted on unswept flat plates with a prescribed favourable pressure gradient (Drake et al., 2008, 2010). Duncan Jr. et al. (2013) extend the work of Drake et al. (2010) by adding sweep angle to account for the instability mechanisms present in three-dimensional flows. In a stationary-CFI-dominated scenario, Duncan Jr. et al. (2013) observe a reduction in the critical roughness Reynolds number compared with the equivalent two-dimensional case of Drake et al. (2010).

Tufts et al. (2017) subsequently performed numerical simulations to investigate the interaction between a stationary crossflow instability and forward-facing steps of various heights under the same flow conditions as Duncan Jr. et al. (2014) and Crawford et al. (2015). The critical step height, above which the steps begins to significantly affect transition, is linked by Tufts et al. (2017) to a strong and sudden amplification of the incoming stationary CFI at the step (see green and magenta curves in figure 1.10 (*a*) and (*b*)). In particular, this amplification stage is attributed to the "constructive interaction" between the incoming stationary crossflow vortices and the step-induced recirculating flow; figure 1.10 (c) depicts the resulting helical motion underpinning the step-CFI interaction model proposed by Tufts et al. (2017).

Nonetheless, lack of evidence supporting this mechanism of interaction was reported in subsequent studies (Eppink, 2018; Eppink and Casper, 2019; Eppink, 2020). In turn, the universal validity of the model proposed by Tufts et al. (2017) to determine critical step heights has been questioned by Rius-Vidales and Kotsonis (2020).

Despite the scientific debate surrounding the mechanism proposed by Tufts et al. (2017), similar perturbation organisation around the step have been consistently reported. The CFI lifts off the wall as it approaches the step and the perturbation profile, i.e., the perturbation *shape* in the wall-normal direction, develops a distinctive secondary peak close to the wall (figure 1.10 (*b*)). There is currently no consensus among previous studies regarding the origin or physical nature of this additional perturbation structure (Tufts et al., 2017; Eppink, 2018; Cooke et al., 2019; Eppink, 2020; Rius-Vidales and Kotsonis, 2021, 2022), nor a clear understanding of its potential impact on transition advancement. The secondary perturbation peak is accompanied in space by a new (i.e., locally-formed) set of vortices, as identified experimentally by Eppink (2018, 2020) and Rius-Vidales and Kotsonis (2021).

There is a growing consensus in the literature that the incoming CFI becomes amplified at the step. However, in contrast to Tufts et al. (2017), this is ascribed by Eppink (2020) to the destabilising effect of the inflectional profiles accompanying the regions of flow separation and reversal of the crossflow velocity component in the near-step regime. Moreover, Eppink (2020) identifies a second spatial stage of stationary-crossflow amplification at the end of the flow-separation region. This is linked to non-linear growth mechanisms triggered by the interaction of the harmonic perturbation components: the deformation of the separation bubble under the action of the crossflow vortices introduces multiple streamwise-oriented vortices with harmonic wavelengths (Eppink, 2020). An enhancement of the harmonic activity in this regime is also reported by Rius-Vidales and Kotsonis (2021), who, conversely, suggest amplification of the harmonic crossflow modes via non-linear forcing of the fundamental mode. Furthermore, Rius-Vidales and Kotsonis (2021) report a strong spanwise modulation of the trajectory of the crossflow vortices at the step, likely driven by the local pressure-gradient changeover.

It bears emphasising that the published studies on the effect of a step on CFI-driven transition differ notably in their numerical choices of design parameters, including step height, Reynolds number, and the amplitude of the incoming CFI. For example, Tufts et al. (2017) investigate step heights from 150 to 400 μm, Eppink (2020) considers step heights from 1270 to 1700 μm, and Rius-Vidales and Kotsonis (2021) examine step heights from 368 to 759 μm. For the flow conditions of Eppink (2020), the steps reach between 53 and 71% of the undisturbed boundary-thickness, whereas for the flow conditions of Rius-Vidales and Kotsonis (2021) –which have guided the numerical setups in this thesis– they reach between 33 and 53% of the undisturbed boundary-thickness. Furthermore, the stationary-CFI evolution is linearly dominated at the step location in the study of Eppink (2020), which is not the case in Rius-Vidales and Kotsonis (2021, 2022).

Concerning the impact of the step on unsteady instability, the literature debates the step-induced mechanisms that promote early transition, which are typically classified into three regimes: mild (subcritical), moderate (critical), and abrupt (super-

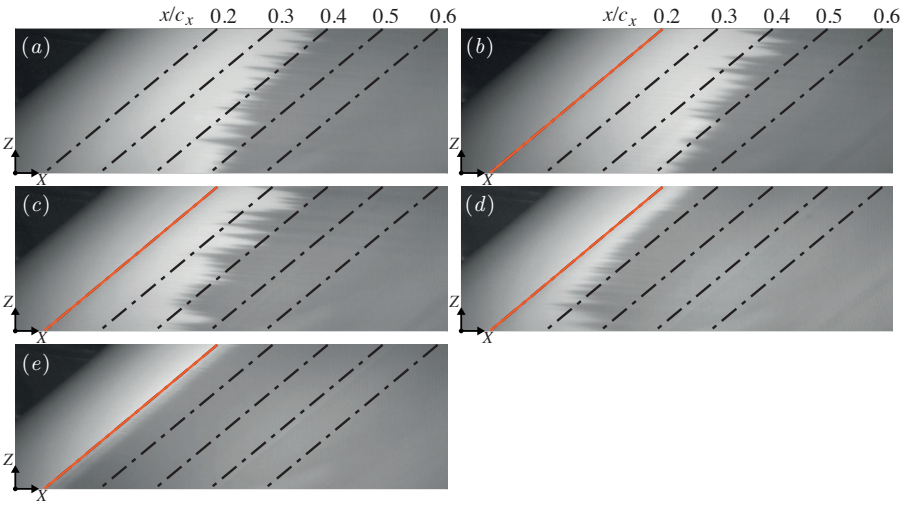

Figure 1.11: Wall temperature maps displaying the effect of the forward-facing step (orange line) on the transition-front pattern in swept-wing flow, reproduced from Rius-Vidales and Kotsonis (2021): reference (no-step) case (a), subcritical transition (c), critical transition (d), supercritical transition (e), and transition delay (b). Flow moves from left to right: bright regions indicate laminar flow, dark regions indicate turbulent flow. Here, x is the coordinate orthogonal to the leading edge (with wing chord $c_x = 0.9$ m), while X and Z denote coordinates aligned with the wind-tunnel walls.

critical) upstream shift of the transition front induced by the step. These transition regimes are illustrated in figure 1.11. Here, the term *abrupt* indicates that the transition front shifts immediately downstream of the step.

The elucidation of the mechanisms responsible for transition advancement in this thesis focuses on the critical and supercritical regimes. For a moderate upstream shift of the transition front –the critical regime– Rius-Vidales and Kotsonis (2022) attribute early transition to the enhancement of *type*-I and *type*-II secondary crossflow instabilities, arising from the destabilisation of the incoming stationary CFI by the step. This proposed mechanism of transition advancement stands in contrast to the conclusion of Eppink (2020), who instead attributes early transition to vortex shedding initiated at the step. The latter mechanism is associated with a shear-layer instability of Kelvin-Helmholtz (KH) type, which is "unlikely to be related to a secondary instability mechanism" (Eppink, 2020).

For an abrupt upstream shift of the transition front at the step –the supercritical regime– Rius-Vidales and Kotsonis (2022) report that the temporal fluctuations leading to early transition do not exhibit the characteristics of classic secondary crossflow instabilities. Specifically, these temporal fluctuations are measured on the inner side of the upwelling (i.e., laterally upward-inclined) region of the crossflow vortex, where the *type*-III secondary instability develops under reference (no-step) conditions (see blue isolines in figure 1.5). However, the observed fluctuations occur in a frequency band distinct from that of the *type*-III instability.

1.3.2. Novel transition delay induced by a step: implications for flow control

The prevailing consensus at the beginning of this thesis was that a two-dimensional forward-facing step is inherently detrimental to three-dimensional laminar subsonic flow. Specifically, the step was believed to universally amplify pre-existing stationary crossflow vortices on interaction, thereby advancing transition. However, a series of discoveries made both externally and within the investigations of this thesis challenge this view. Key recent findings are highlighted next.

On the experimental side, Rius-Vidales and Kotsonis (2021) report an unexpected transition delay (about 3.8% of the wing chord) during investigations into the effect of a forward-facing step on transition advancement (see figure 1.11 (*b*)). Their experiments were conducted at a chord-based Reynolds number of 2.3×10^6 and under *large*-amplitude CFI conditions, i.e., the step is located in a region of non-linear CFI growth. Numerical studies have shown that, under specific design conditions, a forward-facing step stabilises pre-existing stationary crossflow vortices (Casacuberta et al., 2022b) and have identified the underlying stabilisation mechanism (Casacuberta et al., 2024).

Ivanov and Mischenko (2019) also report significant transition delay of swept-wing flow modulated by arrays of surface strips, i.e., consisting of both forward- and backward-facing steps. Their experimental work builds upon the theoretical investigations by Ustinov and Ivanov (2018), who attribute the stabilising effect of surface strips to *base-flow deformation*. Specifically, the addition of the strips reduces the crossflow velocity within the boundary layer. Correspondingly, a classic LST analysis (i.e., based on the Orr-Sommerfeld equation, see § 1.2.6) shows that the strip-deformed unperturbed base flow yields a lower amplification factor for CFI, compared to the no-strip case (Ustinov and Ivanov, 2018).

These findings suggest the potential for new laminar flow control strategies based on surface features. This is supported by experimental and numerical investigations involving an isolated forward-facing step (Rius-Vidales and Kotsonis, 2021; Casacuberta et al., 2022b, 2024) and the present thesis (chapters 4, 5, and 8), as well as sharp strips (Ustinov and Ivanov, 2018; Ivanov and Mischenko, 2019). However, the stabilising mechanism proposed in this thesis differs fundamentally from that of Ustinov and Ivanov (2018), thus underscoring the need for further investigation. Moreover, the CFI-stabilisation mechanism introduced in this thesis is distinct from the well-established control strategy based on discrete micro-roughness elements (Saric et al., 2011; Wassermann and Kloker, 2002, 2005). The latter operates by introducing *finite*-amplitude perturbations that deform the boundary layer and thereby influence instability growth; see the state-of-the-art review of flow control methods below. The working principles behind stabilising steps, and the broader potential of surface-relief-based control devices, are discussed in § 8.2 and in the concluding outlook (§ 9.2) of this thesis.

1.3.3. State of the art of flow control methods

Borodulin et al. (2024) categorise the state of the art in flow-control methods aimed at delaying laminar-turbulent transition into the following groups:

1

(*a*) suppression of perturbations via wave superposition;

(*b*) suppression of perturbations via receptivity mechanisms;

(*c*) modification of the body's boundary conditions (e.g., via cooling);

(*d*) base-flow deformation through finite-amplitude perturbations;

(*e*) direct modification of the base flow as a whole (e.g., by changing the angle of attack, the aerofoil geometry, or by applying boundary-layer suction).

Historically, the major technologies within group **(*e*)**, namely Natural Laminar Flow (NLF), full Laminar Flow Control (LFC), and Hybrid Laminar Flow Control (HLFC), have stood out as the most successful approaches in research programs targeting transition delay. Several large research programs have been carried out in Europe (e.g., LaTec, ALTTA, or HYLTEC) and in the US (e.g., EETT, LEFT, or the Boeing 757 and 787 flight tests), see Joslin (1998b) and Iyer et al. (2017).

NLF is a passive flow control method that aims to delay transition through the appropriate global shaping of the wing. A key geometrical feature of aerofoils designed to sustain *natural* laminar flow is the reaward displacement of the maximum-thickness location, thereby yielding an extended region of favourable pressure gradient (Doetsch, 1940). The latter stabilises the TS instability; hence NLF is well suited for applications involving low sweep-angle conditions up to a critical Reynolds number (Schrauf, 2005). At moderate sweep-angle conditions, the design of NLF relies on a delicate balance between controlling the TS instability and CFI (Redeker et al., 1990). At high sweep-angle conditions, the CFI renders NFL unsuccessful (Joslin, 1998b). As such, widespread industrial adoption of NLF has not occurred, with few exceptions such as the Honda lightweight business jet (Fujino et al., 2003).

In contrast, LFC is an active flow control method that prevents transition at Reynolds numbers above which laminarity cannot be *naturally* sustained (Joslin, 1998a); this typically entails steady wall suction through slots or small holes (Schrauf, 2005). Given the mechanical complexity of most suction systems, LFC is generally applied only to the upper wing surface, which exhibits the highest boundary-layer-edge velocity and thus the greatest friction drag (Bushnell, 2003). In its hybrid form, namely HLFC, LFC (i.e., suction in the leading-edge region) is combined with NLF (i.e., wing shaping to achieve mild favourable pressure gradient in the wing-box part) to respectively control the CFI and TS instability (Gratzer, 1986).

The practical feasibility of HLFC for transport aircraft, and corresponding improvement in fuel efficiency, was demonstrated on the fin of an Airbus A320 (Henke, 1999). Unfortunately, HLFC adds mass, energy, and maintenance penalties: it requires complex sub-systems such as ducts and pump sources, which have collectively hindered the widespread adoption of the technology to date. A novel method that enhances both robustness and simplicity is therefore essential to accelerate the industrial implementation of laminar flow control.

1.4. Scope of the thesis

1.4.1. Research objective

The main purpose of this thesis is **to ascertain, through Direct Numerical Simulations, how a surface forward-facing step modifies the stability and transition mechanisms of laminar incompressible swept-wing boundary-layer flow with a pre-existing stationary crossflow perturbation.** To that end, **a theoretical framework is developed, and the relevant flow structures and physical processes are described and analysed** in detail. The overarching motivation of this thesis is to advance the understanding of design strategies that promote the preservation of laminar swept-wing flow when a surface forward-facing step is present.

1.4.2. Research questions and scientific challenges and opportunities

The discussion in this thesis answers three primary research questions, with pertinent sub-questions, that are articulated and justified as follows:

(I) What are the governing mechanisms of the stationary interaction between a forward-facing step and a pre-existing stationary crossflow perturbation?

- **(I.1)** What is the effect of the step height and of the amplitude of the pre-existing crossflow perturbation in this regard?
- **(I.2)** What are the distinct regimes of growth (or decay) of a crossflow perturbation upstream and downstream of a forward-facing step?
- **(I.3)** Is a stationary crossflow perturbation of primary wavelength universally destabilised upon interaction with a forward-facing step?

The research question **(I)** arises from discrepancies in the literature concerning how salient step-induced flow features alter a pre-existing stationary CFI. The main scientific challenge in this regard is to establish a physically sound explanation of the mechanisms governing the CFI-step interaction. This challenge stems from the fact that multiple effects –all of which co-exist within a short streamwise region– have been reported to correlate with changes in instability behaviour close to the step (Tufts et al., 2017; Eppink, 2020; Rius-Vidales and Kotsonis, 2020, 2021, 2022) and has been addressed in Casacuberta et al. (2021, 2022a) (see chapter 4 in this thesis).

Over the past three decades, numerous studies have reported the ubiquitous presence of streaky structures in unswept forward-facing step flow (Lanzerstorfer and Kuhlmann, 2012; Stüer et al., 1999; Wilhelm et al., 2003; Marino and Luchini, 2009). While this thesis will show that analogous structures also arise in the swept case, there remains no clear consensus regarding the instability mechanisms responsible for the formation of streaks at the step, nor a thorough understanding of their potential interaction with the incoming CFI. A

detailed investigation of the streak phenomenon at the step has been presented in Casacuberta et al. (2025b) (see chapter 6 in this thesis).

The lack of causal understanding of dominant perturbation phenomena at the step is partly attributed to the limitations of classic stability methods, namely LST and PSE (Cooke et al., 2019), when applied to step flow. While impractical for systematic studies due to their high computational cost, the DNS performed in this thesis do not constrain the perturbation behaviour nor assume a perturbation ansatz (§ 1.2.6), other than enforcing spanwise periodicity. The physical insight gained from the DNS has guided the development of novel methodological approaches for assessing the stability of boundary-layer flows over sharp surface features, as elaborated upon in Casacuberta et al. (2022b, 2025b) (see chapters 4 and 6 in this thesis).

In this regard, the inability of classic stability methods to accurately model the behaviour of perturbations near the step suggests a role played by *short-term* non-modal growth (§ 1.2.4) in this region, as further elaborated in Casacuberta et al. (2022b, 2024, 2025b). Non-modal stability theory is well established (Butler and Farrell, 1992; Trefethen et al., 1993; Reddy and Henningson, 1993; Schmid and Henningson, 2001; Schmid, 2007). However, it is not yet evident in the literature how to assess whether a convective instability of initially modal character (such as CFI) undergoes a mixture of modal and non-modal growth within a localised spatial region. Albensoeder et al. (2001) scrutinise the potential role of the lift-up effect –a strong candidate for non-modal growth of three-dimensional perturbations– in step flow by decomposing the production term of the Reynolds-Orr equation (1.14). Despite offering novel insights, their approach leads to an apparent inconsistency at first glance (later shown not to be the case), which calls for further investigation.

This is elaborated as follows: it is well known that the sign of the production term (1.14) establishes the *sense* of kinetic energy exchange between perturbations and the background flow; that is, whether the unperturbed base flow is stabilised or destabilised. This interpretation also applies to the individual terms arising from the decomposition of the production term (Albensoeder et al., 2001). It follows from this mathematical rationale that the lift-up effect may as well act towards stabilising the flow through an inversion of sign. This conclusion appears to contradict the common consensus in the literature, which holds that the lift-up effect is a destabilising flow mechanism responsible for the inception of highly energetic streamwise streaks. This issue has been addressed in Casacuberta et al. (2024) (see chapter 5 in this thesis).

(II) How does a forward-facing step induce an upstream shift of the transition front, relative to a no-step case, and under what conditions this shift is either moderate (the critical scenario) or abrupt in the immediate downstream vicinity of the step (the supercritical scenario)?

(II.1) What forward-facing-step-flow features significantly contribute to advancing the transition front?

(II.2) Is transition advancement ultimately ascribed to the modified properties of one or more types of classic secondary crossflow instabilities?

(II.3) In the context of the transition diagram proposed by Morkovin et al. (1994), does the step cause a switch to the transition path?

The research question **(II)** shifts the focus to the scientific challenges concerning unsteady perturbation phenomena. At present, there is no consensus in the literature on which step-flow mechanism(s) are ultimately responsible for promoting early transition, manifested either as a moderate (critical) or an abrupt (supercritical) shift of the transition front upstream. Major proposed conceptual models include a vortex-shedding mechanism (Eppink, 2020), the existence of a so-called travelling mode within the region of flow recirculation at the step (Tufts et al., 2017), the effects of classic secondary crossflow instabilities (Rius-Vidales and Kotsonis, 2021, 2022), and temporal fluctuations emanating from the inner side of the crossflow vortex (Rius-Vidales and Kotsonis, 2022).

Furthermore, Rius-Vidales and Kotsonis (2022) note an apparent contradiction in the behaviour of the temporal fluctuations that are responsible for supercritical transition induced by the step. While these fluctuations originate from the spatial region where the *type*-III secondary crossflow instability typically develops, their frequency content is significantly higher than that of the *type*-III mode. At the same time, these fluctuations do not correlate spatially with the high-frequency *type*-I and *type*-II secondary crossflow instabilities (Rius-Vidales and Kotsonis, 2022). This suggests that a new class of unsteady instability mechanism promoting early transition becomes active at the step under certain conditions. However, the nature and origin of this mechanism, any role played by the recirculating-flow region at the step, and the effects of incoming-crossflow perturbation amplitude all remain largely unclear. A detailed investigation of step-induced laminar-turbulent transition advancement under supercritical conditions has been presented in Casacuberta et al. (2023, 2025b) (see chapter 8 of this thesis).

(III) Assuming the presence of a forward-facing step, what design strategy can be employed to support the preservation of laminar flow?

Originally, the scope of this thesis was limited to addressing the research questions **(I)** and **(II)**. However, a series of unexpected findings (see chapters 4 and 5 of this thesis) revealed the potential of a forward-facing step to stabilise a pre-existing stationary CFI under specific conditions, as supported experimentally (Rius-Vidales and Kotsonis, 2021). These findings motivated an expansion of the thesis scope to investigate whether surface steps could effectively delay transition (chapter 8) under the previously identified conditions (chapters 4 and 5), and to explore novel strategies for passive flow control (§ 9.2). The latter was conducted within a broader collaborative effort of the same group at TU Delft (Rius-Vidales et al., 2025; Westerbeek et al., 2025), which further demonstrated the potential of smooth surface humps to delay transition in swept-wing flow, leading to an international patent application (Kotsonis et al., 2024).

2

Methodology

Abstract: *This thesis investigates the instability and transition of swept-wing flow using Direct Numerical Simulations (DNS) of the incompressible Navier-Stokes equations. This chapter outlines the employed methodology: it begins by describing the flow problem, guided by reference wind-tunnel experiments on a* 45° *swept wing, along with the main control parameters and governing equations. The modelling approaches are then detailed, covering the setup of both DNS and linear stability methods. Finally, the chapter addresses verification and cross-validation of the computed flow fields.*

Parts of this chapter are published in:

- Casacuberta, J., Hickel, S., and Kotsonis, M., 2021 Mechanisms of interaction between stationary crossflow instabilities and forward-facing steps. *AIAA Paper* 2021-0854.
- Casacuberta, J., Groot, K. J., Hickel, S., and Kotsonis, M., 2022 Secondary instabilities in swept-wing boundary layers: Direct Numerical Simulations and BiGlobal stability analysis. *AIAA Paper* 2022-2330.
- Casacuberta, J., Hickel, S., and Kotsonis, M., 2022 Direct numerical simulation of interaction between a stationary crossflow instability and forward-facing steps. *J. Fluid Mech.* **943**:A46.
- Groot, K. J., Casacuberta, J., Hickel, S., and Kotsonis, M., 2025 Non-orthogonal plane-marching stability equations for the secondary instability of crossflow vortices. Accepted for publication in *Comput. Fluids*.
- Casacuberta, J., Groot, K. J., Hickel, S., and Kotsonis, M., 2025 Direct numerical simulation of swept-wing transition induced by forward-facing steps. Under consideration for publication in *J. Fluid Mech.*

2

Instability and transition of swept-wing flow are investigated through the formulation of a scientific model. Scientific modelling is the process of generating a simplified description of a phenomenon using physical and/or mathematical tools, with the aim of understanding and predicting its behaviour. The present exercise in scientific modelling is summarised as follows.

First, a physical system is constructed, namely a representation of laminar swept-wing flow modulated by stationary crossflow instability under a set of assumptions. Unsteady wall forcing far upstream of the step introduces unsteady perturbation content directly, a modelling convenience bypassing the natural receptivity phase.

Second, a system of partial differential equations with pertinent initial and boundary conditions is chosen to mathematically describe the behaviour of the physical system. The joint physical and mathematical models define the flow problem (§ 2.1).

Third, the flow problem is solved numerically: the numerical methodology employed in this thesis is described in § 2.2 and verified in § 2.3. Before presenting the main discussion of results, theoretical models are developed to characterise the relevant stationary flow structures and the associated energy-transfer mechanisms, based on numerically generated data (§ 3).

2.1. Flow problem

The formulation of the flow problem begins with a definition of the physical system, guided by reference wind-tunnel data, and proceeds with a description of its mathematical representation and control parameters.

2.1.1. Definition of the physical system

The swept-wing flow is modelled as incompressible flow over a flat plate. An aerofoil-like static-pressure distribution is externally prescribed in the inviscid-flow region, distributed along the chordwise (leading-edge-orthogonal) direction. Furthermore, the free-stream velocity vector is decomposed into components pointing in the directions orthogonal and parallel to the wing leading edge. The unperturbed base flow is conceived as invariant in the spanwise (leading-edge-parallel) direction (see § 1.2.2). This assumption lends itself to the definition of two derivative assumptions, namely null growth and periodicity of perturbations in the leading-edge-parallel direction. This justifies restricting the analysis to a domain that mimics the conventions accompanying the reference wing model (see light grey rectangle in figure 2.1 (*a*)).

Reference experimental setup

The physical model of swept-wing flow is guided by wind-tunnel experiments performed on a wing with a sweep angle of $\Lambda = 45°$ (Rius-Vidales and Kotsonis, 2021; Rius-Vidales, 2022). A sketch is shown in figure 2.1. The chord length of the experimental wing model is $c_x = 0.9$ m in the direction orthogonal to the leading edge and $c_X = 1.27$ m in the wind-tunnel streamwise direction. The latter is the direction of $\boldsymbol{Q}_\infty^{\text{tun}}$, i.e., the incoming velocity vector. The superscript "tun" (referring to the wind tunnel) denotes experimentally measured flow properties at the wind-tunnel section, upstream of the wing model. These are to be distinguished from the *free-stream flow* properties at the inlet of the computational domain, which is virtually placed at 5%

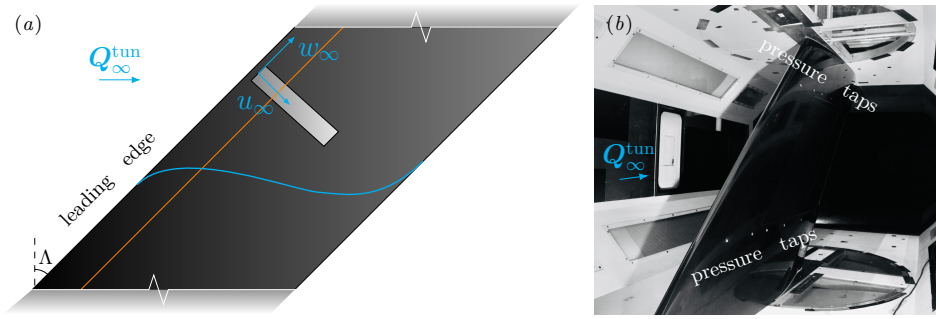

Figure 2.1: (*a*) Sketch of the physical model of swept-wing flow and (*b*) photograph of the reference wing model adapted from Rius-Vidales (2022). In (*a*): top view of the virtually infinite swept wing (dark grey), computational domain (light grey), two-dimensional step (solid orange line), trajectory of the inviscid streamline (cyan line), unperturbed incoming velocity vector, $\boldsymbol{Q}_\infty^{\text{tun}}$, and decomposition of the free-stream velocity vector at the inlet of the domain into components orthogonal (u_∞) and parallel (w_∞) to the leading edge.

of the wing chord. Additionally, the superscript "exp" refers to experimentally measured flow properties at the wind-tunnel section, but associated with the flow over the wing.

The aerofoil is symmetric and features a modified NACA 66018 profile in the chordwise direction of c_x (figure 2.2 (*a*)). The wing model was specifically designed and extensively used for the study of the crossflow instability (see Serpieri and Kotsonis (2016) and Serpieri et al. (2017)). It prevents attachment-line and Görtler-type instabilities by respectively featuring a small leading-edge radius (approximately 1% of the chord) and no concave surface regions. Furthermore, it provides a large area of free-stream flow acceleration (i.e., favourable pressure gradient) to promote growth of CFI in front of TS instability. At the angle of attack at which experiments were conducted, namely $-3°$, the pressure gradient is favourable until approximately 65% of c_X. The measurements were performed on the pressure side of the wing.

The physical model of swept-wing flow is specifically based on the experimental campaign of Rius-Vidales and Kotsonis (2021). Pertinent measurements were conducted in the Low-Turbulence Tunnel (LTT) at Delft University of Technology. Table 2.1 summarises the main properties of the experimental setup and flow conditions. The low value of free-stream turbulence intensity, $Tu = 0.03\%$ relative to $||\boldsymbol{Q}_\infty^{\text{tun}}||$, aims to produce conditions representative of the flight environment (Downs and White, 2013) and ensures that the stationary CFI dominates over the travelling CFI (Deyhle and Bippes, 1996; Bippes, 1999), as demonstrated by Serpieri and Kotsonis (2016) for the present wing model.

Rius-Vidales and Kotsonis (2021) retrieved the external (i.e., outer-flow) evolution using an array of wall-pressure taps on the wing surface, distributed along the wind-tunnel streamwise direction, see figure 2.1 (*b*). The external flow properties are key inputs of the numerical simulations presented in this thesis; therefore, the procedure described by Rius-Vidales and Kotsonis (2021) for recovering them from wall

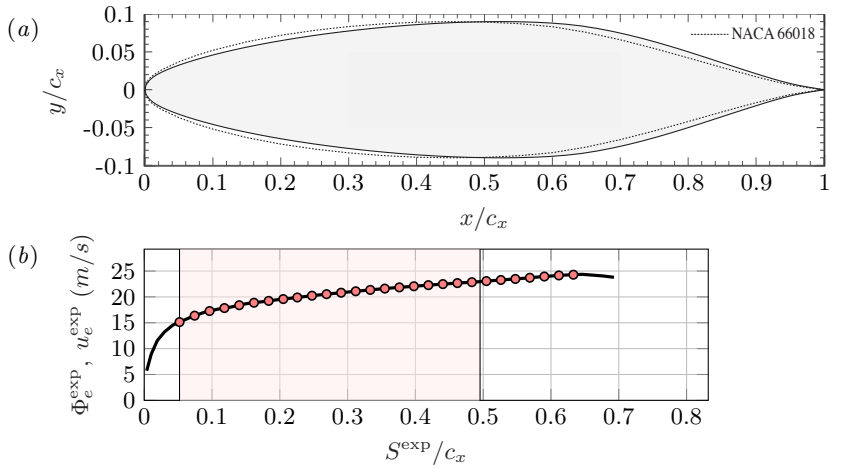

FIGURE 2.2: Aerofoil shape of the experimental wing model in the direction orthogonal to the leading edge (solid black line) and reference NACA 66018 (dotted) in (*a*), reproduced from Rius-Vidales (2022). Outer-flow velocity (2.4) as a function of the arc length of the aerofoil in (*b*) from: experimental measurements (thick line), numerical fit on experimental data (circles), and limits of the computational domain (thin vertical lines).

measurements is detailed next. First, the pressure coefficient at the taps is computed as

$$C_p = \frac{p^{\text{exp}} - p_\infty^{\text{tun}}}{\frac{1}{2}\rho||\boldsymbol{Q}_\infty^{\text{tun}}||^2}, \tag{2.1}$$

where ρ denotes density and p is the static pressure. The p_∞^{tun} is the reference static pressure, computed as the difference between the total and dynamic pressures measured by a pitot-static tube placed upstream of the wing.

The magnitude of the external-flow velocity vector $\boldsymbol{v}_e^{\text{exp}}$ is evaluated as

$$\left(\frac{||\boldsymbol{v}_e^{\text{exp}}||}{||\boldsymbol{Q}_\infty^{\text{tun}}||}\right)^2 = 1 - C_p, \tag{2.2}$$

based on the assumption of static pressure invariance in the direction normal to the wing surface in the boundary-layer region. Equation (2.2) is derived from the Bernoulli equation, which itself assumes steady, incompressible, and irrotational flow. Rius-Vidales and Kotsonis (2021) express the external velocity vector into components parallel to the leading-edge direction, i.e.,

$$w_e^{\text{exp}} = ||\boldsymbol{Q}_\infty^{\text{tun}}|| \sin(\Lambda), \tag{2.3}$$

and orthogonal to w_e^{exp}, i.e.,

$$\Phi_e^{\text{exp}} = \sqrt{||\boldsymbol{v}_e^{\text{exp}}||^2 - (w_e^{\text{exp}})^2}. \tag{2.4}$$

Property	Value
c_x	0.90 m
c_X	1.27 m
Λ	45°
$\|\|\boldsymbol{Q}_\infty^{\text{tun}}\|\|$	26.5 m/s
ρ	1.207 kg/m^3
ν	1.472×10^{-5} m^2/s
Re_{c_X}	2.29×10^6
Tu	0.03%

Table 2.1: Properties of the experimental setup.

By virtue of the assumption of infinite wingspan (§ 1.2.2), w_e^{exp} (2.3) is conceived invariant in the physical system, i.e., globally constant. Finally, a discrete representation of Φ_e^{exp} (2.4) can be evaluated from the pressure-tap measurements through (2.2).

From experiments to the physical system

The measurements on the wing model described above are used to construct a physical system in a three-dimensional domain of swept-wing flow modelled as incompressible flow over a flat plate. The considered domain follows the orientation of the wing; i.e., it extends longitudinally in the leading-edge-orthogonal direction and the normal vectors of inflow and outflow planes are arranged to be orthogonal to the leading-edge-parallel direction. The flat plate (hereafter, the wall) extends in the directions orthogonal and parallel to the wing leading edge. A fixed Cartesian coordinate system is defined, $\boldsymbol{x} = [x\ y\ z]^{\text{T}}$; y is the wall-normal direction, z is the leading-edge parallel direction, and x completes the coordinate system. A sketch of the domain is illustrated in figure 2.3, which is conceptually represented by the projected light grey rectangle in figure 2.1 (a). The velocity components in the x-, y-, and z-directions are respectively denoted by u, v, and w.

For the purpose of modelling, the arc length, S^{exp}, of the aerofoil measured relative to the stagnation line is mapped onto the x-coordinate. The dimensions of the baseline domain are $0 \leq x/\delta_0 \leq 517$, $0 \leq y/\delta_0 \leq 26$, $-4.86 \leq z/\delta_0 \leq 4.86$, see the definition below of the scaling parameter δ_0. The inlet, $x = 0$, is virtually placed at 5% of the wing chord c_x and the outlet at 49% of c_x, resulting in a baseline domain length of 0.4 m.

Three key modelling elements form the foundation for the physical characterisation of swept-wing flow in this thesis, as described below:

(*i*) To account for the effect of sweep angle, a spanwise velocity component, denoted w_∞, is prescribed at the inlet. From equation (2.3), it is established that $|w_\infty| = w_e^{\text{exp}}$ and $w_\infty/u_\infty = -1.241$ (note the orientation of the coordinate system in figure 2.3).

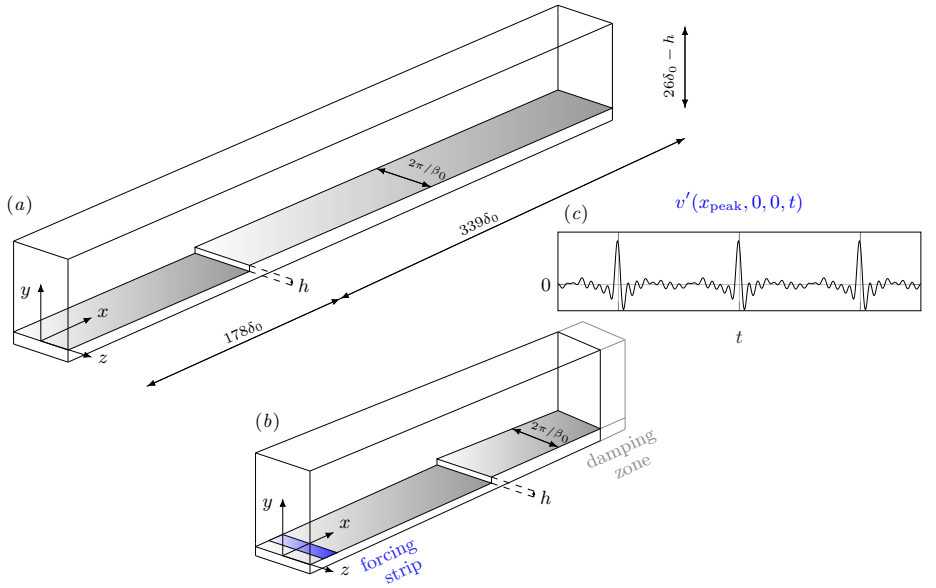

Figure 2.3: Sketch of the domain, including the orientation of the coordinate system and the geometry of the forward-facing step, representative of the steady-state (a) and unsteady (b) DNS computations. The blue area in (b) represents the forcing strip on the wall used to excite unsteady perturbation modes. Panel (c) displays the signal modulating the wall-normal velocity over time at the forcing strip, with x_{peak} denoting the centre of the strip in the chordwise direction.

(ii) The aerofoil free-stream flow evolution in the direction of the wing chord is prescribed in x. To that end, a polynomial fit of logarithmic basis is applied to the experimentally-derived external velocity Φ_e^{exp} (2.4). The analysis in this thesis is restricted to the region of favourable pressure gradient, see circles in figure 2.2 (b). Correspondingly, the chordwise free-stream velocity at the inlet of the domain, $x = 0$, is set to $u_\infty = 15.10$ m/s and the polynomial fit reads

$$\begin{aligned} u_e^{\text{exp}}/u_\infty = {} & 0.0023 \ln^4(x+c) + 0.0377 \ln^3(x+c) \\ & + 0.1752 \ln^2(x+c) + 0.5303 \ln(x+c) + 1.8574, \end{aligned} \tag{2.5}$$

with $c = 0.0468$. A static pressure distribution is ultimately prescribed at $y = y_{\text{max}}$, see § 2.1.3, which is computed using expression (2.5) and the assumption of irrotational flow. The vector of state variables in the external region is denoted by $\boldsymbol{q}_e = [u_e \; v_e \; w_e \; p_e]^{\text{T}} = [\boldsymbol{v}_e \; p_e]^{\text{T}}$, where p_e expresses the external pressure and p_∞ equals p_e at the inflow.

The external chordwise velocity far from the wall, u_e, increases along x, since the free-stream is subject to a favourable pressure gradient. Under classic boundary-layer approximations, invariance of pressure and free-stream velocity along y is assumed. However, in the present full Navier-Stokes representation with a realistic pressure distribution, $u_e = u_e(x, y)$ with $\partial u_e/\partial x \gg \partial u_e/\partial y$.

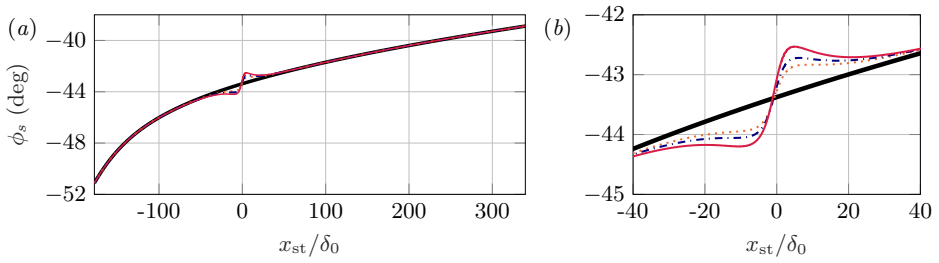

Figure 2.4: Horizontal deflection of the characteristic inviscid streamline along the domain (a), and zoom at the step (b) in the reference case (thick solid black), step case I (dotted orange), II (dash-dotted blue), III (thin solid red). Here, $x_{st} = x - 177.62\delta_0$ denotes the chordwise position relative to the step location.

As common in studies of swept-wing boundary layers, rigorous determination of the crossflow component requires a proper definition of the orientation of a *characteristic* inviscid streamline. The velocity non-uniformity in y poses the challenge of establishing such a definition.

To overcome possible ambiguities, *pseudo*-free-stream properties are characterised, i.e., properties which are representative of the inviscid-flow evolution and are a function of x only. For this purpose, a numerically computed base-flow streamline is initially seeded at $y/\delta_0 \approx 5$ at the inflow; the free-stream properties measured along the computed streamline are assigned as *pseudo*-free-stream properties and are denoted by a hat symbol, e.g., $\hat{v}$. This approach, and inflow seeding point, yields matching boundary-layer properties between the present DNS and the independent numerical solutions to the boundary-layer equations (e.g., figure 2.10 (d)). Other approaches in the literature used to characterise *pseudo*-free-stream properties entail the wall-normal integration of the spanwise vorticity (Spalart and Strelets, 2000).

The *pseudo*-free-stream chordwise velocity, $\hat{u}_e = \hat{u}_e(x)$, is used to define the horizontal deflection of the computed inviscid streamline,

$$\phi_s(x) = \arctan\left(\frac{w_\infty}{\hat{u}_e}\right), \tag{2.6}$$

that is, the angle that the inviscid streamline projected in the x-z plane forms with x. The chordwise evolution of ϕ_s is illustrated in figure 2.4. The base-flow crossflow component, $w_{B,s}$ (see figure 2.10 (e)), and the velocity component parallel to the inviscid streamline direction, $u_{B,s}$, are accordingly defined as

$$u_{B,s} = u_B \cos\phi_s + w_B \sin\phi_s, \tag{2.7a}$$
$$w_{B,s} = w_B \cos\phi_s - u_B \sin\phi_s. \tag{2.7b}$$

(iii) A laminar boundary layer is prescribed at the inlet, which is set to the solution of the Falkner-Skan-Cooke (FSC) equations, $\boldsymbol{v}^{FSC} = [u^{FSC}\ v^{FSC}\ w^{FSC}]^T$.

Property	Value
u_∞	15.10 m/s
w_∞	−18.74 m/s
$Re_{x,\text{in}}$	4.81×10^4
β_H	0.4
δ_0	7.71×10^{-4} m
$\delta^\star_{\text{in}}$	2.26×10^{-4} m

Table 2.2: Main quantities of the physical model of swept-wing flow.

The solution of the FSC equations is a self-similar profile, which satisfies the boundary-layer equations under the infinite-wingspan assumption and represents a family of wedge-type flows (Schlichting, 1979). The FSC equations read

$$f''' + ff'' + \beta_H \left(1 - (f')^2\right) = 0, \tag{2.8a}$$
$$g'' + fg' = 0, \tag{2.8b}$$

where $f'(\eta) = u^{\text{FSC}}/u_\infty$ and $g(\eta) = w^{\text{FSC}}/w_\infty$ represent the velocity components in the x- and z-directions, respectively, and the prime denotes differentiation with respect to the non-dimensional wall-normal coordinate η. The boundary conditions are $f = f' = g = 0$ at $\eta = 0$ and $f' \to 1$, $g \to 1$, as $\eta \to \infty$. The Hartree parameter is evaluated as

$$\beta_H = \frac{2m_H}{m_H + 1} \quad \text{with} \quad m_H = \frac{S^{\text{exp}}\, \mathrm{d}u_e^{\text{exp}}/\mathrm{d}x}{u_e^{\text{exp}}}, \tag{2.9}$$

$\eta = y\sqrt{(u_e^{\text{exp}}(m_H + 1))/(2x\nu)}$, and the velocity component in the y-direction reads $v^{\text{FSC}} = -\sqrt{(\nu u_e^{\text{exp}})/(2x(m+1))}\,[(m+1)f + (m-1)f'\eta]$.

Table 2.2 summarises the main properties at the domain inlet. The arclength distance from the stagnation line is $S^{\text{exp}} = 0.0468$ m, corresponding to 5% c_x, which yields a Hartree parameter of $\beta_H = 0.4$ (2.9). The inflow Reynolds number is defined as $Re_{x,\text{in}} = S^{\text{exp}} u_\infty/\nu$. The boundary-layer thickness based on the inflow chordwise velocity, u^{FSC}, is $\delta_0 = 7.713 \times 10^{-4}$ m, and the corresponding displacement thickness at the inlet is $\delta^\star_{\text{in}} = 2.259 \times 10^{-4}$ m. Throughout this thesis, the inflow free-stream chordwise velocity, u_∞, and the corresponding boundary-layer thickness, δ_0, are adopted as the main characteristic quantities.

Definition of flow fields and perturbation quantities

Following classic stability analysis (§§ 1.2.1 and 1.2.6), the stability of the boundary layer is examined by decomposing the flow field into the unperturbed base flow, $\boldsymbol{q}_{\text{B}}$, and a perturbation field, $\boldsymbol{q}'$ (1.2). In the numerical procedure of this thesis, $\boldsymbol{q}_{\text{B}}$

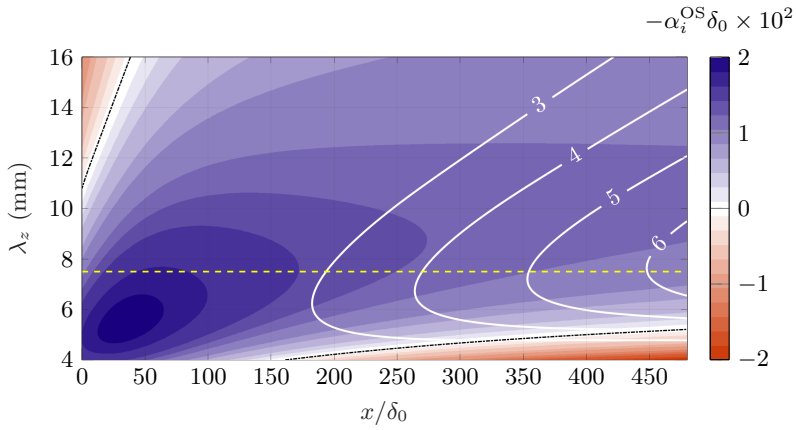

Figure 2.5: Stability diagram of the DNS base flow obtained from a linear local stability method. The colour map expresses the perturbation chordwise growth rate, $-\alpha_i^{\mathrm{OS}}$, solid white lines are isolines of the amplification factor in x, dash-dotted black lines are the neutral curve, horizontal dashed line indicates $\lambda_z = 7.5$ mm, and vertical black line illustrates the virtual step location.

is first computed independently. It then forms the initial condition to, secondly, numerically compute the steady perturbed flow, $\boldsymbol{q}_{\mathrm{DB}}$; that is, the superposition of the unperturbed base flow and the steady content of the perturbation field:

$$\boldsymbol{q}_{\mathrm{DB}} = \boldsymbol{q}_{\mathrm{B}} + \boldsymbol{q}', \text{ subject to } \partial \boldsymbol{q}'/\partial t = 0. \tag{2.10}$$

The flow field $\boldsymbol{q}_{\mathrm{DB}} = [u_{\mathrm{DB}}\ v_{\mathrm{DB}}\ w_{\mathrm{DB}}\ p_{\mathrm{DB}}]^{\mathrm{T}}$ is a steady-state solution of the Navier-Stokes equations when the inflow boundary layer is disturbed with a stationary cross-flow eigenmode (§ 2.2.1), to which a finite amplitude is assigned (§ 2.1.2). The SFD method (Åkervik et al., 2006; Casacuberta et al., 2018) is applied to ensure the fully stationary nature of $\boldsymbol{q}_{\mathrm{DB}}$. Upon subtraction of the pre-computed $\boldsymbol{q}_{\mathrm{B}}$ from $\boldsymbol{q}_{\mathrm{DB}}$, the stationary perturbation field is recovered, i.e., $\boldsymbol{q}'$ subject to $\partial \boldsymbol{q}'/\partial t = 0$. The maxima along y of $|\tilde{u}|_{(0,j)} + |\tilde{u}^{\dagger}|_{(0,j)}$ will be generally employed as the main metric to quantify stationary-perturbation amplification in x without the step present. This amplitude metric is denoted as $A^u_{(0,j)} = \max_y \left(|\tilde{u}|_{(0,j)} + |\tilde{u}^{\dagger}|_{(0,j)}\right)$.

Third, the *total* unsteady flow field is the instantaneous solution of the Navier-Stokes equations when the flow is forced at selected temporal frequencies, continuously in time (§ 2.1.3), and the SFD method is switched off. In a fashion similar to the decomposition of the stationary perturbation field into spanwise Fourier modes (1.8), the *total* unsteady velocity-perturbation field is Fourier-analysed in the spanwise direction and in time and expressed as

$$\boldsymbol{v}' = \sum_{k=-M}^{M} \sum_{j=-N}^{N} \underbrace{\tilde{\boldsymbol{v}}_{(k,j)}(x,y)\ \mathrm{e}^{\mathrm{i}(j\beta_0 z - k\omega_0 t)}}_{\boldsymbol{v}'_{(k,j)}}, \tag{2.11}$$

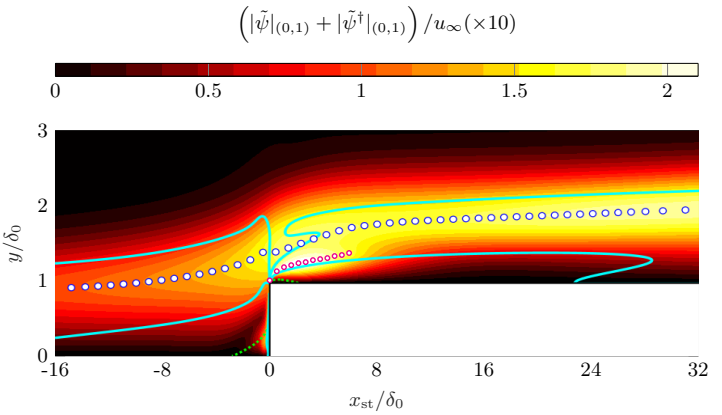

FIGURE 2.6: Flow features at the step: fundamental amplitude function $|\tilde{\psi}|_{(0,1)}$ (colour contour), wall-normal position of primary (i.e., associated to $|\tilde{\psi}|^{\mathrm{top}}_{(0,1)}$, big blue circles) and secondary (i.e., associated to $|\tilde{\psi}|^{\mathrm{str}}_{(0,1)}$, small magenta circles) perturbation peaks, loci of base-flow crossflow inflection points (solid cyan), and base-flow reversal $u_{\mathrm{B}} = 0$ (dotted green).

where $\tilde{\boldsymbol{v}}_{(k,j)} = [\tilde{u}_{(k,j)}\ \tilde{v}_{(k,j)}\ \tilde{w}_{(k,j)}]^{\mathrm{T}} \in \mathbb{C}^3$ denotes the Fourier coefficients, M and N indicate (one half of) the number of temporal and spanwise modes considered, and the parameter $\omega_0 = 2\pi f_0$ expresses the fundamental angular frequency. The moduli of the components of $\tilde{\boldsymbol{v}}_{(k,j)}$ read $|\tilde{u}|_{(k,j)}$, $|\tilde{v}|_{(k,j)}$, and $|\tilde{w}|_{(k,j)}$ and the associated phases are denoted by $\varphi^{u}_{(k,j)}$, $\varphi^{v}_{(k,j)}$, and $\varphi^{w}_{(k,j)}$. An analogous decomposition is applied to the pressure-perturbation field, with $\tilde{p}_{(k,j)} \in \mathbb{C}$ indicating the Fourier coefficients.

The width of the computational domain is set to the spanwise wavelength of the fundamental stationary crossflow eigenmode prescribed at the inlet, $\lambda_z = 2\pi/\beta_0$, and periodic boundary conditions are applied at the transverse boundaries. The choice of wavelength of the stationary CFI in this thesis, $\lambda_z = 9.73\delta_0 = 7.5$ mm, is grounded on the criticality of the crossflow eigenmode with respect to the (maximum) linear amplification factor achieved at the end of the computational domain. This was quantified through a linear local Orr-Sommerfeld analysis (§§ 1.2.1 and 1.2.6) performed on the DNS base flow, for a broad range of λ_z values. Linear local stability methods sufficiently predict the most amplified wavelength of stationary crossflow perturbations despite their inherent parallel-flow assumption (Bippes, 1999). The results of the Orr-Sommerfeld analysis are summarised in figure 2.5, where the colour map represents the local perturbation chordwise growth rate, $-\alpha_i^{\mathrm{OS}}$, and isolines characterise the associated amplification factor in x.

In analogy with the classic LST ansatz (§ 1.2.6), the spatial growth rate in x of a perturbation feature with spanwise wavenumber $j\beta_0$ and angular temporal frequency $k\omega_0$ is computed from the DNS results as

$$\alpha^{q}_{i,(k,j)} = -\frac{1}{|\tilde{q}|^{y=y^l}_{(k,j)}} \frac{\mathrm{d}|\tilde{q}|^{y=y^l}_{(k,j)}}{\mathrm{d}x}. \tag{2.12}$$

In equation (2.12), q represents a flow quantity, such as u or ψ (1.9), and y^l refers to the wall-normal location at which *amplitude* is measured in its corresponding amplitude function. The wall-normal location y^l is generally not constant but follows the spatial evolution of relevant perturbation quantities, see the description below.

In CFI-dominated problems, the amplitude function of a single velocity perturbation component is typically employed to quantify perturbation growth and decay. However, previous work by Tufts et al. (2017) (see figure 1.10) and the results of this thesis (see § 4.2) show that the amplitude functions of the stationary CFI mode develop an additional (secondary) peak near the wall after passing the step in x. Monitoring growth at selected wall-normal locations is therefore deemed necessary for the analysis in this thesis, owing to the co-existence of multiple perturbation structures across y at the step x-location. For clarity, in the analyses of chapters 4 and 6, the *amplitude* measured at the upper peak (see big blue circles in figure 2.6) is denoted by $|\tilde{q}|^{\mathrm{top}}_{(0,1)}$, *amplitude* measured at the lower peak arising downstream of the step (see small magenta circles in figure 2.6) is denoted by $|\tilde{q}|^{\mathrm{str}}_{(0,1)}$, and *amplitude* locally measured at the largest peak for every x is denoted by $|\tilde{q}|^{\mathrm{max}}_{(0,1)}$. The wall-normal location of $|\tilde{u}|^{\mathrm{top}}_{(0,1)}$ is denoted by $\tilde{y}^{u,\mathrm{top}}_{(0,1)}$ in chapter 4 and the wall-normal location of $|\tilde{\psi}|^{\mathrm{str}}_{(0,1)}$ is denoted by $\tilde{y}^{\psi,\mathrm{str}}_{(0,1)}$ in chapter 6.

2.1.2. Control parameters and summary of cases

This section summarises and justifies the choices of main control parameters adopted in this thesis. In some cases, these choices have been guided by the outcomes of recent experimental work (Eppink, 2020; Rius-Vidales and Kotsonis, 2020, 2021, 2022).

Height and location of the step and amplitude of CFI

The step height, h, stands out as a key control parameter. The values considered in this thesis, $h/\delta_0 = 0.59, 0.76$, and 0.97, correspond to subcritical, critical, and supercritical transition, respectively (see § 8.1), in agreement with the experimental findings of Rius-Vidales and Kotsonis (2021). Accordingly, these steps are hereafter referred to as *small*, *moderate*, and *large*, respectively, reflecting their respective transition behaviour in the reference experiments of Rius-Vidales and Kotsonis (2021). However, it is emphasised that the segregation of transition regimes based on h is contingent upon the initial amplitude of the incoming CFI, as demonstrated in this thesis and experimentally (Eppink, 2020; Rius-Vidales and Kotsonis, 2021).

Boundary-layer metrics corresponding to the aforementioned step geometries are summarised in table 2.3. Specifically, $\delta_{99,h}$ denotes the unperturbed boundary-layer thickness at the x-location of the step and

$$Re_h = \frac{u_\infty h}{\nu} \tag{2.13}$$

is the step-height-based Reynolds number. The steps, which attain approximately between 30% and 50% of the unperturbed boundary-layer thickness, are located at $x/\delta_0 = 177.62$; an exception is made in § 8.2, where the step x-location is shifted upstream to $x/\delta_0 = 73.90$, to explore mechanisms of passive CFI stabilisation. The

Boundary-layer parameters per step geometry

Test case name	Note	h/δ_0	$h/\delta_{99,h}$	u_h/u_∞	Re_h	Re_{hh}
step I	small step	0.59	0.33	0.78	470.26	368.17
step II	moderate step	0.76	0.41	0.93	598.51	556.88
step III	large step	0.97	0.53	1.08	769.51	832.08

Table 2.3: Definition and notation of boundary-layer parameters for each step geometry, corresponding to cases where the step is located at $x/\delta_0 = 177.62$ (see table 2.2). The cases of this table are compared in chapters 4 and 8, while chapters 5, 6, and 7 focus exclusively on the "step III" case, see table 2.6.

$x/\delta_0 = 177.62$, corresponds identically to 20% of the chord of the reference wing model (Rius-Vidales and Kotsonis, 2021). The chordwise position relative to the step, $x_{\mathrm{st}} = x - 177.62\delta_0$, is hereafter introduced for ease of representation.

Cases for CFI amplitude

Test case name	Note	$A^u_{(0,1)}\big\vert_{x=0}$	$A^u_{(0,1)}\big\vert_{x_{\mathrm{st}}=0}$
r.*A* (no step), **s.*A*** (step)	small amplitude	$1 \times 10^{-4}\ u_\infty$	$3 \times 10^{-3}\ u_\infty$
r.*B* (no step), **s.*B*** (step)	medium amplitude	$3.5 \times 10^{-3}\ u_\infty$	$1 \times 10^{-1}\ u_\infty$
r.*C* (no step), **s.*C*** (step)	large amplitude	$2.6 \times 10^{-2}\ u_\infty$	$3 \times 10^{-1}\ u_\infty$

Table 2.4: Definition and notation of amplitude cases, where "r" and "s" denote the reference (no-step) and step configurations, respectively. The table lists the amplitude of the fundamental CFI mode, $A^u_{(0,1)}$, at the inlet ($x = 0$) and at the virtual step location ($x_{\mathrm{st}} = 0$), both in the absence of the step. The cases of this table are compared in chapter 7 and, in part, in chapter 8, while chapters 4, 5, and 6 focus exclusively on case "B", see table 2.6.

The initial amplitude of the incoming CFI, A_0 (2.27), is also a main control parameter. Three values of A_0 are considered (see table 2.4), corresponding to distinct perturbation regimes. Specifically, $A_0/u_\infty = 1 \times 10^{-4}$ and $A_0/u_\infty = 3.5 \times 10^{-3}$ yield linear behaviour of the fundamental CFI until approximately the end of the domain (figure 2.11 (*a*)), and until the virtual step location (figure 2.11 (*b*)), respectively. The referenced figures are presented below in the cross-validation section (§ 2.3). In contrast, $A_0/u_\infty = 2.6 \times 10^{-2}$ leads to non-linear CFI behaviour already upstream of the step (figure 2.11 (*c*)). These amplitude regimes are defined from preliminary stability computations on the reference (no-step) base flows. At the same time, the choice of the largest amplitude, $A_0/u_\infty = 2.6 \times 10^{-2}$, is further motivated by the causal link between local CFI amplitude at the step and the onset of supercritical transition, assessed via preliminary NPSE simulations matching the experimental conditions of Rius-Vidales and Kotsonis (2021), see also Casacuberta et al. (2025a).

Cases for *effective* sweep angle

Test case name	w_∞/u_∞	$\lvert\phi_s(0)\rvert$	Forcing method	Amplitude
Baseline	-1.241	$51.136°$	IM ($x = 0$)	$3.5 \times 10^{-3}\ u_\infty$
Test A	-1.241	$51.136°$	BS ($x = 140\delta_0$)	$1 \times 10^{-5}\ u_\infty$
Test B	-0.993	$44.791°$	BS ($x = 140\delta_0$)	$1 \times 10^{-5}\ u_\infty$
Test C	-0.745	$36.670°$	BS ($x = 140\delta_0$)	$1 \times 10^{-5}\ u_\infty$
Test D	-0.496	$26.398°$	BS ($x = 140\delta_0$)	$1 \times 10^{-5}\ u_\infty$
Test E	-0.248	$13.938°$	BS ($x = 140\delta_0$)	$1 \times 10^{-5}\ u_\infty$
Test F	0	$0°$	BS ($x = 140\delta_0$)	$1 \times 10^{-5}\ u_\infty$

Table 2.5: Definition of cases used in the study of effects of the *effective* sweep angle in chapter § 6. *Amplitude* refers to the amplitude of the Inflow Mode (IM), as defined in equation (2.27), in case *Baseline*, and to the wall Blowing-Suction (BS) amplitude, as defined in equation (2.23), in the *Test* cases.

***Effective* sweep angle and wavelength of CFI**

A secondary set of control parameters is defined and used to examine the sensitivity of main perturbation mechanisms at the step. Namely, §§ 5.3.3 and 6.2.5 investigate the effect of the *effective* sweep angle and § 6.2.7 focuses on the effect of the incoming spanwise perturbation wavelength. The strategy employed for the analysis of the *effective* sweep angle effects is described next.

The ratio of spanwise to chordwise free-stream velocity imposed at the DNS inflow, w_∞/u_∞, establishes the orientation of the inviscid streamline. The main flow cases discussed in this thesis use $w_\infty/u_\infty = -1.241$, here referred to as the *Baseline* case. Additional simulations progressively increase w_∞ from $-1.241u_\infty$ to 0 in fixed steps of Δw_∞; these are designated as *Test* cases in table 2.5. The table also lists the angle at the inflow that the inviscid streamline forms with the x-direction, denoted by ϕ_s, and the relevant features of forcing.

The *Baseline* and *Test* cases adopt different strategies to trigger stationary instability growth upstream of the step. Modifying w_∞ inherently alters the nature of incoming boundary-layer perturbations, though not the structure of newly-identified near-wall perturbation features at the step, see chapter 6. The *Baseline* case follows the main DNS setup described in §§ 2.1.3 and 2.2.1. In contrast, some of the *Test* cases operate at small-sweep-angle and even unswept ($w_\infty = 0$) conditions. In unswept flow, the concept of an asymptotically evolving crossflow eigenmode is not tenable. However, for meaningful comparison with the *Baseline* case, a stationary perturbation must pre-exist in all cases. Leveraging the structural similarity between stationary CFI and Klebanoff modes (Klebanoff, 1971; Kendall, 1985) at a perturbation level (Herbert, 1993; Saric et al., 2003), a stationary Klebanoff mode is excited upstream of the step in the *Test* cases with *small* sweep angle (table 2.5). Following the approach of Herbert (1993), the stationary Klebanoff mode is introduced via spanwise modulation of the wall-normal velocity (blowing-suction) at the wall by altering the no-penetration condition at $y = 0$ in the DNS.

Chapter	Topic	Step height	Inflow CFI amplitude	Step location	Analysis	Test case name
4	CFI-step interaction	$h/\delta_0 = 0.59$, $0.76, 0.97$	$A_0/u_\infty = 3.5 \times 10^{-3}$	$x/\delta_0 = 177.62$	Stationary	step: I-III CFI: B
5	The lift-up effect	$h/\delta_0 = 0.97$	$A_0/u_\infty = 3.5 \times 10^{-3}$	$x/\delta_0 = 177.62$	Stationary	step: III CFI: B
6	Streaks at the step	$h/\delta_0 = 0.97$	$A_0/u_\infty = 3.5 \times 10^{-3}$, wall Blowing-Suction	$x/\delta_0 = 177.62$	Stationary	step: III CFI: B, Test A-F
7	Amplitude effects	$h/\delta_0 = 0.97$	$A_0/u_\infty = 1 \times 10^{-4}$, $3.5 \times 10^{-3}, 2.6 \times 10^{-2}$	$x/\delta_0 = 177.62$	Stationary	step: III CFI: A, B, C
8 (§ 8.1.1)	Breakdown by the step	$h/\delta_0 = 0.97$	$A_0/u_\infty = 1 \times 10^{-4}$, $3.5 \times 10^{-3}, 2.6 \times 10^{-2}$	$x/\delta_0 = 177.62$	Unsteady	step: III CFI: A, B, C
8 (§ 8.1.2)	Transition advancement	$h/\delta_0 = 0.59$, 0.76	$A_0/u_\infty = 2.6 \times 10^{-2}$	$x/\delta_0 = 177.62$	Stationary and unsteady	step: I, II CFI: C
8 (§ 8.2)	Transition delay	$h/\delta_0 = 0.76$	$A_0/u_\infty = 2.6 \times 10^{-2}$	$x/\delta_0 = 73.90$	Stationary and unsteady	step: II* CFI: C $\star$: x-shifted

Table 2.6: Summary of cases in the thesis.

2.1.3. Governing equations and boundary conditions

The behaviour of the physical system modelling swept-wing flow (§ 2.1.1) is mathematically described by the incompressible form of the mass,

$$\boldsymbol{\nabla} \cdot \boldsymbol{v} = 0, \tag{2.14}$$

and the momentum (1.1) conservation equations,

$$\frac{\partial \boldsymbol{v}}{\partial t} + \boldsymbol{\nabla} \cdot (\boldsymbol{v} \otimes \boldsymbol{v}) = -\boldsymbol{\nabla} p + \nu \boldsymbol{\nabla} \cdot (\boldsymbol{\nabla} \boldsymbol{v}), \tag{2.15}$$

with pertinent initial and boundary conditions. The density and viscosity remain constant, consistent with the low Mach number conditions in the reference experiments (Rius-Vidales, 2022). Particularly for the unperturbed base flow, the assumption of infinite wingspan (§ 1.2.2) lends itself to the condition of spanwise invariance and therefore to a simplified representation of the base-flow conservation equations, i.e.,

$$\frac{\partial u_\mathrm{B}}{\partial x} + \frac{\partial v_\mathrm{B}}{\partial y} = 0 \tag{2.16}$$

and

$$-u_\mathrm{B}\frac{\partial u_\mathrm{B}}{\partial x} - v_\mathrm{B}\frac{\partial u_\mathrm{B}}{\partial y} - \frac{1}{\rho}\frac{\partial p_\mathrm{B}}{\partial x} + \nu\left(\frac{\partial^2 u_\mathrm{B}}{\partial x^2} + \frac{\partial^2 u_\mathrm{B}}{\partial y^2}\right) = 0, \tag{2.17}$$

$$-u_\mathrm{B}\frac{\partial v_\mathrm{B}}{\partial x} - v_\mathrm{B}\frac{\partial v_\mathrm{B}}{\partial y} - \frac{1}{\rho}\frac{\partial p_\mathrm{B}}{\partial y} + \nu\left(\frac{\partial^2 v_\mathrm{B}}{\partial x^2} + \frac{\partial^2 v_\mathrm{B}}{\partial y^2}\right) = 0, \tag{2.18}$$

$$-u_\mathrm{B}\frac{\partial w_\mathrm{B}}{\partial x} - v_\mathrm{B}\frac{\partial w_\mathrm{B}}{\partial y} + \nu\left(\frac{\partial^2 w_\mathrm{B}}{\partial x^2} + \frac{\partial^2 w_\mathrm{B}}{\partial y^2}\right) = 0. \tag{2.19}$$

The system of equations (2.17-2.19) has been expressed in convective form, which facilitates the analysis and interpretation presented in § 4.1. Different boundary and initial conditions are considered, depending on the case. Common choices are summarised below, with specific differences pointed out as needed.

At the inflow, $\partial p/\partial x = 0$ and the velocity vector, $\boldsymbol{v}_\mathrm{in}$, is prescribed and assigned to the solution of the FSC equations (2.8), i.e., $\boldsymbol{v}_\mathrm{in} = \boldsymbol{v}^\mathrm{FSC}$. No further condition at the inlet is specified in the computations of the unperturbed base flow. However, in the steady perturbed and unsteady flows, the inflow boundary-layer profile is

$$\boldsymbol{v}_\mathrm{in} = \boldsymbol{v}^\mathrm{FSC} + [u'_\mathrm{in}\ v'_\mathrm{in}\ w'_\mathrm{in}]^\mathrm{T}, \tag{2.20}$$

to trigger stationary CFI growth. Here, $[u'_\mathrm{in}\ v'_\mathrm{in}\ w'_\mathrm{in}]^\mathrm{T}$ expresses a stationary crossflow perturbation computed from a linear local stability analysis on the inflow base-flow profile, see § 2.2.1 for details on the numerical implementation.

At the top boundary, the static pressure is prescribed and used to approximate the outer-flow evolution (§ 2.1.1) from the experiments of Rius-Vidales and Kotsonis (2021). The static pressure distribution that is ultimately imposed at $y = y_\mathrm{max}$ is computed using expression (2.5) and the irrotational-flow assumption. It should be noted that the choices of boundary conditions at the top support inflow. As

quantitatively illustrated in figure 2.10 (*b*) below, the accelerated free-stream flow carries a condition of downwash (i.e., $v < 0$) *far* from the wall, with $\partial|v|/\partial y > 0$. This trend exhibits itself in conjunction with mild upwash (i.e., $v > 0$) close to the wall and near the inflow, where the boundary layer undergoes rapid growth in x.

Similar numerical studies of swept-wing flow describe that the penetration condition at the top can become unstable if the wall-normal velocity is "too negative" (Chauvat, 2020). The formulation of the velocity boundary condition in the present thesis ensures that fluctuations are quenched. Namely, the instantaneous velocity components are split into an instantaneous spanwise mean (i.e., spanwise-averaged) and instantaneous fluctuation (i.e., the deviation from the spanwise mean) components. A Neumann-type condition is applied for the spanwise mean component, i.e., $\partial^2[\langle u\rangle\ \langle v\rangle\ \langle w\rangle]/\partial y^2 = 0$, whereas the fluctuating part is artificially damped out, see Hickel and Adams (2008) for further details. Here, the symbol "$\langle\rangle$" expresses spanwise mean operation. Periodic boundary conditions are applied at the transverse faces to constrain the growth of the CFI in x. At the wall, the no-slip and no-penetration conditions are applied, i.e., $[u\ v\ w] = 0$, and a Neumann-type condition is used for pressure in the direction normal to the wall.

At the outflow, a Neumann-type boundary condition is applied to the velocity vector, i.e., $\partial^2[u\ v\ w]/\partial x^2 = 0$. The static pressure is prescribed by assigning it the value corresponding to $x = x_{\max}$ from experimental outer-flow evolution (2.5). In addition, a damping zone is placed towards the rear of the domain to suppress temporal fluctuations in the unsteady flow computations. For the main baseline case (table 2.5), the damping zone encompasses $x/\delta_0 \geq 475$. In selected simulations with the step present, the domain is shortened in x to reduce computational cost; the damping zone is correspondingly shifted to $x/\delta_0 \geq 230$, for the transitional-flow case discussed in § 8.1.1 and to $x/\delta_0 \geq 297$ for the transitional-flow case discussed in § 8.1.2.

The damping approach relies on the Selective Frequency Damping (SFD) method. That is, exclusively in the damping zone, the momentum-conservation equation (1.1) and (2.15) is modified through the addition of a linear forcing term,

$$\dot{\boldsymbol{q}} = \mathbb{NS}(\boldsymbol{q}) - \chi\,(\boldsymbol{q} - \bar{\boldsymbol{q}})\,, \quad \chi \in \mathbb{R}^+, \tag{2.21}$$

that drives the flow field $\boldsymbol{q}$ to $\bar{\boldsymbol{q}}$. The flow field $\bar{\boldsymbol{q}}$ is a low-pass filtered version of $\boldsymbol{q}$, whose evolution equation reads

$$\dot{\bar{\boldsymbol{q}}} = \frac{\boldsymbol{q} - \bar{\boldsymbol{q}}}{\Delta}, \quad \Delta \in \mathbb{R}^+, \tag{2.22}$$

and Δ relates to the cut-off frequency of the filter. The effectivity and efficiency of SFD strongly depend on the choice of model parameters χ and Δ (Åkervik et al., 2006; Jordi et al., 2014; Casacuberta et al., 2018), which are main inputs of the numerical simulation. The choices $\chi = 0.8$ and $\Delta = 5$ are adopted, based on the criterion proposed by Casacuberta et al. (2018). The so-called encapsulated formulation by Jordi et al. (2014) is used for the numerical implementation of SFD in the time-stepping solver.

In the computations of the unsteady flow, the flow field is forced at selected temporal frequencies through a disturbance strip placed at the wall near the inflow, with zero net mass flow. The present approach is largely similar to the one employed by Wassermann and Kloker (2002) to study the evolution of secondary crossflow instability: a disturbance strip is defined, where the wall-normal velocity is modulated continuously in time as follows:

$$v(x,0,z,t) = f_s(x) \sum_{k=1}^{M_{\mathrm{BS}}} A_k^{\mathrm{BS}} \cos\left(\beta_0 z + 2\pi k f_0 t + \phi_k\right), \tag{2.23}$$

where f_0 is the fundamental temporal frequency, M_{BS} is the number of modal components, A_k^{BS} and ϕ_k respectively denote the amplitude and a random phase assigned to each modal component k, and $f_s(x)$ modulates the wall-normal velocity smoothly in x. It reads

$$f_s = \left(\frac{4\left(x - x_{\mathrm{BS,start}}\right)\left(x_{\mathrm{BS,end}} - x\right)}{\left(x_{\mathrm{BS,end}} - x_{\mathrm{BS,start}}\right)^2} \right)^3, \tag{2.24}$$

with $x_{\mathrm{BS,start}}$ and $x_{\mathrm{BS,end}}$ indicating the starting and ending positions of the disturbance strip in x. Generally in this thesis, $x_{\mathrm{BS,start}} = 20\delta_0$ and $x_{\mathrm{BS,end}} = 32\delta_0$; an exception is made in chapter 6, where the wall blowing-suction is used to induce a stationary Klebanoff mode. The function f_s is symmetric and has vanishing first and second derivatives at $x_{\mathrm{BS,start}}$ and $x_{\mathrm{BS,end}}$. At the beginning of the simulation, the velocity at the disturbance strip is weighted by a smooth temporal function as well to alleviate transient effects.

The input choices in equation (2.23) are $f_0 = 1$ kHz, $M_{\mathrm{BS}} = 14$, $A_{\text{1-2}}^{\mathrm{BS}} = 0$, and $A_{\text{3-14}}^{\mathrm{BS}} = 5 \times 10^{-3} u_\infty$, implying that the flow field is forced at temporal frequencies in the range 3 to 14 kHz. Based on preliminary investigations and stability analyses, see Casacuberta et al. (2022a) and § 2.3.3, the lower-frequency components are not explicitly forced in the disturbance strip, but develop naturally further downstream. This modelling choice aims to prevent an excessively strong amplification of *type*-III instability mechanisms upstream of the step. See Högberg and Henningson (1998) and Wassermann and Kloker (2002) for a numerical discussion on the spatial growth trends of low- and high-frequency unsteady instabilities.

The setup choices of the disturbance strip in this thesis produce a transition scenario qualitatively consistent with the reference experiments of Rius-Vidales and Kotsonis (2021) under no-step conditions. In particular, emphasis has been placed on ensuring (1) a similar location of the transition front and (2) on qualitatively reproducing the breakdown of stationary crossflow vortices driven by the amplification of the type-I secondary crossflow instability, see Casacuberta et al. (2025a) for details.

2.2. Modelling methods

The governing equations are solved using Direct Numerical Simulations (DNS). In addition, linear and non-linear stability methods are employed to guide, complement, and cross-validate the DNS results. This section provides a detailed description of the DNS setup and introduces the stability approaches.

2.2.1. Setup of Direct Numerical Simulations

The mass and the momentum-conservation equations (2.14-2.15) are discretised by considering a formulation based on the Pressure-Poisson Equation (PPE). On taking the divergence of (2.15) and combining it with equation (2.14), the following Poisson-type equation is obtained:

$$\boldsymbol{\nabla}^2 p = -\boldsymbol{\nabla} \cdot (u \cdot \boldsymbol{\nabla} u)\,. \tag{2.25}$$

The system of equations that is ultimately chosen to numerically describe the incompressible swept-wing flow is (2.15) and (2.25) instead of (2.14) and (2.15) see, for instance, the discussion by Rempfer (2006) on the role of pressure in preserving the continuity condition. Equations (2.15) and (2.25) are numerically solved by use of an adapted version of the classic fractional step method (Harlow and Welsh, 1965; Chorin, 1968) and are advanced in time with a low-storage third-order explicit Runge-Kutta scheme (Shu, 1988). The Finite Volume (FV) method with a staggered Cartesian grid representation (figure 2.7) is employed for the spatial discretisation.

The computational domain is partitioned into finite volumes, hereafter referred to as cells, bounded by faces of area S_f. The semi-discrete form of the momentum conservation equation (2.15) integrated over a particular volume, reads

$$\frac{\mathrm{d}\boldsymbol{V}_\mathrm{V}}{\mathrm{d}t} = \underbrace{\sum_{f=1}^{6} -\mathcal{C} - \mathcal{P} + \mathcal{D}}_{\boldsymbol{R}_\mathrm{V}}, \tag{2.26}$$

where $\boldsymbol{V}$ is the velocity vector in the FV representation, and $\mathcal{C}$ and $\mathcal{D}$ respectively denote the convection and diffusion terms evaluated at the faces by virtue of the Gauss-Green theorem. Analogously, $\mathcal{P}$ expresses the pressure term.

The sequence to compute the FV flow field from time t^n to a time $t^{n+1} = t^n + \Delta t$ is summarised in algorithm 1. The approach relies first on evaluating a preliminary velocity field and, second, applying a pressure correction to ultimately produce a divergence-free flow field. Here, the subindices V and f respectively denote quantities evaluated in the volume or at the faces of the cells in the staggered grid arrangement. In algorithm 1, a_{ij} expresses the coefficients of the Runge-Kutta scheme, i indicates the Runge-Kutta sub-step, s is the number of sub-steps, Φ is the discretised form of the PPE, Π is a pressure correction, and γ_cor is a scaling parameter for the pressure

Algorithm 1 Fractional step method with explicit Runge-Kutta

1: **for** i = 1 : s **do**
2: $\quad \boldsymbol{V}_\mathrm{V}^{\star(i)} = \boldsymbol{V}_\mathrm{V}^{(n)} + \Delta t \sum_{j=1}^{i} a_{ij} \boldsymbol{R}_\mathrm{V}^{(j)}$ ▷ Compute preliminary velocity
3: $\quad \Pi_f^{(i)} \leftarrow \Phi(S_f, \boldsymbol{V}_f^{\star(i)})$ ▷ Solve the discretised PPE
4: $\quad \boldsymbol{V}_\mathrm{V}^{\star\star(i)} = \boldsymbol{V}_\mathrm{V}^{\star(i)} - \gamma_\mathrm{cor}(\Delta t)\,(\nabla\Pi)_\mathrm{V}^{(i)}$ ▷ Correct velocity
5: $\quad p_f^{(i)} = p_f^{(i)} + \Pi_f^{(i)}$ ▷ Correct pressure
6: **end for**
7: $\boldsymbol{V}_\mathrm{V}^{(n+1)} = \boldsymbol{V}_\mathrm{V}^{\star\star(s)}$

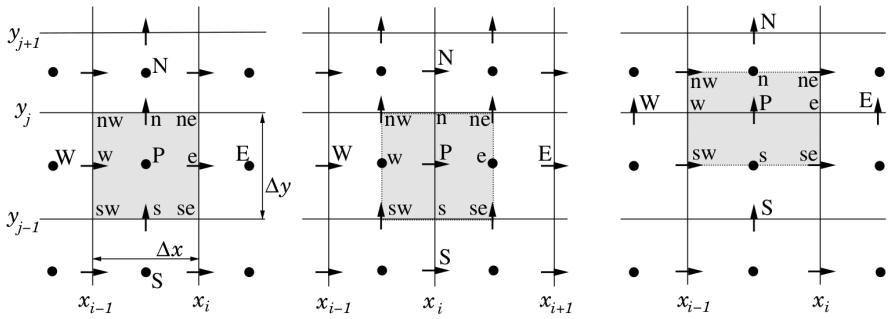

Figure 2.7: Control volumes for a staggered grid: mass conservation (left), x-momentum (centre), and y-momentum (right). Reproduced verbatim from Ferziger et al. (2020).

correction. The time step, Δt, is obtained by prescribing the Courant-Friedrichs-Lewy (CFL) number to unity. As noted by D'Alessandro et al. (2018), the present approach (algorithm 1) differs from the classic fractional step method in that the convection and diffusion terms are treated explicitly. It is noted the pressure remains implicit, thus preventing a splitting error (Sanderse and Koren, 2012). See also the discussion by Armfield and Street (1999) on the variants of the fractional step method on staggered grids.

The discretised PPE (algorithm 1) is solved through a Krylov subspace method, namely the bi-conjugate gradient stabilised (BiCGstab) method (van der Vorst, 1992; Sleijpen et al., 1994). The PPE is solved until a convergence criterion of $\epsilon_{\mathrm{DIV}} = 10^{-9}$ for the steady perturbed flow and $\epsilon_{\mathrm{DIV}} = 10^{-7}$ for the unsteady flow. Here, ϵ_{DIV} expresses the L_2-norm of the velocity divergence. The PPE and the diffusion term (2.26) are discretised in space with a second-order centred scheme. For the convective term, a fifth-order velocity reconstruction at the cell faces is employed, utilising the coefficients provided by Hickel (2008, Eq. 2.29). The final numerical flux is computed as the average of $\mathcal{U}^+$ and $\mathcal{U}^-$ and by the addition of a regularisation term, namely $(1/2)\,|\boldsymbol{v}_{\mathrm{ad}}|\,(\mathcal{U}^+ - \mathcal{U}^-)$. Here, $\mathcal{U}^+$ and $\mathcal{U}^-$ respectively denote the two fifth-order reconstructions of the solution on the same cell face and $|\boldsymbol{v}_{\mathrm{ad}}|$ is the absolute value of the local advection velocity. It is noted that the average of $\mathcal{U}^+$ and $\mathcal{U}^-$ corresponds identically to a sixth-order centred reconstruction with the coefficients from Hickel (2008, Eq. 2.29). The present spatial discretisation approach prevents the growth of spatial dispersion errors in the staggered grid, as demonstrated in preliminary tests. Confidence in the numerical setups, grid topology, and grid density is established in § 2.3, where an extensive cross-validation and verification analysis of the DNS results is presented.

Three layers of ghost cells are placed at the boundaries of the computational domain to apply boundary conditions. As mentioned above (§ 2.1.3), the inflow velocity profile in the steady-perturbed and unsteady-flow computations is disturbed with a stationary crossflow perturbation (2.20). In the ghost cells, the chordwise

velocity-perturbation component is given by

$$u'_{\text{in}} = A_0 \left(\tilde{u}^{\text{in}}_r(y) \left\{ \cos(\alpha^{\text{in}}_r x + \beta_0 z) \right\} - \tilde{u}^{\text{in}}_i(y) \left\{ \sin(\alpha^{\text{in}}_r x + \beta_0 z) \right\} \right), \tag{2.27}$$

2

where $A_0 \in \mathbb{R}^+$ denotes the initial amplitude assigned to the crossflow eigenmode and $\tilde{u}^{\text{in}} = \tilde{u}^{\text{in}}_r + \text{i}\tilde{u}^{\text{in}}_i$ is the normalised amplitude function, with $\max\left\{\text{abs}(\tilde{u}^{\text{in}})\right\} = 1$. The quantity $\alpha^{\text{in}}_r \in \mathbb{R}$ denotes the chordwise wavenumber of the crossflow eigenmode obtained as the solution to a linear local stability analysis on the inflow base-flow profile. A treatment identical to (2.27) is considered for the perturbation components v'_{in} and w'_{in} (2.20). For the Neumann-type boundary conditions (§ 2.1.3), the ghost-cell values are assigned such that the second derivative of the pertinent quantity is null at the boundary.

For the initial condition, the numerically computed steady-state solutions are employed sequentially. The procedure is as follows: first, the computations of the unperturbed base flow, $\boldsymbol{q}_{\text{B}}$, prescribe as initial condition the solution of the FSC equations (2.8). It is noted that the Hartree parameter (2.9) is evaluated individually at every x-station, inasmuch as this renders more efficient simulations, compared to the use of a *global* Hartree parameter. The L_2-norm of the temporal derivatives, ϵ, is used as convergence criterion for the base-flow computations. A value of $\epsilon = 10^{-8}$ is used. Next, the time-converged unperturbed base-flow solution forms the initial condition for the computations of the steady perturbed flow, $\boldsymbol{q}_{\text{DB}}$. The L_2-norm of the difference between the instantaneous solution and the low-pass filtered solution associated with the SFD formulation, ϵ_{SFD}, is used as convergence criterion for the computations of the steady perturbed flow (Åkervik et al., 2006; Casacuberta et al., 2018). A value of $\epsilon_{\text{SFD}} = 10^{-6}$ is used; $\epsilon_{\text{SFD}} > \epsilon$ since the computations of the steady perturbed flow are significantly more expensive than the base-flow runs. The time-converged steady-perturbed-flow solution is subsequently employed as the initial condition for computations of the final unsteady flow.

2.2.2. DNS data analysis

The results from DNS are Fourier analysed to recover the behaviour of steady and unsteady perturbation modes. The analysis proceeds in two steps. First, the three-dimensional stationary perturbation field obtained from simulations of the steady perturbed flow (2.10), is decomposed into spanwise Fourier modes. A discrete Fourier transform of spanwise perturbation signals is performed using a Fast Fourier Transform (FFT) algorithm. Second, a collection in time of three-dimensional DNS snapshots is Fourier analysed in the spanwise direction and in time using a similar FFT procedure. The Fourier coefficients are recovered for perturbation structures with a temporal wavenumber $k\omega_0$ and spanwise wavenumber $j\beta_0$, as expressed in equation (2.11). In the reference no-step case, r.C, a total of 290 DNS snapshots are generated per period of the fundamental temporal frequency, i.e., $f_0 = 1$ kHz. In the transitional step case, s.C, it is ensured that at least 20 snapshots are collected per period of the frequency component most critically affecting transition i.e., $f = 12$ kHz.

The analysis of unsteady perturbation effects is complemented by the use of pointwise temporal signals from numerical probes. The power spectral density (PSD) is estimated using Welch's method of overlapped segments with two Hamming windows

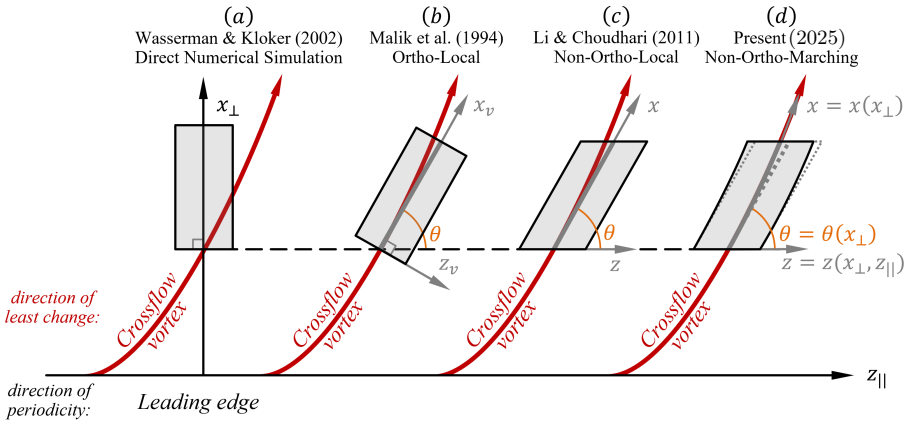

Figure 2.8: Formulations of the secondary crossflow instability problem and choices of coordinate systems in the literature, leveraging spanwise periodicity along the leading-edge direction (denoted $z_{||}$) and various complementary x-direction. Reproduced from Groot et al. (2025). The stability analysis employed in this thesis is based on formulation (d).

with an overlap of 80%.

2.2.3. Overview of stability methods

Two main stability methods are employed in this thesis to complement the results from DNS. First, the incompressible Linear (LPSE) and Non-linear (NPSE) Parabolised Stability Equations (Bertolotti et al., 1992) method is used to cross-validate and complement the stationary-perturbation behaviour obtained from the steady-state DNS results. In the linear PSE approach, the perturbation quantities are expressed as a *slowly* varying shape function, $\tilde{\boldsymbol{q}}$, and a *rapidly* varying wave function, χ, such that

$$\boldsymbol{q}'(x, y, z, t) = \tilde{\boldsymbol{q}}(\xi, y)\, \chi(x, z, t) + \text{c.c.}, \tag{2.28}$$

where $\partial\chi/\partial x = \mathrm{i}\alpha(\xi)$, $\partial\chi/\partial z = \mathrm{i}\beta$, $\partial\chi/\partial t = -\mathrm{i}\omega$, and $\xi = x/Re$ is a slowly varying streamwise scale. A normalisation condition is also imposed to close the system of equations, preventing the shape function $\tilde{\boldsymbol{q}}$ from absorbing rapid variations of growth and oscillation, which remain confined to the wave function χ.

Leveraging the modified character (Bertolotti et al., 1992; Herbert, 1997) of the perturbation equations (1.3) resulting from the PSE ansatz (2.28) and its underlying assumptions, the perturbation behaviour can be determined using a marching approach, which is computationally more efficient than solving the full Navier-Stokes methods. To maintain brevity, the key aspects of the LPSE and NPSE setups used in this thesis are described in appendix B, and the reader is referred to Westerbeek (2020) for further details. Additional background on the PSE formulation, methodology, and numerical aspects related to crossflow perturbations is given by Haynes and Reed (2000).

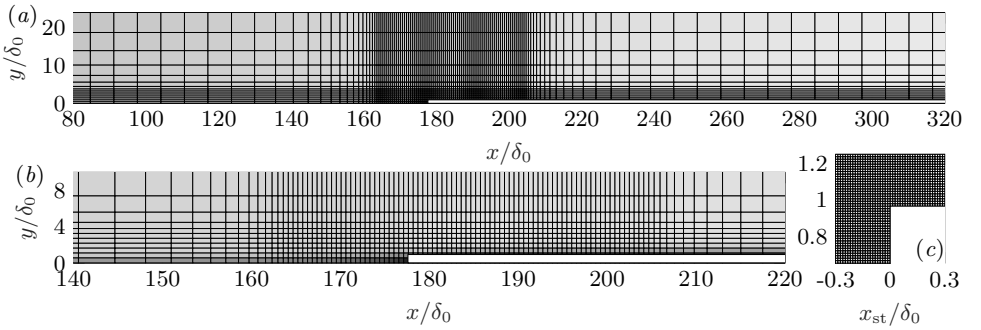

Figure 2.9: Topology of the computational grid in three zoomed views around the step. The grid density in (*c*) corresponds exactly to that of the main steady-state computations, i.e., case s.*B* in table 2.7, while in (*a*,*b*) it is reduced by a factor 40 for visualisation purposes.

Second, two-dimensional linear and two-dimensional plane-marching (the latter is popularly known as PSE-3D (Paredes et al., 2015)) stability approaches are employed to cross-validate the unsteady perturbation behaviour from DNS. In this thesis, these methods are referred to, respectively, as the linear BiGlobal and plane-marching BiGlobal (BiG) approaches, and are formulated using a non-orthogonal coordinate system (figure 2.8 (*d*)). The (non-orthogonal) plane-marching BiG approach extends the (non-orthogonal) local BiG approach used by Groot and Eppink (2021), which is itself based on the framework originally introduced by Li and Choudhari (2011) (figure 2.8 (*c*)). Figure 2.8 (*a*,*b*) illustrates earlier coordinate-system choices of the secondary crossflow instability problem in the literature. The use of a non-orthogonal coordinate system is required in this thesis, because the unsteady perturbations of interest are periodic along the z-direction, i.e., parallel to the step, while the direction of smallest gradient at a given x is not orthogonal to z. The reader is referred to appendix B and Groot et al. (2025) for details on the method formulations, the selection of the local direction of smallest gradient, and numerical considerations.

2.3. Verification and cross-validation

Following the discussion of the DNS setup and stability methods, this section outlines the grid design and presents several diagnostic plots supporting the verification and cross-validation of the unperturbed base flow, the steady perturbed flows corresponding to the three initial CFI-amplitude cases considered in this thesis, and the unsteady flow for the medium-amplitude CFI case (characterised by monochromatic unsteady forcing). Finally, an overview is given of the behaviour of the reference (no-step) unsteady flow under large-amplitude CFI conditions with multi-frequency unsteady forcing, which defines the perturbation environment in the transitional-flow cases with the step present.

Chapters 4 and 5 (no-step case)

Case	$\Delta x^+\|_{\mathrm{st}}$	$\Delta y^+\|_{\mathrm{st}}$	$\Delta z^+\|_{\mathrm{st}}$	$\Delta x^+\|_{\mathrm{out}}$	$\Delta y^+\|_{\mathrm{out}}$	$\Delta z^+\|_{\mathrm{out}}$
No-step	0.52	0.52	5.20	5.68	0.47	4.73
Case	$\lambda_z/\Delta x\|_{\mathrm{st}}$	$\lambda_z/\Delta y\|_{\mathrm{st}}$	$\lambda_z/\Delta z\|_{\mathrm{st}}$	$\lambda_z/\Delta x\|_{\mathrm{out}}$	$\lambda_z/\Delta y\|_{\mathrm{out}}$	$\lambda_z/\Delta z\|_{\mathrm{out}}$
No-step	720	720	72	60	720	72

Chapters 7 and 8 (no-step and step III cases)

Case		**Steady** ($\boldsymbol{q}_{\mathrm{DB}}$)			**Unsteady** ($\boldsymbol{q}$)					
		N_x	N_y	N_z	N_x	N_y	N_z	$\Delta x^+\|_{\mathrm{st}}$	$\Delta y^+\|_{\mathrm{st}}$	$\Delta z^+\|_{\mathrm{st}}$
Step III	s.A	6760	504	72						
	s.B	6760	504	72	5080	504	72	0.56	0.56	5.60
	s.C	5080^1	1008	144	5080^1	1008	144	**1.54**	**0.77**	**7.70**
No-step	r.A	3380	288	72						
	r.B	6760	576	72	5080^1	576	72	0.65	0.65	6.5
	r.C	6760	576	144	6760	576	144	0.67	0.67	3.35

TABLE 2.7: Choices of grid density. Upper sub-table: computations of the steady perturbed flow (2.10) without the step. Grid spacing is shown both at the virtual step location ($|_{\mathrm{st}}$) and near the outflow ($|_{\mathrm{out}}$), expressed in wall units (top) and relative to the fundamental spanwise wavelength (bottom). The N_x, N_y, and N_z denote the number of grid points in the x-, y-, and z-directions, respectively, with $(N_x, N_y, N_z) = (6760, 576, 72)$. Lower sub-table: computations of the steady perturbed (2.10) and unsteady (1.2) flows. In the step cases, N_y is indicative of $x_{\mathrm{st}} \geq 0$. The grid spacing in wall units is evaluated just downstream of the step x-location at the z-location of maximum wall shear, with bold font indicating near breakdown conditions. The superindex "1" indicates that the domain is shorter in x ($245\delta_0$); the height is fixed at $26\delta_0$.

2.3.1. GRID TOPOLOGY AND DENSITY

Five Cartesian grids are designed in this thesis, corresponding to:

- ***(i)*** one case without the step, used for reference,
- ***(ii)*** three cases with steps of different heights (see table 2.3), placed at $x/\delta_0 = 177.62$ and guided by the experiments,
- ***(iii)*** one case with the step placed at $x/\delta_0 = 73.90$, used towards analysing mechanisms of CFI stabilisation.

The grid topology is common to all cases: a smooth hyperbolic refinement is applied in the chordwise direction near the step. For consistency, the reference case is treated in the same manner. Hyperbolic refinement is also applied in the wall-normal direction near the wall. The chosen refinement ratios ensure smooth transitions between

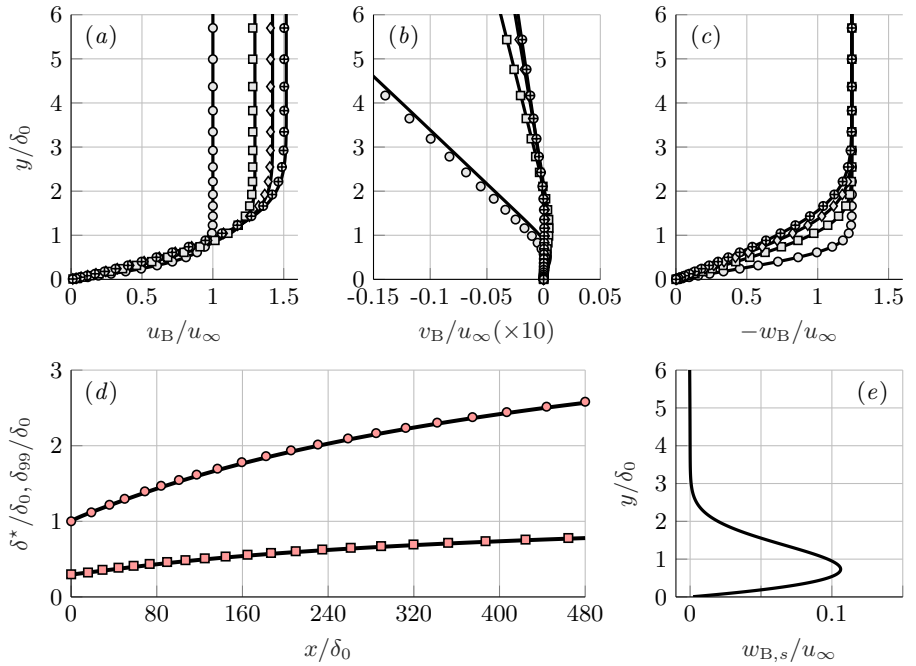

Figure 2.10: Evolution of the unperturbed base flow obtained from DNS (solid lines) and the boundary layer equations (symbols): (*a*) chordwise-, (*b*) wall-normal- and (*c*) spanwise-velocity profiles at $x/\delta_0 = 0$ (circles), 160 (squares), 320 (diamonds), 480 (circles with a cross) and (*e*) crossflow-velocity profile at $x/\delta_0 = 320$. Evolution in x of the boundary-layer thickness (black line and circles) and displacement thickness (black line and squares) in (*d*).

grid regions and produce cells with a unit aspect ratio in the x-y plane, both near the step and far into the free-stream (figure 2.9).

The choices of grid density are subject to the flow field under consideration, see table 2.7 characterising both the steady perturbed and unsteady flows. In addition, three layers of ghost cells are added at the domain boundaries to apply boundary conditions. Regarding the unperturbed base flow, only two spanwise grid points ($N_z = 2$) are considered for its calculation, i.e., effectively solving for a single x-y plane of the flow, leveraging the spanwise invariance of the flow. In table 2.7, N_x, N_y, and N_z respectively indicate the number of grid points in the x-, y-, and z-directions and the grid spacing expressed in wall units is based on the local friction velocity. For an extensive discussion and justification of the grid-density choices, the reader is referred to Casacuberta et al. (2022b) and Casacuberta et al. (2025a).

2.3.2. Unperturbed base flow and steady perturbed flows

The spatial evolution of the unperturbed base flow is shown in figure 2.10, which exhibits good agreement between the DNS results (solid lines) and independent

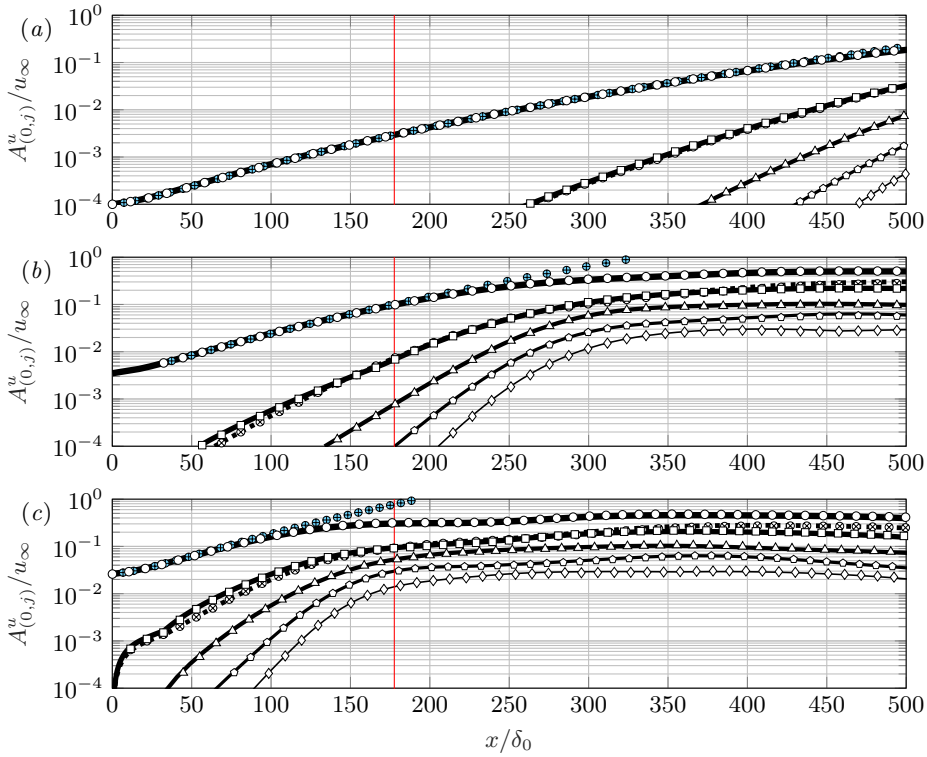

Figure 2.11: Chordwise evolution of the amplitude of the stationary CFI in the reference no-step case with $A_0 = 1{\times}10^{-4}u_\infty$ (a), $A_0 = 3.5{\times}10^{-3}u_\infty$ (b), and $A_0 = 2.6{\times}10^{-2}u_\infty$ (c) from linear PSE (blue symbols), non-linear PSE (white symbols), and DNS (solid lines): spanwise Fourier modes j = 1-5 (thick-to-thin), $j = 0$ (dotted). Vertical red line indicates the virtual step location.

boundary-layer computations (symbols) (see, e.g., Rius-Vidales (2022) for details on the numerical setup), both performed under reference (no-step) conditions. The agreement between the two methods strengthens the validity of the numerical setup choices and model approximations, such as the domain height.

Concerning the steady perturbed flow, two critical aspects arise in the numerical resolution of the equations. First, whilst computations of the base flow are effectively carried out in the x-y plane, the steady perturbed flow incorporates flow modulation in the z-direction. Sufficient resolution in terms of spanwise perturbation modes is necessary to accurately resolve the stages of non-linear perturbation growth and saturation (Haynes and Reed, 2000; Wassermann and Kloker, 2002; Li et al., 2016). Haynes and Reed (2000) perform calculations considering up to the eight spanwise harmonic and Wassermann and Kloker (2002) indicate that "typically 12-16 spanwise modes are considered to be sufficient" in NPSE computations. In the present DNS, this requirement is essentially determined by the grid density in z (see N_z in table 2.7). The validity of the choices made in this thesis is demonstrated by the

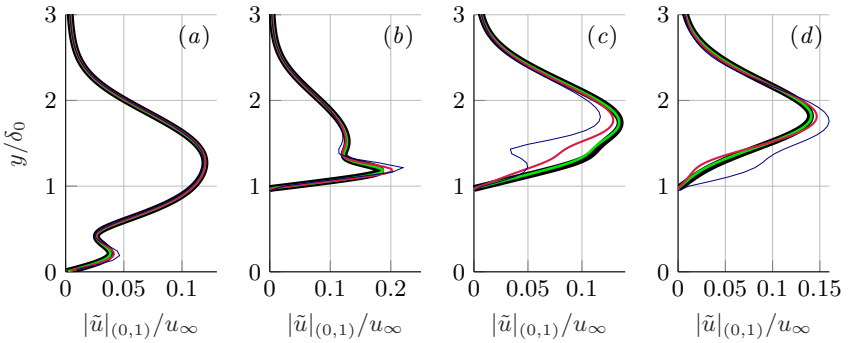

Figure 2.12: Grid sensitivity to the steady perturbed flow at the step. Profiles of the fundamental spanwise perturbation close upstream and close downstream of the step for different choices of wall-normal grid resolution: $N_y = 144$ (blue extra thin), 288 (red thin), 576 (green thick), and 1152 (black extra thick) at $x_{\mathrm{st}}/\delta_0 = -0.8$ (a), 1.5 (b), 9 (c), 17 (d). The largest step (i.e., step III in table 2.3) and medium-amplitude CFI (i.e., $A_0/u_\infty = 3.5 \times 10^{-3}$ in table 2.4) cases are considered.

strong agreement between DNS and NPSE results for the amplitude curves of the fundamental and higher-order harmonic crossflow modes, as illustrated in figure 2.11, showing the small-(a), medium-(b), and large-(c) amplitude CFI cases (table 2.4).

Second, when the step is present, an additional stationary perturbation structure is shown to form locally at the step apex (chapter 6). A grid-convergence study is carried out in this thesis to examine the sensitivity of this highly localised structure to the grid density (table 2.7). The solution is fully grid-converged on the production mesh, as shown in figure 2.12.

2.3.3. Unsteady flows

In addition to the DNS-NPSE comparison for stationary perturbations, the linear local and linear plane-marching BiG approaches (§ 2.2.3) are employed to cross-validate the unsteady perturbation behaviour with the DNS results, as well as to characterise the perturbation environment in the reference (no-step) scenarios, under both medium- and large-amplitude CFI conditions. The BiG problem is solved using the steady perturbed flow obtained from the steady-state DNS computations.

Medium-amplitude CFI (case r.*B*)

Solely for the purpose of cross-validation, monochromatic (single-frequency) unsteady forcing is first applied to the steady perturbed flow under *medium*-amplitude CFI conditions (table 2.4). Two DNS computations, each for a different fundamental frequency, namely, $f_0 = 1$ kHz and 6 kHz, are performed and analysed independently. The disturbance strip used to trigger unsteady perturbation growth is placed just upstream of the neutral point for each considered frequency, as indicated by a BiG stability analysis carried out *a priori*, see Casacuberta et al. (2022a) for details. The initial forcing amplitudes in the disturbance strip (2.23) are $A_1^{\mathrm{BS}}/u_\infty = 10^{-5}$ for $f_0 = 1$ kHz and $A_1^{\mathrm{BS}}/u_\infty = 10^{-3}$ for $f_0 = 6$ kHz.

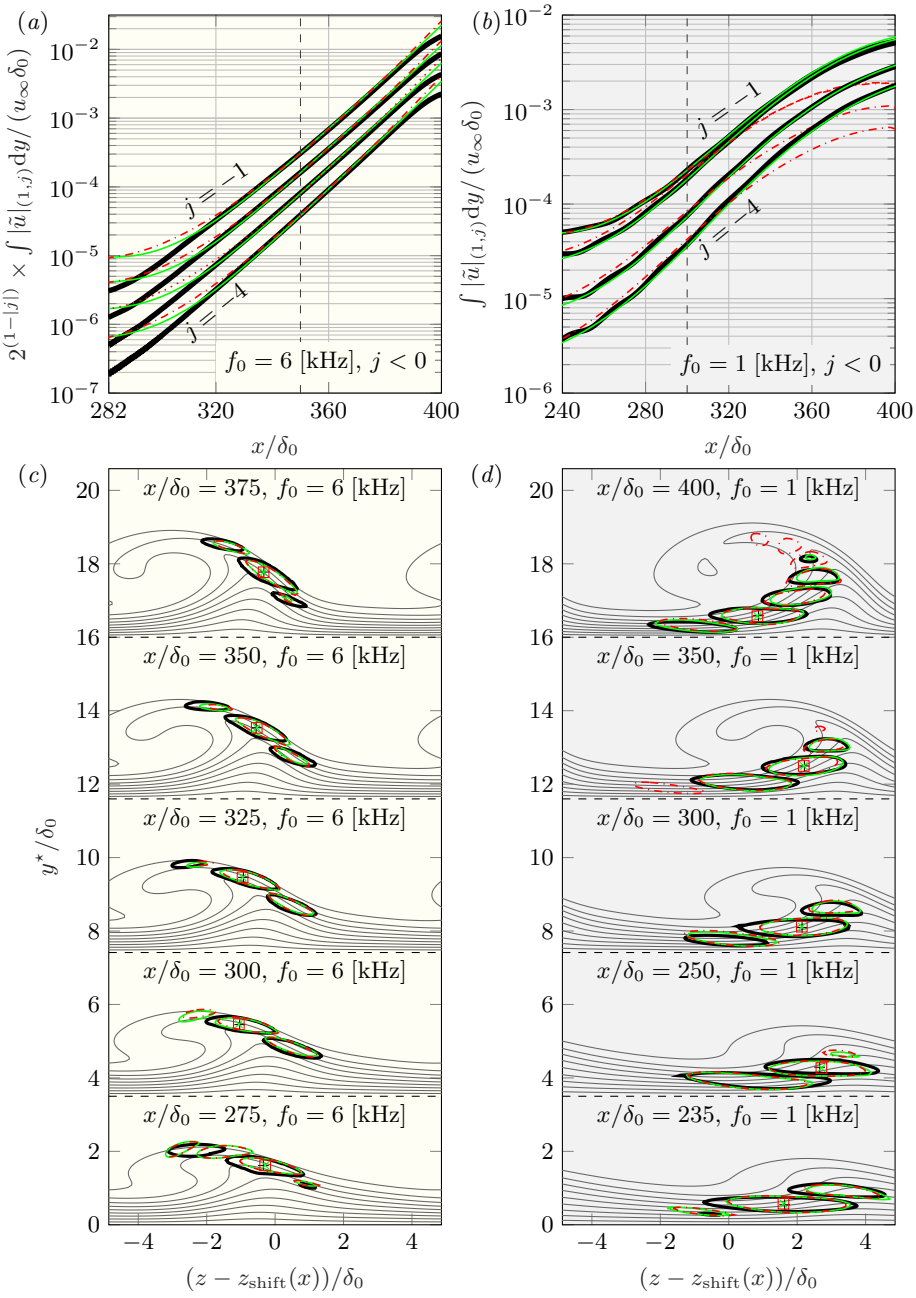

Figure 2.13: Chordwise evolution of the amplitude (a,b) and shape (c,d), evaluated as $\sum_{j=-5}^{5} u'_{(1,j)}$ (2.11), of monochromatic unsteady perturbations. Results are shown for the temporal frequencies $f = 6$ kHz (a,c) and $f = 1$ kHz (b,d), considering the spanwise modes $j = -1$ to -4 (curves top to bottom, see j labels in (a),(b)) from: DNS (thick solid black), plane-marching BiG (thin solid green), and local BiG (dash-dotted red) under *medium*-amplitude CFI conditions (table 2.4). The amplitude curves of the BiG method are matched to the DNS equivalent at $x/\delta_0 = 350$, symbols in (c,d) indicate the position of perturbation phase alignment between methods, and $y^\star$ expresses the relative wall-normal location in (c,d) with dashed lines indicating the wall. The isocontours of perturbation shape in (c,d) represent 30% of the in-plane maximum and grey lines illustrate the steady perturbed flow at levels of 10%, 20%, ... of the free-stream value. The y-scaling in (a) prevents overlapping curves.

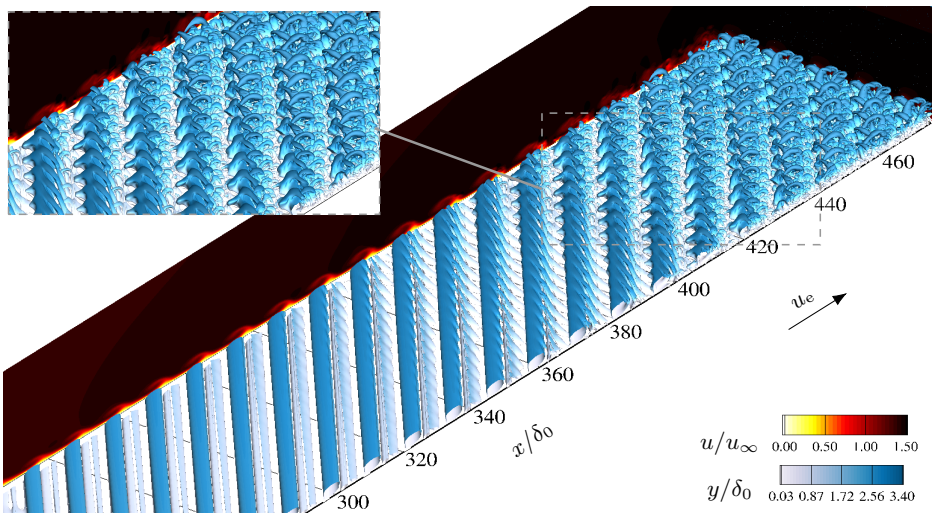

Figure 2.14: Instantaneous Q-criterion isosurfaces coloured by wall distance and y-z, x-y planes of instantaneous chordwise velocity. Zoom of the breakdown region, $400 \leq x/\delta_0 \leq 440$, in the inset. The DNS data are duplicated 4 times in z for illustration purposes.

As expected for monochromatic unsteady forcing at $f = 1$ kHz, the *type*-III secondary instability mechanism dominates in both the DNS and the BiG results. Figure 2.13 (d) illustrates the organisation of the unsteady perturbation field at different x-locations by showing $\sum_{j=-5}^{5} u'_{(1,j)}$, that is, the superposition of spanwise Fourier modes associated with the fundamental frequency $f = 1$ kHz. Figure 2.13 (b) correspondingly quantifies the perturbation amplification. The structure of the perturbation field in the near-wall shear layer is in qualitative agreement with previous numerical and theoretical studies of the *type*-III mechanism (Janke and Balakumar, 2000; Högberg and Henningson, 1998; Bonfigli and Kloker, 2007). A noticeable discrepancy in the upward expansion of the perturbation shape in x is observed in the results from the local BiG approach (figure 2.13 (d)). The origin of this modelling artefact and its impact on the amplitude estimation (figure 2.13 (b)), is discussed in detail in Groot et al. (2025).

For monochromatic unsteady forcing with $f = 6$ kHz, the perturbation contours (figure 2.13 (c)) become localised on the outer side of the upwelling region of the stationary crossflow vortex. This behaviour is therefore associated with the *type*-I secondary instability mechanism (Högberg and Henningson, 1998; Malik et al., 1999; Janke and Balakumar, 2000; Wassermann and Kloker, 2002; Bonfigli and Kloker, 2007). This association is supported by the observation that the location of maximum perturbation *strength* coincides with the region of the maximum spanwise shear in the steady perturbed flow. The amplification in x of the initially small-amplitude, monochromatic unsteady perturbations (figure 2.13 (a)) ultimately leads to laminar breakdown near the end of the computational domain, as shown in figure 2.14, which

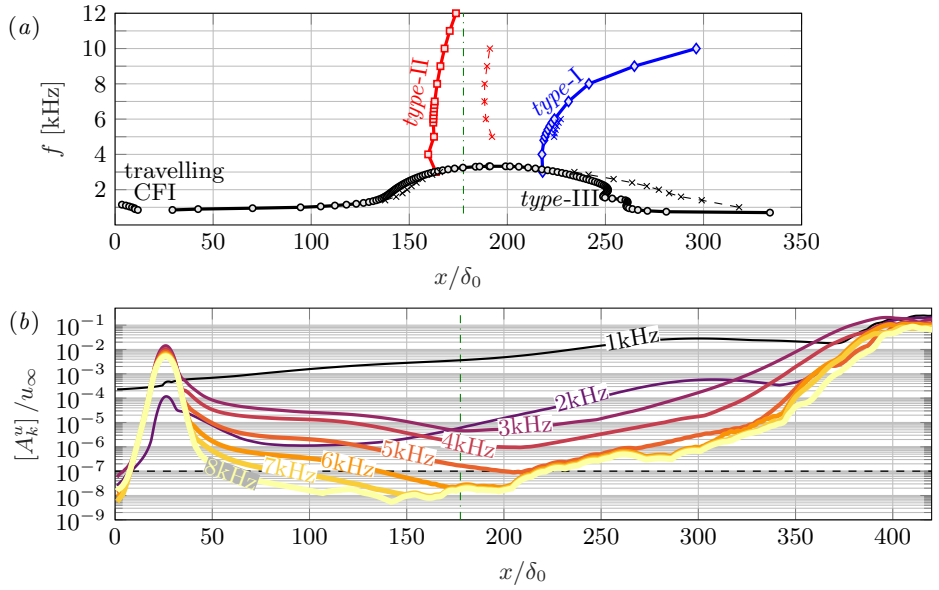

Figure 2.15: Neutral stability curves (a) computed with the local BiG stability approach: primary travelling CFI and *type*-III secondary instability (black line with circles), *type*-I secondary instability (blue line with diamonds), and *type*-II secondary instability (red line with squares). Dashed lines with crosses in (a) additionally indicate plane-marching BiG results, see Groot et al. (2025) for details; these are limited to a portion in f for simplicity. Chordwise evolution of the amplitude (2.29) of the unsteady perturbation modes (b) with temporal frequencies f = 1-8 kHz, in steps of 1 kHz (thin-to-thick and dark-to-bright colour illustrate increasing f value). Dash-dotted green line indicates the virtual step location in (a,b) and dashed black line in (b) indicates the numerical tolerance of the PPE solver (see § 2.2.1).

depicts instantaneous Q-criterion isosurfaces (Hunt et al., 1988). The reader is referred to Casacuberta et al. (2022a) for a more detailed discussion of the breakdown mechanisms observed in the present case.

Large-amplitude CFI (case r.*C*)

The main discussion in this thesis of unsteady perturbation effects and step-induced transition mechanisms is conducted exclusively under *large*-amplitude CFI conditions (table 2.4). The DNS employs the disturbance strip (2.23) to generate perturbations through multi-frequency unsteady forcing near the domain inlet (see § 2.1.3 for details). This section provides an overview of the perturbation behaviour for the reference (no-step) case.

In this context, figure 2.15 (b) shows the spatial evolution of the amplitude of individual unsteady perturbation modes in the case without the step, based on the modal decomposition (2.11) of the DNS perturbation field. In particular, figure 2.15 (b)

Mode	Method	f [kHz]	x/δ_0	$-\alpha_{\theta,i}\delta_0 \sec\theta$	λ_x/δ_0	$N_{\max}$ $(x_{\max}/\delta_0)$
Type-I	BiG local	5.2 ± 0.2	339	0.0994	4.1	16.4 (500)
Type-I	BiG marching	5.2 ± 0.2	350	0.1048	4.2	15.6 (500)
Type-II	BiG local	9.0 ± 1.0	208	0.0685	2.7	11.1 (500)
Type-II	BiG marching	9.0 ± 1.0	233	0.0692	2.7	15.2 (500)
Type-III	BiG local	1.95 ± 0.05	199	0.0546	5.8	4.0 (251)
Type-III	BiG marching	1.8 ± 0.2	205	0.0614	6.3	5.2 (282)

TABLE 2.8: Properties of secondary crossflow instabilities in the *large*-amplitude CFI case without the step (r.C), obtained from stability analysis: most unstable modes, i.e., those for which $\max_x\{-\alpha_{\theta,i}\sec\theta\}$ is largest (see appendix B), and the resulting N-factors. Plane-marching results were stabilised by setting $\Omega_p = 0$; stabilisation with $\Omega_p = 1$ and non-zero s yielded similar but slightly more stable values, see Casacuberta et al. (2025a) for details.

quantifies the chordwise evolution of the following perturbation *amplitude* metric:

$$[A_k^u] = \max_y \left(\sqrt{\sum_{j=-9}^{9} 4|\tilde{u}|^2_{(k,j)}} \right), \tag{2.29}$$

with k = 1-8 indicating the frequencies f = 1-8 kHz. The differences in the peak values observed at the strip in figure 2.15 (b) ($20 \leq x/\delta_0 \leq 32$) between perturbations at f = 1-2 kHz and f = 3-8 kHz stem from the different choices of initial amplitude described in § 2.1.3. In turn, the *actual* amplitude ultimately assigned to each mode at the disturbance strip is also conditioned by the receptivity of the chordwise-velocity perturbation to the imposed wall-normal-velocity forcing.

Downstream of the strip, the higher-frequency perturbations undergo an initial phase of mild spatial decay before eventually amplifying. This behaviour is supported by the results of the linear stability analysis, as shown in figure 2.15 (a), which predicts neutral-point locations generally consistent with the DNS results (figure 2.15 (b)). Table 2.8 summarises the main properties of the secondary-instability eigenmodes obtained from the stability analysis. It is noted that the low amplitudes attained by certain high-frequency perturbations in the DNS –relative to the numerical tolerance of the PPE solver (§ 2.2.1)– may influence the shape and local growth rate of corresponding unsteady modes over a limited region in x. This potential influence has not been quantified explicitly in this work.

The breakdown of the crossflow vortices in the present *large*-amplitude CFI case (table 2.4) is driven by the amplification of the *type*-I secondary instability mechanism.

II

Results and discussion

3

Mathematical frameworks

Abstract: *This chapter presents the main mathematical frameworks developed in this thesis, with a focus on stationary perturbations. Three key formulations are introduced. First, an extended version of the classic Reynolds-Orr equation is developed to characterise the mechanisms of energy exchange for each stationary spanwise perturbation mode individually. Second, a generalised framework is proposed for decomposing perturbations relative to the local base-flow orientation, rather than relative to the wall. Third, the production term of the Reynolds-0rr equation is further decomposed using the second formulation to identify and quantify the specific mechanisms governing kinetic energy transfer between stationary perturbations and the base flow.*

Parts of this chapter are published in:

- Casacuberta, J., Hickel, S., and Kotsonis, M., 2022 Direct numerical simulation of interaction between a stationary crossflow instability and forward-facing steps. *J. Fluid Mech.* **943**:A46.
- Casacuberta, J., Hickel, S., and Kotsonis, M., 2023 Laminar-turbulent transition in swept-wing flows with a supercritical forward-facing step. In *ERCOFTAC Workshop Direct and Large Eddy Simulation* (pp. 151-156). Cham: Springer Nature Switzerland.
- Casacuberta, J., Hickel, S., and Kotsonis, M., 2024 Passive stabilization of crossflow instabilities by a reverse lift-up effect. *Phys. Rev. Fluids* **9**:043903.
- Casacuberta, J., Westerbeek, S., Franco, J. A., Groot, K. J., Hickel, S., Hein, S. and Kotsonis, M., 2025 Streaky perturbations in swept-wing flow over forward-facing step. *Phys. Rev. Fluids* **10**:023902.
- Casacuberta, J., Groot, K. J., Hickel, S., and Kotsonis, M., 2025 Direct numerical simulation of swept-wing transition induced by forward-facing steps. Under consideration for publication in *J. Fluid Mech.*

Three formulations are presented in this chapter, constituting the primary theoretical frameworks used in this thesis to analyse stationary perturbation phenomena at the step.

3.1. Energy-balance equation for stationary spanwise harmonic perturbation modes

The energy-balance equation for stationary spanwise-harmonic perturbation modes presented in this section constitutes an extended formulation of the Reynolds-Orr equation. It is employed to investigate the interaction mechanisms between the forward-facing step and each stationary spanwise perturbation mode individually. As such, the framework introduced below is restricted to the stationary content of the perturbation field (2.10); that is, to $\boldsymbol{v}'$ subject to $\partial \boldsymbol{v}'/\partial t = 0$, or equivalently, to the modes $\boldsymbol{v}'_{(0,j)}$ (1.8). The framework capitalises on the periodicity of perturbations in the spanwise direction, z, and is inspired by the temporal harmonic analysis of Jin et al. (2021).

Let E denote the kinetic energy of stationary perturbations within a volume V, which encompasses the periodic boundaries in the z-direction of length $(2\pi)/\beta_0$. It is defined via the standard Hermitian inner product of the complex-valued stationary perturbation velocity vector $\boldsymbol{v}'_{(0,j)} = [u'_{(0,j)}\ v'_{(0,j)}\ w'_{(0,j)}]^{\mathrm{T}}$ with itself:

$$E = \frac{1}{2}\int_V \sum_{j=-N}^{N} \boldsymbol{v}'^{\,\dagger}_{(0,j)}\, \boldsymbol{v}'_{(0,j)} \mathrm{d}V = \sum_{n=0}^{N} \int_S E_{n\beta_0}\, \mathrm{d}S, \tag{3.1}$$

where S denotes the x-y cross-sectional plane of V. The modal energy density $E_{n\beta_0}$ corresponding to the wavenumber space $n\beta_0$, $n = 0, 1, \ldots, N$ is defined as

$$E_{n\beta_0} = \delta_n \frac{\pi}{\beta_0}\left(|\tilde{u}|^2_{(0,n)} + |\tilde{v}|^2_{(0,n)} + |\tilde{w}|^2_{(0,n)}\right) \qquad \begin{cases} \delta_n = 2, & n > 0 \\ \delta_n = 1, & n = 0. \end{cases} \tag{3.2}$$

This definition accounts for the conjugate symmetry of the Fourier decomposition, as the pair $\boldsymbol{v}'_{(0,n)}$ and $\boldsymbol{v}'_{(0,-n)}$ combine to yield a real-valued structure in physical space. Due to the stationary nature of perturbations, $\mathrm{d}E_{n\beta_0}/\mathrm{d}t = 0$, indicating that the mechanisms governing the evolution of $E_{n\beta_0}$ are in temporal equilibrium.

The contributions of the different energy-transfer mechanisms within a perturbation space $n\beta_0$ are evaluated as follows. The decomposition of stationary perturbations into spanwise modes (1.8) is substituted into the perturbation equation (1.3). By factoring out the z-dependence of terms, the perturbation equation can be re-expressed as

$$0 = \sum_{j=-N}^{N} \left(\mathbb{L}_{(0,j)} + \mathbb{F}^p_{(0,j)} - \sum_{\substack{r=-N \\ j-r\in[-N,N]}}^{N} \left(\underline{\tilde{\boldsymbol{v}}}_{(0,r)} \cdot \mathbb{B}_{(0,j-r)} \right) \right) \mathrm{e}^{\mathrm{i}j\beta_0 z}, \tag{3.3}$$

where $\mathbb{L}_{(0,j)}(x,y) = \mathbb{A}^{\mathrm{I}}_{(0,j)}(x,y) + \mathbb{A}^{\mathrm{II}}_{(0,j)}(x,y) + \mathbb{F}^v_{(0,j)}(x,y)$ and $\mathbb{F}^p_{(0,j)}(x,y)$ represent the linear perturbation operators, while $\mathbb{B}_{(0,j)}(x,y)$ captures the non-linear interactions. The summation constraint in the non-linear term ensures that both indices r

and $j-r$ lie within the truncated mode range $[-N, N]$. The underline notation ($\underline{\boldsymbol{v}}$) indicates a non-dimensional variable, referenced to δ_0 and u_∞ (§ 2.1), as the analysis is conducted using the non-dimensional form of the perturbation equation (1.3). For further details on the derivation, the reader is referred to Casacuberta et al. (2025a). The vector coefficients corresponding to the linear terms are given by

$$\mathbb{A}^{\mathrm{I}}_{(0,j)} = \begin{bmatrix} -\tilde{\underline{u}}_{(0,j)} \dfrac{\partial \underline{u}_{\mathrm{B}}}{\partial \underline{x}} - \tilde{\underline{v}}_{(0,j)} \dfrac{\partial \underline{u}_{\mathrm{B}}}{\partial \underline{y}} \\ -\tilde{\underline{u}}_{(0,j)} \dfrac{\partial \underline{v}_{\mathrm{B}}}{\partial \underline{x}} - \tilde{\underline{v}}_{(0,j)} \dfrac{\partial \underline{v}_{\mathrm{B}}}{\partial \underline{y}} \\ -\tilde{\underline{u}}_{(0,j)} \dfrac{\partial \underline{w}_{\mathrm{B}}}{\partial \underline{x}} - \tilde{\underline{v}}_{(0,j)} \dfrac{\partial \underline{w}_{\mathrm{B}}}{\partial \underline{y}} \end{bmatrix}, \quad \mathbb{F}^{p}_{(0,j)} = \begin{bmatrix} -\dfrac{\partial \tilde{\underline{p}}_{(0,j)}}{\partial \underline{x}} \\ -\dfrac{\partial \tilde{\underline{p}}_{(0,j)}}{\partial \underline{y}} \\ -\mathrm{i}j\underline{\beta}_0 \tilde{\underline{p}}_{(0,j)} \end{bmatrix}, \tag{3.4}$$

$$\mathbb{A}^{\mathrm{II}}_{(0,j)} = \begin{bmatrix} -\underline{u}_{\mathrm{B}} \dfrac{\partial \tilde{\underline{u}}_{(0,j)}}{\partial \underline{x}} - \underline{v}_{\mathrm{B}} \dfrac{\partial \tilde{\underline{u}}_{(0,j)}}{\partial \underline{y}} - \mathrm{i}j\underline{\beta}_0 \underline{w}_{\mathrm{B}} \tilde{\underline{u}}_{(0,j)} \\ -\underline{u}_{\mathrm{B}} \dfrac{\partial \tilde{\underline{v}}_{(0,j)}}{\partial \underline{x}} - \underline{v}_{\mathrm{B}} \dfrac{\partial \tilde{\underline{v}}_{(0,j)}}{\partial \underline{y}} - \mathrm{i}j\underline{\beta}_0 \underline{w}_{\mathrm{B}} \tilde{\underline{v}}_{(0,j)} \\ -\underline{u}_{\mathrm{B}} \dfrac{\partial \tilde{\underline{w}}_{(0,j)}}{\partial \underline{x}} - \underline{v}_{\mathrm{B}} \dfrac{\partial \tilde{\underline{w}}_{(0,j)}}{\partial \underline{y}} - \mathrm{i}j\underline{\beta}_0 \underline{w}_{\mathrm{B}} \tilde{\underline{w}}_{(0,j)} \end{bmatrix}, \tag{3.5}$$

$$\mathbb{F}^{v}_{(0,j)} = \frac{1}{Re} \begin{bmatrix} -j^2 \underline{\beta}_0^2 \tilde{\underline{u}}_{(0,j)} + \dfrac{\partial^2 \tilde{\underline{u}}_{(0,j)}}{\partial \underline{x}^2} + \dfrac{\partial^2 \tilde{\underline{u}}_{(0,j)}}{\partial \underline{y}^2} \\ -j^2 \underline{\beta}_0^2 \tilde{\underline{v}}_{(0,j)} + \dfrac{\partial^2 \tilde{\underline{v}}_{(0,j)}}{\partial \underline{x}^2} + \dfrac{\partial^2 \tilde{\underline{v}}_{(0,j)}}{\partial \underline{y}^2} \\ -j^2 \underline{\beta}_0^2 \tilde{\underline{w}}_{(0,j)} + \dfrac{\partial^2 \tilde{\underline{w}}_{(0,j)}}{\partial \underline{x}^2} + \dfrac{\partial^2 \tilde{\underline{w}}_{(0,j)}}{\partial \underline{y}^2} \end{bmatrix}. \tag{3.6}$$

Regarding the non-linear term, the index $j-r$ in equation (3.3) is here denoted by k, and

$$\mathbb{B}_{(0,k)} = \begin{bmatrix} \dfrac{\partial \tilde{\underline{u}}_k}{\partial \underline{x}} & \dfrac{\partial \tilde{\underline{v}}_k}{\partial \underline{x}} & \dfrac{\partial \tilde{\underline{w}}_k}{\partial \underline{x}} \\ \dfrac{\partial \tilde{\underline{u}}_k}{\partial \underline{y}} & \dfrac{\partial \tilde{\underline{v}}_k}{\partial \underline{y}} & \dfrac{\partial \tilde{\underline{w}}_k}{\partial \underline{y}} \\ \mathrm{i}k\underline{\beta}_0 \tilde{\underline{u}}_k & \mathrm{i}k\underline{\beta}_0 \tilde{\underline{v}}_k & \mathrm{i}k\underline{\beta}_0 \tilde{\underline{w}}_k \end{bmatrix}. \tag{3.7}$$

Equation (3.3) is modally decoupled and cast into scalar energy form by taking the standard Hermitian inner product of the amplitude coefficient $\tilde{\boldsymbol{v}}_{(0,j)}$ (1.8) with the corresponding jth equation stemming from (3.3) such that

$$0 = \mathcal{P}_{n\beta_0} + \mathcal{T}_{n\beta_0} + \mathcal{D}_{n\beta_0} + \mathcal{W}_{n\beta_0} + \mathcal{N}_{n\beta_0}, \; n = 0, 1, \ldots, N, \tag{3.8}$$

with

$$\mathcal{P}_{n\beta_0} = \underline{\tilde{\boldsymbol{v}}}^{\dagger}_{(0,n)}\, \mathbb{A}^{\mathrm{I}}_{(0,n)} + \text{c.c.}, \quad \mathcal{T}_{n\beta_0} = \underline{\tilde{\boldsymbol{v}}}^{\dagger}_{(0,n)}\, \mathbb{A}^{\mathrm{II}}_{(0,n)} + \text{c.c.}, \tag{3.9a}$$

$$\mathcal{D}_{n\beta_0} = \underline{\tilde{\boldsymbol{v}}}^{\dagger}_{(0,n)}\, \mathbb{F}^{v}_{(0,n)} + \text{c.c.}, \quad \mathcal{W}_{n\beta_0} = \underline{\tilde{\boldsymbol{v}}}^{\dagger}_{(0,n)}\, \mathbb{F}^{p}_{(0,n)} + \text{c.c.}, \tag{3.9b}$$

$$\mathcal{N}_{n\beta_0} = -\,\underline{\tilde{\boldsymbol{v}}}^{\dagger}_{(0,n)} \Big(\sum_{\substack{r=-N \\ n-r\in[-N,N]}}^{N} (\underline{\tilde{\boldsymbol{v}}}_{(0,r)} \cdot \mathbb{B}_{(0,n-r)}) \Big) + \text{c.c.}, \tag{3.9c}$$

A factor of $(2\pi)/\beta_0$, which arises from integrating the terms in the z-direction, has been omitted from the energy budget in equation (3.8) for simplicity, but it may be included for the integral quantification of individual terms.

Each term in equation (3.8) characterises a distinct mechanism of kinetic-energy transfer within the perturbation space $n\beta_0$. The sign of each term indicates whether the corresponding mechanism acts locally in a stabilising (i.e., < 0), or destabilising (i.e., > 0), manner. The production term $\mathcal{P}_{n\beta_0}(x,y)$ quantifies the exchange of kinetic energy between the unperturbed base flow and the perturbations $n\beta_0$. The transport term $\mathcal{T}_{n\beta_0}(x,y)$ accounts for the advection of kinetic perturbation energy by the unperturbed base flow. The term $\mathcal{D}_{n\beta_0}(x,y)$ captures viscous effects, typically decomposed into contributions from diffusion and dissipation. Finally, $\mathcal{W}_{n\beta_0}(x,y)$ and $\mathcal{N}_{n\beta_0}(x,y)$ represent the work done by the perturbation pressure and the nonlinear interactions, respectively.

It follows from equation (3.3) that

$$0 = \sum_{n=0}^{N} \mathcal{P}_{n\beta_0} + \sum_{n=0}^{N} \mathcal{T}_{n\beta_0} + \sum_{n=0}^{N} \mathcal{D}_{n\beta_0} + \sum_{n=0}^{N} \mathcal{W}_{n\beta_0} + \sum_{n=0}^{N} \mathcal{N}_{n\beta_0}, \tag{3.10}$$

which is analogous to equation (3.8) but applies to the perturbation field as a whole. Equation (3.10) reduces to the classic Reynolds-Orr equation under specific conditions.

3.2. Decomposition of the perturbation field based on the local orientation of the base flow

The formulation of the perturbation field introduced in § 2.1.1 and considered thus far employs a classic decomposition of the perturbation of interest into components aligned with the flat-plate geometry, i.e., parallel and normal to the wall. A theoretical framework is developed in this thesis, which instead decomposes the perturbation relative to the local base-flow orientation, to provide further insight into the nature of relevant perturbation phenomena (Marxen et al., 2009; Loiseau et al., 2016; Picella et al., 2018). The framework, building on the approaches of Albensoeder et al. (2001) and Lanzerstorfer and Kuhlmann (2011, 2012), is applicable to generic three-dimensional base flows with one invariant spatial direction. As this thesis focuses on the stationary CFI, a stationary perturbation field is assumed; however, extension to unsteady perturbations is straightforward.

In the flat-plate aligned coordinate system, the jth Fourier component of the perturbation field, $\boldsymbol{v}'_{(0,j)}$ (1.8), is expressed initially as

$$\boldsymbol{v}'_{(0,j)} = u'_{(0,j)}\hat{\boldsymbol{i}} + v'_{(0,j)}\hat{\boldsymbol{j}} + w'_{(0,j)}\hat{\boldsymbol{k}}, \tag{3.11}$$

where $u'_{(0,j)}, v'_{(0,j)}, w'_{(0,j)}$ are the complex-valued perturbation components in the x-, y-, and z-directions, respectively, and $\hat{\boldsymbol{i}} = [1\ 0\ 0]^{\mathrm{T}}$, $\hat{\boldsymbol{j}} = [0\ 1\ 0]^{\mathrm{T}}$, $\hat{\boldsymbol{k}} = [0\ 0\ 1]^{\mathrm{T}}$, see § 2.1.1. This thesis proposes to decompose $\boldsymbol{v}'_{(0,j)}$ as the sum

$$\boldsymbol{v}'_{(0,j)} = \boldsymbol{v}'_{t,(0,j)} + \boldsymbol{v}'_{n,(0,j)}, \tag{3.12}$$

of two vector fields that are complex orthogonal. The field $\boldsymbol{v}'_{t,(0,j)}$ is defined as

$$\boldsymbol{v}'_{t,(0,j)} = \tau'_{(0,j)}\hat{\boldsymbol{t}}, \tag{3.13}$$

i.e., as a complex-valued perturbation component $\tau'_{(0,j)}$ in the direction of the vector $\hat{\boldsymbol{t}}$. The latter is the three-dimensional real-valued unit vector which points in the local base flow direction:

$$\hat{\boldsymbol{t}} = \frac{\boldsymbol{v}_{\mathrm{B}}}{||\boldsymbol{v}_{\mathrm{B}}||}, \tag{3.14}$$

where $||\boldsymbol{v}_{\mathrm{B}}||$ denotes the magnitude of $\boldsymbol{v}_{\mathrm{B}}$. An expression for $\tau'_{(0,j)}$ is obtained by evaluating the projection of $\boldsymbol{v}'_{(0,j)}$ onto $\boldsymbol{v}_{\mathrm{B}}$:

$$\mathrm{Re}(\tau'_{(0,j)}) = \frac{\mathrm{Re}(\boldsymbol{v}'_{(0,j)}) \cdot \boldsymbol{v}_{\mathrm{B}}}{||\boldsymbol{v}_{\mathrm{B}}||}, \quad \mathrm{Im}(\tau'_{(0,j)}) = \frac{\mathrm{Im}(\boldsymbol{v}'_{(0,j)}) \cdot \boldsymbol{v}_{\mathrm{B}}}{||\boldsymbol{v}_{\mathrm{B}}||}, \tag{3.15}$$

where the dot denotes scalar product. Introducing ansatz (1.8) into (3.15) yields

$$\mathrm{Re}(\tau'_{(0,j)}) = \frac{1}{\|\boldsymbol{v}_{\mathrm{B}}\|}\big(\gamma^{+}_{(0,j)}\cos(j\beta_0 z) + \gamma^{-}_{(0,j)}\sin(j\beta_0 z)\big) \tag{3.16a}$$

$$\mathrm{Im}(\tau'_{(0,j)}) = \frac{1}{\|\boldsymbol{v}_{\mathrm{B}}\|}\big(\gamma^{+}_{(0,j)}\sin(j\beta_0 z) - \gamma^{-}_{(0,j)}\cos(j\beta_0 z)\big) \tag{3.16b}$$

with

$$\gamma^{+}_{(0,j)}(x,y) = u_{\mathrm{B}}|\tilde{u}|_{(0,j)}\cos(\varphi^{u}_{(0,j)}) + v_{\mathrm{B}}|\tilde{v}|_{(0,j)}\cos(\varphi^{v}_{(0,j)}) + w_{\mathrm{B}}|\tilde{w}|_{(0,j)}\cos(\varphi^{w}_{(0,j)}) \tag{3.17}$$

and

$$\gamma^{-}_{(0,j)}(x,y) = -u_{\mathrm{B}}|\tilde{u}|_{(0,j)}\sin(\varphi^{u}_{(0,j)}) - v_{\mathrm{B}}|\tilde{v}|_{(0,j)}\sin(\varphi^{v}_{(0,j)}) - w_{\mathrm{B}}|\tilde{w}|_{(0,j)}\sin(\varphi^{w}_{(0,j)}). \tag{3.18}$$

Using the sum formulas for sine and cosine, (3.16) can be rewritten as

$$\mathrm{Re}(\tau'_{(0,j)}) = \frac{1}{\|\boldsymbol{v}_{\mathrm{B}}\|}\sqrt{(\gamma^{+}_{(0,j)})^2 + (\gamma^{-}_{(0,j)})^2}\cos\big(j\beta_0 z + \varphi^{\tau}_{(0,j)}\big) \tag{3.19a}$$

$$\mathrm{Im}(\tau'_{(0,j)}) = \frac{1}{\|\boldsymbol{v}_{\mathrm{B}}\|}\sqrt{(\gamma^{+}_{(0,j)})^2 + (\gamma^{-}_{(0,j)})^2}\sin\big(j\beta_0 z + \varphi^{\tau}_{(0,j)}\big) \tag{3.19b}$$

with the phase $\varphi^{\tau}_{(0,j)}$ associated with the perturbation component $\tau'_{(0,j)}$ obtained as

$$\tan(\varphi^{\tau}_{(0,j)}) = -\frac{\gamma^{-}_{(0,j)}}{\gamma^{+}_{(0,j)}}. \tag{3.20}$$

From (3.16), it follows that

$$\tau'_{(0,j)} = \frac{1}{||\boldsymbol{v}_{\mathrm{B}}||}\sqrt{(\gamma^{+}_{(0,j)})^2 + (\gamma^{-}_{(0,j)})^2}\, \mathrm{e}^{\mathrm{i}\left(j\beta_0 z + \varphi^{\tau}_{(0,j)}\right)}, \tag{3.21}$$

and thus

$$\boldsymbol{v}'_{t,(0,j)} = \frac{1}{||\boldsymbol{v}_{\mathrm{B}}||^2}\sqrt{(\gamma^{+}_{(0,j)})^2 + (\gamma^{-}_{(0,j)})^2}\, \mathrm{e}^{\mathrm{i}\left(j\beta_0 z + \varphi^{\tau}_{(0,j)}\right)} \begin{bmatrix} u_{\mathrm{B}} \\ v_{\mathrm{B}} \\ w_{\mathrm{B}} \end{bmatrix}, \tag{3.22}$$

which can also be written as $\boldsymbol{v}'_{t,(0,j)} = (1/||\boldsymbol{v}_{\mathrm{B}}||)\begin{bmatrix} u_{\mathrm{B}}\tau'_{(0,j)} & v_{\mathrm{B}}\tau'_{(0,j)} & w_{\mathrm{B}}\tau'_{(0,j)} \end{bmatrix}^{\mathrm{T}}$ or, equivalently, as $\boldsymbol{v}'_{t,(0,j)} = [\tilde{v}^1_{t,(0,j)}\mathrm{e}^{\mathrm{i}j\beta_0 z}\ \tilde{v}^2_{t,(0,j)}\mathrm{e}^{\mathrm{i}j\beta_0 z}\ \tilde{v}^3_{t,(0,j)}\mathrm{e}^{\mathrm{i}j\beta_0 z}]^{\mathrm{T}}$. Following the nomenclature of the perturbation expressions in global coordinates, the modulus (or amplitude function) of $\tau'_{(0,j)}$ is denoted by $|\tilde{\tau}|_{(0,j)}$. Since $||\hat{\boldsymbol{t}}|| = 1$, $|\tilde{\tau}|_{(0,j)} = ||\boldsymbol{v}'_{t,(0,j)}||$ and therefore

$$|\tilde{\tau}|_{(0,j)} = \frac{\sqrt{(\gamma^{+}_{(0,j)})^2 + (\gamma^{-}_{(0,j)})^2}}{||\boldsymbol{v}_{\mathrm{B}}||}. \tag{3.23}$$

As also described above in equation (1.9), the norm of the *total* perturbation vector, $\boldsymbol{v}'_{(0,j)}$, equals $\sqrt{|\tilde{u}|^2_{(0,j)} + |\tilde{v}|^2_{(0,j)} + |\tilde{w}|^2_{(0,j)}}$ and is denoted by $|\tilde{\psi}|_{(0,j)}$ in this thesis.

The second vector of decomposition (3.12), $\boldsymbol{v}'_{n,(0,j)}$, represents a perturbation acting normal to the base-flow-aligned perturbation component, $\boldsymbol{v}'_{t,(0,j)}$. Whereas the direction tangential to the base flow is uniquely defined (3.14), the direction associated to $\boldsymbol{v}'_{n,(0,j)}$ is, at present, inherently taken as that defined by the difference between $\boldsymbol{v}'_{(0,j)}$ and $\boldsymbol{v}'_{t,(0,j)}$ (3.12). Hence

$$\boldsymbol{v}'_{n,(0,j)} = \begin{bmatrix} |\tilde{u}|_{(0,j)}\mathrm{e}^{\mathrm{i}\left(j\beta_0 z + \varphi^{u}_{(0,j)}\right)} \\ |\tilde{v}|_{(0,j)}\mathrm{e}^{\mathrm{i}\left(j\beta_0 z + \varphi^{v}_{(0,j)}\right)} \\ |\tilde{w}|_{(0,j)}\mathrm{e}^{\mathrm{i}\left(j\beta_0 z + \varphi^{w}_{(0,j)}\right)} \end{bmatrix} - \frac{1}{||\boldsymbol{v}_{\mathrm{B}}||^2}\sqrt{(\gamma^{+}_{(0,j)})^2 + (\gamma^{-}_{(0,j)})^2}\, \mathrm{e}^{\mathrm{i}\left(j\beta_0 z + \varphi^{\tau}_{(0,j)}\right)} \begin{bmatrix} u_{\mathrm{B}} \\ v_{\mathrm{B}} \\ w_{\mathrm{B}} \end{bmatrix}. \tag{3.24}$$

The amplitude function $||\boldsymbol{v}'_{n,(0,j)}||$ associated with the perturbation component $\boldsymbol{v}'_{n,(0,j)}$ is hereafter denoted by $|\tilde{\eta}|_{(0,j)}$; it can be directly obtained by relating the amplitude function (or moduli) of $\boldsymbol{v}'_{(0,j)}$ and $\boldsymbol{v}'_{t,(0,j)}$:

$$||\boldsymbol{v}'_{(0,j)}||^2 = ||\boldsymbol{v}'_{t,(0,j)}||^2 + ||\boldsymbol{v}'_{n,(0,j)}||^2, \tag{3.25}$$

since $\boldsymbol{v}'_{t,(0,j)}$ and $\boldsymbol{v}'_{n,(0,j)}$ are complex orthogonal,

$$\boldsymbol{v}'_{t,(0,j)} \cdot \boldsymbol{v}'_{n,(0,j)} = \boldsymbol{v}'_{t,(0,j)} \cdot \boldsymbol{v}'_{(0,j)} - ||\boldsymbol{v}'_{t,(0,j)}||^2 = 0, \tag{3.26}$$

which follows from the fact that $\boldsymbol{v}'_{t,(0,j)} = (\boldsymbol{v}'_{(0,j)} \cdot \boldsymbol{v}_\mathrm{B}/||\boldsymbol{v}_\mathrm{B}||^2)\boldsymbol{v}_\mathrm{B}$ (3.13). Here, the dot denotes the standard Hermitian inner product:

$$\boldsymbol{v}'_{t,(0,j)} \cdot \boldsymbol{v}'_{n,(0,j)} = \sum_{k=1}^{3} \boldsymbol{v}'^{\,\dagger}_{n,(0,j)}(k)\, \boldsymbol{v}'_{t,(0,j)}(k), \tag{3.27}$$

with k denoting the components of the corresponding vector field.

Finally, the vector components of the normal perturbation (3.24), $\boldsymbol{v}'_{n,(0,j)} = [\upsilon'^1_{n,(0,j)}\ \upsilon'^2_{n,(0,j)}\ \upsilon'^3_{n,(0,j)}]^\mathrm{T}$, may be written more compactly as

$$\upsilon'^k_{n,(0,j)} = \underbrace{\sqrt{|\tilde{v}^k|^2_{(0,j)} + (\xi_{(0,j)} v^k_\mathrm{B})^2 - 2\xi_{(0,j)} v^k_\mathrm{B} |\tilde{v}^k|_{(0,j)} \cos(\varphi^{v^k}_{(0,j)} - \varphi^{\tau}_{(0,j)})}}_{|\tilde{v}^k_n|_{(0,j)}}\ \mathrm{e}^{\mathrm{i}(j\beta_0 z + \varphi^{v^k}_{n,(0,j)})}, \tag{3.28}$$

with $k = 1, 2, 3$, $v^1 = u$, $v^2 = v$, $v^3 = w$, $\xi_{(0,j)} = \sqrt{(\gamma^+_{(0,j)})^2 + (\gamma^-_{(0,j)})^2}/||\boldsymbol{v}_\mathrm{B}||^2$, and associated phase

$$\tan(\varphi^{v^k}_{n,(0,j)}) = \frac{|\tilde{v}^k|_{(0,j)} \sin(\varphi^{v^k}_{(0,j)}) - \xi_{(0,j)} v^k_\mathrm{B} \sin(\varphi^{\tau}_{(0,j)})}{|\tilde{v}^k|_{(0,j)} \cos(\varphi^{v^k}_{(0,j)}) - \xi_{(0,j)} v^k_\mathrm{B} \cos(\varphi^{\tau}_{(0,j)})}. \tag{3.29}$$

For consistency with classic perturbation formulations, equations (3.24) and (3.28) can be equivalently compacted as $\boldsymbol{v}'_{n,(0,j)} = [\tilde{v}^1_{n,(0,j)} \mathrm{e}^{\mathrm{i}j\beta_0 z}\ \tilde{v}^2_{n,(0,j)} \mathrm{e}^{\mathrm{i}j\beta_0 z}\ \tilde{v}^3_{n,(0,j)} \mathrm{e}^{\mathrm{i}j\beta_0 z}]^\mathrm{T}$.

A key advantage of the mathematical formulation developed in this section lies in its ability to associate physical and structural meaning with the two vector components defined by equation (3.12). The $\boldsymbol{v}'_t$ characterises the regions of streamwise-velocity excess and deficit in the flow, whereas $\boldsymbol{v}'_n$ represents typically the weak cross-stream flow pattern that is responsible for momentum redistribution. More specifically, the field $\boldsymbol{v}'_n$ manifests structurally as perturbation rolls (i.e., streamwise-vortical structures). It is therefore noted that, in the flow problems analysed in this thesis, the streamwise-velocity perturbation component $\boldsymbol{v}'_t$ is the main contribution to the perturbation kinetic energy.

3.3. Decomposition of the production term of the Reynolds-Orr equation

The framework introduced in the previous section (§ 3.2) serves multiple analytical purposes. Specifically, in various parts of this thesis, the behaviour of perturbations is assessed by examining how they gain or lose energy through interaction with the laminar base flow. To this end, the production mechanism introduced in § 3.1 is further decomposed using the concepts developed in § 3.2. The formulation presented below in this section considers the fundamental spanwise mode, i.e., perturbations with $\beta = \beta_0$, but can be directly generalised to any higher-order mode ($\beta > \beta_0$). Based on the analysis in § 3.1, the kinetic energy transfer rate between the unperturbed base flow and the fundamental spanwise mode in a volume V is characterised

as

$$P_{\beta_0} = -\int_V (\boldsymbol{v}'_{(0,1)} + \text{c.c.}) \cdot \Big((\boldsymbol{v}'_{(0,1)} + \text{c.c.}) \cdot \nabla \Big) \boldsymbol{v}_\text{B} \, \text{d}V = -\frac{2\pi}{\beta_0} \int_S \Lambda_{\beta_0} \, \text{d}x\text{d}y \quad (3.30)$$

where $\Lambda_{\beta_0} = \mathcal{P}_{\beta_0}$ (see equations 3.8 and 3.9). In equation (3.30), S denotes the x-y cross-sectional surface of a volume V that encompasses the step in x and extends from the wall to the free-stream in y. Generally in this thesis, V extends towards the periodic boundaries in z.

Following the approach of Albensoeder et al. (2001) and Lanzerstorfer and Kuhlmann (2012), the production term (3.30) is decomposed into four contributions,

$$P_{\beta_0} = I_1^{\beta_0} + I_2^{\beta_0} + I_3^{\beta_0} + I_4^{\beta_0}, \quad (3.31)$$

by introducing the decomposition of equation (3.12) into equation (3.30). Each term $I_m^{\beta_0}, m = 1\text{-}4$ in equation (3.31) characterises a particular mechanism contributing to the exchange of kinetic energy between the base flow and the fundamental spanwise perturbation mode.

The term $I_2^{\beta_0}$ is the lift-up effect (Ellingsen and Palm, 1975; Landahl, 1975, 1980), which is a flow mechanism widely associated to the amplification of streaky structures in shear flow (Brandt, 2014). This mechanism entails the exchange of kinetic energy between the base flow, $\boldsymbol{v}_\text{B}$, and streamwise perturbations, $\boldsymbol{v}'_{t,(0,1)}$, by the action of cross-stream perturbations, $\boldsymbol{v}'_{n,(0,1)}$. It reads

$$I_2^{\beta_0} = -\int_V (\boldsymbol{v}'_{t,(0,1)} + \text{c.c.}) \cdot \Big((\boldsymbol{v}'_{n,(0,1)} + \text{c.c.}) \cdot \nabla \Big) \boldsymbol{v}_\text{B} \, \text{d}V = -\frac{2\pi}{\beta_0} \int_S \Lambda_2^{\beta_0} \, \text{d}x\text{d}y, \quad (3.32)$$

with

$$\begin{aligned} \Lambda_2^{\beta_0} = &\Big(\tilde{v}_t^1 \ \tilde{v}_n^{1\dagger} + \text{c.c.} \Big) \frac{\partial u_\text{B}}{\partial x} + \underbrace{\Big(\tilde{v}_t^1 \ \tilde{v}_n^{2\dagger} + \text{c.c.} \Big) \frac{\partial u_\text{B}}{\partial y}}_{\kappa_2^{\beta_0}} + \Big(\tilde{v}_t^2 \ \tilde{v}_n^{1\dagger} + \text{c.c.} \Big) \frac{\partial v_\text{B}}{\partial x} \\ &+ \Big(\tilde{v}_t^2 \ \tilde{v}_n^{2\dagger} + \text{c.c.} \Big) \frac{\partial v_\text{B}}{\partial y} + \Big(\tilde{v}_t^3 \ \tilde{v}_n^{1\dagger} + \text{c.c.} \Big) \frac{\partial w_\text{B}}{\partial x} + \underbrace{\Big(\tilde{v}_t^3 \ \tilde{v}_n^{2\dagger} + \text{c.c.} \Big) \frac{\partial w_\text{B}}{\partial y}}_{\delta_2^{\beta_0}}, \end{aligned} \quad (3.33)$$

where the subscript $(0,1)$ has been removed in equation (3.33) for conciseness. It is emphasised that $\tilde{v}_t^k$ and $\tilde{v}_n^k$, with $k = 1, 2, 3$, denote the amplitude coefficients of the vector components of the tangential, $\boldsymbol{v}'_t$, and normal, $\boldsymbol{v}'_n$, perturbations, respectively (see § 3.2). In § 5.3, it is shown that $\kappa_2^{\beta_0}$ and $\delta_2^{\beta_0}$ in equation (3.33) add the main contribution to the lift-up effect at the step.

The remaining terms stemming from the decomposition of production,

$$I_1^{\beta_0} = -\int_V (\boldsymbol{v}'_{n,(0,1)} + \text{c.c.}) \cdot \Big((\boldsymbol{v}'_{n,(0,1)} + \text{c.c.}) \cdot \nabla \Big) \boldsymbol{v}_\text{B} \, \text{d}V \quad (3.34)$$

and

$$I_4^{\beta_0} = -\int_V (\boldsymbol{v}'_{t,(0,1)} + \text{c.c.}) \cdot \Big((\boldsymbol{v}'_{t,(0,1)} + \text{c.c.}) \cdot \nabla \Big) \boldsymbol{v}_\text{B} \, \text{d}V \tag{3.35}$$

respectively characterise a self-induction mechanism of the cross-stream and streamwise perturbation structures. In particular, the mechanism of I_4 is referred to in this thesis as the "push-forward effect" in analogy to the principle of the lift-up effect. Finally,

$$I_3^{\beta_0} = -\int_V (\boldsymbol{v}'_{n,(0,1)} + \text{c.c.}) \cdot \Big((\boldsymbol{v}'_{t,(0,1)} + \text{c.c.}) \cdot \nabla \Big) \boldsymbol{v}_\text{B} \, \text{d}V, \tag{3.36}$$

which is a mechanism associated to perturbation streaks evolving into perturbation rolls (Antkowiak and Brancher, 2007). A treatment analogous to equations (3.32) and (3.33) may be performed for $I_1^{\beta_0} = (-2\pi/\beta_0) \int_S \Lambda_1^{\beta_0} \, \text{d}x\text{d}y$, $I_3^{\beta_0} = (-2\pi/\beta_0) \int_S \Lambda_3^{\beta_0} \, \text{d}x\text{d}y$, and $I_4^{\beta_0} = (-2\pi/\beta_0) \int_S \Lambda_4^{\beta_0} \, \text{d}x\text{d}y$; by the inherent addition of the complex conjugate, the terms $I_m^{\beta_0}$ and $\Lambda_m^{\beta_0}$ with $m =$ 1-4 are real valued.

4

Stationary interaction between crossflow instability and forward-facing steps

Abstract: *This chapter introduces the main structures and mechanisms governing the stationary interaction between a pre-existing stationary CFI and steps of varying heights. The fundamental spanwise CFI mode gradually lifts up as it approaches the step and passes over it. The flow environment around the step is characterised by a sudden spanwise modulation of the base flow streamlines. Additional stationary perturbation structures are induced at the step, which manifest in the form of spanwise-aligned velocity streaks near the wall. Shortly downstream of the step, the fundamental CFI maintains a rather constant amplification for the smallest steps studied. Surprisingly, the fundamental CFI is significantly stabilised shortly downstream of the largest step, an observation further examined in chapter 5. Amplification of the high-order harmonic crossflow modes downstream of the step is observed and ascribed to an inflectional instability of the deformed step-flow profiles.*

A note on nomenclature: *This chapter focuses exclusively on stationary effects. The spanwise perturbation modes are denoted by* $\boldsymbol{v}'_{(0,j)}$*, where the prime marks perturbation,* j *is the spanwise modal index, and the zero indicates stationary behaviour. Unperturbed base-flow quantities are denoted by the subscript B, for example,* $\boldsymbol{v}_B$*.*

Parts of this chapter are published in:

- Casacuberta, J., Hickel, S., and Kotsonis, M., 2021 Mechanisms of interaction between stationary crossflow instabilities and forward-facing steps. *AIAA Paper* 2021-0854.
- Casacuberta, J., Hickel, S., and Kotsonis, M., 2022 Direct numerical simulation of interaction between a stationary crossflow instability and forward-facing steps. *J. Fluid Mech.* **943**:A46.

The purely stationary interaction between a pre-existing stationary crossflow instability (CFI) and forward-facing steps of varying heights is examined in this chapter. The analysis begins with a description of the topology of the laminar unperturbed base flow at the step (§ 4.1). This is followed by the investigation of perturbation behaviour at the step (§ 4.2) and downstream of it (§ 4.3), divided into effects of the fundamental and the higher-order harmonic CFI modes. The analysis is further strengthened by a comparison between the perturbation behaviour observed in the DNS results and independent calculations obtained with the PSE (§ 2.2.3) approach. The flow problems investigated in this chapter correspond to step cases I, II, and III (table 2.3) and *medium*-amplitude CFI conditions (table 2.4).

4.1. Topology of the base flow at the step

4.1.1. Evolution of the base-flow pressure and velocity

When a forward-facing step is present, the organisation of the incoming boundary layer is significantly altered and a pressure field different than that observed in the reference (no-step) case is induced around the step. As detailed in § 2.1.1, the free-stream features a favourable chordwise pressure gradient throughout the DNS domain. However, whereas $\partial p_{\mathrm{B}}/\partial x < 0$ everywhere in the reference (no-step) case, this does not hold close to the step.

Figure 4.1 (*a*) depicts $\partial p_{\mathrm{B}}/\partial x$ in step case II (see table 2.3 in § 2.1.1 for the definition of step cases), which is representative of the trend observed in all step cases. In line with the behaviour described by Duncan Jr. et al. (2014) and Tufts et al. (2017), regions of adverse pressure gradient are induced upstream and downstream of the step, whereas a strong region of favourable pressure gradient arises locally at the step corner. Sufficiently downstream of the step x-location, $x_{\mathrm{st}} = 0$, the static pressure field gradually relaxes back to that of the reference (no-step) case. This is illustrated in figure 4.1 (*b*) portraying the chordwise evolution of pressure along a streamline of the base flow. Furthermore, figure 4.1 (*b*) highlights that a fluid particle moving close to the step corner experiences strong pressure variations in a short x-distance. It is also important to note that, while the step height is smaller than the incoming boundary layer thickness, the strong pressure variations in the wall-normal direction evidently extend beyond the boundary layer. This has strong consequences in the ability of classic boundary layer approximations, in which pressure invariance along y is usually assumed, to describe such flows.

While the influence on pressure is relatively straightforward, the three-dimensional organisation of the base flow at the step is significantly more complex. Figure 4.2 displays profiles of the base-flow velocity components near the step. Upstream of the step, u_{B} and w_{B} have decelerated with respect to the reference (no-step) case and upwash (i.e., vertical fluid motion with v_{B}) is induced away from the wall. When passing over the step, u_{B} and w_{B} experience a local chordwise acceleration and deceleration within a short x-distance. When considering u_{B}, this trend is particularly prominent near the wall; the velocity profile first displays a secondary maximum close to the surface, which decays in strength rapidly in x. In a similar fashion, upwash induced upstream of the step is first enhanced and later suppressed downstream of

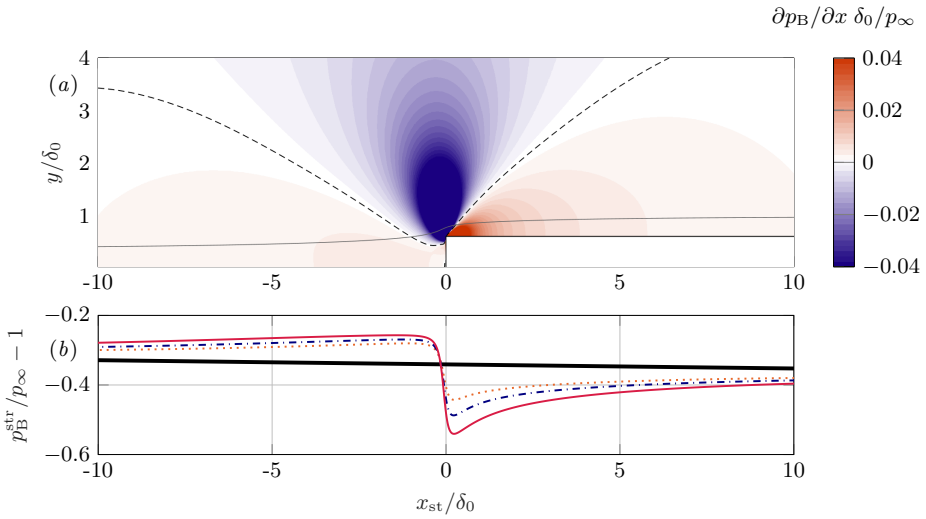

Figure 4.1: Base-flow chordwise pressure gradient (colour map), $\partial p_B/\partial x = 0$ (black dashed line), projected base-flow streamline seeded at $x/\delta_0 = 0$, $y/\delta_0 \approx 0.2$ (gray solid line) in step case II (a). Static pressure along the streamline (b) in the reference (no-step) case (thick solid black), step case I (dotted orange), II (dash-dotted blue), III (thin solid red).

the step in the near-wall region. This is not the case for w_B, whose profile does not display abrupt variations in x close to the surface. The latter is largely attributed to the lack of spanwise variations in pressure, inasmuch as the step geometry is invariant in the z-direction. Nevertheless, the w_B velocity component is implicitly affected by the step through the coupling of all three components in the momentum conservation equations.

The notably different relative evolution of u_B and w_B near the wall, a feature which manifests in the experiments of Eppink (2020) as well, carries a significant horizontal deflection (i.e., change of orientation in the x-z plane) of the base-flow streamlines, as illustrated in figure 4.3. In absence of the step, the streamlines in the boundary layer are practically aligned with the direction of the outer inviscid streamlines, as commonly reported in classical literature on swept-wing boundary layers (Bippes, 1999). However, when a step is present, the base-flow streamlines close to the wall significantly deviate from the direction of the inviscid flow and bend outboard, i.e., towards the negative z-direction, upstream of the step. Locally, in the vicinity of the step corner, the streamlines display an abrupt inboard turn, i.e., towards the positive z-direction. Further downstream, a relaxation towards the inviscid streamline direction is observed. The importance of these observations will be discussed in later sections.

The mechanisms responsible for the strong inboard/outboard motion of the base flow near the step are further analysed. The *local* base-flow direction in the x-z plane is characterised by σ_B corresponding to the angle that the unit vector locally tangent

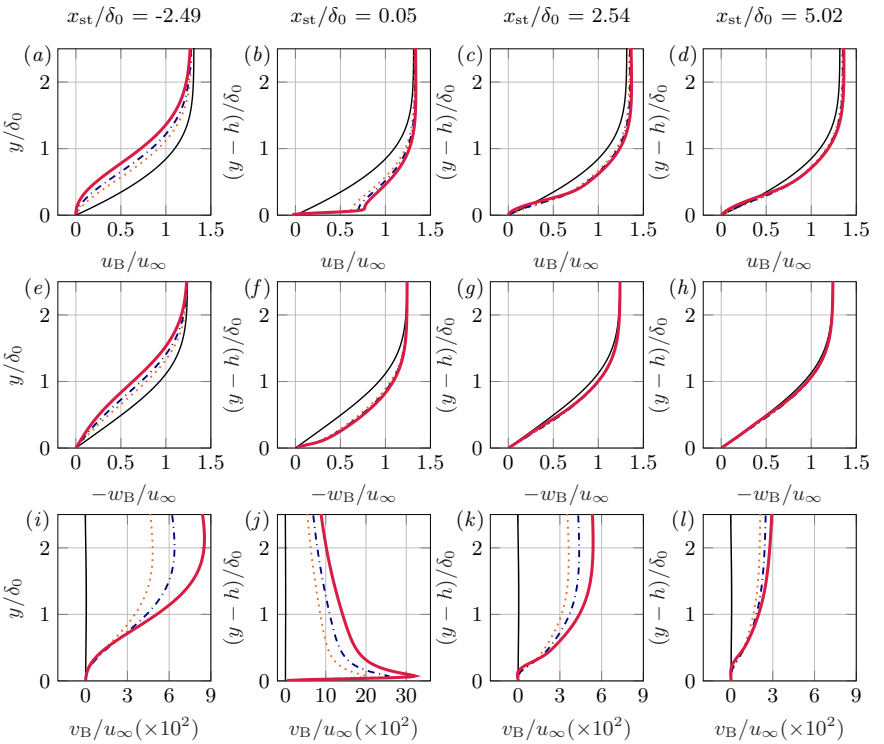

FIGURE 4.2: Chordwise (top), spanwise (middle), wall-normal (bottom) base-flow velocity profiles at $x_{st}/\delta_0 = -2.49$ (*a,e,i*), 0.05 (*b,f,j*), 2.54 (*c,g,k*), 5.02 (*d,h,l*). Reference (no-step) case (thin solid black), step case I (dotted orange), II (dash-dotted blue), III (thick solid red).

to a base-flow streamline projected in the x-z plane forms with x:

$$\tan(\sigma_B) = \frac{w_B}{u_B}. \tag{4.1}$$

The spatial rate of change of σ_B in x is

$$\frac{\partial \sigma_B}{\partial x} = \frac{u_B \frac{\partial w_B}{\partial x} - w_B \frac{\partial u_B}{\partial x}}{u_B^2 + w_B^2} \tag{4.2}$$

or, alternatively, by introducing equations (2.17) and (2.19) in equation (4.2),

$$\begin{aligned}\frac{\partial \sigma_B}{\partial x} = &\frac{1}{u_B^2 + w_B^2}\left\{ \underbrace{-v_B \frac{\partial w_B}{\partial y}}_{\mathcal{A}_w} + \underbrace{\nu\left(\frac{\partial^2 w_B}{\partial x^2} + \frac{\partial^2 w_B}{\partial y^2}\right)}_{\mathcal{D}_w} \right. \\ &\left. - \left(\frac{w_B}{u_B}\right)\left(\underbrace{-v_B \frac{\partial u_B}{\partial y}}_{\mathcal{A}_u} \underbrace{-\frac{1}{\rho}\frac{\partial p_B}{\partial x}}_{\mathcal{P}} + \underbrace{\nu\left(\frac{\partial^2 u_B}{\partial x^2} + \frac{\partial^2 u_B}{\partial y^2}\right)}_{\mathcal{D}_u} \right) \right\}.\end{aligned} \tag{4.3}$$

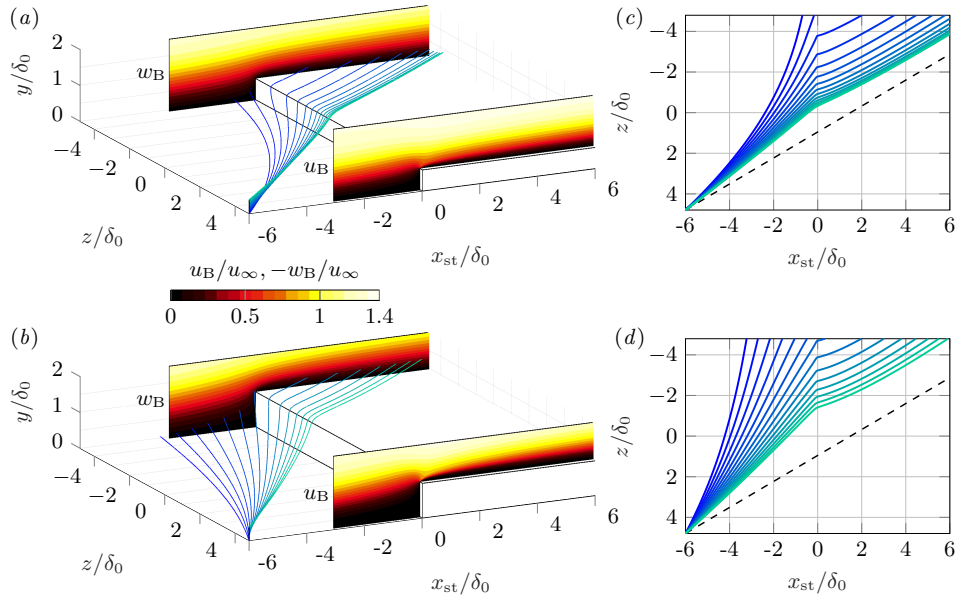

Figure 4.3: Three-dimensional (a,b) and corresponding projected (c,d) base-flow streamlines with seeds placed at $(x_{st}, y, z)/\delta_0 = (-6, (0, 0.4], 4.79)$ and x-y planes of chordwise velocity ($z > 0$) and spanwise velocity ($z < 0$) in step case I (a,c) and III (b,d). Dashed black line is an equivalent near-wall streamline in the reference (no-step) case seeded at the same y position as the lower streamline in the corresponding step case.

Equation (4.3) expresses the spatial rate of change of the angle σ_B in x as a function of the momentum-transport mechanisms in the x- and z-base-flow momentum conservation equations. Since $w_B < 0$ everywhere, $\sigma_B < 0$ in the presently used coordinate system. Considering that the current analysis is restricted to regions of non-separated flow, i.e., where $u_B > 0$, $\partial\sigma_B/\partial x > 0$ signifies inboard-turning base-flow motion, whereas $\partial\sigma_B/\partial x < 0$ signifies outboard-turning base-flow motion.

Figure 4.4 (a) portrays the chordwise evolution of $\partial\sigma_B/\partial x$ at $y = \tilde{y}^{u,\mathrm{top}}_{(0,1)}$ (see the amplitude definitions introduced in § 2.1.1), the wall-normal location at which the core of the fundamental CFI passes over the step, here corresponding to $(y-h)/\delta_0 \approx 0.5$ at $x_{st} = 0$. Figure 4.4 (a) highlights that at this wall-normal location, the base-flow motion at the step is inboard-dominated. Moreover, the inboard motion appears to be a function of the step height.

Figure 4.4 (c) and (d) additionally represents the decomposition of the rate of change in step case III as a sum of contributions of the different momentum-transport mechanisms defined in equation (4.3). On the one hand, the terms $-v_B\partial u_B/\partial y$ and $-v_B\partial w_B/\partial y$ act by decelerating the u_B and w_B boundary layer profiles; momentum advection in the wall-normal direction moves low-momentum fluid towards upper portions of the boundary layer. However, these terms yield a quasi-null total contribution in figure 4.4 (c) since they act opposite to each other and streamline bending

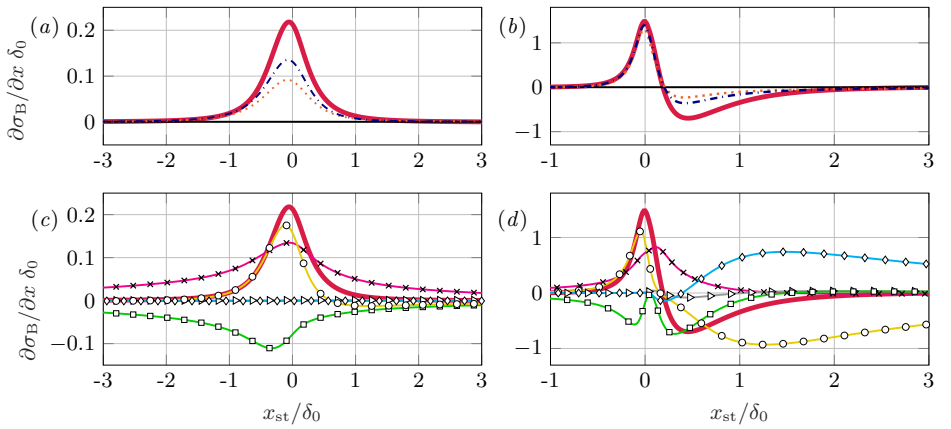

FIGURE 4.4: Rate of change in x of the horizontal deflection of base-flow streamlines, $\partial\sigma_B/\partial x$, at the wall-normal location $y = \tilde{y}^{u,top}_{(0,1)}$ (a) and at $y/\delta_0 = h/\delta_0 + 0.12$ (b) in the reference (no-step) case (thin solid black), step I (dotted orange), II (dash-dotted dark blue), III (thick solid red). Rate of change decomposition for step III (c,d corresponding to a,b, respectively) expressed as the contributions defined in equation (4.3) (c,d): $\partial\sigma_B/\partial x$ (thick solid red), $\mathcal{A}_w$ (magenta and crosses), $\mathcal{D}_w$ (grey and triangles), $\mathcal{A}_u$ (green and squares), $\mathcal{P}$ (yellow and circles), $\mathcal{D}_u$ (light blue and diamonds).

results from an excess of u_B over w_B, or vice-versa. On the other hand, the pressure force accelerates u_B in x since the region above the step corner displays large $\partial p_B/\partial x < 0$ (figure 4.1). This causes an imbalance between u_B and w_B, which manifests as inboard bending of the base-flow streamlines at the step, *far* from the wall. As earlier mentioned, w_B does not explicitly react to changes of pressure in the z-direction, as the base flow is spanwise invariant.

Furthermore, the effect of the step on the streamline bending appears to strongly depend to the wall-normal location of interest. In the near-wall region, the motion of the base flow in the x-z plane is more pronounced than in the region far from the wall. This is illustrated in figure 4.4 (b) characterising $\partial\sigma_B/\partial x$ at $y/\delta_0 = h/\delta_0 + 0.12$, when compared to figure 4.4 (a). Initially at $x_{st} = 0$, the base-flow motion is inboard-dominated. Changing rapidly in x, it displays a sharp outboard turn, whereas the streamlines far from the wall maintain a mild inboard motion. This creates a strong diverging pattern of base-flow streamlines within a short wall-normal distance.

The mechanisms leading to the sudden inboard-outboard streamline bending in the near-wall regime are highlighted in figure 4.4 (d) representing step case III. In a fashion similar to the results of figure 4.4 (c), the favourable pressure gradient induced at the step corner first largely contributes to the sharp inboard turn. When moving downstream of $x_{st} = 0$, the effect of the pressure force reverses; the strong adverse pressure gradient close to the wall (figure 4.1) decelerates u_B in x. This effect, in combination with the imbalance between the advection momentum transport mechanisms $-v_B\partial u_B/\partial y$ and $-v_B\partial w_B/\partial y$, cause the base-flow streamlines near

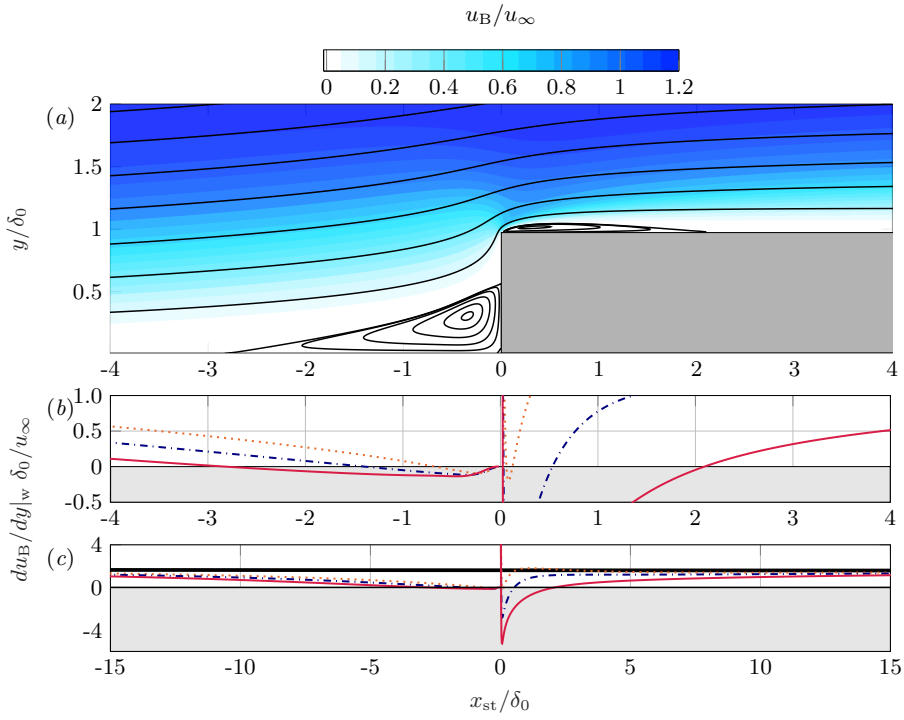

Figure 4.5: Base-flow chordwise velocity (colour map) with lines of constant streamfunction (solid black) (a). Wall shear $du_B/dy|_w$ (b,c): reference (no-step) case (thick solid black), step case I (dotted orange), II (dash-dotted blue), III (thin solid red).

the wall to bend outboard. Further downstream, the step-induced upwash decays and eventually, the viscous forces associated to the gradients of u_B take over as the dominant mechanism opposing the effect of pressure.

4.1.2. Local flow reversal and modification of the crossflow component

Next to the strong spanwise streamline modulation, flow separation (i.e., reversal of u_B) is a main feature of the base flow near the step. The existence of step-induced regions of recirculating flow in the three-dimensional swept-wing boundary layer and the associated connection with the development of crossflow instabilities is a point of debate in recent studies. Whereas flow reversal upstream of the step is expected and widely reported (Tufts et al., 2017; Eppink, 2020), discrepancies arise with regard to the downstream region. In the present DNS, flow reversal downstream of the step is identified in all step cases, as highlighted by the negative wall shear ($du_B/dy|_w$) measured in this region (figure 4.5). However, in step case I the strength of the reverse flow is significantly lower than in step cases II and III, see table 4.1.

Region	Property	Definition	Step I	Step II	Step III
Upstream	Start	x_{st}/δ_0	-0.67	-1.39	-2.82
	Height	y/h	0.44	0.50	0.58
	Strength	$-u_{\mathrm{B_{min}}}/\hat{u}_e$	0.19×10^{-2}	0.38×10^{-2}	0.70×10^{-2}
Downstream	End	x_{st}/δ_0	0.12	0.53	2.09
	Height	$(y-h)/\delta_0$	a	0.03	0.07
	Strength	$-u_{\mathrm{B_{min}}}/\hat{u}_e$	0.10×10^{-2}	1.44×10^{-2}	2.67×10^{-2}

Table 4.1: Properties of the flow recirculation regions at the step based on the dividing streamline. Here, a indicates below grid resolution.

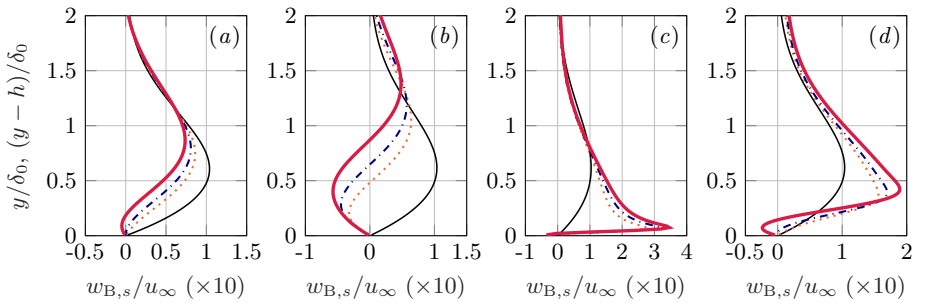

Figure 4.6: Crossflow velocity profile near the step: reference (no-step) case (thin solid black), step case I (dotted orange), II (dash-dotted blue), III (thick solid red) at $x_{\mathrm{st}}/\delta_0 = -9.56$ (a), -0.97 (b), 0.05 (c), 2.86 (d).

The topology of the regions of recirculating flow is further analysed by the use of a streamfunction (Ψ_{B}) representation of the spanwise-invariant base flow in the x-y plane. Figure 4.5 portrays isolines of Ψ_{B} in step case III. Their organisation is in agreement with the widely reported behaviour of two-dimensional forward-facing-step flows; see Wilhelm et al. (2003) and Marino and Luchini (2009), for instance. The region of recirculating flow upstream of the step reattaches at the vertical face of the wall. A second smaller region of flow separation arises immediately downstream of the step. It shall be stressed that in the present three-dimensional boundary-layer flow, the recirculating regions extend *infinitely* in the spanwise direction and the reattachment point in figure 4.5 ought to be conceived as an attachment line along z. As noted by Tufts et al. (2017), the flow separation in three-dimensional space represents helical flow that arises from the combination of recirculation motion and spanwise velocity.

The geometrical properties of the separation regions upstream and downstream of the step are quantitatively characterised by means of the corresponding projected dividing streamline, i.e., the isoline of Ψ_{B} that connects the separation and reattachment points. A summary of properties is given in table 4.1. An increase in step height leads to a significant elongation of the separation zones in x, specially in the down-

stream region. However, the cores of the reverse-flow regions are maintained close to $x_{\mathrm{st}} = 0$. The peak reverse-flow velocity within the downstream recirculation regions is 1.4% and 2.7% in step cases II and III respectively, relative to the local *pseudo*-free-stream velocity. These values are significantly lower than the threshold required for global or absolute instability mechanisms to develop in classic pressure-induced separation bubbles (Alam and Sandham, 2000; Rodríguez et al., 2013).

Previous investigations identify the regions of flow reversal as a key feature to explain the modified properties of the incoming CFI at the step. Tufts et al. (2017) suggest interaction between the step-induced recirculating flow and the crossflow vortices. As will be shown in § 4.2.3 and 4.2.4, there appears to be little evidence in the present results to support the model proposed by Tufts et al. (2017). Stationary CFI growth at the step is ascribed by Eppink (2020) to the destabilising effect of the inflectional profiles that develop due to flow separation and/or reversal of the crossflow component. Crossflow reversal, i.e., change of sign of the crossflow velocity, is captured in the present DNS as well. This phenomenon is linked to the abrupt change of orientation of the near-wall streamlines discussed in the previous section.

The crossflow component, $w_{\mathrm{B},s}$, as defined in equation (2.7), originates from the imbalance between chordwise and spanwise momentum in the boundary layer, relative to the orientation of the inviscid streamline. In the no-step case, the crossflow velocity is positive in the presently used coordinate system. In the vicinity of the step, the influence of the step-induced pressure gradient is weak in the free-stream region. Consequently, the angle between the inviscid streamline and x, ϕ_s (2.6), does not change significantly in x; this is illustrated in figure 2.4 in § 2.1.1. The pronounced outboard bending of the streamlines in the near-wall region upstream of the step reverses the crossflow velocity, which becomes negative in all step cases close to the wall. This is illustrated in figure 4.6(a),(b). From equation (2.7), it can be conceived as a consequence of the effective deceleration of u_{B}, as compared to w_{B}, whereas $\phi_s \approx -45^\circ$ does not undergo large variations in x.

At the immediate downstream vicinity of the step, the flow behaviour follows an opposite trend. The sudden inboard motion of the near-wall flow associated to the rapid acceleration of u_{B} (figure 4.2(b)) carries a strong acceleration of the crossflow component, which becomes positive again. As highlighted in figure 4.6(c), the peak value of the crossflow component in the step cases attains more than twice the value in the reference (no-step) case. When moving further downstream, u_{B} decelerates in x close to the wall (figure 4.2(c)), in the region of adverse pressure gradient. As a consequence, a second zone of crossflow reversal emerges near the wall, see figure 4.6(d). Further from the wall, the excess of u_{B} relative to w_{B} induced at the step corner maintains the crossflow component in the step cases positive and stronger than in the reference (no-step) case.

4.2. Evolution of the perturbation field at the step

In classic studies of the stationary CFI, special attention is placed on the topology and behaviour of the characteristic co-rotating vortices that arise in the steady

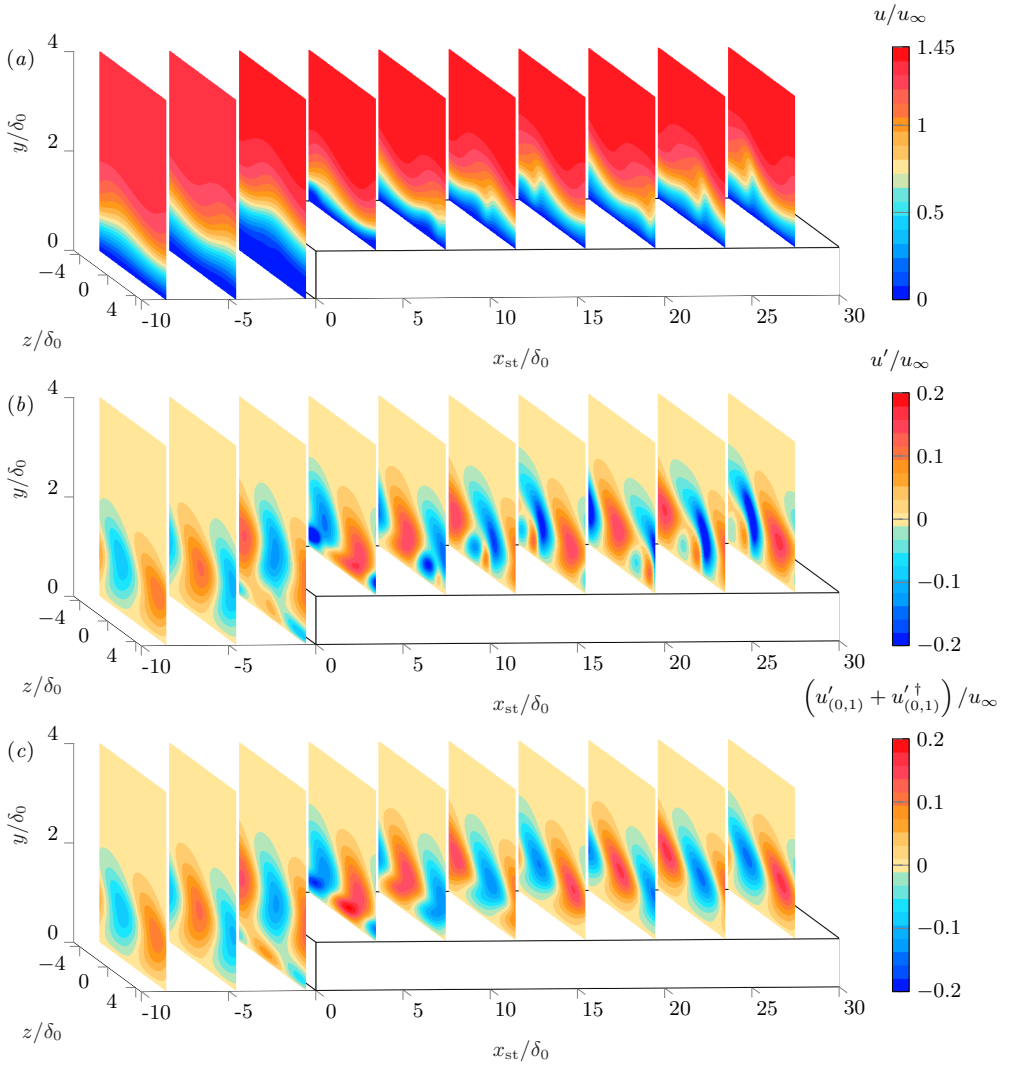

Figure 4.7: Organisation of the chordwise velocity of the steady perturbed flow (a), total perturbation field (b), fundamental perturbation field (c) in step case III.

perturbed flow. The evolution of stationary crossflow vortices is accompanied by a characteristic *wavy* fluid motion, i.e., a modulation of the flow field in the spanwise and the chordwise directions. Naturally, the wavy motion is accentuated as the perturbation amplifies in x. A graphical representation of the developed chordwise velocity field in the reference (no-step) case is shown in figure A.1 in appendix A. It must be noted that the isolated form of the CFI as a perturbation structure manifests

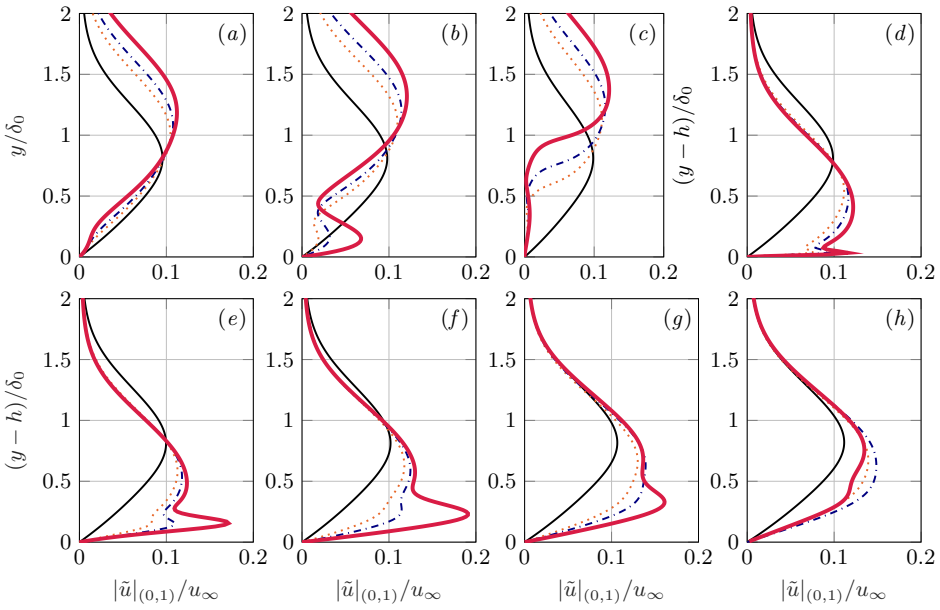

Figure 4.8: Amplitude function $|\tilde{u}|_{(0,1)}$ profiles close to the step: $x_{st}/\delta_0 = -2.04$ (a), -0.45 (b), -0.07 (c), 0.01 (d), 0.61 (e), 2 (f), 5 (g), 8 (h). Reference (no-step) case (thin solid black), step case I (dotted orange), II (dash-dotted blue), III (thick solid red).

itself as patches of vorticity of alternating sign in z (Bippes, 1999; Hosseinverdi and Fasel, 2016) accompanied by spanwise-distributed regions of perturbation-velocity excess and deficit (see appendix A). Under reference (no-step) conditions, since the activity of the harmonic components is weak at the x-position of the step (see figure 2.11 (b) in § 2.3.2), the fundamental perturbation component, $u'_{(0,1)} + u'^{\dagger}_{(0,1)}$, is very similar as the total perturbation field near the step (figure A.1 in appendix A).

The presence of the forward-facing step and the associated changes on the underlying base flow further complicate the identification of vortical structures. In particular, close to the step, it is challenging to visually identify the structure of the developed crossflow vortices using classical vortex-identification techniques such as the Q-criterion (Hunt et al., 1988). In step case I, the characteristic spanwise-modulated pattern in the steady perturbed flow is maintained rather invariant when passing the step in x (see figure A.2 in appendix A). This is not the case in step III, as a strong distortion of the steady-perturbed flow motion is evident and the organisation of the total perturbation field immediately downstream of the step is more pronounced (figure 4.7 (a),(b)), than in the reference (no-step) case. At the same time, the total and the fundamental perturbation fields in step III differ significantly from each other (figure 4.7 (b),(c)), suggesting an enhancement of the harmonic activity at the step. To segregate pertinent mechanisms, the analysis is commenced by describing the evolution of the fundamental perturbation field, $\boldsymbol{q}'_{(0,1)} = [\boldsymbol{v}'_{(0,1)}\ p'_{(0,1)}]^{\mathrm{T}}$.

4.2.1. Organisation of the fundamental perturbation field

Sufficiently upstream of the step, the profile along y of the amplitude function of the fundamental Fourier component, $|\tilde{u}|_{(0,1)}$, displays the single-peaked topology characteristic of the CFI. Nevertheless, in the upstream vicinity of the step, profiles of $|\tilde{u}|_{(0,1)}$ develop a secondary peak close to the wall in all step cases; see figure 4.8(*a-c*). When considering the corresponding three-dimensional perturbation representation, $u'_{(0,1)} + u'^{\dagger}_{(0,1)}$, the secondary peak in the amplitude function manifests as a system of velocity-perturbation streaks of alternating sign along the spanwise direction. This is illustrated in figure 4.7 (*c*).

Downstream of the step, a near-wall peak in the amplitude function $|\tilde{u}|_{(0,1)}$ coexisting with the original primary peak is captured as well, see figure 4.8(*d-h*). The existence of a secondary peak in the amplitude function profile is found for all $x_{\mathrm{st}} > 0$ in the near-step regime and for all step cases. When moving downstream of $x_{\mathrm{st}} = 0$ in the largest step case, the secondary peak exhibits strong growth in amplitude and eventually becomes more prominent than the primary peak. This trend is reverted further downstream, as the secondary peak decays in amplitude rapidly in x and merges back to the main profile. The associated near-wall perturbation-streak system (figure 4.7 (*c*)) behaves accordingly. Weak manifestations of the secondary peak in the amplitude function $|\tilde{u}|_{(0,1)}$ develop in step cases I and II as well, but never surpass the primary peak in strength.

The existence of a secondary near-wall peak in the perturbation shape has been reported in previous investigations and pointed out as a relevant feature of the interaction between the incoming CFI and the step (Tufts et al., 2017; Eppink, 2020). Furthermore, the aforementioned works, and more recently Rius-Vidales and Kotsonis (2021), indicate that the incoming CFI deflects away from the wall when passing over the step. The present results support this observation, as shown in figure 4.8 (*a-c*). Additionally, the near-wall streaks downstream of the step are accompanied by stationary vortex-like perturbation structures that coexist with the incoming (crossflow) perturbation structures at the step; these manifest as spanwise-distributed patches of opposite vorticity and have the same spanwise wavenumber as the primary vortices. Nevertheless, these near-wall perturbation structures accompanying the streaks are hereafter referred to as *secondary* since they are additional elements not present in the reference (no-step) case. An in-depth investigation of the origin and behaviour of such velocity-perturbation streaks at the step is provided in chapter 6.

4.2.2. Perturbation amplification upstream of the step

Next to describing the spatial evolution of the fundamental perturbation system $\boldsymbol{q}'_{(0,1)}$, a main goal motivating the current analysis is to quantify the effect of the step in altering the properties of the pre-existing stationary CFI. First, the focus is put here on effects upstream of the step.

A first metric employed to characterise the amplification of the fundamental CFI is the chordwise evolution of amplitude identified as the primary peak of $|\tilde{u}|_{(0,1)}$. This amplitude definition is denoted by $A^u_{(0,1)}$ in this thesis (see § 2.1.1 for details on amplitude definitions); as pointed out previously, a secondary peak in the perturbation amplitude function develops upstream of the step but, unlike the downstream

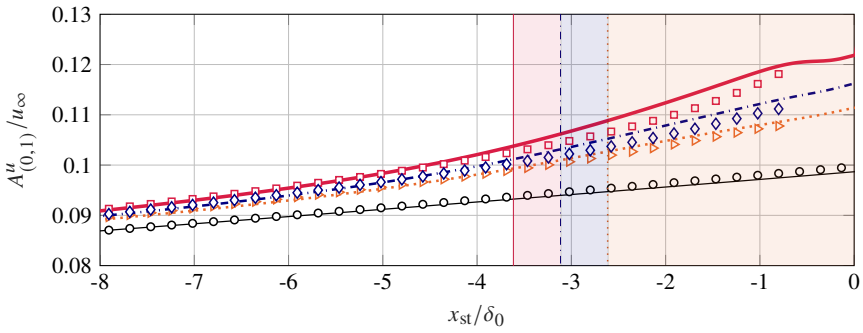

Figure 4.9: Amplitude of the fundamental chordwise-velocity perturbation component from DNS (lines) and PSE (symbols) upstream of the step: reference (no-step) case (thin solid black line and circles), step case I (dash-dotted orange line and triangles), II (dash-dotted blue line and diamonds), III (thick solid red line and squares). Vertical lines indicate beginning of disagreement between DNS and PSE (1% relative error).

region, it does not surpass the primary peak in strength in any step case. Thus, $|\tilde{u}|^{\text{top}}_{(0,1)} = |\tilde{u}|^{\text{max}}_{(0,1)}$ (§ 2.1.1) upstream of the step. It is emphasised that the latter relation does not apply when considering the perturbation components $w'_{(0,1)}$ and $v'_{(0,1)}$ since secondary peak(s) may become more prominent than the primary peak.

Lines in figure 4.9 indicate the chordwise evolution of $A^u_{(0,1)}$ obtained from DNS. Based on the choice of amplitude $A^u_{(0,1)}$, it is evident that the fundamental CFI becomes gradually amplified upstream of the step. Moreover, the overall upstream amplification with respect to the reference case appears to be proportional to the step height.

To gain additional insight into the underlying mechanisms for the observed upstream amplification, it is instructive to monitor reduced approximations to the instability growth. A powerful technique in this context is the Parabolised Stability Equations (PSE) approach (see § 2.2.3) applied to the DNS base flow. The comparison between DNS and PSE exposes the effect of inherent PSE assumptions, such as quasi-parallelism, on the manifestation of amplification due to the step. On the other hand, the present problem serves as an ideal platform to assess the limitations of a classic stability method as the PSE when it is applied in the presence of a sharp geometrical discontinuity. Cooke et al. (2019) report that the PSE method suffers from lack of numerical convergence when it is marched over the step due to the restriction concerning the minimum marching step size.

The linear PSE (also referred to as LPSE in this thesis) are solved in the domain $x_{st} < 0$. The choice of initial (inflow) DNS perturbation amplitude considered in the present analysis (namely the *medium*-amplitude case in table 2.4 of § 2.3.2) yields a largely linear behaviour of the CFI until reasonably close to the step (see figure 2.11 (*b*) in § 2.3.2). Thus, the LPSE method has been considered for the analysis of the upstream regime. The LPSE setup considered here is identical to that employed for the cross-validation with the reference (no-step) DNS case in § 2.3.2. The amplitude

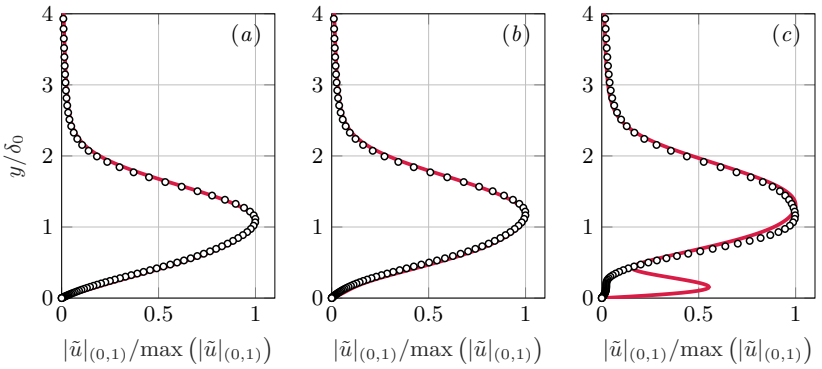

Figure 4.10: Profiles of the normalised amplitude function $|\tilde{u}|_{(0,1)}$ from DNS (solid line) and PSE (symbols) upstream of the step at $x_{\mathrm{st}}/\delta_0 = -4.5$ (a), -2.5 (b), -0.5 (c).

obtained by solving the LPSE is represented by symbols in figure 4.9. A first main observation is numerical convergence of the method until the upstream vicinity of the step; this result was unanticipated, inasmuch as the near-step region contains areas of flow recirculation and non-negligible chordwise base-flow derivatives and upwash, *a priori* violations of the underlying assumptions of the PSE method (Herbert, 1997). A second major result of figure 4.9 is that the LPSE capture a main part of the upstream amplification process, as indicated by the match in amplitude evolution between DNS and LPSE until significantly close to the step. Therefore, the CFI primarily undergoes linear growth evolution supported by the step-distorted base flow and the strong non-parallel effects introduced by the step do not significantly impact the main amplification process in the upstream regime.

The perturbation shape profiles obtained by DNS and LPSE are in excellent agreement in the region of reasonably close amplitude match, see figure 4.10 (a),(b) representing step case III. Figure 4.10 (c) additionally portrays the perturbation shape at an x-station immediately upstream of the step. Major differences in figure 4.10 (c) arise in the near-wall region; the secondary peak present in the results from DNS is not captured by the linear PSE. The present results show that the PSE method is robust in a region with non-negligible non-parallel effects.

It shall be noted that in the present DNS, the fundamental CFI amplifies upstream of the step in a regime where the strength of the base-flow crossflow component significantly decrease in x (figure 4.6). Under parallel-flow approximations, Mack (1984) indicates that the linear local instability characteristics are governed by the *directional* profile, i.e., the profile of the three-dimensional boundary layer in the direction of the wavenumber vector (Bippes, 1999); in a classic swept-wing boundary layer without steps, the wavenumber vector is roughly parallel to the direction of the crossflow component (2.7). However, the present results pose the question whether the inference of stability characteristics of the perturbation system from the properties of the crossflow profile holds valid near the step.

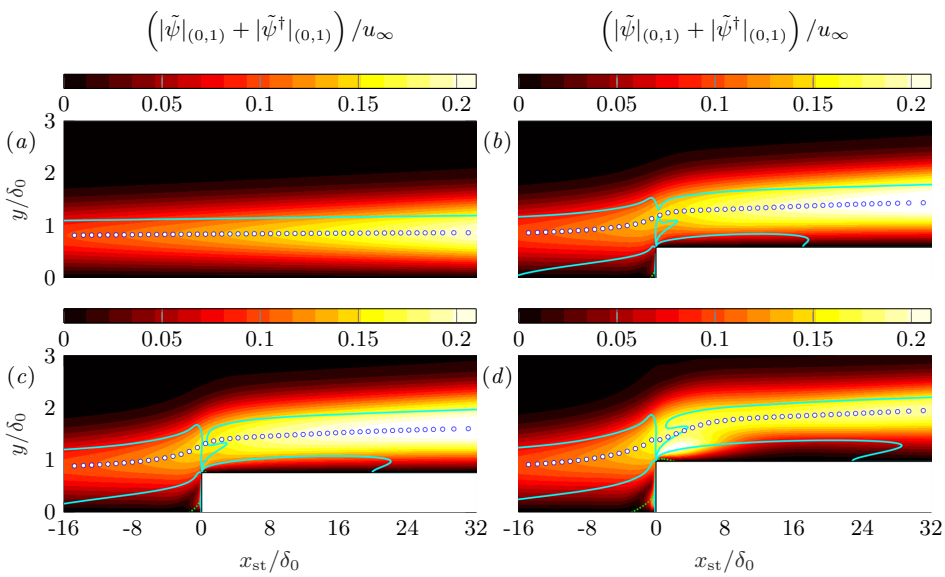

Figure 4.11: Fundamental *total* amplitude function contour, wall-normal position of maximum amplitude $|\tilde{\psi}|^{\mathrm{top}}_{(0,1)}$ (circles), loci of base-flow crossflow inflection points (solid cyan), base-flow reversal $u_{\mathrm{B}} = 0$ (dotted green) in the reference (no-step) case (*a*), step case I (*b*), II (*c*), III (*d*).

4.2.3. Modal and non-modal growth of CFI at the step

The discussion on the mechanisms of interaction between the fundamental CFI and step-induced flow features is next extended to the region around the step, and the physical nature of the mechanisms that govern the perturbation evolution.

When studying the stationary three-dimensional perturbation behaviour in a two-dimensional separated boundary layer, Marxen et al. (2009) find that a mixture of modal and non-modal growth governs the perturbation evolution. Similarities with Marxen et al. (2009) appear in the presently inspected flow, specifically, the step-induced region of favourable-to-adverse pressure gradient and the separation bubble. Nevertheless, a major difference in the present case is the existence of the modal CFI upstream of the step, which was not considered by Marxen et al. (2009). Based on the observations of Marxen et al. (2009), the rapid deflection of the base flow compared to the reference (no-step) case can be expected to be fertile condition for non-modal growth in the present case. To examine potential non-modal mechanisms near the step, the growth rate of the fundamental velocity-perturbation vector, $\boldsymbol{v}'_{(0,1)}$, decomposed following the base-flow orientation (3.12) introduced in chapter § 3 is evaluated. In the case of pure modal growth, different velocity components ought to exhibit a (reasonably) common growth rate, implying the existence of a single growing eigenmode (Marxen et al., 2009).

The following analysis is carried out by considering the amplitude functions corresponding to the modulus of the fundamental perturbation vector itself, $|\tilde{\psi}|_{(0,1)}$ (1.9),

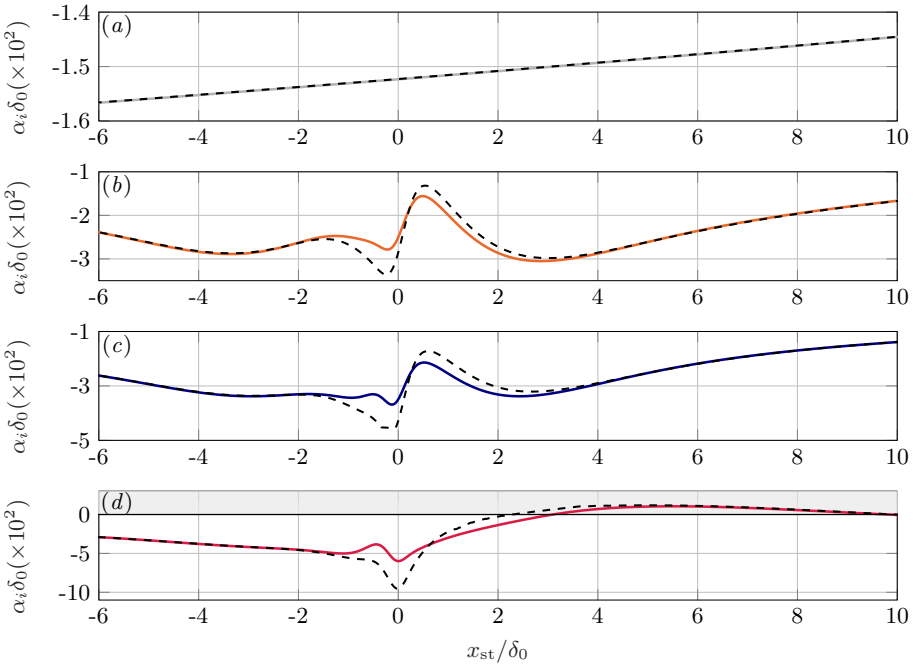

Figure 4.12: Growth rates associated to $|\tilde{\psi}|^{top}_{(0,1)}$ (dashed) and $|\tilde{\tau}|^{top}_{(0,1)}$ (solid) in the reference (no-step) case (a), step case I (b), II (c), III (d).

and to the component of the perturbation vector tangential to the base-flow direction, $|\tilde{\tau}|_{(0,1)}$ (3.23). The former is portrayed in figure 4.11 for the reference (no-step) case and for the step cases. In step III (figure 4.11 (d)), the near-wall secondary peak in the perturbation amplitude function downstream of the step surpasses the primary peak in strength. Similar observations apply to $|\tilde{\tau}|_{(0,1)}$. Under these circumstances, the global maxima of the perturbation amplitude function inherently measures the growth of the near-wall secondary structures. A more representative characterisation of the amplification of the incoming perturbation is instead obtained by tracking the evolution of the original primary peak. A similar metric can be devised considering $|\tilde{\psi}|^{top}_{(0,1)}$ and $|\tilde{\tau}|^{top}_{(0,1)}$ instead of $|\tilde{\psi}|^{max}_{(0,1)}$ and $|\tilde{\tau}|^{max}_{(0,1)}$ (see § 2.1.1 for amplitude definitions). The wall-normal locations associated with $|\tilde{\psi}|^{top}_{(0,1)}$ are indicated in figure 4.11 by solid circles. Additionally, dotted and solid lines in figure 4.11 represent $u_B = 0$ and the location of inflection points in the crossflow component, respectively.

Figure 4.12 shows the chordwise evolution of the growth rate associated to $|\tilde{\psi}|^{top}_{(0,1)}$ and $|\tilde{\tau}|^{top}_{(0,1)}$ computed as defined in equation (2.12). In the reference no-step case, as well as sufficiently upstream and downstream of the step, the fundamental perturbation vector and its component parallel to the base flow have a similar growth rate. Following the discussion provided by Marxen et al. (2009), this indicates that

perturbation growth is largely due to a modal instability, which is naturally associated to the incoming CFI. On the other hand, the significant differences between the growth rate evolution in the vicinity of the step in figure 4.12 (b,c,d) provide a first indication of possible non-modal perturbation growth. Since the single modal crossflow instability manifests again shortly downstream of the step, it is reasonable to consider a combination of modal and non-modal mechanisms governing the perturbation evolution at the step.

The realisation that different (base-flow-oriented) perturbation components display a significantly different growth rate evolution at the step poses the challenge of establishing a global estimation for the amplification in this regime. For instance, immediately downstream of the step, $u'_{(0,1)}$ shows destabilisation whereas $v'_{(0,1)}$ shows stabilisation. Based on this disparity, one may conclude that energy-based criteria, simultaneously encompassing the evolution of all perturbation components, are more suitable. The norm of the fundamental perturbation vector, $|\tilde{\psi}|_{(0,1)}$ (1.9), which relates to the perturbation kinetic energy of the fundamental spanwise mode (1.10), serves hereafter as a metric to characterise the growth or decay of stationary perturbation at the step.

In a fashion similar to the previous analysis, *growth* is next measured at the wall-normal location of the primary peak of the amplitude function, $|\tilde{\psi}|^{\mathrm{top}}_{(0,1)}$, thus avoiding possible artefacts from the amplification of the secondary near-wall structures at the step. The chordwise evolution of amplitude associated to $|\tilde{\psi}|^{\mathrm{top}}_{(0,1)}$ in the vicinity of the step is illustrated in figure 4.13. At first glance, the amplitude curves of step cases I and II maintain a rather constant growth in the region where non-modal growth sets in, possibly indicating that its effect is mild in comparison to the modal growth associated to the original pre-existing instability. However, step case III appears to differ considerably. The curve of step case III initially displays growth downstream of the step, but this is rapidly followed by a sudden and strong amplitude decay in the downstream direction. Therefore, based on the current choice of amplitude characterisation, the fundamental CFI emerges significantly stabilised immediately downstream of a *large* step.

The current observations are in contrast to conclusions drawn by Tufts et al. (2017), who indicate that for *large* steps (i.e., influencing transition), the interaction between the downstream region of flow recirculation and the incoming crossflow vortices amplifies the perturbation. Eppink (2020), who investigates steps that extend relatively high into the boundary layer, reports stationary crossflow amplification at the step as well; the author attributes it to the destabilising effect of the inflectional profiles arising in the regions of flow separation. Increasing the step height results in enhanced stationary CFI growth driven by the enhancement of reverse-flow regions (Eppink, 2020). Notwithstanding the differences in step height and flow conditions between this thesis and the aforementioned studies, these works do not discriminate between the locally-formed near-wall structures inherent to forward-facing step flow (chapter 6) and the pre-existing CFI. As such, in the region where the near-wall structures dominate, a local rapid growth is recorded, see Tufts et al. (2017, cf. figure A5) and Eppink (2020, cf. figures 11 and 14). In contrast, in this thesis, monitoring only the amplitude of the primary incoming instability (i.e., the CFI) that develops

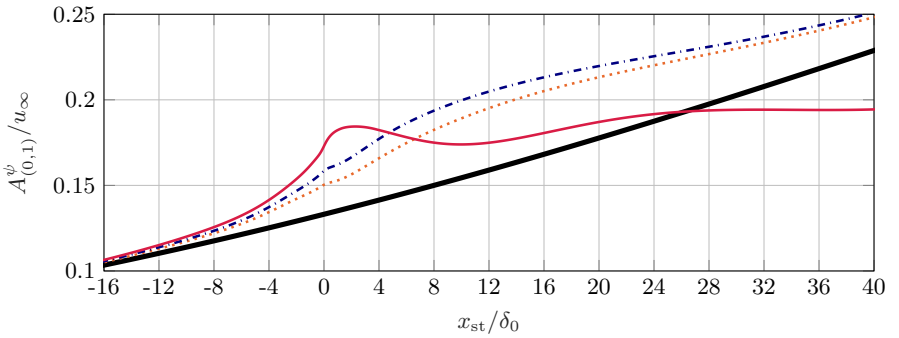

Figure 4.13: Chordwise evolution of the amplitude associated to $|\tilde{\psi}|^{\mathrm{top}}_{(0,1)}$ in the reference (no-step) case (thick solid black), step case I (dotted orange), II (dashed-dotted blue), III (thin solid red).

farther from the wall, reveals a milder impact –and even a stabilising effect– caused by the step (figure 4.13).

In summary, the present DNS indicate that the near-step regime encompasses a mixture of perturbation mechanisms acting simultaneously. Secondary near-wall structures are induced at the step; their growth is not captured by the linear PSE, despite the remarkable ability of the latter to model the amplitude and shape of the incoming crossflow instability up to close vicinity of the step. Additionally, differences in the growth rate in different directions point to non-modal effects feeding growth to certain perturbation components. Finally, large differences in perturbation growth rate are identified, depending on the wall-normal position at which the latter is evaluated. Previous work on forward-facing-step flows in absence of a crossflow instability (Lanzerstorfer and Kuhlmann, 2012) has identified spanwise-distributed near-wall velocity streaks, structurally similar to the secondary structures reported here. This suggests that the near-wall vortex-like structures and streaks can exist independently from (but possibly triggered and conditioned in wavelength and phase by) the pre-existing CFI. Furthermore, regardless of their nature and origin, the near-wall secondary structures decay rapidly in x and eventually merge with the primary crossflow vortices. Accordingly, it becomes important to characterise the impact of the step on the incoming fundamental CFI by evaluating the stability properties of the perturbation system in the region *far* from the wall, where the incoming primary structures lift up and pass over the step.

4.2.4. Perturbation misalignment and energy-transfer mechanisms at the step

Based on the observations in the previous section, non-modal growth mechanisms, in conjunction to the primary modal instability growth, likely play a role near the step. Marxen et al. (2009) relate a modal instability in which all perturbation components exhibit a common growth rate in x to the perturbation vector maintaining its orientation with respect to the base flow. Following this reasoning, the observed

differences displayed by different perturbation components in figure 4.12 suggests a link to a local misalignment between the base-flow vector and the perturbation vector at the step. This misalignment can be expected in a region of strong and sudden spanwise base-flow modulation (figures 4.3 and 4.4). To explore this in detail, the perturbation-vector field $\boldsymbol{v}'_{(0,j)}$ and its component aligned with the base-flow direction, $\boldsymbol{v}'_{t,(0,j)}$, are considered (3.12). The analysis carried out next is generalised for any Fourier component, but the subsequent discussion focuses on the fundamental mode, which is the scope of the current section. Since $\boldsymbol{v}'_{(0,j)}$ and $\boldsymbol{v}'_{t,(0,j)}$ are complex-valued, the *a priori* complex-valued angle, $\zeta_{(0,j)}$, between $\boldsymbol{v}'_{(0,j)}$ and $\boldsymbol{v}'_{t,(0,j)}$, is introduced (Scharnhorst, 2001)

$$\cos\left(\zeta_{(0,j)}\right) = \frac{\boldsymbol{v}'_{(0,j)} \cdot \boldsymbol{v}'_{t,(0,j)}}{||\boldsymbol{v}'_{(0,j)}||\,||\boldsymbol{v}'_{t,(0,j)}||}, \tag{4.4}$$

whereas the real-valued Euclidean angle, $\zeta_{\mathrm{E},(0,\mathrm{j})}$, between $\boldsymbol{v}'_{(0,j)}$ and $\boldsymbol{v}'_{t,(0,j)}$, is defined as (Scharnhorst, 2001)

$$\cos\left(\zeta_{\mathrm{E},(0,\mathrm{j})}\right) = \frac{\mathrm{Re}\left(\boldsymbol{v}'_{(0,j)} \cdot \boldsymbol{v}'_{t,(0,j)}\right)}{||\boldsymbol{v}'_{(0,j)}||\,||\boldsymbol{v}'_{t,(0,j)}||}. \tag{4.5}$$

It must be noted that

$$\boldsymbol{v}'_{(0,j)} \cdot \boldsymbol{v}'_{t,(0,j)} = \left(\boldsymbol{v}'_{t,(0,j)} + \boldsymbol{v}'_{n,(0,j)}\right) \cdot \boldsymbol{v}'_{t,(0,j)} = \boldsymbol{v}'_{t,(0,j)} \cdot \boldsymbol{v}'_{t,(0,j)} = ||\boldsymbol{v}'_{t,(0,j)}||^2 \tag{4.6}$$

since $\boldsymbol{v}'_{t,(0,j)}$ and $\boldsymbol{v}'_{n,(0,j)}$ are complex orthogonal, as demonstrated in § 3.2. As a consequence, expressions (4.4) and (4.5) are equivalent and thus $\zeta_{(0,j)} = \zeta_{\mathrm{E},(0,\mathrm{j})}$. Furthermore, considering equality (4.6), expression (4.4) can be re-written as

$$\cos\left(\zeta_{(0,j)}\right) = \frac{||\boldsymbol{v}'_{t,(0,j)}||}{||\boldsymbol{v}'_{(0,j)}||} = \frac{|\tilde{\tau}|_{(0,j)}}{|\tilde{\psi}|_{(0,j)}}, \tag{4.7}$$

implying that $\zeta_{(0,j)} = \zeta_{(0,j)}(x, y)$.

The rate of change of the angle $\zeta_{(0,j)}$ in x can be directly related to the relative growth rate evolution of the perturbation components through

$$\frac{\partial}{\partial x}\left(\cos\left(\zeta_{(0,j)}\right)\right) = \frac{\frac{\partial}{\partial x}\left(|\tilde{\tau}|_{(0,j)}\right)|\tilde{\psi}|_{(0,j)} - \frac{\partial}{\partial x}\left(|\tilde{\psi}|_{(0,j)}\right)|\tilde{\tau}|_{(0,j)}}{|\tilde{\psi}|^2_{(0,j)}}, \tag{4.8}$$

and it follows that

$$\frac{\frac{\partial}{\partial x}\left(|\tilde{\tau}|_{(0,j)}\right)}{|\tilde{\tau}|_{(0,j)}} \neq \frac{\frac{\partial}{\partial x}\left(|\tilde{\psi}|_{(0,j)}\right)}{|\tilde{\psi}|_{(0,j)}} \Rightarrow \frac{\partial}{\partial x}\left(\zeta_{(0,j)}\right) \neq 0. \tag{4.9}$$

The condition expressed by equation (4.9) can be evaluated for a particular Fourier component at any (x, y) location of the corresponding amplitude functions.

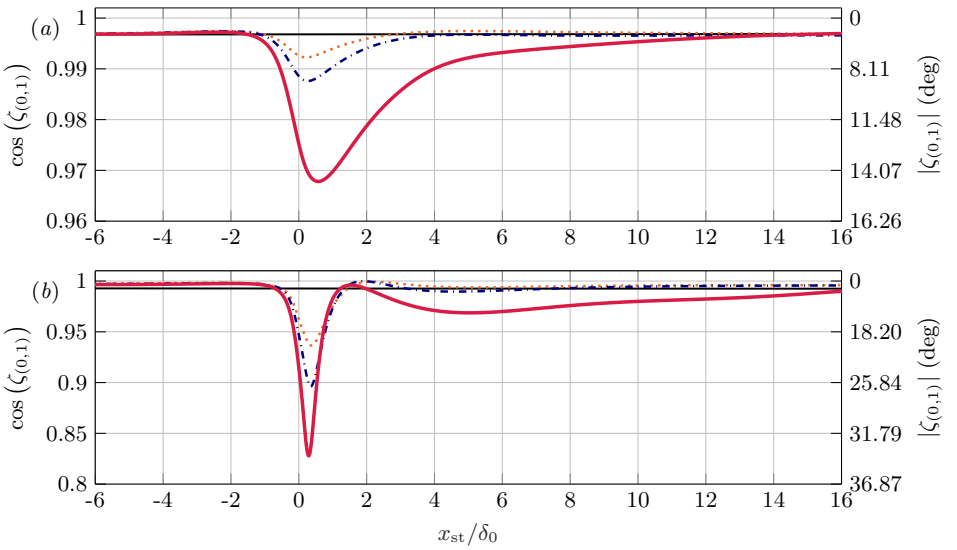

Figure 4.14: Chordwise evolution of the perturbation-to-base-flow angle $\zeta_{(0,1)}$ at the wall-normal location of $|\tilde{\tau}|^{\text{top}}_{(0,1)}$ (a) and at $y/\delta_0 = h/\delta_0 + 0.2$ (b) in the reference (no-step) case (thin solid black), step case I (dotted orange), II (dashed-dotted blue), III (thick solid red).

From the results of figure 4.12, the occurrence of non-modal growth at the step has been justified based on the different growth rate evolution associated to $|\tilde{\psi}|^{\text{top}}_{(0,1)}$ and $|\tilde{\tau}|^{\text{top}}_{(0,1)}$. The wall-normal position associated to $|\tilde{\psi}|^{\text{top}}_{(0,1)}$ (figure 4.11) and $|\tilde{\tau}|^{\text{top}}_{(0,1)}$, $\tilde{y}^{\psi,\text{top}}_{(0,1)}$ and $\tilde{y}^{\tau,\text{top}}_{(0,1)}$, are reasonably close to each other in the vicinity of the step in case III, and are almost identical in cases I and II. Under the assumption $\tilde{y}^{\psi,\text{top}}_{(0,1)} \approx \tilde{y}^{\tau,\text{top}}_{(0,1)}$, when evaluated at this common wall-normal position, the condition expressed by equation (4.9) is reduced to

$$\alpha^{\tau}_{i,(0,j)} \neq \alpha^{\psi}_{i,(0,j)} \Rightarrow \frac{\partial}{\partial x}\left(\zeta_{(0,j)}\right) \neq 0. \tag{4.10}$$

Thus, differences in the growth rate evolution in figure 4.12 appear to be linked to the fundamental perturbation vector changing its orientation with respect to the base-flow vector.

Figure 4.14 (a) portrays the chordwise evolution of $\zeta_{(0,1)}(x, \tilde{y}^{\tau,\text{top}}_{(0,1)})$. In the reference (no-step) case, the angle remains constant at approximately 4.6 degrees. That is, the fundamental perturbation vector maintains its orientation with respect to the base-flow vector while growing in x, as can be expected in the case of a single modal (crossflow) instability. Furthermore, it conforms with the results of figure 4.12 (a), where the perturbation vector and its tangential component are shown to follow a common growth rate.

When considering the step cases, $\zeta_{(0,1)}(x, \tilde{y}^{\tau,\text{top}}_{(0,1)})$ changes significantly in x in the

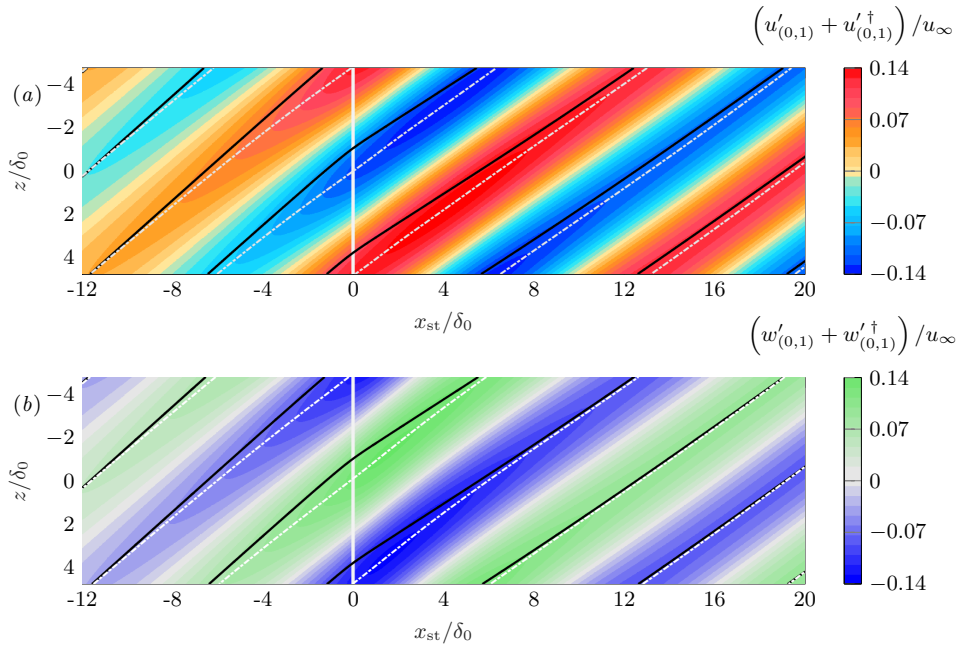

Figure 4.15: Chordwise (a) and spanwise (b) fundamental perturbation-velocity fields at $y/\delta_0 = 1.48$ in step case III. In-plane base-flow streamlines (solid lines) and perturbation wavefronts (dash-dotted lines).

vicinity of the step, see figure 4.14 (a). Approximately in the range $x_{st}/\delta_0 \in [-1.5, 4]$, in line with the condition expressed by equation (4.10), both *large* differences in growth rate evolution in figure 4.12 (b,c,d) and in the rate of change of $\zeta_{(0,1)}(x, \tilde{y}^{\tau}_{(0,1)})$ in x in figure 4.14 (a) are evident. Significant chordwise variations of $\zeta_{(0,1)}$ are captured in the near-wall region downstream of the step as well, see figure 4.14 (b) representing a constant wall-normal location. Figure 4.15 gives further evidence that the CFI does not follow the base-flow advection direction at the step. Considering step case III, figure 4.15 portrays x-z planes of $u'_{(0,1)} + u'^{\dagger}_{(0,1)}$ and $w'_{(0,1)} + w'^{\dagger}_{(0,1)}$ with projected base-flow streamlines (solid lines) and wavefronts of the perturbation field in the plane (dash-dotted lines).

In classic spatial LST analysis (§ 1.2.6), the wavenumber vector is typically used to characterise the perturbation propagation direction (Mack, 1984; Arnal, 1994). The wavenumber vector is normal to the wavefronts, hence the results of figure 4.15 show graphical evidence that the trajectory of the wavefronts and the projected base-flow streamlines gradually diverge upstream of the step. In line with the results of figure 4.14 (a), the wavenumber vector displays sudden change of orientation with respect to the base-flow direction immediately downstream of the step. Eppink (2020) similarly reports that isocontours of chordwise-velocity perturbation bend vigorously

Production	no-step	step case I	step case II	step case III
$P_{\beta_0}/P^\star$	1.00	1.85	2.13	1.01
$P_{\beta_0\,\mathrm{abs}}/P^\star_{\mathrm{abs}}$	1.00	1.63	1.89	2.35

Table 4.2: Regular (top) and absolute value (bottom) integral evaluation of the Reynolds-Orr production term P_{β_0} downstream of the step normalised by the reference (no-step) case $P^\star$.

close to the step, before re-aligning with the direction of the inviscid streamlines.

The possible implication of the misalignment between perturbations and the base flow on the perturbation growth and decay at the step is scrutinised next by means of the production term of the Reynolds-Orr equation (see §§ 3.1 and 3.3). Specifically, the term P_{β_0} (3.30) is considered here, which characterises the exchange of kinetic energy between the base flow and the fundamental perturbation. The sign of P_{β_0} informs whether kinetic energy is transferred from the base flow to the perturbation field ($P_{\beta_0} > 0$), i.e., the process is destabilising, or vice-versa ($P_{\beta_0} < 0$).

For the present analysis, the production term P_{β_0} is evaluated by considering a volume V defined by $0 \leq x_{\mathrm{st}}/\delta_0 \leq 10$, $h/\delta_0 \leq y_{\mathrm{st}}/\delta_0 \leq 6$, $z_{\min} \leq z \leq z_{\max}$ since the current aim is to quantify perturbation mechanisms downstream of the step. Table 4.2 summarises the quantitative results normalised with the reference (no-step) case, where $P^\star$ denotes integration of the signed production and $P^\star_{\mathrm{abs}}$ integration of its local absolute value. The integral of the absolute value confirms that the presence of the step enhances the exchange of kinetic energy between the base flow and the fundamental perturbation field. The perturbation-to-base-flow misalignment (and posterior realignment) induced at the step inherently carries growth (and decay) of the normal perturbation component, $\boldsymbol{v}'_{n,(0,1)}$, relative to the tangential component, $\boldsymbol{v}'_{t,(0,1)}$ (3.12). Rapid change in x of the perturbation component acting normal to the base-flow streamlines appears to enhance the energy transfer between base flow and perturbations. Chapter 5 confirms this finding and examines the physical mechanism underpinning the behaviour.

Additionally, figure 4.16 illustrates the integrand of P_{β_0}, $(-2\pi/\beta_0)\Lambda_{\beta_0}$, see equations (3.9) and (3.30). Immediately upstream of $x_{\mathrm{st}} = 0$, in all step cases, an enhancement of kinetic-energy transfer towards the perturbation field, i.e., $(-2\pi/\beta_0)\Lambda_{\beta_0} > 0$, is captured. This is in agreement with the results of figure 4.9, highlighting that the incoming CFI is gradually amplified as it approaches the step. Downstream of the step, $(-2\pi/\beta_0)\Lambda_{\beta_0}$ maintains a dominant positive contribution in cases I and II (figure 4.16 (b),(c)), which is consistent with the rather constant amplification trend depicted in figure 4.13. For step case III, a prominent region of negative $(-2\pi/\beta_0)\Lambda_{\beta_0}$ arises (figure 4.16 (d)) in the region where the perturbation amplitude decays (figure 4.13). Overall, the present results show that the production term itself is sufficient to characterise major stability features of the step-modified fundamental perturbation field. Chapter 7 assesses the remaining terms of the energy-balance equation for stationary modes developed in § 3.1, providing a complete energy budget at the step. Amplitude effects will be also addressed in chapter 7.

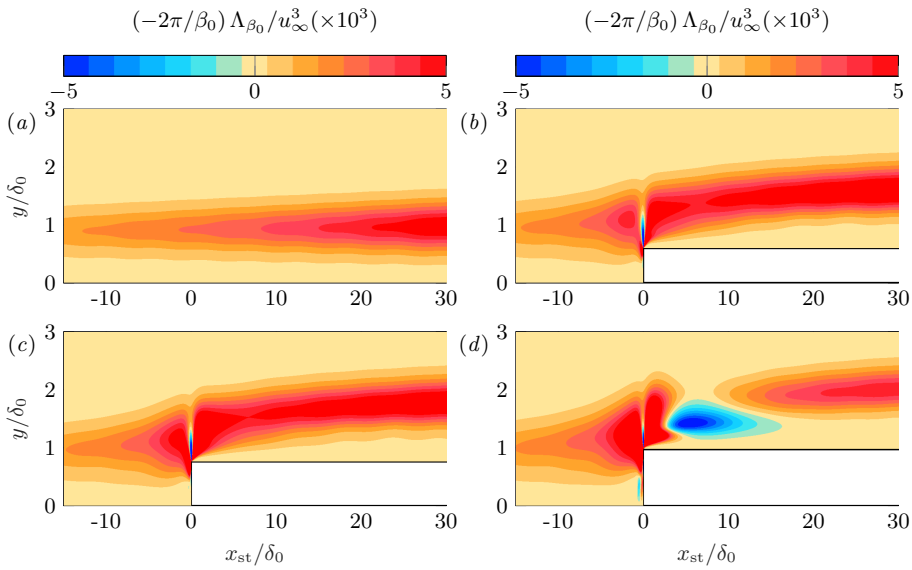

Figure 4.16: Integrand of the Reynolds-Orr production term P_{β_0} in the reference (no-step) case (a), step case I (b), II (c), III (d).

4.3. Perturbation evolution downstream of the step

The analysis is next extended to the region further downstream of the step, up to approximately $x_{\mathrm{st}}/\delta_0 = 30$. Previous work identified dominant harmonic activity in this regime (Eppink, 2020; Rius-Vidales and Kotsonis, 2021).

The evolution of the harmonic field $\boldsymbol{v}'_{(0,2)}$ (i.e., the mode with wavenumber $\beta = 2\beta_0$ in the Fourier decomposition (1.8)) is characterised in figure 4.17, where the associated total amplitude function is shown. Careful inspection of the topology of the field reveals similarities with that of the fundamental Fourier component, $\boldsymbol{v}'_{(0,1)}$. Specifically, secondary stationary near-wall perturbation structures develop as well immediately downstream of the step. They manifest in the form of spanwise-distributed regions of opposite vorticity with a spanwise wavenumber of $2\beta_0$. In the smallest step case, the pre-existing harmonic perturbation elements remain as dominant structures downstream of the step since additional near-wall ones are rather weak. This is not the case in step III, for which the new secondary near-wall structures display rapid growth in x and eventually overtake the incoming ones as main perturbation feature. Naturally, the $u'_{(0,2)}$ streaks expand accordingly, which explains the particular behaviour of the amplitude function for step III depicted in figure 4.17 (d). Similarly, Eppink (2020) identifies streamwise-oriented vortices localised in the near-step regime, which are connected to the harmonic content of the perturbation field. The origin of these secondary structures is ascribed by Eppink (2020) to the

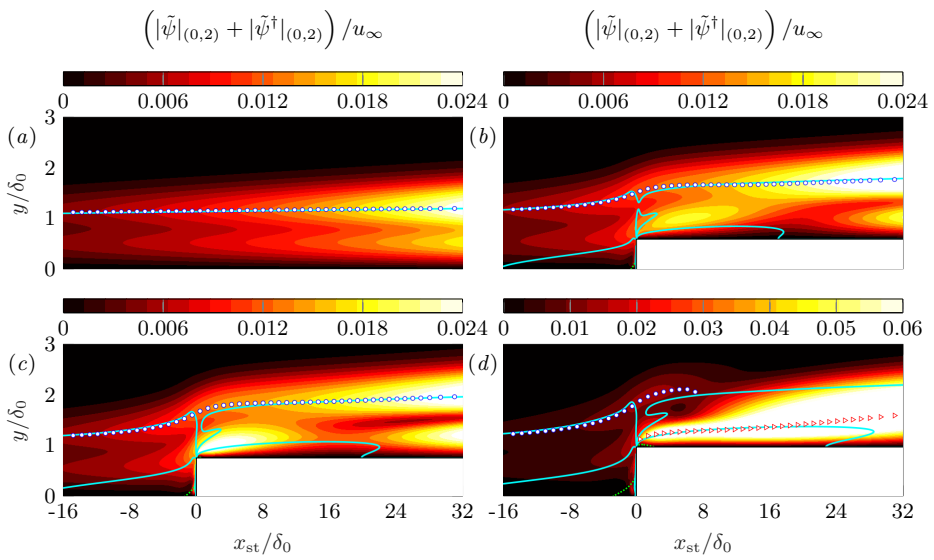

FIGURE 4.17: Harmonic $(0,2)$ *total* amplitude function contour, wall-normal position of $|\tilde{\psi}|^{\mathrm{top}}_{(0,2)}$ (circles), loci of base-flow crossflow inflection points (solid cyan), base-flow reversal $u_{\mathrm{B}} = 0$ (dotted green) in the reference (no-step) case (a), step case I (b), II (c), III (d). Wall-normal position of $|\tilde{\psi}|^{\mathrm{max}}_{(0,2)}$ downstream of the step in case III (triangles).

modulation of the step-induced upper separation bubble under the action of the incoming crossflow vortices.

A visual correlation is identified between the location of the maxima of the near-wall secondary peak in the amplitude function $|\tilde{\psi}|_{(0,2)}$ in step cases II and III and the location of the secondary step-induced inflection points in the crossflow component close to the wall (figure 4.17 (c),(d)). Eppink (2020) postulates that stationary CFI amplification at the step corner is triggered by the destabilising effect of the step-induced inflection points. As shown in § 4.2.3 and § 4.2.4, this is not the case for the pre-existing fundamental CFI since it is locally stabilised by a sufficiently large step. Nonetheless, the results of figure 4.17 suggest a local destabilising effect of the near-wall step-induced inflection points when considering the harmonic field $\boldsymbol{v}'_{(0,2)}$.

To shed light on this possibility, a linear local and parallel stability analysis, based on the Orr-Sommerfeld eigenvalue problem (see § 1.2.6), is conducted on the base-flow profiles in the range $4 \leq x_{\mathrm{st}}/\delta_0 \leq 50.2$ considering $\beta = 2\beta_0$. In all step cases, an eigensolution whose associated eigenvalue becomes unstable within a particular x-range (figure 4.18 (b-d)) is identified, which remains stable in the equivalent eigenspectrum of the reference (no-step) case (figure 4.18 (a)). This eigenvalue is referred to as *critical* in the present analysis and denoted by $\alpha^{\mathrm{OS}} = \alpha_r^{\mathrm{OS}} + \mathrm{i}\alpha_i^{\mathrm{OS}}$. Therefore, the step-distorted base-flow profiles appear to support the exponential amplification of small-amplitude perturbations with half the spanwise wavelength of the fundamental

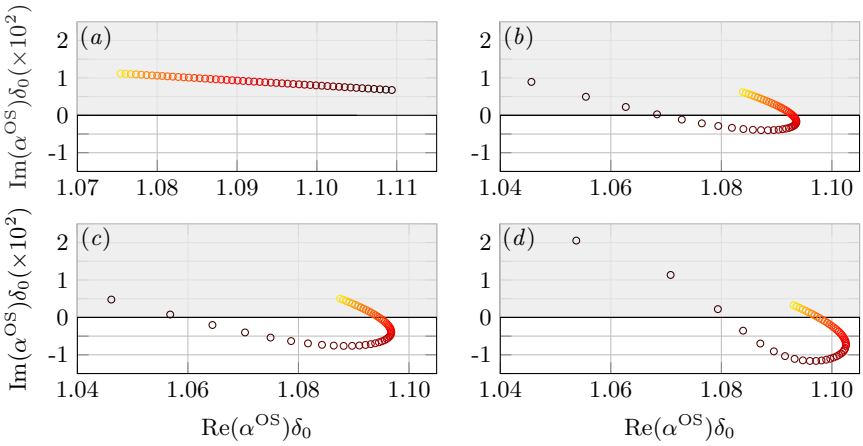

Figure 4.18: Trajectory of the critical unstable eigenvalue of the Orr-Sommerfeld eigenspectrum for increasing x in equispaced partitions in the range $x_{\mathrm{st}}/\delta_0 \in [4, 50.2]$ with $\beta = 2\beta_0$: smooth case (a), step case I (b), II (c), III (d). Dark-to-bright colour corresponds to increasing x.

crossflow mode.

Furthermore, the amplification factor in x of the critical unstable Orr-Sommerfeld eigenmode is proportional to the step height. In line with observations of Eppink (2020), for the particular case of the field $\boldsymbol{v}'_{(0,2)}$, an increase in the step height appears to increase the destabilising influence of the step-distorted inflectional base-flow profiles. Additionally, in results not shown here, linear local unstable eigensolutions are also identified when the analysis is repeated for higher-order harmonics. Although not fully conclusive, this model suggests that near-wall perturbations with $\beta > \beta_0$ triggered at the step corner are amplified further downstream through an Orr-Sommerfeld type of mechanism, possibly associated to the step-induced near-wall inflection points.

The behaviour of the harmonic Fourier modes for the DNS at the largest step (i.e., step case III) is quantitatively characterised in figure 4.19 portraying the evolution in x of the amplitude associated to $|\tilde{u}|^{\max}_{(0,j)}$, j = 0-6. As suggested by the results of the Orr-Sommerfeld analysis, growth of the high-order harmonics is captured downstream of the step. Additionally, figure 4.19 depicts the amplitude curves obtained by solving the linear and the non-linear PSE on the DNS base flow downstream of (but not at) the step.

The numerical setup of the present non-linear PSE (NPSE) simulations is identical to that employed in previous sections (§ 2.3.2), albeit a major difference: the initial condition of the marching scheme is provided by the local DNS solution at a selected x-position downstream of the step. Furthermore, for NPSE, this DNS (Fourier-analysed) initial condition is simultaneously assigned to all modes considered in the simulation at the common initial marching position.

It is found that a NPSE solution is able to march from $x_{\mathrm{st}}/\delta_0 = 8.57$ and reason-

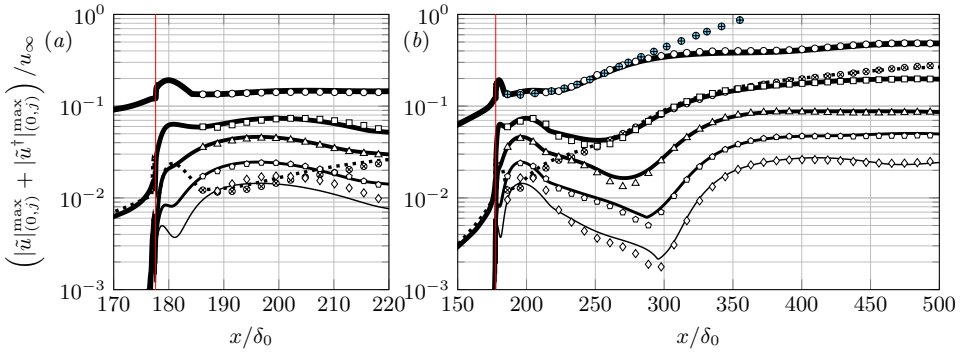

Figure 4.19: Chordwise evolution of the amplitude associated to $|\tilde{u}|^{\max}_{(0,j)}$, j = 1-5 (thick-to-thin), $j = 0$ (dotted), from DNS (solid lines), linear PSE (blue symbols), non-linear PSE (white symbols), in the near-step regime (a), downstream of the step (b) for the step case III. Vertical red line indicates the step location.

ably match the results from DNS (see figure 4.19). Excellent agreement is obtained sufficiently far from the step. Therefore, NPSE initialised from DNS data is able to resolve the perturbation evolution downstream of the step, even when an initial condition extracted reasonably close to the step is considered. Shifting the starting position of the NPSE simulation upstream of $x_{\mathrm{st}}/\delta_0 = 8.57$ rapidly results in a significant loss of accuracy. Similarly, the solution to linear PSE (LPSE) marched from $x_{\mathrm{st}}/\delta_0 = 8.57$ reasonably matches the local trend displayed by the fundamental crossflow component in the DNS and NPSE until approximately $x_{\mathrm{st}}/\delta_0 = 100$. Thereby, the present results show evidence that after passing the largest step, the fundamental CFI evolves following linear perturbation mechanisms.

This finding is contrary to the observed behaviour in the reference no-step case, where linear and non-linear PSE start to display differences much closer to the virtual location of the step (see figure 2.11 (b) in § 2.3.2). The fundamental perturbation experiences a significant stabilisation at the largest step, as previously detailed in § 4.2.3 and illustrated in figure 4.13. In § 4.2.4, this behaviour has been connected to the effective transfer of kinetic energy between the base flow and the fundamental perturbation, which is quantitatively characterised by the linear production term in the Reynolds-Orr equation (table 4.2 and figure 4.16 (d)). It is hypothesised that the enhancement of this linear perturbation effect under the influence of the step overshadows the impact of the non-linear interactions to the evolution of the fundamental CFI. This interpretation is further reinforced by the results presented in chapter 5, and by the rapid emergence of differences between linear and non-linear PSE initialised downstream of step cases I and II using the same methodology as employed for step case III; in step cases I and II, the behaviour of the linear production term is closer to that exhibited by the no-step case (figure 4.16).

It shall be noted that linear behaviour of the fundamental CFI downstream of the largest step arises in a regime with significant amplification of the harmonic

components (figure 4.19). As shown in figure 4.18, harmonic growth near the step can potentially be linked to the unstable nature of the base-flow profiles to spanwise wavelengths smaller than the fundamental one. In contrast, Eppink (2020) attributes stationary crossflow growth downstream of *large* steps –approximately beginning at the end of the separated-flow region– to a non-linear effect; the author justifies this based on the presence of secondary structures with harmonic wavelengths in this region (Eppink, 2020). It can be anticipated that, in order to assess whether the CFI follows linear or non-linear growth mechanisms downstream of the step, a multi-parametric space ought to be defined. The present results show that the height of the step stands out as dominant parameter in this regard and chapter 7 further explores how the amplitude of the pre-existing perturbation also influences the growth behaviour.

5

The lift-up effect at the step

Abstract: *Building on the insights from the previous chapter regarding enhanced production at the step, this chapter identifies a novel mechanism by which the forward-facing step significantly stabilises a pre-existing stationary CFI. The mechanism is termed here reverse lift-up effect, inasmuch as it acts reversely to the classic lift-up effect; that is, kinetic energy of an already existing shear-flow instability is transferred to the underlying laminar flow through the action of cross-stream perturbations. The framework and analysis of this chapter apply to generic three-dimensional flows and surface features of arbitrary shape with one invariant spatial direction.*

A note on nomenclature: *This chapter focuses exclusively on stationary effects and the fundamental (i.e., primary-wavelength) crossflow perturbation. The fundamental spanwise perturbation mode is denoted by* $\boldsymbol{v}'_{(0,1)}$*, where the prime marks perturbation and the zero indicates stationary behaviour. Unperturbed base-flow quantities are denoted by the subscript B, for example,* $\boldsymbol{v}_B$*. This chapter also analyses model problems, where a generic perturbation is represented by* $\hat{\boldsymbol{v}}'$*.*

Parts of this chapter are published in:

- Casacuberta, J., Hickel, S., and Kotsonis, M., 2024 Passive stabilization of crossflow instabilities by a reverse lift-up effect. *Phys. Rev. Fluids* **9**:043903.

In this chapter, a key claim from the previous chapter –that a forward-facing step does not universally destabilise a pre-existing fundamental CFI on interaction– is elaborated and a supporting mechanism is proposed. Building on the observations in § 4.2.4, the production term is decomposed following the framework introduced in § 3.3 and examined. The analysis in § 5.1 reveals that the critical production term reverses sign (i.e., it acts stabilising) for the step geometry that was shown to stabilise the pre-existing CFI in chapter 4. This finding gives rise to the concept of a novel *reverse lift-up effect*, a perturbation mechanism formalised in § 5.2 through two model problems: plane Poiseuille flow and blowing-suction in two-dimensional boundary-layer flow. The chapter concludes with an analysis of the origin and sensitivity of the reverse lift-up effect at the step to flow specifications (§ 5.3). The main flow problem investigated in this chapter corresponds to step case III (table 2.3) and *medium*-amplitude CFI conditions (table 2.4).

5

5.1. Mechanisms of stationary perturbation stabilisation by the step

This section first characterises the CFI stabilisation identified in chapter 4 under identical flow conditions and step geometry. Figure 5.1 illustrates the organisation of the fundamental (i.e., with wavenumber $\beta = \beta_0$) stationary perturbation field around the step using a perturbation metric different than that considered in chapter 4. Specifically, building on the projection formulation developed in § 3.2, figure 5.1 shows the streamwise-velocity perturbation component $\tau'_{(0,1)}$ (3.13); i.e., the component tangential to the local base-flow direction. It represents approximately 98% of the total kinetic energy budget –in relation to the cross-stream component– of the $\beta = \beta_0$ wavenumber space. It is emphasised here that the present perturbation decomposition into components tangential and normal to the base flow (§ 3.2) is applied to the fundamental spanwise mode (i.e., mode $|j| = 1$ in equation (1.8)), which is the focus of the present chapter.

The significant exchange of kinetic energy between the base flow and fundamental perturbations at the step observed in § 4.2.4 is next scrutinised by decomposing the production term of the Reynolds-Orr equation using the framework developed in § 3.3. Figure 5.2 portrays the integrands of $I_m^{\beta_0}, m =$ 1-4, stemming from the decomposition of P_{β_0} (3.31), in the step (*a*-*c*) and reference no-step (*d*-*f*) cases. As expected, the term $I_2^{\beta_0}$ holds the dominant contribution to energy production in the no-step case, see figure 5.2 (*e*). This highlights the role played by the weak cross-stream pattern ($\boldsymbol{v}'_{n,(0,1)}$) produced by the instability which, by displacing base-flow momentum, it enhances regions of streamwise-velocity deficit and excess ($\boldsymbol{v}'_{t,(0,1)}$); consequently, the CFI is amplified spatially (Saric et al., 2003). In the presence of the step, the mechanism $I_2^{\beta_0}$ remains a dominant contribution in absolute value (figure 5.2 (*b*)), albeit an enhancement of the mechanism associated to $I_4^{\beta_0}$ is captured *locally* near the step corner (figure 5.2 (*c*)). This latter feature has been reported as well in studies of near-wall streaks in unswept forward-facing-step flows (Lanzerstorfer and Kuhlmann, 2012).

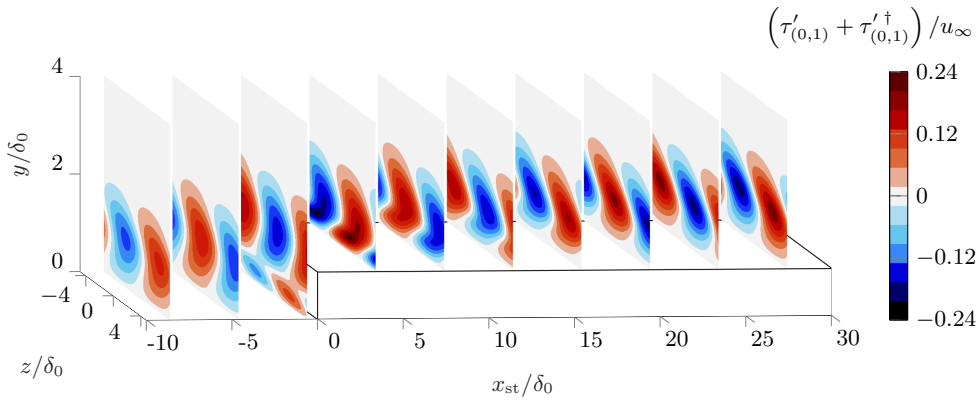

FIGURE 5.1: Organisation of the streamwise-velocity perturbation component around the step.

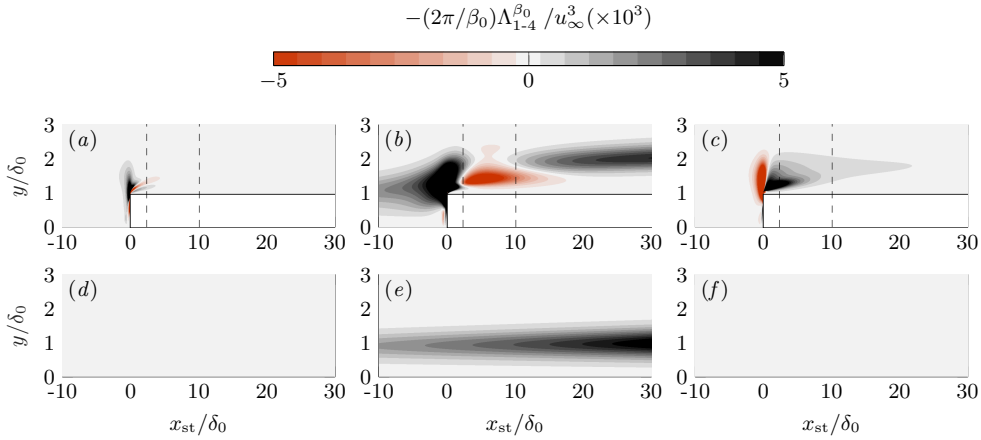

FIGURE 5.2: Spatial organisation of the integrand of $I_1^{\beta_0} + I_3^{\beta_0}$ in [(a) and (d)], $I_2^{\beta_0}$ in [(b) and (e)], $I_4^{\beta_0}$ in [(c) and (f)] in the step (top) and reference no-step (bottom) cases. Dashed black lines indicate x-range of CFI kinetic energy decay, as indicated by the thin solid red line in figure 4.13.

Figure 5.2 (b) shows that the dominant production term $I_2^{\beta_0}$ reverses sign shortly downstream of the step, approximately from $x_{st}/\delta_0 = 2.3$, see red contour in figure 5.2 (b). This thesis proposes that this phenomenon essentially corresponds to the lift-up effect acting in a stabilising manner, that is, by transferring kinetic energy from the perturbation field to the underlying flow. This mechanism is termed in this thesis as *reverse* lift-up effect since, originally, the *classic* lift-up effect was conceived as a mechanism responsible for actually destabilising streamwise streaks through the action of cross-stream perturbations (Ellingsen and Palm, 1975; Landahl, 1975, 1980).

The x-position where $I_2^{\beta_0}$ first changes sign approximately matches the location at which the CFI kinetic energy decays in x downstream of the step, as quantified by the thin solid red line in figure 4.13.

Downstream of the stabilising region, the perturbation structures gradually reorganise towards reference (no-step) conditions (see the description in § 5.3 below) and a destabilising influence of $I_2^{\beta_0}$ progressively sets in again (see black contour in figure 5.2 (b)). In this flow environment, the *strength* of $I_2^{\beta_0} > 0$ (figure 5.2 (b)) is lower than in reference conditions (figure 5.2 (e)), implying that the transfer rate of kinetic energy towards the perturbation field is below reference (no-step) conditions. This is consistent with the reduced growth rate in x of the CFI after passing the region of $I_2^{\beta_0} < 0$ in the step case, evident in figure 4.13 (see thin solid red line). When moving further downstream, far from the flow distortion introduced by the step, the growth rate of the CFI eventually increases significantly and becomes closer to the no-step case.

5.2. On the concept of a reverse lift-up effect

The previous section introduced the notion of a *reverse* lift-up effect, a perturbation mechanism that acts stabilising and *reversely* to the classic lift-up effect. Two model problems are discussed next to illustrate and strengthen the validity of this novel concept in simpler flow environments entailing canonical flow problems: plane Poiseuille flow and blowing-suction in two-dimensional boundary-layer flow.

5.2.1. Description of model problem I (plane Poiseuille flow)

The first model problem entails (itoptimal perturbations (Schmid and Brandt, 2014) in incompressible plane Poiseuille flow. This is a classic example of perturbation growth driven by the lift-up effect (Schmid and Henningson, 2001) and due to the simplicity of the base-flow topology serves as an archetypal demonstration of the reverse lift-up effect. The base-flow field reads $\boldsymbol{v}_\mathrm{B} = [u_\mathrm{B}(y)\ 0\ 0]^\mathrm{T}$ with $u_\mathrm{B} = u_0\left(1 - y^2/h^2\right)$ where u_0 denotes the peak velocity of u_B at centerline; i.e., at $y = 0$. The solid walls are placed at $y = \pm h$. A sketch of the flow problem and coordinate system is depicted in figure 5.3. Counter-rotating perturbation rolls are prescribed as an initial perturbation condition. They are x-invariant wave-like flow patterns that act orthogonal to base-flow streamlines; i.e., they represent a cross-stream perturbation as characterised by $\boldsymbol{v}_n'$ in equation (3.12).

Through the lift-up effect (Schmid and Henningson, 2001), the rolls redistribute base-flow momentum and induce streamwise perturbation streaks, i.e., regions of streamwise-velocity deficit and excess as characterised by $\boldsymbol{v}_t'$ in equation (3.12). The streamwise streaks are invariant in the x-direction as well. While the streaks display a rapid initial growth in time, the rolls remain practically unaltered in time. The *optimal* perturbation rolls, i.e., the flow pattern which yields the largest transient growth of kinetic perturbation energy, and the corresponding optimal response for a chosen time horizon ($tu_0/h = 27.895$) have been obtained through a singular value decomposition of the corresponding matrix exponential. The calculations are carried out with the code OptimalDisturbance.m provided by Schmid and Brandt (2014), using

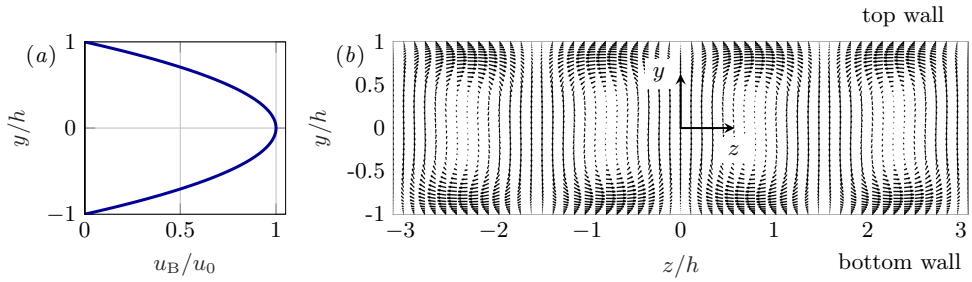

FIGURE 5.3: Sketch of model problem I: base-flow profile u_B (a) and organisation of *optimal* perturbation rolls $\hat{\boldsymbol{v}}' = [0\ \hat{v}'\ \hat{w}']^T$ at the initial time instant (b).

a spanwise wavenumber of $\beta_0 h = 2.04$ and a Reynolds number of $Re = u_0 h/\nu = 1000$.

5.2.2. Analysis of model problem I (plane Poiseuille flow)

The Reynolds-Orr equation (1.14) is invoked next, relating the rate of change of kinetic perturbation energy in time with the effect of production, P_{β_0}, and viscous dissipation, D_{β_0} (see also § 3.1). The pre-imposed perturbation rolls act by redistributing low- and high-momentum fluid and thus they feed growth to streamwise streaks; i.e., production $P_{\beta_0} > 0$, naturally implying that the streamwise streaks grow by extracting energy from the base-flow shear. Concerning the overarching discussion in this present chapter, the realisation that the lift-up effect –characterised by $I_2^{\beta_0}$ (§ 3.3)– is the main mechanism driving here the perturbation amplification (Schmid and Henningson, 2001) follows from the fact that $I_1^{\beta_0} = I_3^{\beta_0} = I_4^{\beta_0} = 0 \Rightarrow P_{\beta_0} = I_2^{\beta_0}$ (3.31). This is illustrated as follows: the base flow is a parallel flow (i.e., $\partial u_B/\partial y$ is the only active base-flow shear), thus the integrands of $I_m^{\beta_0}, m = 1\text{-}4$ (see for example equations 3.32 and 3.33), simplify as

$$\Lambda_1^{\beta_0} = \tilde{v}_n^1\, \tilde{v}_n^{2\dagger}\, \frac{\partial u_B}{\partial y} + \text{c.c.}, \quad \Lambda_2^{\beta_0} = \tilde{v}_t^1\, \tilde{v}_n^{2\dagger}\, \frac{\partial u_B}{\partial y} + \text{c.c.} \tag{5.1a}$$

$$\Lambda_3^{\beta_0} = \tilde{v}_n^1\, \tilde{v}_t^{2\dagger}\, \frac{\partial u_B}{\partial y} + \text{c.c.}, \quad \Lambda_4^{\beta_0} = \tilde{v}_t^1\, \tilde{v}_t^{2\dagger}\, \frac{\partial u_B}{\partial y} + \text{c.c.} \tag{5.1b}$$

In turn, particularly for the present flow problem, the perturbation components tangential and normal to base-flow streamlines may be related explicitly to the perturbation components tangential and normal to the wall as $\boldsymbol{v}_t' = [u'\ 0\ 0]^T$ and $\boldsymbol{v}_n' = [0\ v'\ w']^T$. Therefore, $\Lambda_1^{\beta_0} = \Lambda_3^{\beta_0} = \Lambda_4^{\beta_0} = 0$ and

$$P_{\beta_0} = I_2^{\beta_0} = -\frac{2\pi}{\beta_0} \int_S (\tilde{u}\, \tilde{v}^\dagger\, \frac{\partial u_B}{\partial y} + \text{c.c.})\, \mathrm{d}S = -\frac{4\pi}{\beta_0} \int_S |\tilde{u}||\tilde{v}| \frac{\partial u_B}{\partial y} \cos(\varphi^u - \varphi^v)\, \mathrm{d}S. \tag{5.2}$$

Equation (5.2) highlights that the *sense* of energy transfer between the base flow and the perturbation field (through the lift-up effect) is dictated by the sign of

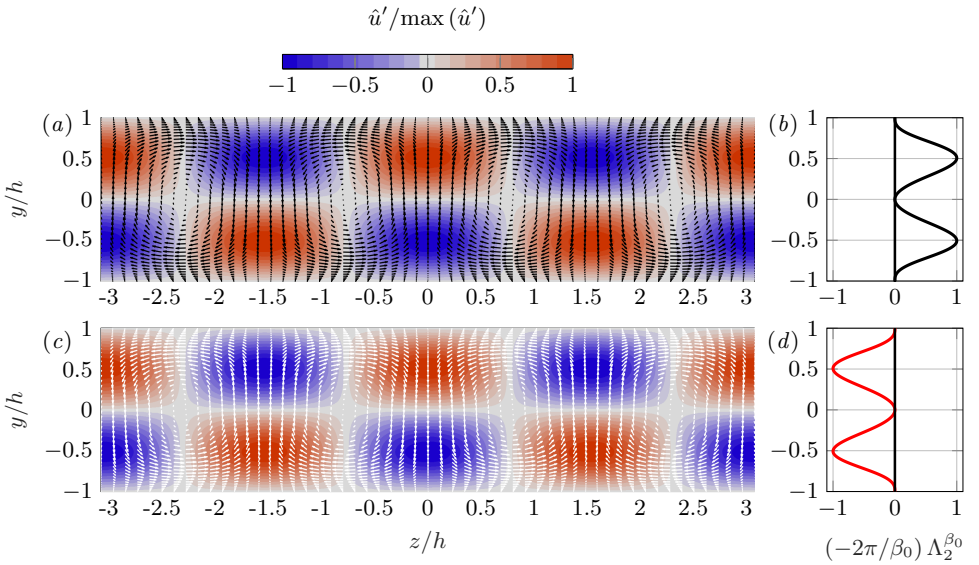

Figure 5.4: Organisation of perturbations in a *classic* (*a*) and a *reverse* (*c*) scenario of the lift-up effect in plane Poiseuille flow at a fixed time instant: cross-stream rolls (arrows) and streamwise streaks (colour contour). Integrand of the lift-up term $I_2^{\beta_0}$ normalised with respect to its maximum value in y, characterising the top (*b*) and bottom (*d*) cases.

$\cos(\varphi^u - \varphi^v)$; i.e., by the phase difference between cross-stream rolls and streamwise streaks establishing their relative placement along the spanwise direction z. By their relative phase in the present configuration, see figure 5.4 (*a*), $(-2\pi/\beta_0)\,\Lambda_2^{\beta_0} > 0$ for all y (figure 5.4 (*b*)). The latter implies that the action of the cross-stream rolls ($\boldsymbol{v}_n'$) acts destabilising and base-flow kinetic energy feeds growth to the streamwise streaks ($\boldsymbol{v}_t'$). This illustrates the typical scenario of the classic lift-up effect. It is noted that in the present model problem, $\Lambda_2^{\beta_0} = \Lambda_2^{\beta_0}(y)$ since both the base flow and the perturbation field are invariant in x.

In essence, the core analysis of the present chapter revolves around the fact that the same principle holds, but operates in a reverse fashion, if the relative spatial placement between cross-stream rolls and streamwise streaks (i.e., their spanwise phase) is altered. This is illustrated as follows: consider that at the time instant depicted in figure 5.4 (*a*,*b*), the spanwise phase of the rolls, φ^v, is shifted by π radians such that the term $\cos(\varphi^u - \varphi^v)$ in equation (5.2) reverses its sign. In such new perturbation environment, depicted in figure 5.4 (*c*), $(-2\pi/\beta_0)\,\Lambda_2^{\beta_0} < 0$ for all y (figure 5.4 (*d*)). In the new scenario, $I_2^{\beta_0} < 0$ implying that $P_{\beta_0} < 0$ and since $D_{\beta_0} < 0$ always, $\mathrm{d}E_V/\mathrm{d}t < 0$ (1.14). Therefore, the perturbation field undergoes stabilisation locally in time, which shall be interpreted as the flow exhibiting a tendency towards recovering the original (unperturbed) laminar base state: low-momentum fluid is displaced towards the regions of streamwise-velocity excess (i.e., red regions in figure

5.4) and high-momentum fluid is displaced towards the regions of streamwise-velocity deficit (i.e., blue regions in figure 5.4). Consequently, a *reverse lift-up effect* now takes place.

In short, the lift-up effect involves the superposition of perturbation streaks and streamwise-vortical structures (cross-stream rolls). In the classic sense, their interaction with the shear layer amplifies the streaks. However, for certain spanwise phase shifts between the streaks and vortical structures, the same interaction with the shear layer produces a stabilising response. At present, the novel proposed reverse lift-up effect has been exemplified on a pre-existing streaky flow field by altering artificially the spatial organisation of the perturbation content acting normal (the rolls) and tangential (the streaks) to the base flow. It is shown in § 5.3 below that essentially the same perturbation effect, but conditioned naturally by the abrupt spatial variation of the flow organisation, stabilises significantly a pre-existing convective instability in boundary-layer flow.

On a historical note, the notion that the lift-up effect is a powerful destabilising flow mechanism originates mainly from the work of Ellingsen and Palm (1975) and Landahl (1975, 1980). They formalised that a three-dimensional cross-stream perturbation in shear flow may induce growth of perturbation kinetic energy (by the lift-up effect) irrespective of whether the flow supports a modal (exponential) instability. While the concept of a stabilising (reverse) lift-up effect may seem paradoxical at first glance, it actually follows naturally from the model of Ellingsen and Palm (1975) if a non-zero initial perturbation streak field is considered. This is elaborated upon in detail in § 5.2.5.

5.2.3. Description of model problem II (blowing-suction in two-dimensional boundary-layer flow)

The second model problem illustrates the principle of the reverse lift-up effect in boundary-layer flow. It entails streamwise perturbation streaks in a two-dimensional spatially-accelerating (i.e., favourable pressure gradient) boundary layer over a flat plate. When developing in the streamwise direction, the streaks interact with localised steady wall blowing-suction; § 2.1.3 provides details on the blowing-suction setup, which is here constrained to steady modulation (i.e., $f_0 = 0$ in equation (2.23)). The elements of the perturbation field in this (model) flow problem resemble structurally those of the step case discussed in this present chapter. The multiple similarities between both perturbation scenarios pave the road for full characterisation of the reverse lift-up effect in the highly deformed three-dimensional step flow (§ 5.3). For the sake of representation, the acceleration of the free-stream in the streamwise direction, x, and the inlet Reynolds number in the model problem are similar to the step case. However, it is emphasised that the base flow is here unswept, i.e., $\boldsymbol{v}_\mathrm{B} = [u_\mathrm{B}(x,y)\ v_\mathrm{B}(x,y)\ 0]^\mathrm{T}$.

This model problem is configured to simulate the interaction of two distinct sets of perturbations, represented as $\hat{\boldsymbol{v}}'$: the field $\hat{\boldsymbol{v}}'$ is composed of a pair of (cross-stream) counter-rotating perturbation rolls prescribed at the inflow and streamwise perturbation streaks which amplify in x as a result of the lift-up effect (Luchini, 2000) induced by the action of the rolls on the base-flow shear. The wavelength

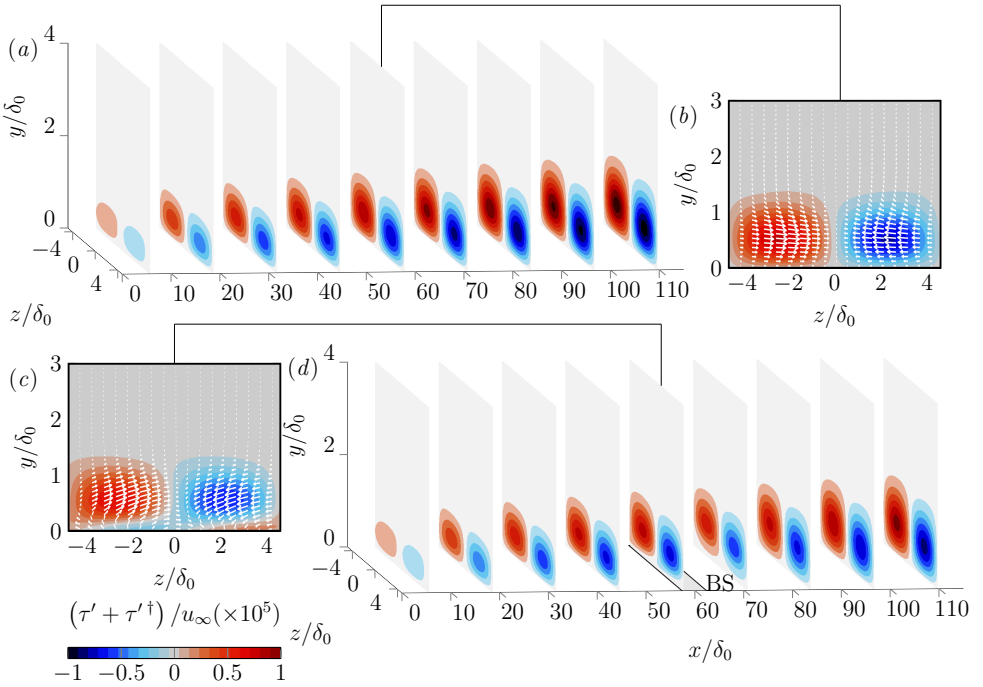

Figure 5.5: Evolution of the streamwise-velocity perturbation in no-blowing-suction (a,b) and blowing-suction (c,d) cases (colour map): three-dimensional organisation (a,d) and y-z planes (b,c) at $x/\delta_0 = 59$ with white arrows illustrating the in-plane organisation of the cross-stream-velocity perturbation. Wall blowing-suction strip depicted as grey rectangle in (d).

in the spanwise direction z of the perturbation rolls is identically that of the CFI mode in the step case and equals the spanwise domain length. The dimensions of the computational domain are $0 \leq x/\delta_0 \leq 123$ in the streamwise direction, $0 \leq y/\delta_0 \leq 26$ in the wall-normal direction, and $-4.86 \leq z/\delta_0 \leq 4.86$ in the spanwise direction. It is strengthened that both the pre-imposed inflow rolls and the spatially-forming streamwise streaks are stationary perturbation structures, i.e., $\partial\hat{\boldsymbol{v}}'/\partial t = 0$.

Corresponding flow fields of this model problem are obtained numerically via DNS in three sequential steps. First, the unperturbed base flow is computed. Second, steady-state DNS generates streamwise streaks in the boundary layer by prescribing, at the inflow, a pair of cross-stream rolls superimposed on the laminar profile. Finally, steady blowing-suction (BS) at the wall is applied: a disturbance strip modulates the wall-normal velocity harmonically according to equation (2.23). The width of the strip in the x-direction is kept small to produce a *local* effect, which is representative of the flow environment around the step discussed in §§ 5.1 and 5.3. The spanwise phase of the wall-normal velocity in the strip, $\phi_1 = \pi/2$ (2.23), is chosen such that the BS strip acts by locally stabilising the incoming streamwise streaks. The amplitude of the modulation at the strip, $A_1^{\mathrm{BS}} = 1 \times 10^{-6} u_\infty$ (2.23), yields a scenario of linearly

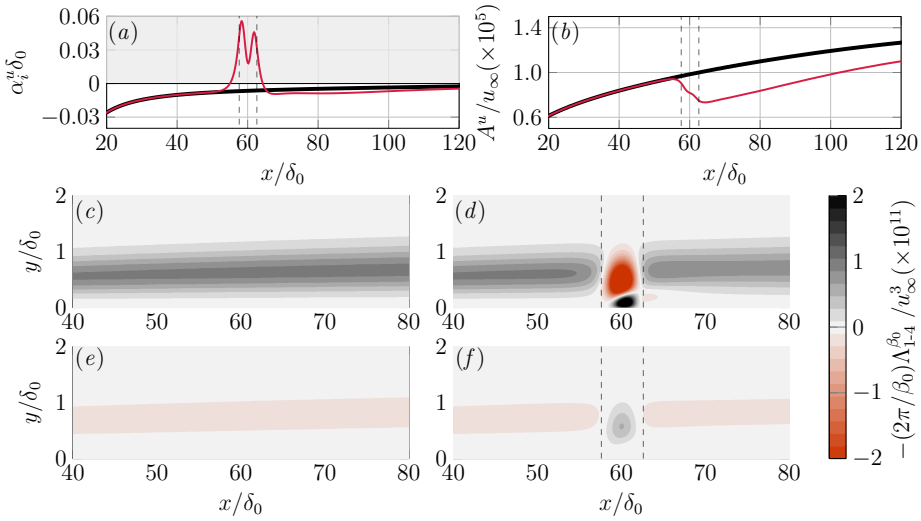

Figure 5.6: Evolution in x of perturbation spatial growth rate (a) and amplitude (b) in no-blowing-suction (thick black) and blowing-suction (thin red) cases. Spatial organisation of the integrand of $I_2^{\beta_0}$ [(c) and (d)] and $I_1^{\beta_0} + I_3^{\beta_0} + I_4^{\beta_0}$ [(e) and (f)] in no-blowing-suction (c,e) and blowing-suction (d,f) cases. Dashed vertical lines indicate the starting and ending positions of the blowing-suction wall strip.

dominated perturbation evolution. To retrieve perturbation information, the full perturbation field is decomposed into spanwise Fourier modes.

5.2.4. Analysis of model problem II (blowing-suction in two-dimensional boundary-layer flow)

The spatial evolution of the streaks is illustrated in figure 5.5 (a) depicting the streamwise-velocity (i.e., base-flow tangential) perturbation, τ' (3.13). At present, the streaks grow monotonically in x, as highlighted by the trend of their spatial growth rate, α_i, in figure 5.6 (a) (solid black line); it is emphasised that $\alpha_i < 0$ here implies growth in space. By the organisation of the flow in the present model problem, the representation of velocity perturbations acting tangential to the wall in x, u', and tangential to the base-flow streamlines, τ', are largely similar.

It is well known that the (classic) lift-up effect drives the perturbation amplification in this scenario. For instance, Luchini (2000) describes that "perturbations produced in this way are driven by the lift-up phenomenon, that is, by the continued accumulation over downstream distance of longitudinal-velocity differences arising from slow convection in the transverse plane." The term $I_2^{\beta_0}$ characterising the lift-up effect naturally adds here the main contribution to energy production, see figure 5.6 (c), in relation to negligible contributions by $I_1^{\beta_0}, I_3^{\beta_0}, I_4^{\beta_0}$, see figure 5.6 ($e$), and $I_2^{\beta_0} > 0$ for all x.

A popular method used to stabilise elongated streamwise streaks is wall blowing-suction, see for instance Lundell and Alfredsson (2003). To produce a stabilising effect, a blowing region is placed underneath the high-speed streak and a suction region is placed underneath the low-speed streak. The aim of this section is to highlight that the concept of a reverse lift-up effect offers a simple way to understand and quantify the mechanism of perturbation stabilisation by blowing-suction. To this end, a BS surface disturbance strip is next positioned in the region $57.62 \leq x/\delta_0 \leq 62.62$, see figure 5.5 ($d$) illustrating the surface strip in relation to the spatially-developing streaks. In the vicinity of the surface strip, the wall-normal velocity *opposes* the incoming streaks and thus it reduces the *strength* of the incoming streak system locally in space. This effect is quantified by the large increase and change in sign of the spatial growth rate, see solid red line in figure 5.6 (a), and corresponding decay of perturbation amplitude, see solid red line in figure 5.6 (b). Finally, the results in figure 5.6 (a,b) show additionally that the original perturbation mechanism (i.e., the classic lift-up effect) is gradually recovered downstream of the BS strip.

In the blowing-suction scenario, the velocity induced at the wall reverses locally the interplay between cross-stream- (white arrows in figure 5.5 (b,c)) and streamwise- (colour map in figure 5.5) velocity perturbations due to their relative spanwise phase. That is, the cross-stream- and streamwise-velocity perturbations act *in-phase* (i.e., against) in the blowing-suction case, whilst they act *out-of-phase* (i.e., in favor) in the no-blowing-suction case; see the comparison between figure 5.5 (c) and figure 5.5 (b). Following the rationale discussed in § 5.2.2, but now in the context of spatially-developing perturbations, a reversal of the sign of $I_2^{\beta_0}$ is consequently monitored locally around the surface blowing-suction strip (see red region in figure 5.6 (d)). From the viewpoint of production, the latter shall be interpreted as the cross-stream perturbations now acting by transferring kinetic energy of the pre-existing streamwise streaks towards the underlying flow. At the same time, figure 5.6 (f) shows that the mechanisms of $I_1^{\beta_0}$, $I_3^{\beta_0}$, $I_4^{\beta_0}$ remain negligible in the region of blowing-suction. Therefore, the stabilisation via blowing-suction originates purely from a reverse lift-up effect; i.e., a reversal of the sense of kinetic-energy transfer with respect to the original (classic lift-up) mechanism.

5.2.5. A historical perspective on the classic and the reverse lift-up effect

Ellingsen and Palm (1975) and Landahl (1975, 1980) are credited mainly for formalising the lift-up effect, the destabilising flow mechanism responsible for the widespread presence of streaky structures in many shear-flow configurations (Brandt, 2014). At first glance, the novel concept of a stabilising (reverse) lift-up effect introduced in this thesis seemingly opposes their main conclusion. This is not the case; this section elaborates upon the fact that the reverse lift-up effect may be regarded as an additional solution to the model of Ellingsen and Palm (1975). This is expanded upon in the following manner: Ellingsen and Palm (1975) assume a parallel (base) flow with $\boldsymbol{v}_{\mathrm{B}} = [u_{\mathrm{B}}(y)\ 0\ 0]^{\mathrm{T}}$, which is incompressible, not stratified, and confined between two parallel walls. They consider the first component of the linearised inviscid

perturbation equation, i.e.,

$$\frac{\partial \hat{u}'}{\partial t} + \hat{v}' \frac{\partial u_{\mathrm{B}}}{\partial y} = 0. \tag{5.3}$$

For an x-invariant (Ellingsen and Palm, 1975) cross-stream perturbation, $\hat{v}'$, the solution to equation (5.3) between a time $t = t_0$ and t_1 is

$$\hat{u}' = \hat{u}'_0 - \hat{v}' \frac{\partial u_{\mathrm{B}}}{\partial y} \Delta t, \tag{5.4}$$

where $\hat{u}'$ expresses a streamwise-velocity perturbation, $\Delta t = t_1 - t_0$, $\hat{u}'_0 = \hat{u}'(t = t_0)$, and $\hat{v}' \neq \hat{v}'(t)$ under the present formulation (Ellingsen and Palm, 1975). Ellingsen and Palm (1975) state that equation (5.4) "shows that $\hat{u}'$ increases linearly with time." While the observation of Ellingsen and Palm (1975) is that in this context $\hat{u}'$ evolves algebraically (as opposed to exponentially) in time, in fact $\hat{u}'$ and hence the kinetic perturbation energy might as well decay (algebraically) in time.

This is exemplified as follows. Consider a wave-like perturbation ansatz; i.e., $\hat{u}' = \tilde{u}\mathrm{e}^{\mathrm{i}\beta_0 z} + \text{c.c.}$ and $\hat{v}' = \tilde{v}\mathrm{e}^{\mathrm{i}\beta_0 z} + \text{c.c}$, where $\tilde{u} = |\tilde{u}|\mathrm{e}^{\mathrm{i}\varphi^u}, \tilde{v} = |\tilde{v}|\mathrm{e}^{\mathrm{i}\varphi^v}$, z denotes the spanwise direction, β_0 indicates the perturbation wavenumber in the direction z, and it is assumed that $\varphi^u(t) = \varphi^u(t = t_0)$ for $t_0 \leq t \leq t_1$. Upon introducing these perturbation expressions into equation (5.4), two conditions are retrieved. Namely, $|\tilde{u}| = |\tilde{u}|_0 - \cos(\varphi^v - \varphi^u)\,|\tilde{v}|\Delta t \partial u_{\mathrm{B}}/\partial y$ and $\varphi^v - \varphi^u = 0, \pi$. Therefore, the original model of Ellingsen and Palm (1975) admits two main solutions:

$$|\tilde{u}| = |\tilde{u}|_0 + |\tilde{v}| \frac{\partial u_{\mathrm{B}}}{\partial y} \Delta t \quad (\textit{classic lift-up effect}) \tag{5.5a}$$

$$|\tilde{u}| = |\tilde{u}|_0 - |\tilde{v}| \frac{\partial u_{\mathrm{B}}}{\partial y} \Delta t \quad (\textit{reverse lift-up effect}) \tag{5.5b}$$

Ellingsen and Palm (1975) write that "we therefore deduce [from equation 5.4] that the base flow $u_{\mathrm{B}}(y)$ is unstable to this kind of infinitesimal disturbance [i.e., a prescribed cross-stream perturbation]." However, equations (5.5a) highlight that, locally in time, the flow field may be actually destabilised (i.e., signifying an increase in kinetic perturbation energy) by a *classic* lift-up effect or stabilised (i.e., signifying a decrease in kinetic perturbation energy) by a *reverse* lift-up effect to a cross-stream-velocity perturbation ($\hat{v}'$) if a streamwise-velocity perturbation ($\hat{u}'$) pre-exists.

5.3. On the stabilising or destabilising contribution of the lift-up effect at the step

Following the analysis of model problems, this section refocuses the attention to the lift-up phenomenon at the step.

5.3.1. The role of the perturbation phase

To identify the origin of the reversed action of the lift-up effect ($I_2^{\beta_0}$) at the step described in § 5.1, the following expressions are considered:

$$\kappa_2^{\beta_0} = 2 \frac{\partial u_{\mathrm{B}}}{\partial y} |\tilde{v}_t^1|_{(0,1)} |\tilde{v}_n^2|_{(0,1)} \cos\left(\varphi^{\tau}_{(0,1)} - \varphi^{v^2}_{n,(0,1)}\right), \tag{5.6}$$

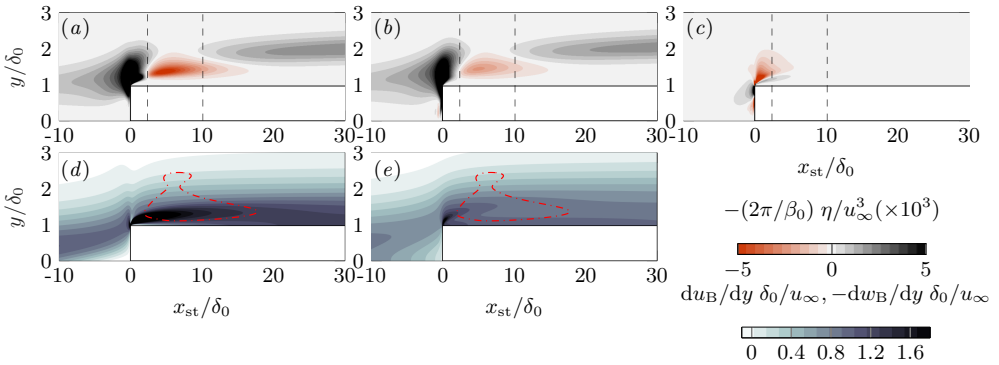

5

Figure 5.7: Spatial organisation of terms of equation (3.33): $\eta = \kappa_2^{\beta_0}$ (a), $\delta_2^{\beta_0}$ (b), and remainder (c). Dashed lines indicate the x-range of CFI kinetic energy decay, as marked by the thin solid red line in figure 4.13. Evolution of base-flow shear $\mathrm{d}u_\mathrm{B}/\mathrm{d}y$ (d) and $-\mathrm{d}w_\mathrm{B}/\mathrm{d}y$ (e) with isoline of $\Lambda_2^{\beta_0} \approx 0$ (dash-dotted red).

$$\delta_2^{\beta_0} = -2\frac{\partial w_\mathrm{B}}{\partial y}|\tilde{v}_t^3|_{(0,1)}|\tilde{v}_n^2|_{(0,1)}\cos\left(\varphi^\tau_{(0,1)} - \varphi^{v^2}_{n,(0,1)}\right), \tag{5.7}$$

namely the terms of equation (3.33) that have the largest contribution to $I_2^{\beta_0}$ (3.32) in the step case, as quantitatively demonstrated in figure 5.7 (a-c). From equation (5.6), $\kappa_2^{\beta_0}$ is conceived as the contribution to lift-up ($I_2^{\beta_0}$) by which the wall-normal shear of the base-flow u_B (with $\partial u_\mathrm{B}/\partial y > 0$) amplifies $\boldsymbol{v}_{t,(0,1)}$ in the direction x. Similarly, $\delta_2^{\beta_0}$ (5.7) expresses the contribution by which the wall-normal shear of the base-flow w_B (with $\partial w_\mathrm{B}/\partial y < 0$) amplifies $\boldsymbol{v}_{t,(0,1)}$ in the direction z.

The base-flow gradients $\mathrm{d}u_\mathrm{B}/\mathrm{d}y$ and $\mathrm{d}w_\mathrm{B}/\mathrm{d}y$ do not change sign in the flow regime dominated by the reverse lift-up effect. This is shown in figure 5.7 (d,e). A small region of flow reversal (i.e., $\mathrm{d}u_\mathrm{B}/\mathrm{d}y < 0$) downstream at the step is localised at the step apex and no significant impact of this flow structure on the presently discussed mechanism can be identified. Therefore, the sign of both $\kappa_2^{\beta_0}$ and $\delta_2^{\beta_0}$, i.e., whether they are stabilising or destabilising contributions to $I_2^{\beta_0}$, is dictated by a unique and common factor, namely $\cos(\varphi^\tau_{(0,1)} - \varphi^{v^2}_{n,(0,1)})$. The latter evaluates the relative phase between the component of the cross-stream velocity perturbation in y, *acting* on the wall-normal shears of the base flow, i.e., $\varphi^{v^2}_{n,(0,1)}$ (equation 3.29), and the streamwise-velocity perturbation component, i.e., $\varphi^\tau_{(0,1)}$ (equation 3.20). In short, the stabilising or destabilising contribution of the lift-up effect at the step is established by the relative arrangement of cross-stream- and streamwise-velocity perturbations.

To provide a conceptual model of CFI stabilisation by the step, the organisation of the fields $\boldsymbol{v}'_{t,(0,1)}$ and $\boldsymbol{v}'_{n,(0,1)}$ is examined in relation to the identified dominant factor, $\cos(\varphi^\tau_{(0,1)} - \varphi^{v^2}_{n,(0,1)})$, in equations (5.6) and (5.7). Figure 5.8 shows streamwise-velocity perturbation $\tau'_{(0,1)}$ (equation 3.13) represented by colour contour with white arrows illustrating the organisation of the counter-rotating cross-

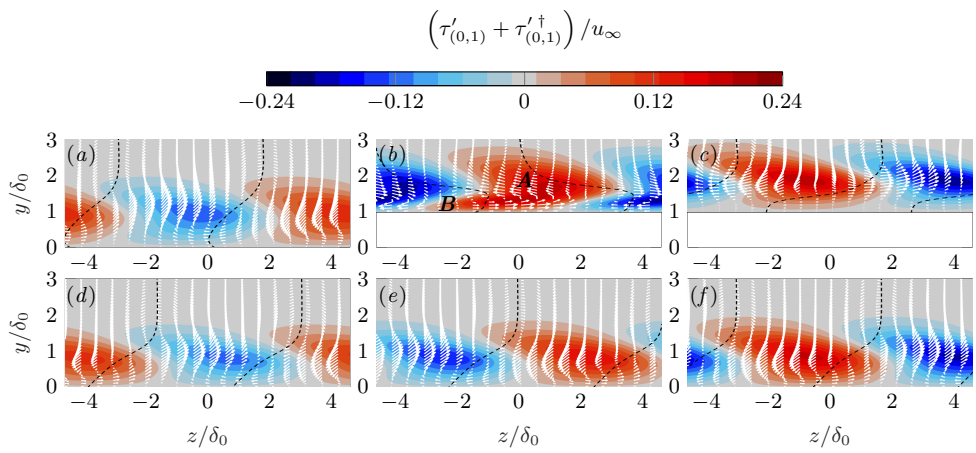

Figure 5.8: Streamwise-velocity perturbation (colour map) in y-z planes for the step (top) and reference no-step (bottom) cases at $x_{st}/\delta_0 = -10$ [(a) and (d)], 5 [(b) and (e)], 20 [(c) and (f)]. In-plane organisation of the cross-stream-velocity perturbation ($\boldsymbol{v}'_{n,(0,1)}$) depicted as white arrows. Dashed black segregates regions of perturbation upwash and downwash ($v'^2_{n,(0,1)} = \boldsymbol{v}'_{n,(0,1)}(2) = 0$).

stream perturbation ($\boldsymbol{v}'_{n,(0,1)}$) in y-z planes for the step case and the reference no-step case. Upstream of the step (figure 5.8 (a)), the perturbation behaviour qualitatively resembles reference (no-step) conditions (figure 5.8 (d-f)); that is, the action of perturbation upwash (i.e., $v'^2_{n,(0,1)} = \boldsymbol{v}'_{n,(0,1)}(2) > 0$) dominates in regions of streamwise-velocity deficit (i.e., $\tau'_{(0,1)} < 0$) and vice-versa. This interplay between perturbation components highlights the essence of the classic lift-up effect, namely the cross-stream velocity perturbations redistribute base-flow momentum by displacing low-momentum fluid upward and high-momentum fluid downward. Therefore, regions of streamwise-momentum deficit and excess are enhanced spatially. In such scenario, the cross-stream- and streamwise-velocity perturbation structures act *out-of-phase*, i.e., $|\varphi_{t,(0,1)} - \varphi^{v^2}_{n,(0,1)}| > \pi/2$, resulting in perturbation growth (as indicated by the thick solid black line in figure 4.13).

In the close vicinity of the step (figure 5.8 (b)), the perturbation organisation is altered significantly, as compared to reference (no-step) conditions at the same x-location (figure 5.8 (e)). At first glance, vigorous perturbation amplification in x is captured near the wall (region labelled as "B"). This behaviour is ascribed to the inception of newly-formed streaks close to the wall. The origin and governing mechanisms of these step-localised streaks –first reported in chapter 4 and qualitatively characterised in § 4.2.1– are examined in detail in chapter 6. Their relevance to advancing the laminar-turbulent transition is discussed in chapters 7 and 8. This present chapter focuses on the behaviour of the original CFI that develops farther from the wall (region labelled as "A").

In region "A" in figure 5.8 (b), perturbation upwash (i.e., $v'^2_{n,(0,1)} = \boldsymbol{v}'_{n,(0,1)}(2) >$

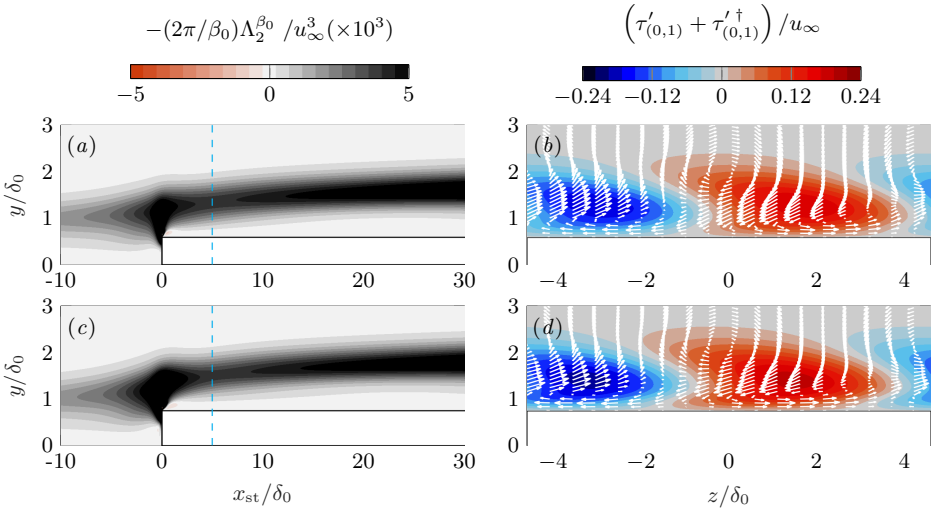

Figure 5.9: Spatial organisation of the integrand of $I_2^{\beta_0}$ in additional steps, namely step case I (a) and II (c) (see table 2.3). Corresponding behaviour of the streamwise-velocity perturbation (colour map) and in-plane organisation of the cross-stream-velocity perturbation (white arrows) at $x/\delta_0 = 5$ (indicated by dashed cyan line) for step case I (b) and II (d).

0) dominates in regions of streamwise-velocity excess (i.e., $\tau'_{(0,1)} > 0$) and vice-versa. Thus, the action of the cross-stream velocity perturbation ($\boldsymbol{v}'_{n,(0,1)}$) now weakens the incoming regions of streamwise-momentum deficit and excess and hence reduces the amplitude of $\boldsymbol{v}'_{t,(0,1)}$. Following the discussion provided in §§ 5.2.2 and 5.2.4 regarding the model problems, the cross-stream- and streamwise-velocity perturbation structures now act *in-phase*, i.e., $|\varphi^{\tau}_{(0,1)} - \varphi^{v^2}_{n,(0,1)}| < \pi/2$, and $I_2^{\beta_0} < 0$. Therefore, the process is locally stabilising and a decay of the perturbation energy in x is consequently monitored (see thin solid red line in figure 4.13). Eventually when moving further downstream of the step, the cross-stream- and streamwise-velocity perturbation structures re-organise towards undisturbed (i.e., no-step) conditions and they act *out-of-phase* again (figure 5.8 (c)).

The new near-wall perturbation rolls induced and enhanced in the step flow (white arrows in figure 5.8 (b)) take over the incoming cross-stream perturbation motion and induce locally a reverse lift-up effect by acting *against* (i.e., dampening) the incoming CFI. Based on the current analysis, these near-wall rolls accompanying the streaks at the step appear to be the main step-flow feature responsible for the CFI stabilisation reported in chapter 4.

5.3.2. Effects of step height

The model of perturbation interaction described above is applicable to steps of different height and shape. At present, this is exemplified by considering additional steps with $h/\delta_0 = 0.59$ and 0.76, i.e., step cases I and II in this thesis (see table

2.3). Both these step geometries were shown in chapter 4 to act destabilising and thus to increase the amplitude of the incoming CFI upon interaction. Conformably, here it is reported that $I_2^{\beta_0} > 0$ for all x around these additional steps, see figure 5.9 (a,c). Moreover, in line with the discussion above, the qualitative interplay between perturbation components features no-step conditions, i.e., $\boldsymbol{v}_{t,(0,1)}$ and $\boldsymbol{v}_{n,(0,1)}$ act *out-of-phase* (figure 5.9 (b,d)). In the step geometries portrayed in figure 5.9, the near-wall rolls induced at the step are significantly weaker than in the main (stabilising) step case analysed in this present chapter and, by their topology and organisation, they do not reverse the sense of energy production at the step.

It is noted that similar mechanisms have been observed in other flow problems involving streaky perturbations. For instance, Sescu and Afsar (2018) investigate the stabilisation of Görtler vortices by streamwise wall deformation, which is pointed out to be a control strategy even more efficient than an analogous blowing-suction arrangement in some cases. In words of Sescu and Afsar (2018), the role of the surface deformations is to "weaken the lift-up effect" by correspondingly accelerating and decelerating fluid particles (Sescu and Afsar, 2018). The passive control mechanism of Sescu and Afsar (2018) appears to have similarities with the perturbation phenomenon discussed in this present chapter.

5.3.3. Effects of amplitude and spanwise velocity

Step-height effects on the reversal of the sign of $I_2^{\beta_0}$ have been analysed above, albeit for fixed sweep angle and initial amplitude of incoming perturbations. This section takes a step further towards universality of reverse lift-up and discusses effects of spanwise velocity (i.e., representative of sweep-angle conditions for aircraft design) and perturbation amplitude. For this purpose, the input parameter w_∞/u_∞ (see § 2.1.1) is increased from -1.24 to -0.25 in steps of $\Delta w_\infty = 0.248$ and fixed u_∞. This corresponds to a deflection of the inviscid streamline at $x = 0$ (i.e., the local angle that it forms with the x-axis) shifted from $|51|^\circ$ to $|14|^\circ$, see table 2.5. The (changing) step-flow evolution is analysed in relation to main stabilising and destabilising mechanisms described above.

For the current analysis, a stationary perturbation is introduced via stationary blowing-suction placed upstream of the step; see § 2.1.2 for details on how modifying the parameter w_∞/u_∞ alters the nature of the incoming instability. The present choice of blowing-suction *strength*, $A_1^{\mathrm{BS}} = 1 \times 10^{-5} u_\infty$ (equation 2.23) yields weaker perturbations $\boldsymbol{v}'_{t,(0,1)}$ and $\boldsymbol{v}'_{n,(0,1)}$ than the main step case analysed above in §§ 5.1 and 5.3.1. This entails that the instability behaviour is fully linearly-dominated, to strengthen that the reverse lift-up effect is a universal linear mechanism characterised by the linear production term (§§ 3.1 and 3.3).

The latter is exemplified by figure 5.10 ($I.a$) portraying this lower amplitude case at reference free-stream conditions, i.e., $w_\infty/u_\infty = -1.24$. Namely, the spatial evolution of the integrand of $I_2^{\beta_0}$ is qualitatively identical to that of figure 5.2 (b). As expected, the interplay between cross-stream and streamwise perturbations reverses downstream of the step (figure 5.10 ($I.c, d$)), when compared to conditions upstream of the step (figure 5.10 ($I.b$)). Figure 5.10 (II-$V.a$) illustrates further that, as the parameter $|w_\infty/u_\infty|$ is decreased (see from top to bottom), the red contour vanishes

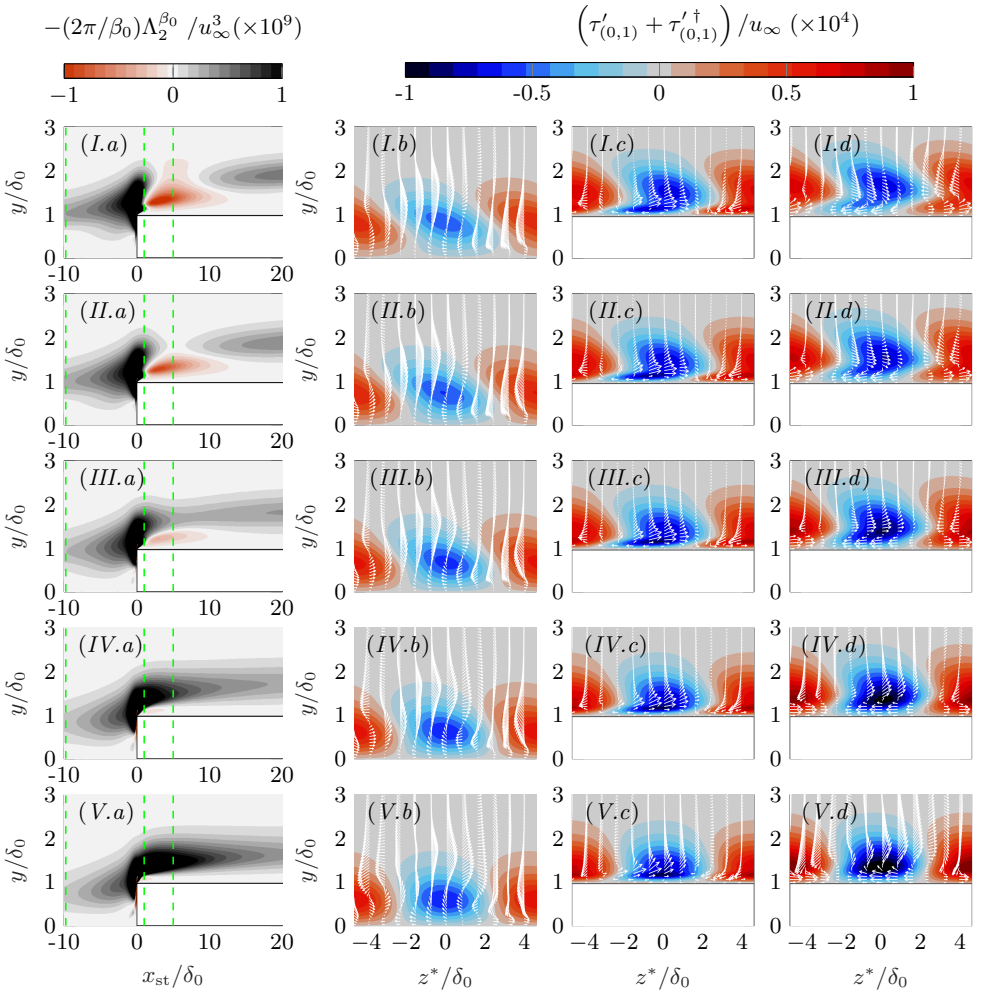

Figure 5.10: Spatial evolution of the integrand of $I_2^{\beta_0}$ (left). Streamwise-velocity perturbation (colour contour) in y-z planes at $x_{st}/\delta_0 = -10$ (b), 1 (c), 5 (d) with in-plane organisation of cross-stream-velocity perturbation (white arrows). Top to bottom illustrates cases $|w_\infty/u_\infty| = 1.24$, 0.99, 0.75, 0.50, 0.25 following table 2.5 (cases labelled as *Test*). Dotted green lines indicate $x_{st}/\delta_0 = -10$, 1, 5 and the coordinate z^* denotes spanwise shift corresponding to centered low-speed streak.

and the integrand of $I_2^{\beta_0}$ adds a positive (i.e., destabilising) contribution only. That is, for decreasing $|w_\infty/u_\infty|$, cross-stream perturbation downwash only dominates in regions of perturbation excess and vice-versa (figure 5.10 (*II*-*V*)). As a consequence, in cases with low $|w_\infty/u_\infty|$, the regions of momentum excess and deficit become more amplified than in cases with high $|w_\infty/u_\infty|$, see figure 5.10 (d). In summary, for the current fixed step height, reversal of the sign of $I_2^{\beta_0}$ sets in when a particular

threshold of $|w_\infty/u_\infty|$ is reached.

5.3.4. Discussion

To complement previous propositions, this final section elaborates on a physical model relating the reversal of the sign of $I_2^{\beta_0}$ with step-flow features. Inspection of the flow organisation reveals that the cross-stream perturbation field, $\boldsymbol{v}'_{n,(0,1)}$, develops a strong rotational motion around the axis of the newly-formed near-wall streaks at the step; i.e., the additional flow structures at the step described in § 4.2.1 and labelled as "B" in figure 5.8 (*b*). This enhancement of cross-stream perturbations around the streaks is quantitatively characterised in figure 6.3 (*b*).

Previously, Eppink (2018) reported experimentally that a new set of vortices forms in the instantaneous flow very close to the wall at the step. Key for the present discussion is that in cases with sufficiently large $|w_\infty/u_\infty|$ (i.e., top subplots in figure 5.10), the dominant rotational motion of $\boldsymbol{v}'_{n,(0,1)}$ at the near-wall streaks takes over the incoming cross-stream pattern. See white arrows in figure 5.10 (*c*,*d*), i.e., after passing the step in x, as compared to figure 5.10 (*b*).

Karp and Hack (2018) explain that streaks of sufficient amplitude embedded in convex mean-flow streamlines result in enhanced streamwise perturbation vortices (i.e., perturbation rolls) through the action of centrifugal forces. In a fashion similar to the scenario of Karp and Hack (2018), the streamlines of the flow at the step display convex curvature in the x-y plane (see figure 4.5 in § 4.1) and especially in the x-z plane (see figure 4.3 in § 4.1). The reader is additionally referred to Eppink (2020) and Rius-Vidales and Kotsonis (2021) for an experimental discussion on this flow feature. Following the analysis of Karp and Hack (2018), the presence of strongly amplified near-wall perturbation streaks (i.e., structure "B" in figure 5.8 (*b*)) in conjunction with strong convex streamline curvature, is fertile condition for enhanced cross-stream perturbation close downstream of the step. It is noted that the curvature of streamlines in the x-y plane is independent of w_∞. However, spanwise-velocity effects alter the topology and strength of near-wall rolls (figure 5.10). Under the present model, this suggests a link to streamline curvature in the x-z plane.

Finally, considering the spanwise phase of perturbation rolls induced at the step, in relation to the phase of incoming CFI, the motion of the rolls may act either *in favor* or *against* the incoming instability. That is, the convection of streamwise momentum in the cross-stream plane by the rolls either enhances ($I_2^{\beta_0} > 0$) or weakens ($I_2^{\beta_0} < 0$) the incoming streamwise-momentum deficit and excess representing the CFI. Overall, this process depends upon the local flow organisation at the step, as set by factors such as the step height (§ 5.3.2) and w_∞/u_∞ (§ 5.3.3).

6

A novel step-flow structure: near-wall streaks

Abstract: *Chapter 4 identified novel stationary velocity-perturbation streaks forming locally at the step. The present chapter explores the mechanisms of growth of these stationary streaks at the step and provides insight into their origin, nature, and spatial organisation. Stationary streaks are found to be a universal feature of swept forward-facing-step flow subjected to three-dimensional perturbations in the incoming boundary layer. The streaks at the step are primarily ascribed to the lift-up effect. They arise as a linear perturbation response of the highly sheared step flow to the cross-stream pattern of incoming perturbations. A mechanism of base-flow deceleration additionally contributes to feeding growth to the streaks. Linear stability analysis carried out through the Harmonic Navier-Stokes method confirms that the streaks are a linear perturbation phenomenon. Effects of spanwise perturbation wavelength and effective sweep angle on the mechanisms of the streaks are also assessed.*

A note on nomenclature: *This chapter focuses exclusively on stationary effects. The spanwise perturbation modes are denoted by* $\boldsymbol{v}'_{(0,j)}$*, where the prime marks perturbation,* j *is the spanwise modal index, and the zero indicates stationary behaviour. Unperturbed base-flow quantities are denoted by the subscript B, for example,* $\boldsymbol{v}_B$*.*

Parts of this chapter are published in:

- Casacuberta, J., Hickel, S., and Kotsonis, M., 2021 Mechanisms of interaction between stationary crossflow instabilities and forward-facing steps. *AIAA Paper* 2021-0854.
- Casacuberta, J., Westerbeek, S., Franco, J. A., Groot, K. J., Hickel, S., Hein, S. and Kotsonis, M., 2025 Streaky perturbations in swept-wing flow over forward-facing step. *Phys. Rev. Fluids* **10**:023902.

Chapters 4 and 5 primarily investigate how the pre-existing CFI interacts with the forward-facing step. Chapter 4 also reveals that this interaction gives rise, locally at the step, to a secondary flow structure, namely stationary velocity-perturbation streaks. The present chapter examines the origin, nature, and spatial organisation of these streaks. A focused study on the topic is motivated by the results of chapters 7 and 8, which show that the significant amplification of these streaks at the step sets the conditions for laminar-turbulent transition advancement.

First, § 6.1 qualitatively and quantitatively characterises the streak evolution at the step. Then, § 6.2 shows that the streaks are a linear non-modal perturbation of the step flow, initially driven by the lift-up effect ($I_2^{\beta_0}$) and subsequently amplified spatially by the push-forward effect ($I_4^{\beta_0}$). Finally, the influence of perturbation wavelength and effective sweep angle on the streak-amplification factor is assessed. The main flow problem investigated in this chapter corresponds to step case III (table 2.3) and *medium*-amplitude CFI conditions (table 2.4).

6

6.1. Organisation of the streaks at the step

The analysis begins by qualitatively and quantitatively characterising the evolution of the streaks at the step. Concerning the overarching subject of this chapter, stationary spanwise-harmonic velocity-perturbation streaks with wavenumbers $\beta = j\beta_0, j = 2, \ldots, N$, form and co-exist in the downstream vicinity of the step. This is claimed on noting that a streaky structure manifests in each mode of the spanwise Fourier decomposition of the stationary perturbation field (1.8). Topologically, the streaks appear as alternating regions of velocity excess and deficit distributed along the step-edge direction, z. They develop spatially very close to the wall and underneath the pre-existing CFI that develops farther from the wall. A main goal of this chapter is to explore the origin and evolution of the streaks at the step; to isolate pertinent effects, a distinction is made between streaks manifesting in the fundamental, i.e., $j = 1$ in equation (1.8), and high-order harmonic, i.e., $j \geq 2$ in equation (1.8), perturbation modes. For simplicity, the main body of the discussion focuses first on fundamental streaks. Later on, in § 6.2.4, mechanisms of the perturbation streaks of higher order will be discussed.

Figure 6.1 portrays the three-dimensional organisation of the fundamental velocity-perturbation fields, $u'_{(0,1)}$, $w'_{(0,1)}$, and $v'_{(0,1)}$ at the step. As described in § 4.2.1, for all velocity components, the main structure of the incoming CFI lifts off the wall gradually as it approaches the step; see also § 4.1 providing a discussion on the corresponding three-dimensional organisation of the base-flow streamlines at the step. Just after passing the upper step corner, the near-wall portion of the stationary perturbation field is amplified significantly (Tufts et al., 2017; Eppink, 2020), when compared to conditions far upstream of the step, see figure 6.1. The present results show that this effect manifests more prominently in the chordwise-velocity component, $u'_{(0,1)}$, than in the other velocity components ($v'_{(0,1)}$ and $w'_{(0,1)}$): strongly amplified oval-shaped $u'_{(0,1)}$-streaks located underneath the incoming CFI are evident in figure 6.1 (*a*).

For the choice of step height and strength of the incoming CFI considered in this chapter, namely step case III in table 2.3 and *medium*-amplitude CFI conditions in

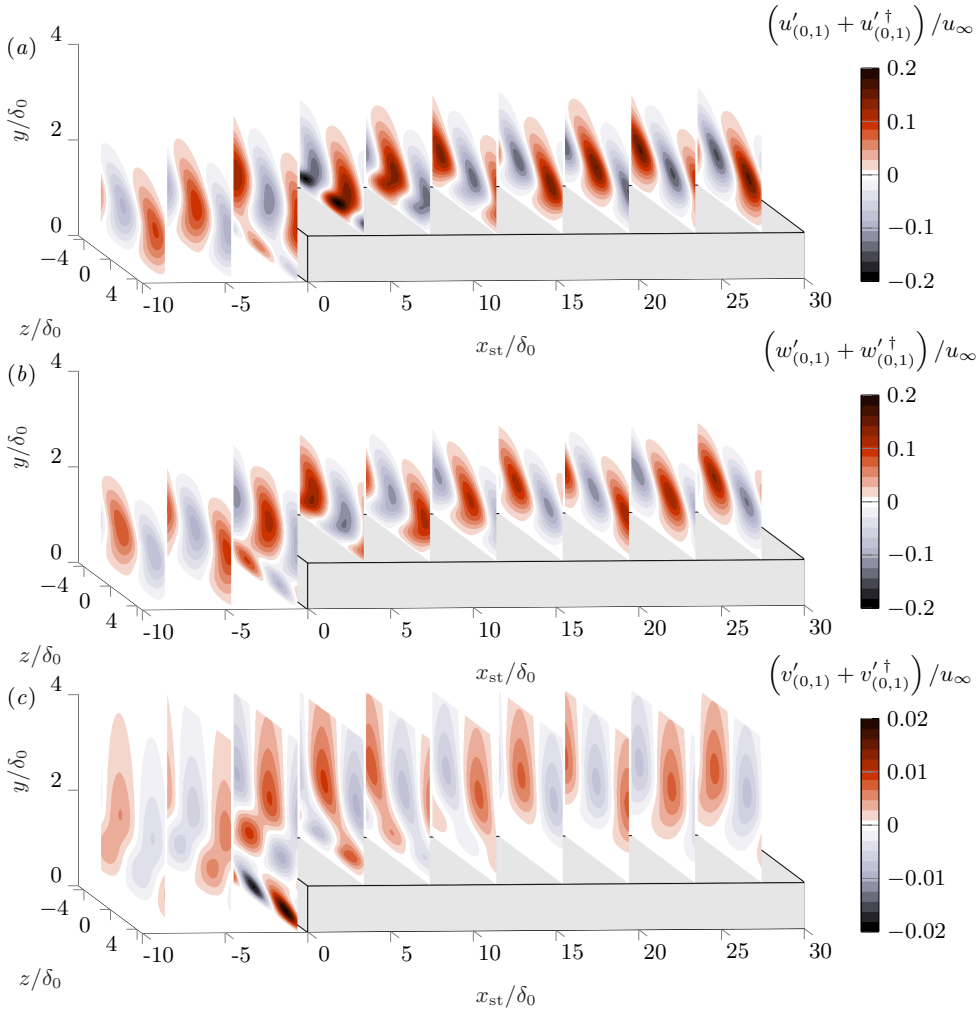

FIGURE 6.1: Organisation of the chordwise (a), spanwise (b), and wall-normal (c) fundamental velocity-perturbation fields ($\beta = \beta_0$). Note the different scale in plot (c).

table 2.4, the amplitude of near-wall streaks forming at the step decays downstream in x, with the streaks ultimately vanishing (figure 6.1 (a)). It is noted that near-wall velocity-perturbation streaks form as well in the upstream vicinity of the step, see figure 6.1. However, they appear to originate independently from the streaks downstream of the step, as they mainly reside in the locally separating flow upstream of the step. The focus of this present chapter is specifically placed on the streaky structures forming downstream of the step, where premature laminar-turbulent transition originates, as will be seen in chapter 8.

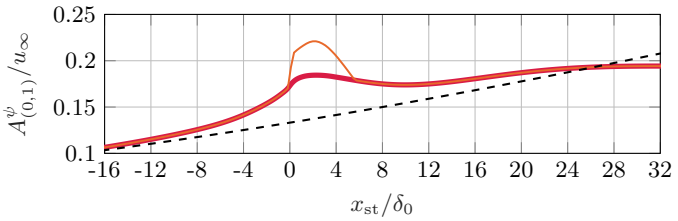

FIGURE 6.2: Chordwise evolution of perturbation *amplitude* (§ 2.1.1): $A^{\psi}_{(0,1)} = |\tilde{\psi}|^{\max}_{(0,1)}$ in the step (thin solid orange) and reference no-step (thin dashed black) cases, $A^{\psi}_{(0,1)} = |\tilde{\psi}|^{\mathrm{top}}_{(0,1)}$ in the step case (thick solid red).

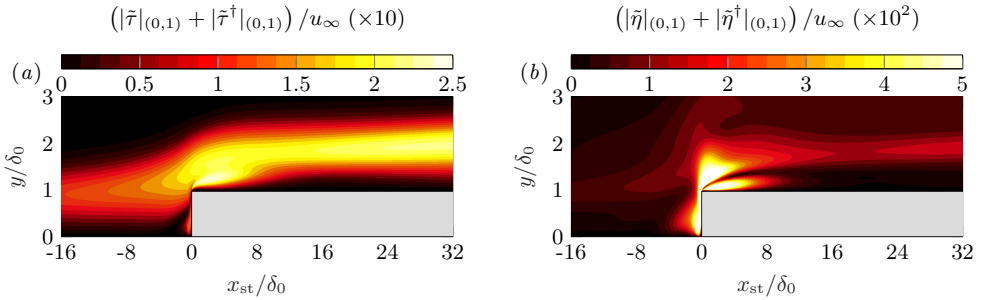

FIGURE 6.3: Amplitude function of (*a*) streamwise, $|\tilde{\tau}|_{(0,1)}$, and (*b*) cross-stream, $|\tilde{\eta}|_{(0,1)}$, velocity perturbations, both considering fundamental perturbations with $\beta = \beta_0$.

The streaks are generated locally at the upper step corner, develop spatially very close to the wall, and co-exist in y with the incoming CFI, which makes their quantitative characterisation particularly challenging. Moreover, as shown in § 4.2.3, the different velocity-perturbation components exhibit different growth rates in x in the vicinity of the step. Therefore, to assess streak amplification at the step in a *global* exploratory sense, perturbation growth is first evaluated based on the norm of the *total* perturbation vector, i.e., $|\tilde{\psi}|_{(0,1)}$ (1.9). Figure 2.6 in § 2.1.1 illustrates the evolution of $|\tilde{\psi}|_{(0,1)}$ alongside key step-flow features, including the recirculating-flow regions and the loci of base-flow crossflow inflection points.

Tufts et al. (2017) report that the perturbation shape (i.e., the profile along y) develops a secondary peak after passing the step in x. This feature is also observed in the results of this thesis, both in the chordwise-velocity perturbation (figure 4.8 in § 4.2) and in the *total* perturbation (see figure 2.6 in § 2.1.1). This thesis interprets the near-wall secondary peak as the manifestation of the streaks in the spanwise Fourier coefficient (1.8). Following the discussion in § 4.2, to distinguish streak amplification from the evolution of the original CFI, amplitudes are monitored at two wall-normal locations: the lower (near-wall) peak quantifies streak growth, while the upper peak

tracks the incoming CFI. Figure 6.2 illustrates these growth metrics, evaluated at the wall-normal locations marked by circles in figure 2.6 in § 2.1.1.

Since the secondary peak in the perturbation shape surpasses the primary one locally around the step, *amplitude* measured at the wall-normal location dominated by the streaks is larger than *amplitude* measured at the wall-normal location dominated by incoming CFI (figure 6.2). Consequently, estimating instability amplification by the global maximum of the perturbation profile in y inherently characterises growth of the near-wall streaks just downstream of the step, but growth of the CFI farther from it.

Finally, figure 6.3 displays the imprint of the streaks on the streamwise- (a) and cross-stream- (b) velocity perturbation components. The structural identification of the streaks at the upper step corner, see figure 6.1, is consistent with the rapid amplification in x of the streamwise-velocity perturbation at that location (figure 6.3 (a)). Moreover, as discussed in § 5.3.4, this amplification is accompanied by growth of the cross-stream perturbation component, which figure 6.3 (b) quantitatively confirms.

6.2. Origin and nature of the streaks at the step

This section discusses the mechanisms that drive the growth and initial development of the streaks and whether to classify it as a modal or a non-modal instability. The focus of §§ 6.2.1, 6.2.2, and 6.2.3 is exclusive to the streaks of fundamental wavelength. In § 6.2.4, the analysis is extended to streaks of high-order harmonic wavelength.

6.2.1. The role of the lift-up effect

The origin of the streaks at the step is investigated by use of the production term of the Reynolds-Orr equation (see §§ 3.1 and 3.3). Specifically, the evolution in x of $(-2\pi/\beta_0)\Lambda_{\beta_0}$ (3.30) and $(-2\pi/\beta_0)\Lambda_m^{\beta_0}, m =$ 1-4, (3.32) all probed at $y = \tilde{y}_{(0,1)}^{\psi,\mathrm{str}}$ (see § 2.1.1), is shown in figure 6.4. This probing coordinate corresponds to the wall-normal location of the *core* of the streaks, i.e., linked to the secondary peak in the perturbation shape $|\tilde{\psi}|_{(0,1)}$ at the step (indicated by small magenta circles in figure 2.6 (a) in § 2.1.1). Inspection of the spatial evolution of terms $(-2\pi/\beta_0)\Lambda_m^{\beta_0}, m =$ 1-4, provides insight into the location and *strength* of the associated mechanisms. Their sign informs whether kinetic energy is transferred from the base flow to the perturbation field, i.e., $(-2\pi/\beta_0)\Lambda_m^{\beta_0} > 0$, or vice-versa, i.e., $(-2\pi/\beta_0)\Lambda_m^{\beta_0} < 0$. This applies identically to production itself, i.e., $(-2\pi/\beta_0)\Lambda_{\beta_0}$.

Figure 6.4 shows that production (thick solid black line) grows rapidly in x close downstream of the step, where the streaks first appear, and reveals that the increase of production is driven mainly by $I_2^{\beta_0}$ (dashed red line), i.e., the lift-up effect. To elaborate further on this dominant role played by the mechanism of $I_2^{\beta_0}$, figure 6.5 (a) additionally illustrates the spatial organisation of its integrand (3.33) superimposed on the projected base-flow streamlines in the x-y plane; the latter represents identically figure 4.5 in § 4.1.2. The corresponding three-dimensional organisation of streamlines at the step is depicted in figure 4.3. Two main destabilising flow regimes (i.e., with $(-2\pi/\beta_0)\ \Lambda_2^{\beta_0} > 0$) develop at the step, see labels "A" and "B" in figure 6.5 (a). Regime "A" is associated to the new near-wall streaks incepted close

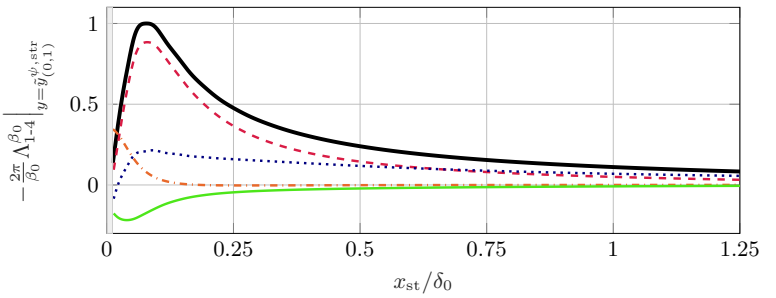

FIGURE 6.4: Chordwise evolution of production terms (3.31) at the wall-normal location of the core of streaks: $\Lambda_1^{\beta_0}$ (dash-dotted orange), $\Lambda_2^{\beta_0}$ (dashed red), $\Lambda_3^{\beta_0}$ (thin solid green), $\Lambda_4^{\beta_0}$ (dotted blue), and Λ_{β_0} (thick solid black). All curves are normalised relative to maximum Λ_{β_0}.

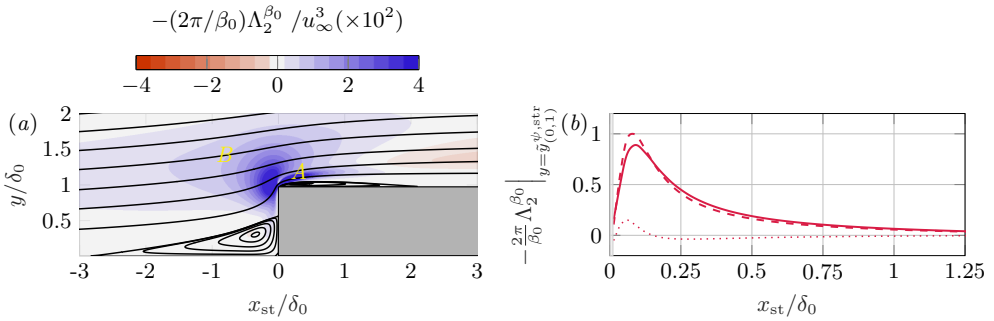

FIGURE 6.5: Spatial evolution of $(-2\pi/\beta_0)\Lambda_2^{\beta_0}$ (3.33) with streamlines of the base flow (a) and chordwise evolution of individual terms of equation (3.33) at the wall-normal location of the core of the streaks (b): $(-2\pi/\beta_0)\kappa_2^{\beta_0}$ (solid, see equation (5.6)), remainder (dotted), global term $(-2\pi/\beta_0)\Lambda_2^{\beta_0}$ (dashed). All curves are normalised relative to maximum $\Lambda_2^{\beta_0}$.

downstream of the step, while regime "B" is mainly linked to the amplification of the incoming CFI as it approaches the step, a feature quantitatively characterised in § 4.2.2.

In regime "A" of figure 6.5 (a), the term $\kappa_2^{\beta_0}$ in equation (3.33) –further expanded in equation (5.6)– is the main contribution to $\Lambda_2^{\beta_0}$ and thus *drives* the action of the lift-up effect. This is quantitatively demonstrated in figure 6.5 (b) evaluating individual terms of equation (3.33) at $y = \tilde{y}_{(0,1)}^{\psi,\mathrm{str}}$. The term $\kappa_2^{\beta_0}$ (5.6) may be interpreted as the vertical (i.e., pointing in y) perturbation by the cross-stream pattern ($\boldsymbol{v}_n'$) acting on the base-flow shear $\partial u_{\mathrm{B}}/\partial y$ and feeding growth to the streamwise-velocity perturbation ($\boldsymbol{v}_t'$) in x. The dominant influence of $\kappa_2^{\beta_0}$ at the step reconciles with the perturbation behaviour illustrated in figure 6.1 above, when it is examined through a classic wall-oriented perturbation decomposition, as characterised by equation (1.13).

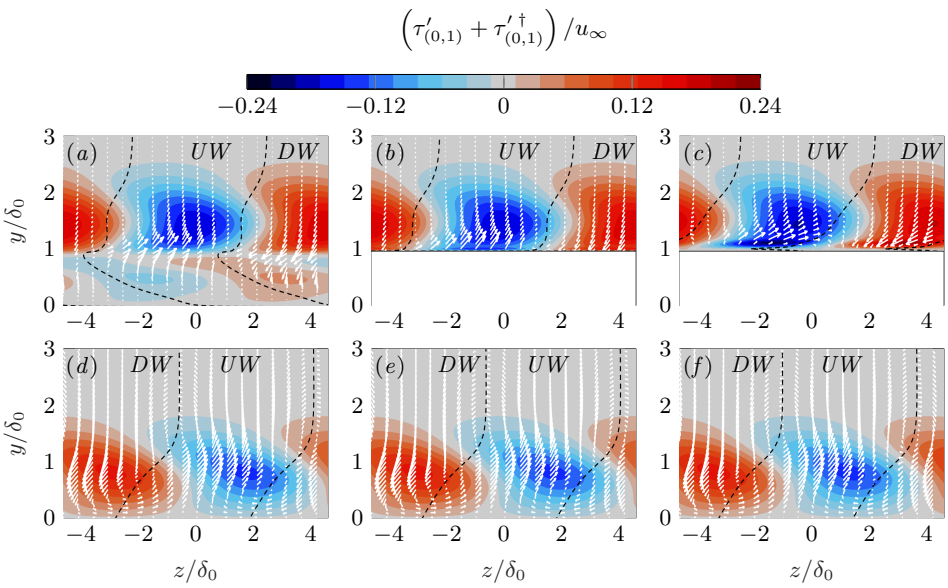

Figure 6.6: Streamwise-velocity perturbation (colour contour) in y-z planes for the step (top) and reference no-step (bottom) cases at $x_{\mathrm{st}}/\delta_0 = -0.02$ [(a) and (d)], 0.04 [(b) and (e)], 0.52 [(c) and (f)]. In-plane organisation of the cross-stream-velocity perturbation (white arrows). Dashed lines segregate cross-stream-perturbation upwash (label UW) and downwash (label DW).

That is, the perturbation component parallel to the wall and aligned with x, $u'_{(0,1)}$, manifests more prominently than the component aligned with z, $w'_{(0,1)}$ (figure 6.1). The resulting streaks at the step are initially aligned with the x-direction, because the lift-up effect favours the amplification of the streamwise-oriented perturbation component (Marxen et al., 2009) and the base-flow streamlines at the step bend vigorously towards the x-direction, see figure 4.3 (b,d).

Finally, it is instructive to visualise the arrangement of streaks at the step induced by the lift-up effect as shown in figure 6.6. Specifically, figure 6.6 illustrates the perturbation organisation in y-z planes in the step (top) and no-step (bottom) cases at same (increasing) x-positions. Figure 6.7 complements figure 6.6 by adding the unperturbed base flow; i.e., $||\boldsymbol{v}_{\mathrm{B}}|| + (\tau'_{(0,1)} + \tau'^{\dagger}_{(0,1)})$, where $||\boldsymbol{v}_{\mathrm{B}}||$ is the modulus of the local base-flow vector. In short, figure 6.7 expresses the velocity of the steady perturbed flow (2.10) in the local streamline direction. In the presence of the step, the incoming crossflow vortices lift off the wall as they approach the step in x. In a perturbation sense, the highly-energetic $\boldsymbol{v}'_t$-structures correspondingly shift upward significantly in the upstream vicinity of the step, see colour contours in figure 6.6 (a) representing $x_{\mathrm{st}}/\delta_0 = -0.02$, when compared to reference conditions (figure 6.6 (d)). It is noted that figure 6.6 illustrates the scalar perturbation associated to $\boldsymbol{v}'_{t,(0,1)}$, namely $\tau'_{(0,1)}$ (3.13).

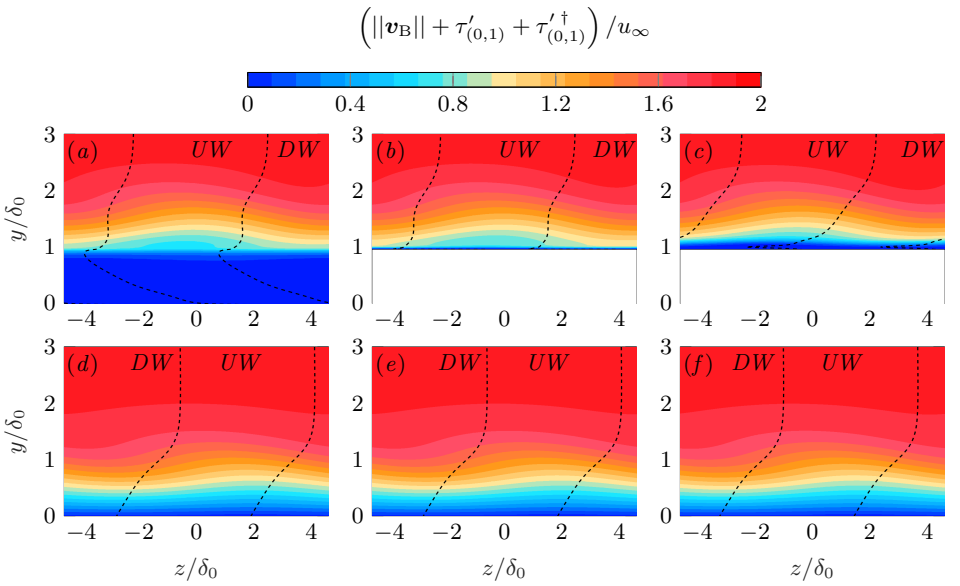

FIGURE 6.7: Steady total streamwise flow (colour contour), in y-z planes for the step (top) and reference no-step (bottom) cases at $x_{st}/\delta_0 = -0.02$ [(a) and (d)], 0.04 [(b) and (e)], 0.52 [(c) and (f)]. Dashed lines segregate cross-stream-perturbation upwash (label UW) and downwash (label DW), see figure 6.6.

However, the cross-stream perturbation pattern $\boldsymbol{v}'_{n,(0,1)}$ maintains a dominant contribution at a similar location to reference (no-step) conditions, i.e., at approximately $y/\delta_0 \approx 1$. The *strength* of $\boldsymbol{v}'_{n,(0,1)}$ is characterised by the length of white arrows in figure 6.6. At the same time, the base flow at the step is highly sheared, see figure 4.2. This combination of effects sets the conditions for the *weak* cross-stream perturbation to effectively displace low-momentum fluid upward and high-momentum fluid downward at the upper step corner and thus give rise to rapidly-amplified streamwise streaks of alternating sign in z (figure 6.6 (b,c)). Specifically in unswept (i.e., two-dimensional) forward-facing-step flow in a channel, Wilhelm et al. (2003) similarly report that even very small incoming perturbations, namely less than 1% of the mean-flow velocity, produce noticeable streaky structures at the step. The multiple similarities between both studies suggests that the streaks are a linear perturbation of forward-facing-step flow that develops as a "sensitive reaction to incoming perturbations" (Wilhelm et al., 2003).

6.2.2. THE ROLE OF THE PUSH-FORWARD EFFECT

The lift-up effect plays a pivotal role in the inception of streaks at the step. However, the results of figure 6.4 indicate that the push-forward mechanism, $I_4^{\beta_0}$ (3.35), contributes as well to energy production, P_{β_0} (3.30), at the streaks location. Even more

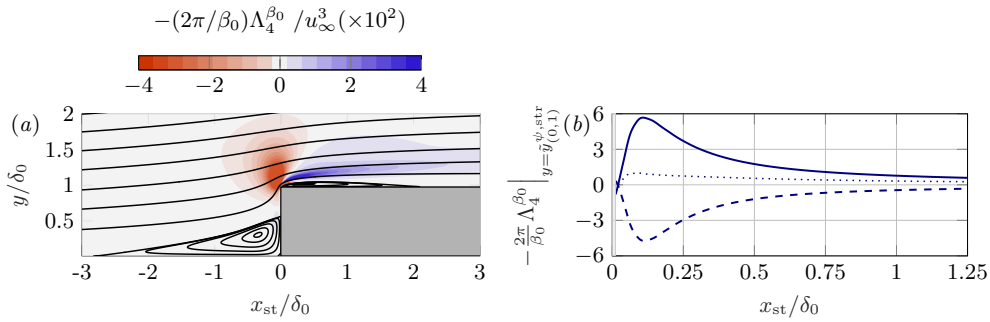

Figure 6.8: Spatial evolution of $(-2\pi/\beta_0)\Lambda_4^{\beta_0}$ from equation (6.1) with streamlines of the base flow (a) and chordwise evolution of individual terms of equation (6.1) at the wall-normal location of the core of the streaks (b): $(-2\pi/\beta_0)\chi_4^{\beta_0}$ (solid), sum of remainder (dashed), global term $(-2\pi/\beta_0)\Lambda_4^{\beta_0}$ (dotted). All curves are normalised relative to $\max(\Lambda_4^{\beta_0})$.

so, the contribution of $I_4^{\beta_0}$ (dotted blue in figure 6.4) surpasses that of $I_2^{\beta_0}$ (dashed red in figure 6.4) eventually in x. As previously mentioned, the mechanism of $I_4^{\beta_0}$ may be understood as a self-induction effect of the field $\boldsymbol{v}_t'$ onto itself. That is, the streamwise-velocity perturbation displaces base-flow momentum in the direction of the perturbation and hence inherits some of its energy.

This is expanded upon in the following manner: figure 6.8 (a) depicts the spatial evolution of the integrand of $I_4^{\beta_0}$ (3.35), $(-2\pi/\beta_0)\Lambda_4^{\beta_0}$, with

$$\begin{aligned}\Lambda_4^{\beta_0} = &\left(\tilde{v}_t^1\ \tilde{v}_t^{1\dagger} + \text{c.c.}\right)\frac{\partial u_\mathrm{B}}{\partial x} + \left(\tilde{v}_t^1\ \tilde{v}_t^{2\dagger} + \text{c.c.}\right)\frac{\partial u_\mathrm{B}}{\partial y} + \left(\tilde{v}_t^2\ \tilde{v}_t^{1\dagger} + \text{c.c.}\right)\frac{\partial v_\mathrm{B}}{\partial x} \\ &+ \left(\tilde{v}_t^2\ \tilde{v}_t^{2\dagger} + \text{c.c.}\right)\frac{\partial v_\mathrm{B}}{\partial y} + \left(\tilde{v}_t^3\ \tilde{v}_t^{1\dagger} + \text{c.c.}\right)\frac{\partial w_\mathrm{B}}{\partial x} + \left(\tilde{v}_t^3\ \tilde{v}_t^{2\dagger} + \text{c.c.}\right)\frac{\partial w_\mathrm{B}}{\partial y},\end{aligned} \tag{6.1}$$

where the subscript $(0,1)$ has been removed for conciseness. A prominent region of $(-2\pi/\beta_0)\ \Lambda_4^{\beta_0} > 0$ develops close downstream of the step, see figure 6.8 (a), and figure 6.8 (b) quantitatively demonstrates that the term

$$\chi_4^{\beta_0} = \left(\tilde{v}_{t,(0,1)}^1 \tilde{v}_{t,(0,1)}^{1\dagger} + \text{c.c.}\right)\frac{\partial u_\mathrm{B}}{\partial x} = 2|\tilde{v}_{t,(0,1)}^1|^2 \frac{\partial u_\mathrm{B}}{\partial x} \tag{6.2}$$

in equation (6.1) has the largest contribution to $I_4^{\beta_0}$ in this region. Based on the main criterion followed above, figure 6.8 (b) evaluates individual terms of equation (6.1) at the wall-normal location of the streaks, i.e., at $y = \tilde{y}_{(0,1)}^{\psi,\mathrm{str}}$ (§ 2.1.3).

From equation (6.2) and the results of figure 6.8 (b), it may be concluded that the stabilising or destabilising contribution of $I_4^{\beta_0}$ at the step is dictated essentially by whether the base-flow velocity u_B accelerates or decelerates in x. If the base flow decelerates, i.e., $\partial u_\mathrm{B}/\partial x < 0$, then $\chi_4^{\beta_0} < 0 \Rightarrow I_4^{\beta_0} > 0$, implying that kinetic energy is transferred from the base flow to the perturbation field and the process

is locally destabilising. The inverse holds true if the base flow accelerates in x, i.e., $\partial u_\mathrm{B}/\partial x > 0 \Rightarrow I_4^{\beta_0} < 0$. In § 4.1, it is shown that the pressure gradient around the step carries local flow acceleration (i.e., $\partial u_\mathrm{B}/\partial x > 0$) close upstream of the step, which is immediately followed in x by local flow deceleration (i.e., $\partial u_\mathrm{B}/\partial x < 0$) close downstream of the step. In conformity with this description, the mechanism of $I_4^{\beta_0}$ acts first stabilising and then destabilising as the perturbation ascends the step apex, see figure 6.8 (a).

Following this rationale, the inception of energetic streamwise streaks just downstream of the step, embedded in a locally decelerating boundary layer in x, activates the mechanism of $I_4^{\beta_0}$. In combining the observations from § 6.2.1 and the current section, the initial inception of near-wall streaks at the step is mainly ascribed to the lift-up effect, but their subsequent amplification in x is driven by a combination of lift-up, $I_2^{\beta_0}$, and push-forward, $I_4^{\beta_0}$. Lanzerstorfer and Kuhlmann (2012) report as well a non-negligible contribution of the mechanism of $I_4^{\beta_0}$ on streaks in unswept forward-facing-step flow albeit with a major difference noted with the present investigations. In the aforementioned work, the authors state that the perturbation streaks are self-sustained by a feedback of the recirculating flow on the upper wall of the step. For the case considered in this thesis, recirculating flow is present at the step as well (see § 4.1.2), however, the streaks are sustained by the pre-existing CFI influencing the step flow.

6.2.3. Modal and non-modal growth of streaks

This section examines whether the presently discussed near-wall streaks that form at the step are the result of modal or non-modal instability. It is well established that non-modal growth driven by the lift-up effect, typically manifests as rapidly-formed streamwise streaks. However, the lift-up effect plays a role as well in other perturbation systems such as Görtler instability, see the discussion by Marxen et al. (2009). As noted by Floryan and Saric (1982) and Floryan (1986), Görtler instability exhibits a *very weak cellular motion* in the cross-stream plane, where the streamwise-velocity perturbation correspondingly originates from a *defect in the mean flow* due to the convection of streamwise momentum by the cross-stream vortex-like motion.

In previous work, Görtler instability has been suggested as the mechanism behind near-wall streaky structures in two-dimensional (Chiba et al., 1995) and three-dimensional (Rius-Vidales and Kotsonis, 2022), forward-facing-step flow. Next to it, an instability of inflectional crossflow type (Eppink, 2020) and spatial non-modal growth are additional candidates for the amplification of streaky structures at the step. To segregate between modal and non-modal effects at the step, the methodology of Marxen et al. (2009) is followed in this section. Marxen et al. (2009) decompose the velocity-perturbation vector into components tangential and normal to the local orientation of base-flow streamlines. That is, the velocity-perturbation vector is decomposed in the local streamwise and cross-stream directions, as formulated in equation (3.12) in this thesis. In the case of purely modal growth, all velocity components ought to display a similar spatial growth rate, implying the existence of a single (growing or decaying) perturbation *eigenmode* (Marxen et al., 2009).

It is noted that in non-parallel flow this can only be attained approximately,

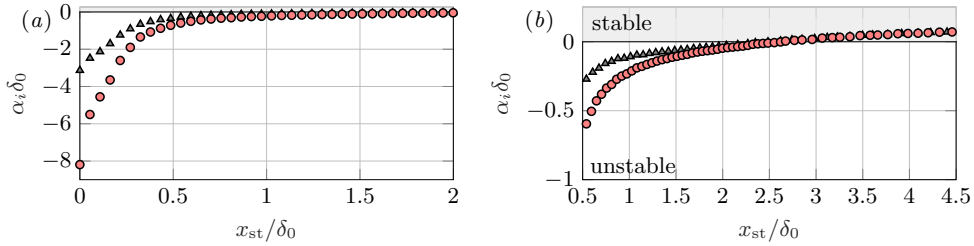

Figure 6.9: Spatial growth rates of the total, $|\tilde{\psi}|_{(0,1)}$ (triangles), and streamwise, $|\tilde{\tau}|_{(0,1)}$ (circles), perturbations at the wall-normal location of streaks, $y = \tilde{y}^{\psi,\mathrm{str}}_{(0,1)}$, in the ranges $0 \leq x_{\mathrm{st}}/\delta_0 \leq 2$ (a) and $0.5 \leq x_{\mathrm{st}}/\delta_0 \leq 4.5$ (b).

inasmuch as the different velocity components corresponding to a modal instability mechanisms display minor differences, see Saric (1975), Bertolotti et al. (1992, cf. § 4.1), and Gaster (2000). However, in the case of non-modal growth by the lift-up effect, the amplification of the streamwise-aligned perturbation component is significantly favored over its cross-stream counterpart and the growth rate of one component can be an order of magnitude larger than another, or even of opposite sign (i.e., one component growing while the other component decays).

The evolution of perturbation growth rates in x –evaluated following the definition given in equation (2.12)– in the near-wall step flow is illustrated in figure 6.9. Red circles characterise the growth rate of the streamwise-velocity perturbation, $\boldsymbol{v}'_{t,(0,1)}$, i.e., based on the amplitude function $|\tilde{\tau}|_{(0,1)}$ (3.23), and black triangles characterise the growth rate of the perturbation vector itself, $\boldsymbol{v}'_{(0,1)}$, i.e., based on the amplitude function $|\tilde{\psi}|_{(0,1)}$ (1.9). Both amplitude functions are measured at a common wall-normal position associated to the streaks, $y = \tilde{y}^{\psi,\mathrm{str}}_{(0,1)}$ (§ 2.1.3). Initially from $x_{\mathrm{st}} = 0$ (representing the step corner where the streaks are first incepted), the evolution of growth rates in figure 6.9 differs considerably. The significantly larger spatial growth rate (in absolute value) of $\boldsymbol{v}'_{t,(0,1)}$, when compared to $\boldsymbol{v}'_{(0,1)}$, implies that growth of streamwise perturbations is favored over cross-stream perturbations. Following the discussion of Marxen et al. (2009), this is an imprint of spatial non-modal growth produced by the convection of streamwise momentum in the cross-stream plane through *lift-up* (§ 6.2.1), which cannot be described by an individual perturbation eigenmode inherent to the step-flow profiles in this case. The growth rate of the streamwise-velocity perturbation being larger than that of the perturbation itself in turn implies that the cross-stream perturbation locally decays in space while inducing the streamwise streaks at the step.

6.2.4. Co-existence of high-order harmonic streaks at the step

The main discussion thus far has revolved around mechanisms of the fundamental, $\beta = \beta_0$, streaks. However, as mentioned above, the streaks of fundamental wavenum-

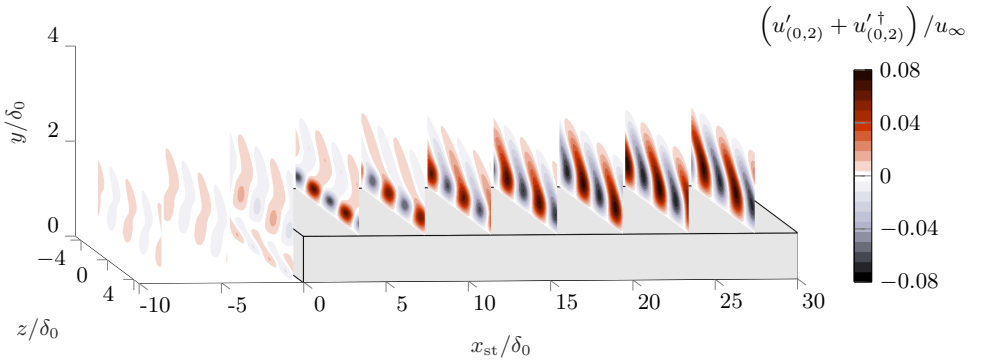

FIGURE 6.10: Organisation of the chordwise velocity-perturbation field with $\beta = 2\beta_0$.

ber co-exist at the step with streaks of higher-order harmonic wavenumber, $\beta > \beta_0$. The origin of the latter is the focus in this section.

In the numerical procedure of this thesis, a stationary crossflow eigenmode with $\beta = \beta_0$ is prescribed at the inflow (§§ 2.1.1 and 2.2.1). Gradually in x, high-order harmonic components of the CFI with $\beta = j\beta_0, j = 2, \ldots, N$ amplify spatially due to non-linear perturbation interactions. When approaching the step in x, all incoming harmonics lift off the wall and pass over the step. Near-wall velocity-perturbation streaks are induced locally at the upper step corner, which manifest at spanwise perturbation wavenumbers of $\beta = j\beta_0, j = 2, \ldots, N$, hence they are contained in each spanwise perturbation mode (1.8). This organisation of streaks was illustrated in figure 6.1 (*a*) above for mode $\beta = \beta_0$ and it is here depicted for mode $\beta = 2\beta_0$ in figure 6.10; the latter is representative of the behaviour of perturbations with $\beta > 2\beta_0$.

Next, the methodology of § 6.2.1 characterising the lift-up effect is reproduced for streaks with $\beta > \beta_0$. It is found that the production terms $I_2^{j\beta_0}$ add the dominant energy contribution (versus $I_1^{j\beta_0}$, $I_3^{j\beta_0}$, $I_4^{j\beta_0}$) for all high-order harmonic perturbation fields, $\boldsymbol{v}'_{(0,j)}$ with $j \geq 2$. Inspection of the flow organisation reveals that, similarly to the fundamental spanwise perturbation mode, the cross-stream pattern $\boldsymbol{v}'_{n,(0,j)}$ of each incoming high-order spanwise perturbation mode displaces low-momentum fluid upward and high-momentum fluid downward on interaction with the step flow. Consequently, spanwise-alternating regions of streamwise-momentum deficit and excess form near the wall in a short span of space, which manifest as rapidly-formed streamwise streaks in the corresponding field $\boldsymbol{v}'_{t,(0,j)}$.

In conclusion, if multiple harmonic stationary perturbations co-exist upstream of the step, then corresponding streaky structures will be induced at the step at respective spanwise wavelengths. The streak formation appears to be governed linearly for each incoming mode, individually; to be noted, the initial spanwise phase of the newly-formed streaks is inherently set by the modal non-linear arrangement of harmonic modes upstream of the step. Chapter 7 elaborates upon the fact that, when

moving further downstream of the step, subsequent non-linear interaction among the fundamental and high-order harmonic streaky structures takes places under certain conditions. Specifically, chapter 7 shows that, whether non-linear streak interaction takes place at the step, is contingent upon the amplitude of the incoming CFI. This non-linear mechanism appears to dictate whether the near-wall streaks are sustained or vanish further downstream of the step.

6.2.5. Effect of spanwise velocity

The discussion in the previous sections has explored the origin and non-modality of the streaks. A heuristic experiment is performed next to further confirm that the streaks at the step cannot be supported as an additional (modal) crossflow instability of the inflectional step-flow profiles. The input parameter w_∞/u_∞ (§ 2.1.1), which is proportional to the global sweep angle governing the flow, is increased gradually in small steps of Δw_∞ for fixed u_∞; the approach discussed next is largely similar to that employed in § 5.3.3. For a purely two-dimensional base flow, $w_\infty/u_\infty = 0$, the crossflow-velocity profile vanishes. In this scenario CFI is not tenable and thus, if streaks manifest, they may not be ascribed to CFI. The flow cases discussed in this section are labelled as *Test A-F* in table 2.5.

The organisation of the perturbation field at the step is shown in figure 6.11 for decreasing $|w_\infty/u_\infty|$ (top to bottom). The planes in the top row illustrate *Test A* in table 2.5, i.e., $\max(|w_\infty/u_\infty|)$, which corresponds identically to the free-stream conditions of the main case discussed in §§ 6.1 and 6.2 in this chapter. The planes in the bottom row characterise *Test F* in table 2.5, i.e., $w_\infty/u_\infty = 0$, which corresponds to a purely two-dimensional base flow. The results of figure 6.11 (*left* and *right*) highlight that a region of additional perturbation amplification at the upper step corner manifests in all cases. Figure 6.11 (*centre*) additionally depicts the perturbation field upstream of the step for reference. The corresponding three-dimensional organisation of the perturbation planes of figure 6.11 is shown in figures A.3 and A.4 in appendix A. Overall, these results confirm the universal existence and structural similarities of stationary perturbation streaks at the step for the full range of tested spanwise velocities. Streaks manifest in unswept and low-sweep-angle conditions, hence evidence is provided that they are not an additional (modal) crossflow instability.

6.2.6. The streaks as a linear perturbation phenomenon

In the section below (§ 6.2.7), effects of spanwise wavelength on the mechanisms of the streaks at the step are assessed through linear stability analysis. Parametric studies of incoming instability specifications, as well as other critical parameters such as the Reynolds number, require efficient simulation tools. The PSE approach or the Orr-Sommerfeld equation (see § 2.2.3) are classic methods for efficient stability calculations. However, these methods suffer from limitations in highly non-parallel flow such as the present step flow; see also the discussion on non-modal growth effects at the step in §§ 4.2.3 and 6.2.3.

To overcome these aforementioned limitations, the Harmonic Navier-Stokes (HNS) method is employed in this chapter to assess the stability of the step flow. The HNS is an efficient approach to instability modelling considering the full form of Navier-

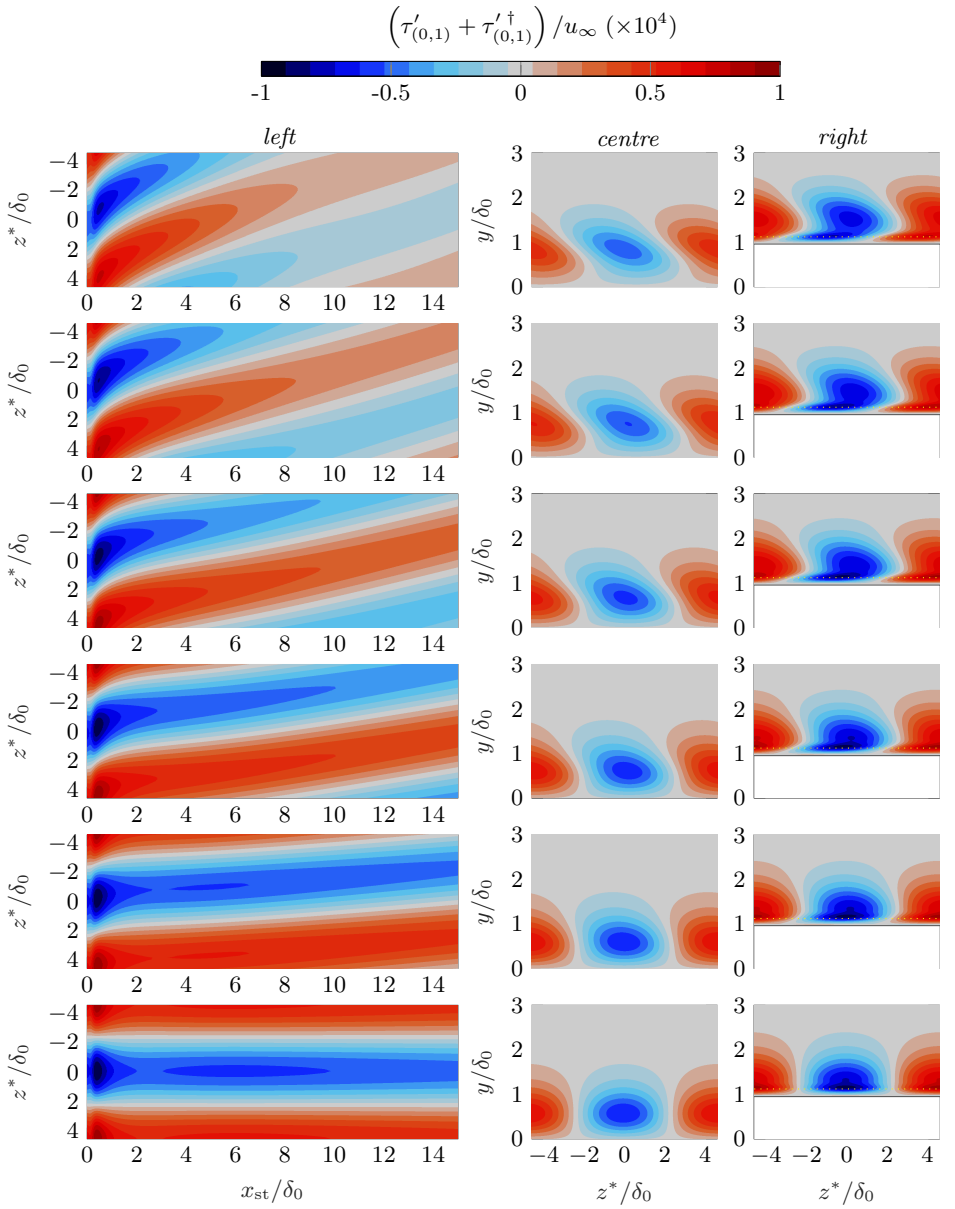

FIGURE 6.11: Evolution of perturbation streaks at $y/\delta_0 = 1.12$ (*left*) and in y-z planes upstream of the step, $x_{st}/\delta_0 = -10$ (*centre*), and downstream of the step, $x_{st}/\delta_0 = 1$ (*right*). Top to bottom illustrates streamwise-velocity perturbation as colour contour from case $\max(|w_\infty/u_\infty|)$ (*Test A*) to case $w_\infty/u_\infty = 0$ (*Test F*) following table 2.5. Dotted horizontal yellow line is the y-location of the x-z plane and the coordinate z^* indicates spanwise shift for centred low-speed streak.

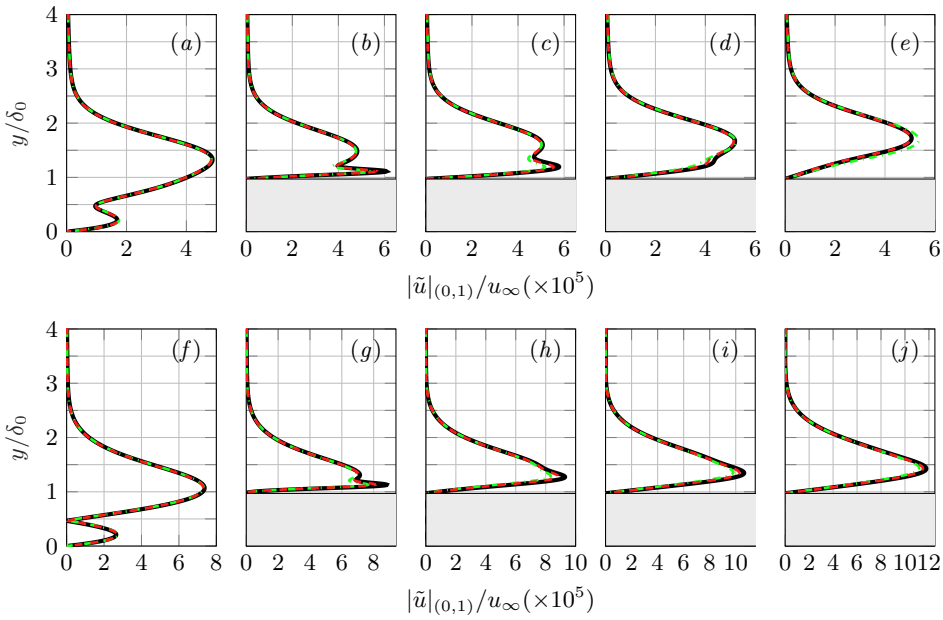

Figure 6.12: Profiles along y of the amplitude function $|\tilde{u}|_{(0,1)}$ at the step from DNS (solid black), AHLNS (dash-dotted green), and DeHNSSo (dashed red) at $x_{st}/\delta_0 = -0.5$ [(a) and (f)], 0.5 [(b) and (g)], 2.5[(c) and (h)], 5 [(d) and (i)], 10 [(e) and (j)]. Top row shows $\max(|w_\infty/u_\infty|)$ conditions, see *Test A* in table 2.5, and bottom row shows $w_\infty/u_\infty = 0$ conditions, see *Test F* in table 2.5.

Stokes equations with one or more directions of harmonic perturbation evolution, i.e., the z-direction in the present flow problem. Considering the outcomes of §§ 4.2.3 and 6.2.3, HNS allows for the modelling of both non-modal and non-parallel effects at the step without pre-imposed assumptions on the class of growth mechanisms that develop. Moreover, the computational cost of HNS is significantly reduced compared to DNS, which is key to produce a large data-set of perturbation fields. Two different HNS frameworks are employed in this chapter, namely the Delft Harmonic Navier-Stokes Solver, DeHNSSo (Westerbeek et al., 2024), and the Adaptive Harmonic Linearized Navier-Stokes, AHLNS (Franco and Hein, 2018). Henceforth, they are jointly referred to as (AL)HNS for convenience. Both frameworks solve the linear Harmonic Navier-Stokes equations, but feature implementation differences, see the discussion in Casacuberta et al. (2025b).

The results from DNS and (AL)HNS are compared in this section; the goal of this comparison is threefold: first, to cross-validate the results of § 6.2.7. Second, to strengthen that the streaks are a linear perturbation of the step flow, as elaborated upon in §§ 6.2.1 and 6.2.3. Third, to demonstrate the accuracy of novel (AL)HNS methods for stability calculations in highly non-parallel (step) flows.

Figure 6.12 portrays profiles of the fundamental chordwise-velocity perturbation amplitude function, i.e., $|\tilde{u}|_{(0,1)}$, at different x-locations obtained from AHLNS (dash-

dotted green), DeHNSSo (dashed red), and DNS (solid black). It is noted that figure 6.12 (*a-e*) represents max ($|w_\infty/u_\infty|$) conditions (i.e., *Test A* in table 2.5) and figure 6.12 (*f-j*) represents $w_\infty/u_\infty = 0$ conditions (i.e., *Test F* in table 2.5). The present calculations consider a spanwise perturbation wavelength of $\lambda_z = 7.5$ mm. The growth and further decay in x of near-wall perturbation streaks close downstream of the step is well captured by (AL)HNS. Minor differences between DeHNSSo and AHLNS are noted in the amplitude of the streaks just after their point of inception. It is emphasisd that a match between methods in figure 6.12 is obtained despite the inherent assumption of linearity in (AL)HNS. That is, the (AL)HNS methods seek numerical solutions to the linearised form of the perturbation equations; the streak evolution is fully captured, hence the streaks at the step are a linear perturbation phenomenon. The present match of DNS with linear methods further downstream of the step is likely contingent upon the use of a *moderate* amplitude of the incoming CFI (table 2.5) in the analysis in this present chapter.

6

6.2.7. Effect of spanwise wavenumber

The choice of spanwise perturbation wavelength in this thesis, $\lambda_z = 2\pi/\beta_0 = 7.5$ mm (§ 2.1.1), yields the largest (linear) amplification factor of the stationary CFI at the end of the domain in reference (no-step) conditions. However, there is no reason to assume, *a priori*, that this value yields as well the largest amplification factor of streaks at the step. This section analyses the effect of spanwise wavelength on the spatial amplification of streaks at the step.

A parametric study using linear stability analysis on the swept base flow with $w_\infty/u_\infty = -1.241$ (table 2.5) has been carried out with (AL)HNS (§ 6.2.6) to identify most critically amplified streaks in relation to the wavelength of upstream-existing perturbation modes. A range of input perturbation wavelengths is tested, namely $\lambda_z \in [4.5, 7.5]$ mm, in steps of $\Delta\lambda_z = 0.5$ mm. Figure 6.13 depicts perturbation amplification factors in x evaluated as

$$N(x, \lambda_z) = N^\star(x, \lambda_z) - N^\star(x_{\mathrm{str}}, \lambda_z) \tag{6.3}$$

with

$$N^\star(x, \lambda_z) = \ln\left(\frac{|\tilde{u}|^{\max}_{(0,1)}(x, \lambda_z)}{|\tilde{u}|^{\max}_{(0,1)}(0, \lambda_z)}\right) \tag{6.4}$$

and x_{str} denoting the x-position where the amplitude of near-wall streaks surpasses that of CFI developing above. Considering the discussion of § 2.1.1 on amplitude definitions, amplitude of the near-wall streaks in figure 6.13 (*a*) is monitored approximately in the range $0 \leq x_{\mathrm{st}} \leq 4$. Downstream of it, the measure of amplitude characterises CFI.

The results of figure 6.13 (*a*) indicate that the maximum amplification factor of streaks is attained for $\lambda_z = 5$ mm. For reference, this value is more than six times the step height. Following the main discussion above, the differences in amplification factor of streaks at the step (figure 6.13 (*a*)) can be linked to a measure of *growth efficiency* of the incoming perturbation pattern. Here, the term growth efficiency expresses the sense of correlation between the profiles (i.e., the shape along y) of

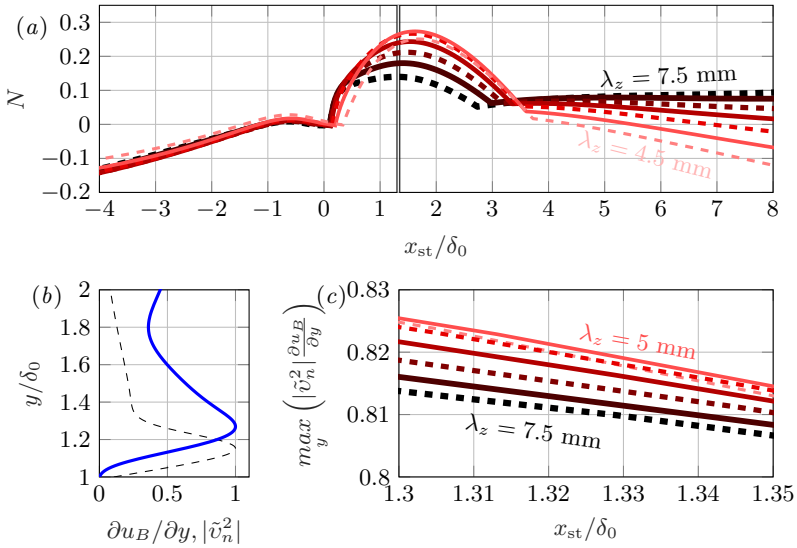

Figure 6.13: Evolution in x of the perturbation amplification factor (6.3) computed with AHLNS (§ 6.2.6) on the swept base flow with $w_\infty/u_\infty = -1.241$ (table 2.5) for $\lambda_z \in [4.5, 7.5]$ mm, in steps of $\Delta\lambda_z = 0.5$ mm: thin-to-thick (and, bright-to-dark) line style illustrates increasing λ_z (a). Normalised profiles of $|\tilde{v}_n^2|$ (solid blue) and $\partial u_B/\partial y$ (dashed black) for $\lambda_z = 5$ mm at $x_{st}/\delta_0 = 1.3$ (b). Evolution in x of the maximum along y of the correlation between $|\tilde{v}_n^2|$ and $\partial u_B/\partial y$ (c). Solid vertical lines in (a) indicate $1.3 \leq x_{st}/\delta_0 \leq 1.35$.

the incoming cross-stream perturbation component, $\boldsymbol{v}'_{n,(0,j)}$ (3.12), and the base-flow shears; the *most efficient* interaction between these two agents will induce the largest spatial transient growth of kinetic perturbation energy locally downstream of the step. This concept shares the same foundations as *optimal* perturbations (Böberg and Brösa, 1988; Butler and Farrell, 1992; Andersson et al., 1999; Luchini, 2000). However, in the present case, the set of possible initial perturbations is bounded and given by the shape of each considered spanwise wavelength of the pre-existing perturbation in the incoming stream.

This effect is here quantified through the term $\kappa_2^{\beta_0}$ (5.6), which was shown above to add the main contribution to the lift-up effect in the region dominated by the near-wall streaks (figure 6.5 (b)). Following the mathematical definition of $\kappa_2^{\beta_0}$ (3.3) and its physical interpretation in step flow (§ 6.2.1), it is identified that the normal perturbation shape $|\tilde{v}_n^2|$ (3.28) and the base-flow shear $\partial u_B/\partial y$ yield maximum correlation for $\lambda_z = 5$ mm. This implies that, the product between the profiles of $|\tilde{v}_n^2|$ and $\partial u_B/\partial y$ (see figure 6.13 (b)) at a representative x-position produces a profile whose peak attains maximum strength for $\lambda_z = 5$ mm. The latter is quantitatively characterised in figure 6.13 (c) considering $x_{st}/\delta_0 \approx 1.3$, i.e., close upstream of the point of maximum amplification of the smaller-wavelength streaks.

7

Influence of amplitude on the mechanisms of stationary interaction

Abstract: *This chapter assesses the effect of incoming-CFI amplitude on the key stationary-perturbation mechanisms elucidated in previous chapters. The interaction between a sufficiently amplified CFI and the step induces a pronounced deformation of the near-wall shear layer, a feature that plays a key role in promoting transition (chapter 8). To elucidate the origin of this deformation, the energy-balance equations introduced in chapter 3 are examined for varying CFI amplitudes. The analysis reveals that the shear-layer deformation arises through two primary mechanisms:* (1) *an inflectional instability of the base-flow profiles downstream of the step (chapter 4) and* (2) *a non-linear interaction between spanwise perturbation modes within the region dominated by the perturbation streaks (chapter 6).*

A note on nomenclature: *This chapter focuses exclusively on stationary effects. The spanwise perturbation modes are denoted by* $\boldsymbol{v}'_{(0,j)}$*, where the prime marks perturbation,* j *is the spanwise modal index, and the zero indicates stationary behaviour. Unperturbed base-flow quantities are denoted by the subscript B, for example,* $\boldsymbol{v}_B$*, whereas steady perturbed-flow quantities are denoted by the subscript DB, for example,* $\boldsymbol{v}_{DB}$*. The steady perturbed flow results from the superposition of the unperturbed base flow and the stationary perturbation field.*

Parts of this chapter are published in:

- Casacuberta, J., Hickel, S., and Kotsonis, M., 2023 Laminar-turbulent transition in swept-wing flows with a supercritical forward-facing step. In *ERCOFTAC Workshop Direct and Large Eddy Simulation* (pp. 151-156). Cham: Springer Nature Switzerland.
- Casacuberta, J., Groot, K. J., Hickel, S., and Kotsonis, M., 2025 Direct numerical simulation of swept-wing transition induced by forward-facing steps. Under consideration for publication in *J. Fluid Mech.*

The previous chapters have examined the mechanisms governing the stationary interaction between the incoming CFI and the step. The present chapter evaluates how variations in incoming-CFI amplitude affect these key mechanisms. While chapters 4, 5, and 6 focus exclusively on the *medium*-amplitude CFI case (table 2.4), the analysis is now extended to the *small*- and *large*-amplitude CFI cases (table 2.4), for a fixed step height (step III in table 2.3). The main emphasis is placed on the *large*-amplitude CFI case, which corresponds to the flow conditions under which laminar-turbulent transition mechanisms are analysed in this thesis (chapter 8).

Since this chapter provides the foundation for the characterisation of unsteady perturbation effects discussed in chapter 8, the analysis centres on the response of the steady perturbed flow, $\boldsymbol{q}_{\mathrm{DB}}$, to varying CFI amplitudes; that is, the flow resulting from the superposition of the unperturbed base flow, $\boldsymbol{q}_{\mathrm{B}}$, and the stationary perturbation field, $\boldsymbol{q}'$, as given in equation (2.10). The §§ 7.1 and 7.2 analyse, respectively, the impact of CFI amplitude on the organisation of the steady perturbed flow and the evolution stationary perturbations at the step. Finally, § 7.3 interprets these results by scrutinising the associated kinetic energy transfer mechanisms at the step, following the framework developed in § 3.1.

7

7.1. Topology of steady perturbed flows

Under reference (no-step) conditions, the stationary co-rotating crossflow vortices (see § 1.2.3), are the main flow structure of the steady perturbed flow. These vortices modulate the boundary layer in both the chordwise and spanwise directions. Naturally, this modulation is enhanced as the CFI amplitude is increased, as evident in figure 7.1 (*b*) and (*c*), which compares the topology of the stationary crossflow vortex for cases r.*B* and r.*C* at $x_{\mathrm{st}}/\delta_0 = 9.4$. As expected, in the *small*-amplitude case r.*A* (figure 7.1 (*a*)), the structure of the steady perturbed flow remains largely similar to that of the unperturbed base flow. All planes in figure 7.1 are shown at $x_{\mathrm{st}}/\delta_0 = 9.4$, a position representative of the flow organisation close downstream of the step, but beyond the reattachment point; see figure 7.2 for reference. Specifically, figure 7.1 depicts z-y planes of

$$u_{\mathrm{DB},s} = u_{\mathrm{DB}}\cos(\phi_s) + w_{\mathrm{DB}}\sin(\phi_s), \tag{7.1}$$

the velocity component in the steady perturbed flow which points in the direction of the inviscid streamline (2.6). It is to be noted that equation (2.7) expresses the representation of the unperturbed base flow (i.e., $\boldsymbol{q}_{\mathrm{B}}$) oriented relative to the inviscid streamline, whereas the analysis in this chapter applies the same concept to the steady perturbed flow (i.e., $\boldsymbol{q}_{\mathrm{DB}}$), see equation (2.10). Additionally, black arrows in figure 7.1 illustrate the in-plane velocity components normal to the wall, v_{DB}, and normal to the direction of the inviscid streamline,

$$w_{\mathrm{DB},s} = w_{\mathrm{DB}}\cos(\phi_s) - u_{\mathrm{DB}}\sin(\phi_s). \tag{7.2}$$

When the step is present, the organisation of the steady perturbed flow undergoes significant local deformation around the step. This effect is evident in the *medium*-

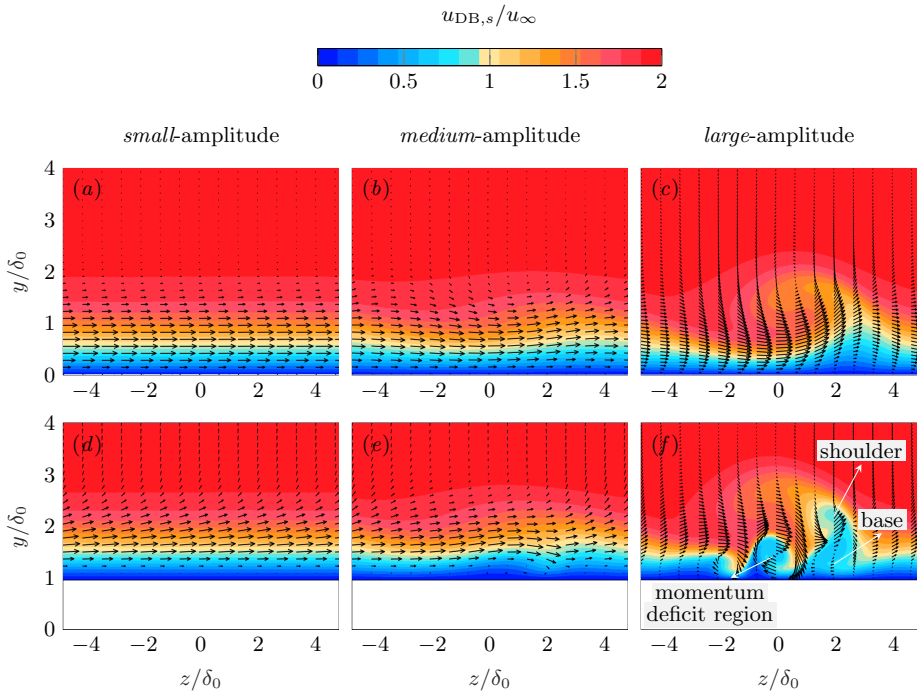

Figure 7.1: Topology of the steady perturbed flow illustrated by z-y planes of velocity $u_{\mathrm{DB},s}$ at $x_{\mathrm{st}}/\delta_0 = 9.4$. No-step cases r.$A$, r.$B$, r.$C$ (a-c) and step cases s.A, s.B, s.C (d-f), see table 2.4. The black arrows illustrate the in-plane organisation of the steady perturbed flow ($w_{\mathrm{DB},s}$ and v_{DB}).

and *large*-amplitude cases, s.B and s.C, compared to their amplitude-equivalent no-step counterparts, r.B and r.C, see figure 7.1 (e,f) versus figure 7.1 (b,c).

The step modifies the steady perturbed flow primarily through deformation of the near-wall shear layer. In case s.C, this deformation leads to the formation of a streamwise-momentum deficit region beneath the crossflow-vortex crest (figure 7.1 (f)) eventually in x, a flow feature that has also been observed in time-averaged experimental measurements (Rius-Vidales and Kotsonis, 2022). Here, the term *streamwise-momentum deficit* refers to a deficit in the component $u_{\mathrm{DB},s}$ (7.1). Simultaneously, the main structure of the original crossflow vortex is altered by its interaction with the step: see the *base*, $(y,z)/\delta_0 \approx (1.5, 2)$, and part of the *shoulder* of the crossflow vortex, $(y,z)/\delta_0 \approx (2.5, 2)$ (figure 7.1 (f)), compared with the corresponding no-step case (figure 7.1 (c)). In chapter 8, the near-wall shear-layer deformation downstream of the step will be shown to play a key role in the mechanisms of laminar breakdown, both in the supercritical (§ 8.1.1) and the critical (§ 8.1.2) transition regimes. The present results demonstrate that this deformation arises purely from the stationary interaction between the incoming CFI and the step; that is, it constitutes an inherent feature of the steady perturbed flow.

The organisation of the steady perturbed flow downstream of the step –specifically, past the region of recirculating flow– qualitatively resembles the flow organisation described by Wassermann and Kloker (2005) in the context of a swept-wing boundary-layer subject to a pressure-gradient changeover. In the analysis presented in this thesis, the presence of the step induces a localised region of adverse pressure gradient downstream of the step (see figure 4.1 and § 4.1.1), and reversal of the crossflow-velocity profile (see figure 4.6 and § 4.1.2). Wassermann and Kloker (2005) report that the reversal of the crossflow-velocity profile induces a redistribution of the spanwise shear and promotes the amplification of additional CFI modes, which may rotate in the sense opposite to the pre-existing ones.

In the case of the step, the streamwise-momentum deficit region that develops beneath the pre-existing stationary crossflow vortex (see colour contours in figure 7.1 (*f*)) structurally resembles a crossflow vortex rotating in the opposite sense to the incoming one (see black arrows in figure 7.1 (*f*)). Notwithstanding the structural similarities between the present step flow and the flow environment of Wassermann and Kloker (2005), the origin of the streamwise-momentum deficit region is attributed to a different set of mechanisms, as elaborated in § 7.3.

The deformation of the shear layer past the step increases in strength with the amplitude of the incoming CFI. This appears evident in figure 7.1 (*d-f*). To quantify this effect, the wall-shear field

$$\xi_{\mathrm{w}}(x,z) = \sqrt{\left(\frac{\partial u_{\mathrm{DB}}}{\partial y}\right)^2 + \left(\frac{\partial w_{\mathrm{DB}}}{\partial y}\right)^2}\,\Bigg|_{\mathrm{wall}} \tag{7.3}$$

is evaluated for the step cases, namely s.*A*-s.*C*, and portrayed in figure 7.2 (*a-c*) in the range $-5 \leq x_{\mathrm{st}}/\delta_0 \leq 25$. Additionally, figure 7.2 (*d-f*) quantitatively characterises the x-evolution of the root-mean-square of ξ_{w} along z (solid black line), denoted by $\mathrm{rms}|_z$. For reference, the same wall-shear metric for the unperturbed base flow is included and represented by dashed grey line. In the *small*-amplitude case s.*A*, the steady perturbed flow contains regions of reverse flow both upstream of and downstream of the step, as indicated by the cyan isoline marking $\partial u_{\mathrm{DB}}/\partial y = 0$ at the wall in figure 7.2 (*a*).

In case s.*B*, the reverse-flow region extends further in x and becomes modulated at the fundamental spanwise wavelength. This is evident in the similar z-evolution of low- and high-wall-shear regions and the shape of the cyan isoline in figure 7.2 (*b*). Tufts et al. (2017) similarly report that the deformation of the recirculating-flow region follows a pattern dictated by the (fundamental) spanwise wavenumber of the incoming CFI. When the amplitude of the incoming CFI is further increased in case s.*C* (figure 7.2 (*c*)), the reverse-flow regions fragment into individual irregular patches. Eppink (2020) also observes the emergence of *isolated* recirculating-flow patches "in some cases" (i.e., for particular combinations of the step height and incoming perturbation amplitude).

The red circles in figure 4.7 represent Infrared (IR) thermal measurements from Rius-Vidales and Kotsonis (2021). In their experiments, the heated wing surface exhibits z-distributed regions of high and low temperature, corresponding to areas

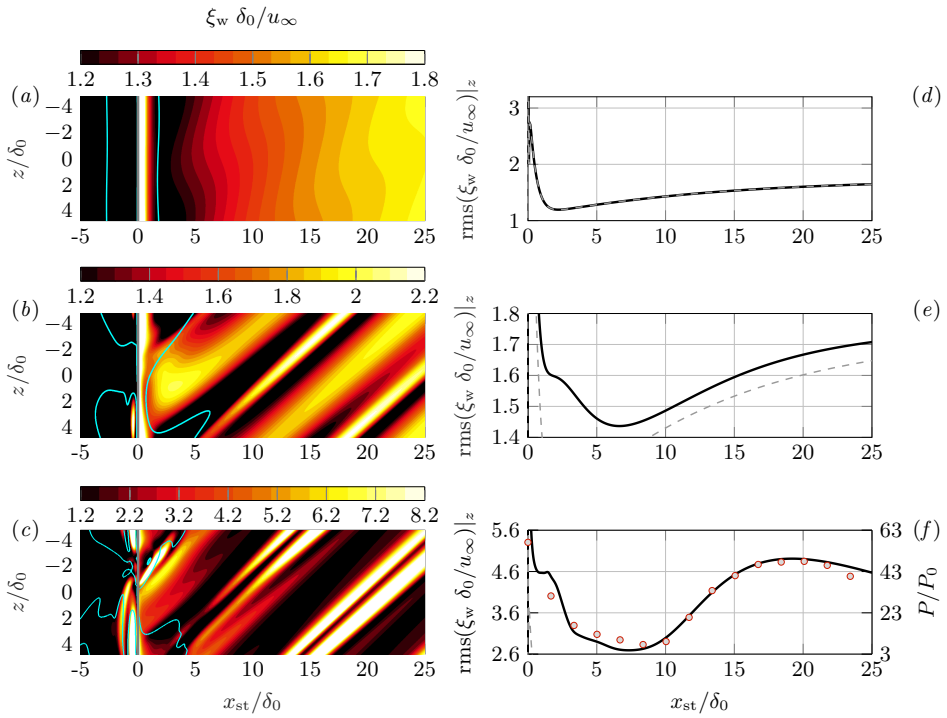

FIGURE 7.2: Wall shear (ξ_w) contour with cyan isoline indicating $\partial u_{DB}/\partial y = 0$ at the wall (*a*-*c*). Evolution in x of the rms along z of wall shear (*d*-*f*) in cases s.*A* (*a*,*d*), s.*B* (*b*,*d*), s.*C* (*c*,*f*): steady perturbed flow from DNS (solid black line), unperturbed base flow from DNS (dashed grey line), and spatial Power Spectral Density (PSD) of infrared thermal measurements from Rius-Vidales and Kotsonis (2021) extracted at the CFI wavelength (red circles).

of weaker and stronger wall-shear stress. A spatial Power Spectral Density (PSD) analysis of the wall-temperature measurements is performed along the z-direction. The normalised PSD of the fundamental spanwise wavenumber, which dominates the wall-shear evolution, serves as key metric. It is depicted in figure 7.2 (*f*) as red circles and denoted as P/P_0. Overall, very good qualitative agreement is observed between the near-wall flow behaviour obtained from DNS (case s.*C*) and experiments (Rius-Vidales and Kotsonis, 2021), as shown by the solid black line and red circles in figure 7.2 (*f*).

7.2. Overview of perturbation evolution

The mechanisms governing the stationary modulation of the shear layer at the step are scrutinised in this section. The main focus of the analysis is on the *medium*- (s.*B*) and *large*-amplitude (s.*C*) cases since the behaviour of the *small*-amplitude (s.*A*) case at the step is qualitatively similar to s.*B*.

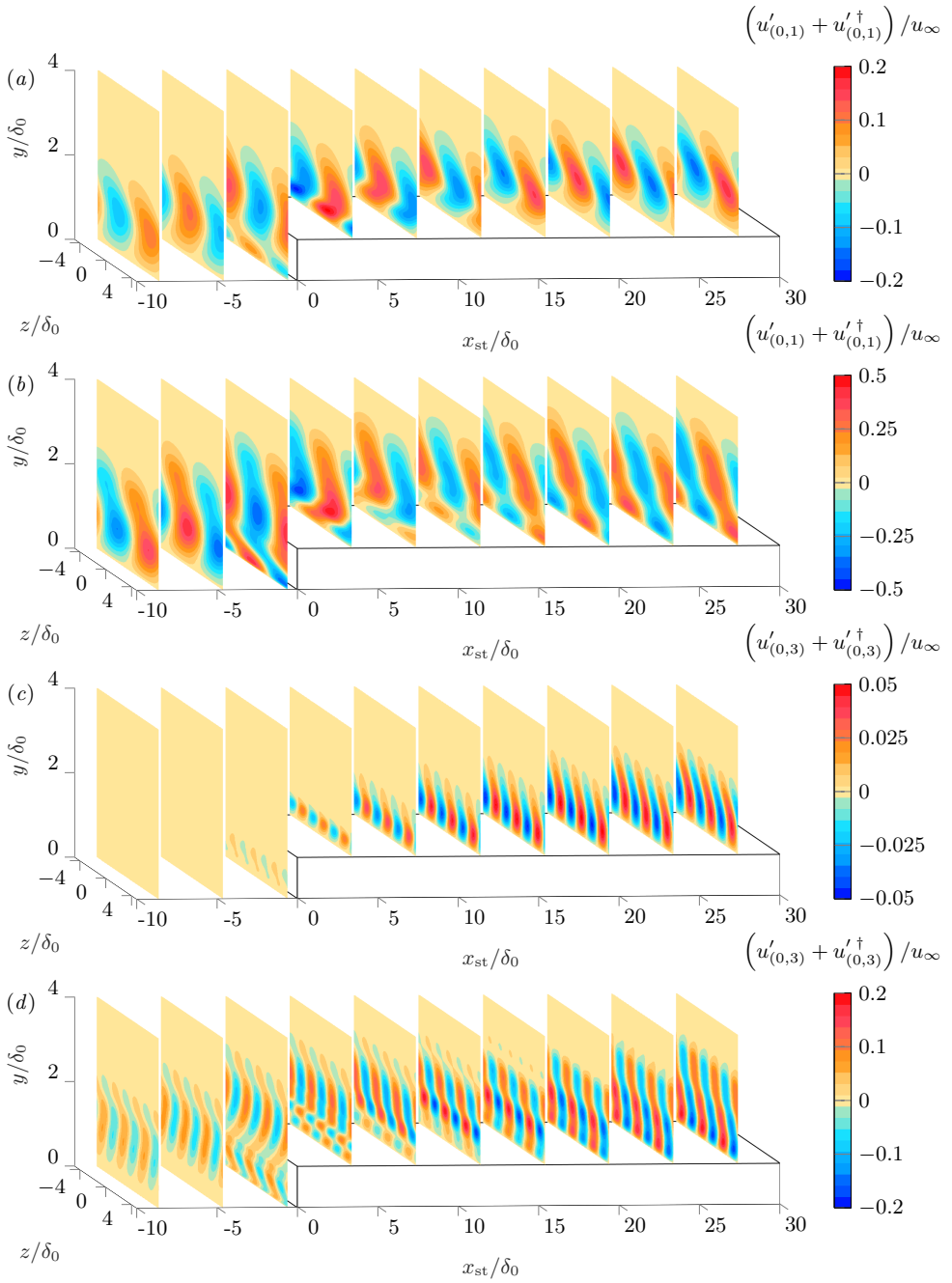

Figure 7.3: Organisation of stationary spanwise perturbation modes in the *medium*-, s.B (a,c), and *large*-amplitude, s.C (b,d), CFI cases: $\beta = \beta_0$ (a,b) and $3\beta_0$ (c,d). The incoming modes in (c) are invisible due to their small amplitude compared to modes downstream of the step.

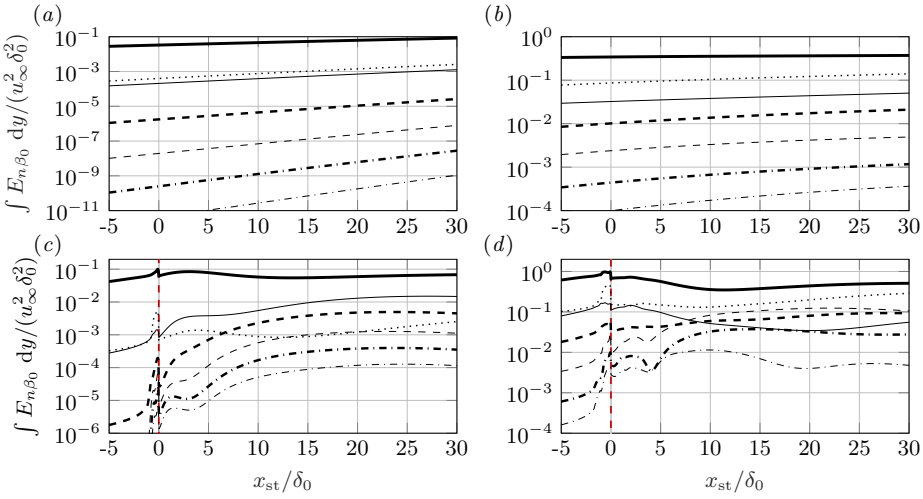

FIGURE 7.4: Evolution in x of the kinetic energy of spanwise-harmonic perturbation spaces, $\int E_{n\beta_0}\,\mathrm{d}y$: $n = 0$ (dotted), 1 (thick solid), 2 (thin solid), 3 (thick dashed), 4 (thin dashed), 5 (thick dash-dotted), 6 (thin dash-dotted) for *medium*-amplitude r.B (a), s.B (c) and *large*-amplitude r.C (b), s.C (d) cases. Vertical dashed line indicates the step location.

7

Figure 7.3 compares the stationary perturbation field at the step under *medium*- (a,c) and *large*-amplitude (b,d) CFI conditions. Sub-plots (a,b) correspond to the fundamental spanwise mode, $\beta = \beta_0$, while sub-plots (c,d) correspond to the third harmonic, $\beta = 3\beta_0$. Thus, figure 7.3 (a) is identical to figure 4.7 (c) in § 4.2. In this chapter, the spanwise mode $\beta = 3\beta_0$ is generally used to illustrate the behaviour of the higher-order spanwise modes, $\beta > \beta_0$. This choice is made in particular because mode $\beta = 2\beta_0$ exhibits perturbation effects at the step that differ from those of the other harmonic modes under *large*-amplitude CFI conditions, see § 7.3.

Initially around the step the organisation of the stationary perturbation field is qualitatively similar in all amplitude cases investigated in this thesis: the fundamental stationary CFI gradually lifts off the surface as it approaches the step in x (figure 7.3 (a,b)) and passes over it (chapter 4). Upon interacting with the step flow, it produces stationary velocity-perturbation streaks of alternating sign in z just downstream of the upper step corner (chapter 6); the spanwise wavenumber of the streaks is identically $\beta = \beta_0$, thus they appear within the fundamental spanwise perturbation mode in figure 7.3 (a,b), together with the CFI. When moving downstream of the step the perturbation behaviour in the *medium*-amplitude case s.B is qualitatively identical to that of the *small*-amplitude case s.A. However, a significant difference arises in the *large*-amplitude case s.C: while in s.A and s.B the near-wall streaks rapidly decay in x (figure 7.3 (a)), in case s.C, they undergo a second phase of growth in x after decaying initially (figure 7.3 (b)). The observed similarities between the spatial evolution of near-wall streaks (figure 7.3 (b)) and wall shear (figure 7.2 (c,f)) suggest that wall-shear measurements at the step do not explicitly characterise the

evolution of the original stationary crossflow vortices when the streaks are active.

As elaborated upon in § 6.2.4, near-wall perturbation streaks induced locally at the step apex also manifest in the high-order stationary spanwise modes, $\beta > \beta_0$; this feature is illustrated here in figure 7.3 (*c*,*d*). The evolution of $u'_{(0,3)}$ in case s.*B* (figure 7.3 (*c*)) is representative of the behaviour of the other high-order spanwise perturbation modes, as they all exhibit a qualitatively similar trend in x. In contrast, in the *large*-amplitude case s.*C*, a range of perturbation mechanisms become active simultaneously, leading to different growth regimes, depending on the specific high-order spanwise mode. This disparity in spatial amplification trends among the spanwise perturbation modes is quantified through their kinetic energy, given by $\int E_{n\beta_0}\,\mathrm{d}y, n = 0, 1, 2, \ldots$, as defined in equation (3.2).

The evolution of perturbation kinetic energy in x is characterised in figure 7.4. Figure 7.4 (*a*,*b*) depicts reference (no-step) conditions, i.e., cases r.*B* and r.*C*. Figure 7.4 (*c*) illustrating case s.*B* confirms that high-order spanwise perturbation modes undergo analogous growth phases. The common amplification immediately downstream of $x_{\mathrm{st}} = 0$ is attributed to the inception of the streaks (§ 6.2.4), and the subsequent and more extended growth regime in x is linked to the modal inflection instability of the step-distorted base-flow profiles to small-wavelength stationary perturbations described in § 4.3. The localised overshooting (figure 7.4 (*c*,*d*)) just upstream of $x_{\mathrm{st}} = 0$ is primarily due to the formation of near-wall streaky structures in this region as well (see figure 7.3 (*a*,*b*)).

The rather coherent evolution in x of high-order spanwise perturbation modes in case s.*B* contrasts with the irregular evolution observed in case s.*C* (figure 7.4 (*d*)). Notably, a significant stabilisation of mode $\beta = 2\beta_0$ is observed, along with a reordering of the energetic hierarchy of the perturbation modes, compared to reference conditions (figure 7.4 (*b*)). Overall, the disorderly evolution in x of the high-order perturbation modes in case s.*C* results in the distinct deformation of the steady shear layer at the step, as shown in figure 7.1 (*f*). In line with the main outcomes of chapters 4 and 5, the present results further strengthen that the influence of the step on incoming stationary perturbations ought not to be solely ascribed to a global enhancement (or weakening) of the stationary crossflow vortex structure.

7.3. Mechanisms of energy transfer

In § 3.1, energy-balance equations for stationary spanwise perturbation modes were formulated. The framework developed in § 3.1 is employed in this section to asses effects of incoming perturbation amplitude on the mechanisms of interaction between stationary perturbations and the step. As described previously, each term in equation (3.8) characterises a mechanism contributing to the time rate of change of kinetic energy within a spanwise-harmonic perturbation space. In this present context, the term *perturbation space* refers to the combination of a stationary spanwise perturbation mode and its complex conjugate, i.e., $\boldsymbol{v}'_{(0,n)} + \boldsymbol{v}'_{(0,-n)}$, $n = 0, 1, \ldots, N$ (§ 3.1). For the analysis of this section, the stationary perturbation decomposition (1.8) is truncated at $N = 20$. The methodology is first exemplified under *medium*-amplitude CFI conditions by comparing the step and no-step scenarios. The analysis is then

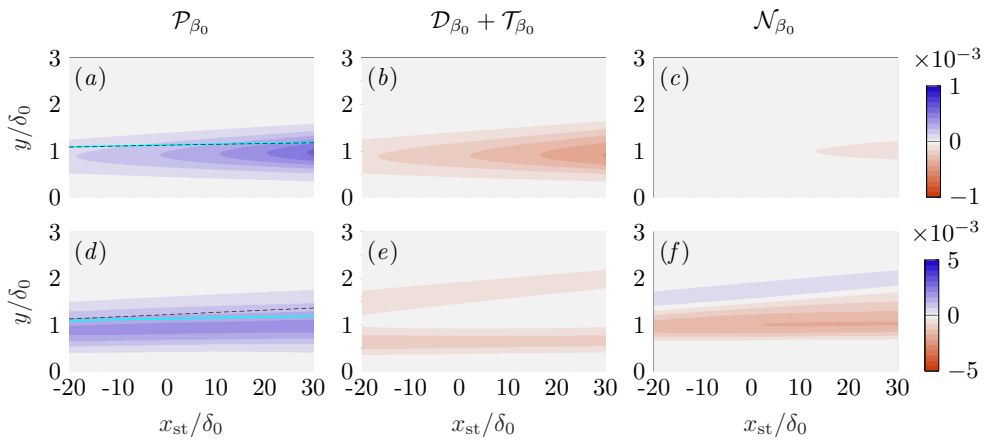

Figure 7.5: Spatial evolution of budget terms of equation (3.8) for $n = 1$ in cases r.B (top) and r.C (bottom): energy production (a,d), viscous effects and energy advection (b,e), work of non-linear interactions (c,f). Loci of crossflow inflection points in the unperturbed base flow (solid cyan line) and by the addition of the mean-flow distortion (dashed black line) in (a,d).

extended to *large*-amplitude CFI conditions.

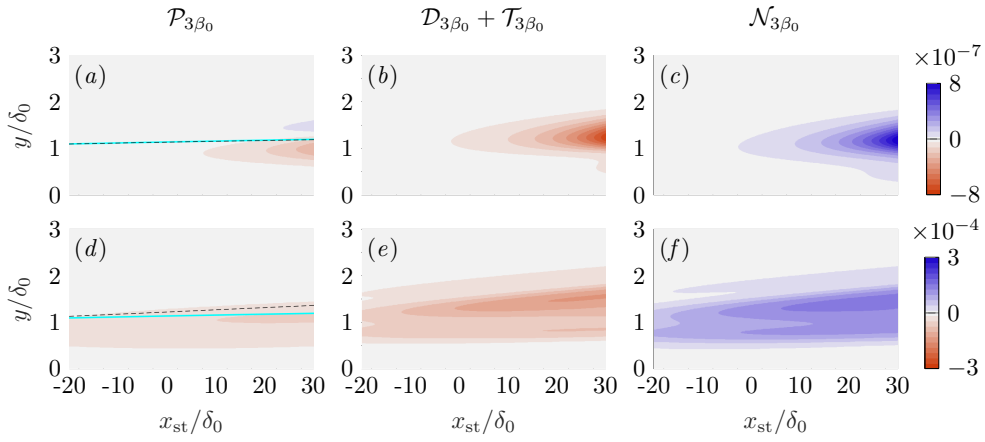

Figure 7.6: Spatial evolution of budget terms of equation (3.8) for $n = 3$ in cases r.B (top) and r.C (bottom): energy production (a,d), viscous effects and energy advection (b,e), work of non-linear interactions (c,f). Loci of crossflow inflection points in the unperturbed base flow (solid cyan line) and by the addition of the mean-flow distortion (dashed black line) in (a,d).

First, consider the fundamental space $n = 1$, corresponding to perturbations with $\beta = \beta_0$ and reference (no-step) conditions. The spatial evolution of the terms of equation (3.8) is shown in figure 7.5 (a-c). Production adds the dominant positive

contribution (figure 7.5 (*a*)), where $\mathcal{P}_{\beta_0} > 0$ indicates kinetic energy transfer from the unperturbed base flow to the primary-wavelength perturbations (see § 3.3 and chapter 5 for further details). Non-linear interactions contribute negligibly to the energy budget (figure 7.5 (*c*)), consistent with the agreement between solutions from the linear and non-linear PSE approach in this x-region (figure 2.11 (*b*)). Viscous effects and advection are the main mechanisms balancing out the production of kinetic energy, i.e., $\mathcal{D}_{\beta_0} + \mathcal{T}_{\beta_0} < 0$.

This interplay between perturbation mechanisms is typically reversed in the high-order perturbation spaces, $n > 1$, with the analysis still strictly confined to reference (no-step) conditions. Specifically, perturbation growth is primarily driven by non-linear interactions, $\mathcal{N}_{n\beta_0}$, $n > 1$, whilst linear production, $\mathcal{P}_{n\beta_0}$, $n > 1$, contributes in a stabilising manner. Figure 7.6 (*a-c*) illustrates this behaviour for $n = 3$, which is is representative of the high-order harmonic perturbation spaces in case r.*B*. The quantitative impact of individual perturbation spaces is characterised in figure 7.9 (*a-e*), which presents the integral contribution of the terms of equation (3.8) over a domain S defined by $-20 \leq x_{\mathrm{st}}/\delta_0 \leq 30$ and $y/\delta_0 \leq 6$.

The presence of the step significantly alters the mechanisms of kinetic energy transfer of stationary perturbations. Under *medium*-amplitude CFI conditions, the inclusion of the step causes production to act locally stabilising at the step in the space $n = 1$, as indicated by the red contour in figure 7.7 (*a*) signifying $\mathcal{P}_{\beta_0} < 0$. This phenomenon has been associated to a reverse lift-up effect in chapter 5. Conversely, the opposite trend is observed for high-order harmonic perturbation spaces. That is, under reference (no-step) conditions, production yields a stabilising contribution (figures 7.6 (*a-c*) and 7.9 (*d,e*)), whereas it acts destabilising at the step (figures 7.8 (*a-c*) and 7.10 (*d,e*)).

In § 4.3, it is shown that the step flow destabilises stationary high-order harmonic perturbations through an inflectional mechanism. Specifically, linear stability analysis carried out in § 4.3 identifies an unstable stationary eigensolution of the base-flow profiles, albeit it emerges exclusively for $\beta > \beta_0$, and within the x-range where the profiles downstream of the step develop an inflection point near the wall. The flow environment analysed in § 4.3 is identically case s.*B* here. These aforementioned results from the linear stability analysis (§ 4.3) reconcile with the present observation that linear production of high-order harmonic perturbations peaks at the location of step-induced inflection points (see figure 7.8 (*a*) illustrating $\mathcal{P}_{3\beta_0}$ for reference). The cyan lines in figure 7.8 (*a*) mark the loci of inflection points in the crossflow profile of the unperturbed base flow; the lower branch is exclusive to step conditions, as evident from the comparison with figure 7.6 (*a*).

Amplitude effects on energy-transfer mechanisms at the step are next assessed by extending the analysis to *large*-amplitude CFI conditions. Specifically, the reference (no-step) case r.*C* is characterised in figures 7.5 (*d-f*) and 7.6 (*d-f*) illustrating the perturbation spaces $n = 1$ and 3, respectively. The step case s.*C* is characterised in figures 7.7 (*d-f*) and 7.8 (*d-f*), also illustrating the perturbation spaces $n = 1$ and 3. The corresponding energy budgets are presented in figures 7.9 (*f-j*), for reference (no-step) conditions, and 7.10 (*f-j*), for step conditions.

Overall, case r.*C* exhibits qualitatively similar behaviour to case r.*B*. That is,

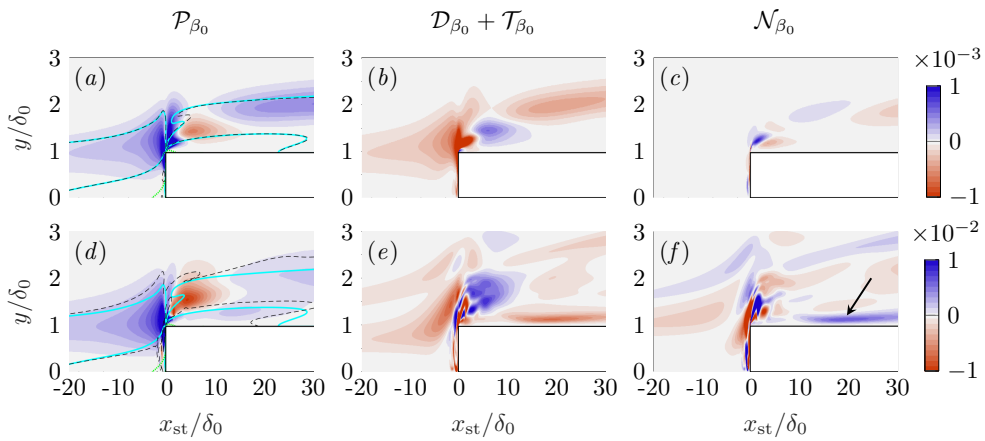

Figure 7.7: Spatial evolution of budget terms of equation (3.8) for $n = 1$ in cases s.B (top) and s.C (bottom): energy production (a,d), viscous effects and energy advection (b,e), work of non-linear interactions (c,f). Loci of crossflow inflection points in the unperturbed base flow (solid cyan line) and by the addition of the mean-flow distortion (dashed black line), and base-flow reversal $u_{\mathrm{B}} = 0$ (dotted green line) in (a,d).

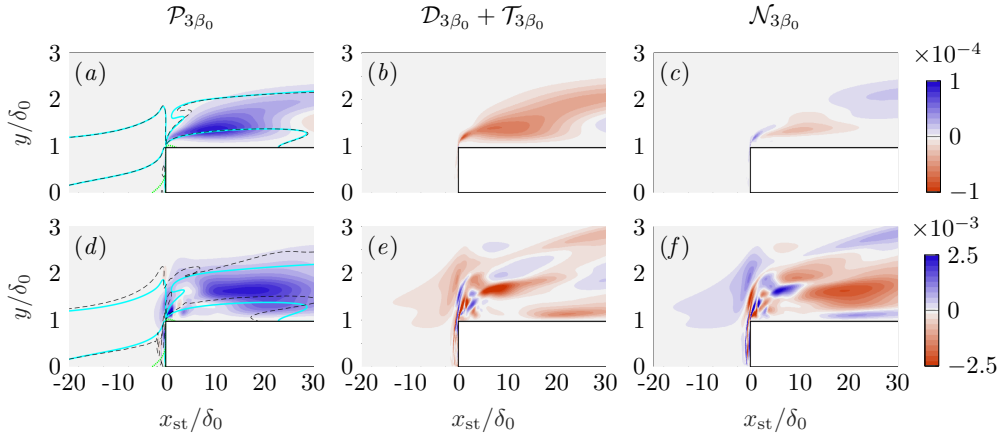

Figure 7.8: Spatial evolution of budget terms of equation (3.8) for $n = 3$ in cases s.B (top) and s.C (bottom): energy production (a,d), viscous effects and energy advection (b,e), work of non-linear interactions (c,f). Loci of crossflow inflection points in the unperturbed base flow (solid cyan line) and by the addition of the mean-flow distortion (dashed black line), and base-flow reversal $u_{\mathrm{B}} = 0$ (dotted green line) in (a,d).

energy production drives the amplification of the fundamental CFI mode ($\beta = \beta_0$, figure 7.9 (g)), while non-linear interactions drive the amplification of high-order harmonic CFI modes ($\beta > \beta_0$, figure 7.9 (h-j)). However, as expected for a stronger

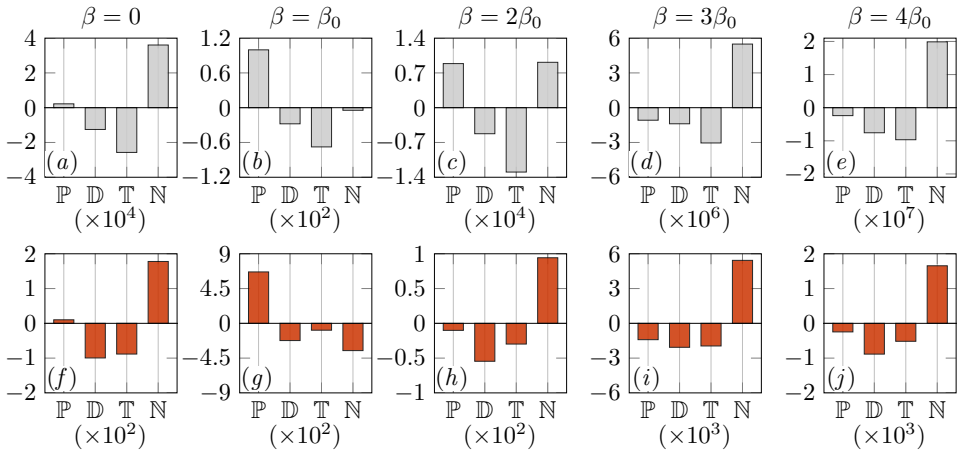

Figure 7.9: Integral contribution over the domain S of budget terms of equation (3.8) in no-step conditions: case r.B (top) and r.C (bottom) for $n = 0$ (*a*,*f*), 1 (*b*,*g*), 2 (*c*,*h*), 3 (*d*,*i*), 4 (*e*,*j*). Blackboard bold symbols denotes quantities integrated over S.

7

stationary crossflow vortex, the non-linear interactions acting on individual modes are overall more pronounced in case r.C compared to r.B (figure 7.9).

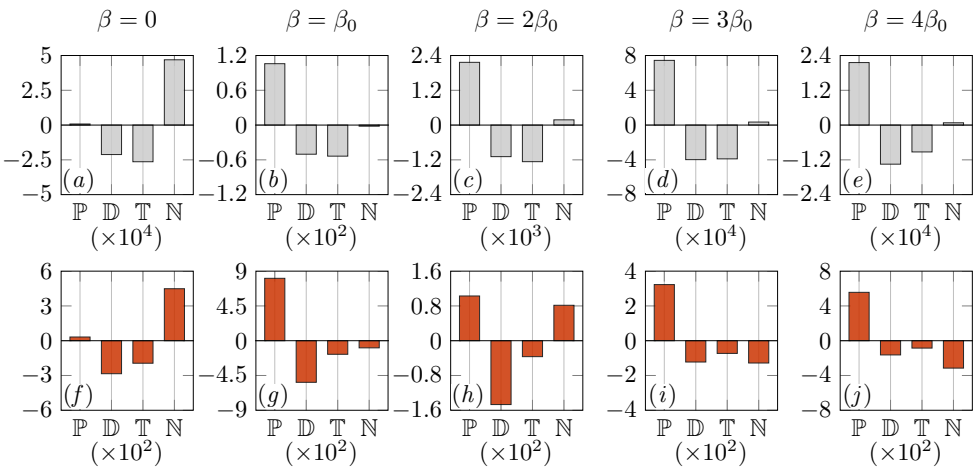

Figure 7.10: Integral contribution over the domain S of budget terms of equation (3.8) in step conditions: case s.B (top) and s.C (bottom) for $n = 0$ (*a*,*f*), 1 (*b*,*g*), 2 (*c*,*h*), 3 (*d*,*i*), 4 (*e*,*j*). Blackboard bold symbols denotes quantities integrated over S.

With the step present, high-order perturbation modes destabilised analogously by the inflectional instability at the step (§ 4.3) exhibit a similar rate of growth

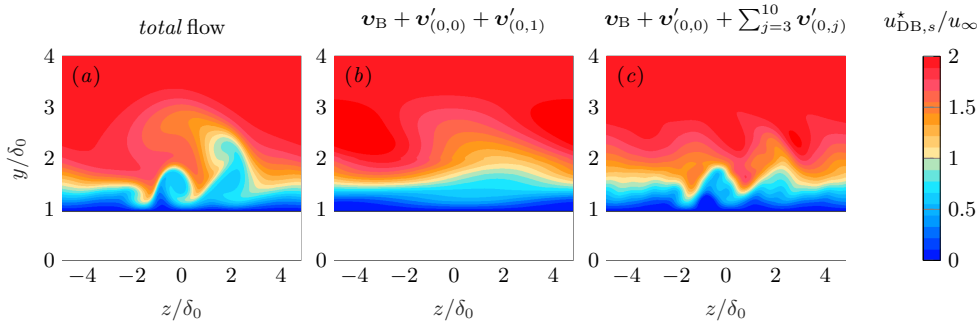

Figure 7.11: Topology of steady perturbed flows illustrated by z-y planes at $x_{st}/\delta_0 = 9.4$ of velocity $u^\star_{DB,s}$ (2.7). The symbol $\star$ indicates that the flow is built considering the superposition of unperturbed base flow, $\boldsymbol{v}_B$, and different numbers of spanwise modes, j: *total* flow $u_{DB,s}$ (a), modes $j = 0, 1$ (b), modes $j = 0$, 3-10 (c).

in figure 7.4 (c); i.e., representing the *medium*-amplitude case s.B. While the same inflectional mechanism is also present in the *large*-amplitude case s.C, it is observed that the spanwise mode $\beta = 2\beta_0$ undergoes significant stabilisation in x downstream of the step (figure 7.4 (d)). The present energy-balance analysis enlightens that the mechanism of production at the step (i.e., reflecting the imprint of the inflectional instability) is notably weaker in the perturbation space $n = 2$, compared to $n > 2$, under *large*-amplitude CFI conditions.

In addition to this linear effect, a key result of the present chapter is that a non-linear mechanism significantly influences the perturbation evolution in case s.C. To illustrate this, consider first the perturbation space $n = 1$. An elongated contour of $\mathcal{N}_{\beta_0} > 0$, i.e., signifying a destabilising contribution of non-linear interactions, emerges near the wall from $x_{st}/\delta_0 = 10$ (see arrow in figure 7.7 (f)). This feature is absent in cases s.A and s.B. In case s.C, the elongated contour of $\mathcal{N}_{\beta_0} > 0$ spatially coincides with the location where the near-wall streaks of fundamental wavelength –initially generated at the upper step corner– amplify in x following a brief phase of spatial stabilisation (figure 7.3 (b)). By contrast, in case s.B, the corresponding streaks vanish rapidly in x (figure 7.3 (a)). In results not shown here, a structurally similar elongated contour of the non-linear mechanism is found to manifests also in the perturbation space $n = 0$, i.e., the non-oscillatory component $\beta = 0$, and in the higher-order perturbation spaces such as $n = 3, 4, 5$. The strength of $\mathcal{N}_0 > 0$ in this region is comparable to that of $\mathcal{N}_{\beta_0} > 0$ and exceeds that of the higher harmonics.

The spatial amplification of near-wall streaks in the high-order perturbation modes correlates spatially with regions where $\mathcal{N}_{n\beta_0} > 0$, $n > 2$, near the wall. This is illustrated in figures 7.3 (d) and 7.8 (f) for $n = 3$. Confirmation of a significant growth of the mean-flow distortion at the step in case s.C is provided by the pronounced alteration of the underlying flow topology near the wall. This is apparent when comparing the fields $\boldsymbol{v}_B$ and $\boldsymbol{v}_B + \boldsymbol{v}'_{(0,0)}$, as illustrated by the different organisation of solid cyan and dashed black lines in figure 7.8 (d). These lines represent,

respectively, the loci of inflection points in the crossflow profile of the unperturbed base flow, $\boldsymbol{v}_{\mathrm{B}}$, and the modified flow $\boldsymbol{v}_{\mathrm{B}} + \boldsymbol{v}'_{(0,0)}$. Thus, the present results suggest that a non-linear perturbation effect is responsible for the spatial amplification of the near-wall streaky structures (assessed up to the perturbation space $n = 6$) and the mean-flow distortion sufficiently downstream of the step.

Overall, the dominant mechanisms of perturbation interaction at the step under *large*-amplitude conditions (i.e., case s.C) are summarised as follows:

(*i*) A spatial stabilisation of the fundamental CFI due to a linear effect, specifically the reversal of the mechanism of production close downstream of the step, consistent with the reverse lift-up effect proposed in chapter 5.

(*ii*) A non-linear spatial amplification of near-wall perturbation streaks at the step. Such near-wall streaks are initially induced at the upper step corner by a linear non-modal mechanism (§§ 6.2.1 and 6.2.3) and appear in each individual spanwise perturbation mode (§ 6.2.4). A subset of these streaks (evaluated up to the sixth spanwise mode) undergoes further non-linear amplification in x.

(*iii*) A selective destabilising influence of a family of step-induced inflectional profiles to perturbations with $\beta \leq 2\beta_0$ (non-active) *versus* $\beta > 2\beta_0$ (active). This mechanism induces a reordering of the energetic hierarchy of high-order harmonic spanwise perturbation modes, compared to reference (no-step) conditions.

The significant deformation of the near-wall shear layer downstream of the step, which grows in strength in x and ultimately leads to the formation of the streamwise-momentum deficit region (figure 7.1 (f)), is primarily attributed to mechanisms **(*ii*)** and **(*iii*)** above. By leveraging the decomposition of the perturbation field into spanwise modes, a low-order reconstruction has been performed. The *skeleton* of the rapid modulation in z of successive regions of high- and low-momentum fluid, emerges from the superposition of modes within the range $3\beta_0 \leq \beta \leq 10\beta_0$ (see figure 7.11). As described previously, these modes are subject to the linear destabilising effect of the inflectional mean-flow profiles *farther* from the wall and to the mechanism of non-linear streak amplification very close to the wall.

8

Mechanisms of laminar-turbulent transition

Abstract: *This chapter assesses laminar-turbulent transition in the presence of the forward-facing step. The analysis begins by examining transition advancement and elucidating the mechanisms leading to either supercritical or critical transition. In both cases, transition advancement arises from a novel shear-layer instability at the step. The most critically amplified instability eigenmode feeds growth from the near-wall shear-layer deformed by the interaction between the incoming CFI and the step (chapter 7). In the critical case, the onset of key transitional-flow structures is spatially delayed, thereby positioning the transition front between the supercritical and reference (no-step) scenarios. In the second part, this chapter explores the possibility of transition delay induced by the step, building on the insights from chapters 4 and 5 regarding the potential of the step for stabilising the pre-existing CFI.*

A note on nomenclature: *This chapter discusses both stationary and unsteady effects. The perturbation modes are denoted by* $\boldsymbol{v}'_{(k,j)}$*, where the prime marks perturbation,* k *is the temporal modal index, and* j *is the spanwise modal index. Steady perturbed-flow quantities are denoted by the subscript DB, for example,* $\boldsymbol{v}_{DB}$*. The steady perturbed flow results from the superposition of the unperturbed base flow and the stationary perturbation field. Results from two-dimensional linear stability analysis performed on the steady perturbed flow obtained from DNS are denoted as "BiG".*

Parts of this chapter are published in:

- Casacuberta, J., Hickel, S., and Kotsonis, M., 2023 Laminar-turbulent transition in swept-wing flows with a supercritical forward-facing step. In *ERCOFTAC Workshop Direct and Large Eddy Simulation* (pp. 151-156). Cham: Springer Nature Switzerland.
- Casacuberta, J., Groot, K. J., Hickel, S., and Kotsonis, M., 2025 Direct numerical simulation of swept-wing transition induced by forward-facing steps. Under consideration for publication in *J. Fluid Mech.*

Building on the analysis of stationary perturbation effects, this chapter investigates the mechanisms of laminar-turbulent transition in the presence of the forward-facing step. The first part of the chapter focuses on transition advancement; specifically, § 8.1.1 and § 8.1.2 address supercritical transition (i.e., an abrupt shift of the transition front upstream) and critical transition (i.e., a moderate shift of the transition front upstream), respectively. Both sections include analyses of unsteady perturbation phenomena, instantaneous flow organisation, and the resulting modification of the transition path. Two-dimensional linear stability analysis (see § 2.2.3 and § B.2 in appendix B for details) is employed in all cases to assess the behaviour of unsteady instability modes at the step. The second part of this chapter (§ 8.2) explores the potential for transition delay induced by the step.

In the first part of this chapter (§ 8.1), the flow problems investigated correspond to step case III (supercritical transition) and case II (critical transition), see table 2.3. Consistent with the analysis thus far in this thesis, the step is located at $x/\delta_0 = 177.62$. The influence of the incoming CFI amplitude (table 2.4) on conditioning supercritical transition at the step is assessed. In the second part of this chapter (§ 8.2), the step location is shifted to $x/\delta_0 = 73.90$, see table 2.6. This modification of the step location is exclusive to § 8.2 within the scope of the thesis. The analyses of both the critical transition and transition delay are conducted under *large*-amplitude CFI conditions (table 2.4).

8

8.1. Transition advancement by the step

8.1.1. Supercritical transition

Mean skin friction

First, an overview of the cases is provided using mean-flow metrics. More specifically, the time- and spanwise-averaged skin-friction coefficient is used to segregate between laminar and turbulent regimes. It is evaluated as

$$\langle C_f \rangle = \langle \frac{\overline{\tau_w}}{\frac{1}{2}\rho u_\infty^2} \rangle, \tag{8.1}$$

where $\overline{\tau_w}$ denotes the time-averaged wall-shear stress and $\langle \cdot \rangle$ expresses spanwise-averaging operation. The chordwise evolution of $\langle C_f \rangle(x)$ (8.1) is illustrated in figure 8.1. Table 2.4 defines the amplitude cases considered in this chapter. The height of the step is fixed (see step case III in table 2.3). Black empty circles in figure 8.1 characterise the *large*-amplitude reference (no-step) case, r.*C*. The significant increase of $\langle C_f \rangle$ towards the end of the domain signifies the breakdown of the stationary cross-flow vortices. In case r.*C*, the laminar-turbulent transition front is approximately located at 40% of the chord of the wing model used to guide the DNS set-up (see § 2.1.1), i.e., at $x/\delta_0 \approx 400$. When the step is present for identical amplitude of the incoming stationary CFI, i.e., case s.*C*, the transition front moves drastically to the downstream vicinity of the step (see red empty squares in figure 8.1). However, this does not hold for the *medium*-amplitude CFI case, s.*B* (see red squares with a cross in figure 8.1), indicating that the mechanisms of supercritical transition do not manifest at a *moderate* amplitude of the incoming CFI. For reference, black circles

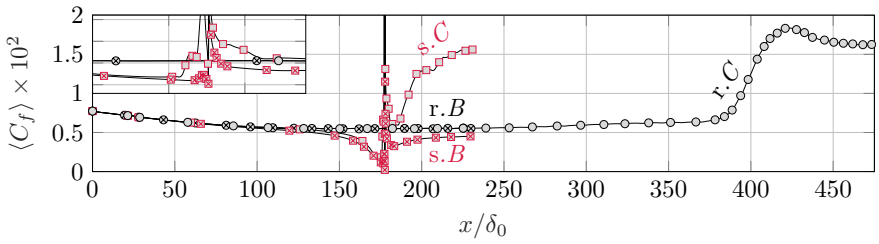

Figure 8.1: Chordwise evolution of the spanwise- and time-averaged skin friction coefficient in the *medium*-amplitude cases r.B (black circles with a cross) and s.B (red squares with a cross) and *large*-amplitude cases r.C (black empty circles) and s.C (red empty squares). Vertical line indicates the step location, and the top inset provides a zoomed view over the range $170 \leq x/\delta_0 \leq 184$.

with a cross represent the amplitude-equivalent no-step case, r.B.

With regard to the overarching discussion in this thesis, experimental work has shown that subcritical (i.e., small), critical (i.e., moderate), and supercritical (i.e., abrupt) movement of the transition front upstream correlate with increasing step height for a fixed amplitude of incoming stationary CFI (Rius-Vidales and Kotsonis, 2021). The present DNS results illustrate that the categorisation of transition regimes in swept-wing flow due to a forward-facing step is not uniquely set by the step height alone, as also observed experimentally (Eppink, 2020). The amplitude of the incoming CFI plays a key role as well; this point is further explored below, building on the insights presented in chapter 7. The remainder of the analysis in § 8.1.1 focuses on *large*-amplitude CFI conditions, under which advancement of laminar-turbulent transition is observed.

Mechanisms of unsteady perturbation at the step

The mechanisms of unsteady perturbation at the step are first assessed quantitatively through temporal probe data, i.e., point-wise measurements of instantaneous velocity. As mentioned above, the present analysis is restricted to the step case s.C that exhibits supercritical transition; the reader is referred to § 2.3.3 for an overview of unsteady perturbation evolution in the amplitude-equivalent no-step case, r.C.

The deformation of the near-wall shear-layer beneath the crossflow vortex's crest (figure 7.1 (f)), is a primary source of unsteady activity. This deformation was identified in chapter 7 as a feature inherent to the steady perturbed flow (§ 7.1) that eventually develops in x into a region of streamwise-momentum deficit. This is first evaluated through power spectral density (PSD) analysis of time-resolved probe data (figure 8.2 (b,c)) at three x-locations immediately downstream of the step, but upstream of laminar breakdown. Additionally, perturbation growth is assessed via the modal decomposition of the perturbation field in the spanwise direction and in time, as defined in equation (2.11).

Unsteady perturbation content at the step appears in both a low-frequency band, peaking at $f \approx 1$ kHz, and a high-frequency band, with peaks at $f \approx 9$ kHz and $f \approx 12$ kHz. Perturbations with $f \approx 12$ kHz primarily develop along the inclined

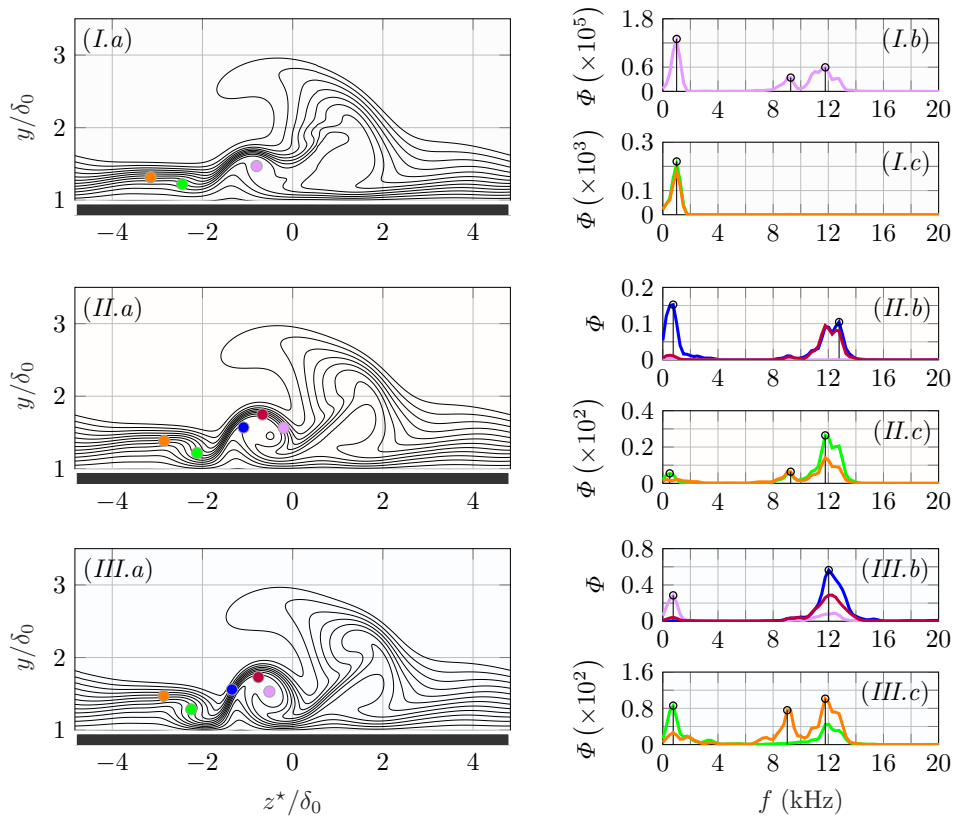

Figure 8.2: Topology of the steady perturbed flow in case s.C (a) and power spectral density, Φ, of temporal probe data (b,c) identified by same colour of a corresponding probe in (a) at $x_{\mathrm{st}}/\delta_0 = 5$ (I), 8 (II), 10 (III). Contours in (a) are isolines of $u_{\mathrm{DB},s}$ (2.7) ranging from 0 to $1.5u_\infty$. The coordinate $z^\star$ indicates a spanwise shift relative to the intersection between the stationary crossflow vortex and the streamwise-momentum deficit region at the step.

lateral shear layer of the streamwise-momentum deficit region at the step (see dark blue probe in figure 8.2), whereas those at $f \approx 9$ kHz are concentrated along the shear layer adjacent to the streamwise-momentum deficit region on the left side (see orange probe in figure 8.2). While low-frequency perturbations initially dominate around the step corner (figure 8.2 (I)), high-frequency perturbations progressively become dominant when moving downstream of the step (figure 8.2 (II,III)). This trend is further illustrated by the amplitude function of unsteady perturbation modes at individual frequencies of $f = 1$ kHz (a) and 12 kHz (b), respectively expressed as $\sqrt{\sum_{j=-13}^{13} |\tilde{u}|^2_{(k,j)}}, k = 1, 12$ in figure 8.3. Consistent with the probe analysis, figure 8.3 shows that higher-frequency perturbations exhibit greater spatial growth rates. Overall, perturbations at $f = 12$ kHz ultimately reach the largest amplitude

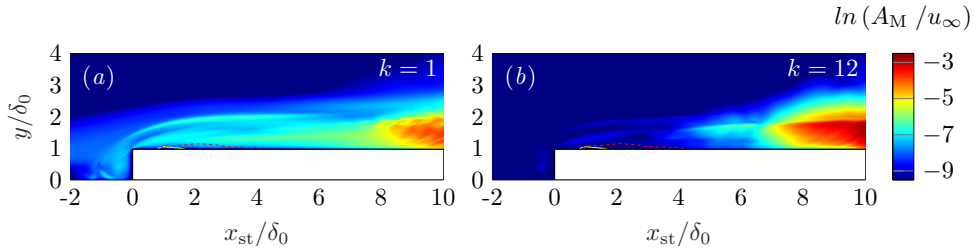

Figure 8.3: Amplitude functions of unsteady perturbation modes: 1 kHz (a), 12 kHz (b), where $A_{\mathrm{M}} = \sqrt{\sum_{j=-13}^{13} |\tilde{u}|^2_{(k,j)}}$. Flow reversal ($u_{\mathrm{DB}} = 0$) in planes of the steady perturbed flow at $z/\delta_0 = -1.7$ (yellow solid line) and $z/\delta_0 = 4.8$ (red dotted line).

downstream of the step.

It may be postulated that the low-frequency unsteadiness at the step represents a manifestation of classic *type*-III secondary crossflow instability, amplified by the deformation of the stationary crossflow vortex at the step. This hypothesis is supported by the organisation of the perturbation shape of the $f = 1$ kHz component around the *base* (see figure 7.1 (f)) of the stationary crossflow vortex, which corresponds to the typical location of *type*-III secondary crossflow instability in no-step conditions (Koch et al., 2000). A potential mechanism involving flapping or breathing of the shear layer at the step (Eppink, 2020), which could contribute to the low-frequency unsteadiness, is not evident in the DNS.

In parallel, the high-frequency perturbations at the step appear to originate from a shear-layer instability, as proposed by Eppink (2020). First and foremost, a correlation is observed between the spatial organisation of major unsteady perturbation structures and the pronounced deformation of the near-wall shear layer downstream of the step. This is illustrated in figure 8.4 (a) depicting the instantaneous organisation of the $f = 12$ kHz unsteady perturbation field (expressed as $\sum_{j=-13}^{13} \tilde{u}_{(12,j)} \mathrm{e}^{\mathrm{i}(j\beta_0 z)} + \tilde{u}_{(-12,j)} \mathrm{e}^{\mathrm{i}(j\beta_0 z)}$) in relation to the embedding flow. As the streamwise-momentum deficit region develops in the chordwise direction, the unsteady perturbation gradually shifts towards its laterally inclined shear layer (see figure 8.4 (*II.a*,*III.a*). It will be shown below that large-scale vortex shedding emanates from this upwelling region of the streamwise-momentum deficit region.

Second, linear stability analysis (see § 2.2.3 and § B.2 in appendix B for details) of the steady perturbed flow identifies three eigenmodes that are explosively unstable at high frequencies (9-12 kHz), and do not manifest under reference (no-step) conditions. These modes are henceforth referred to as *step modes*. Perturbation shapes corresponding to the most unstable instances are shown in figure 8.5, with further characteristics reported in table 8.1. Initially in x, the step modes are located above the reverse-flow region and can be distinguised by the presence of one, two, or three local regions of large $|\tilde{u}_{\mathrm{BiG}}|$ in z, corresponding to their mode index. They are therefore denoted step-mode$_1$, step-mode$_2$, and step-mode$_3$, respectively. The

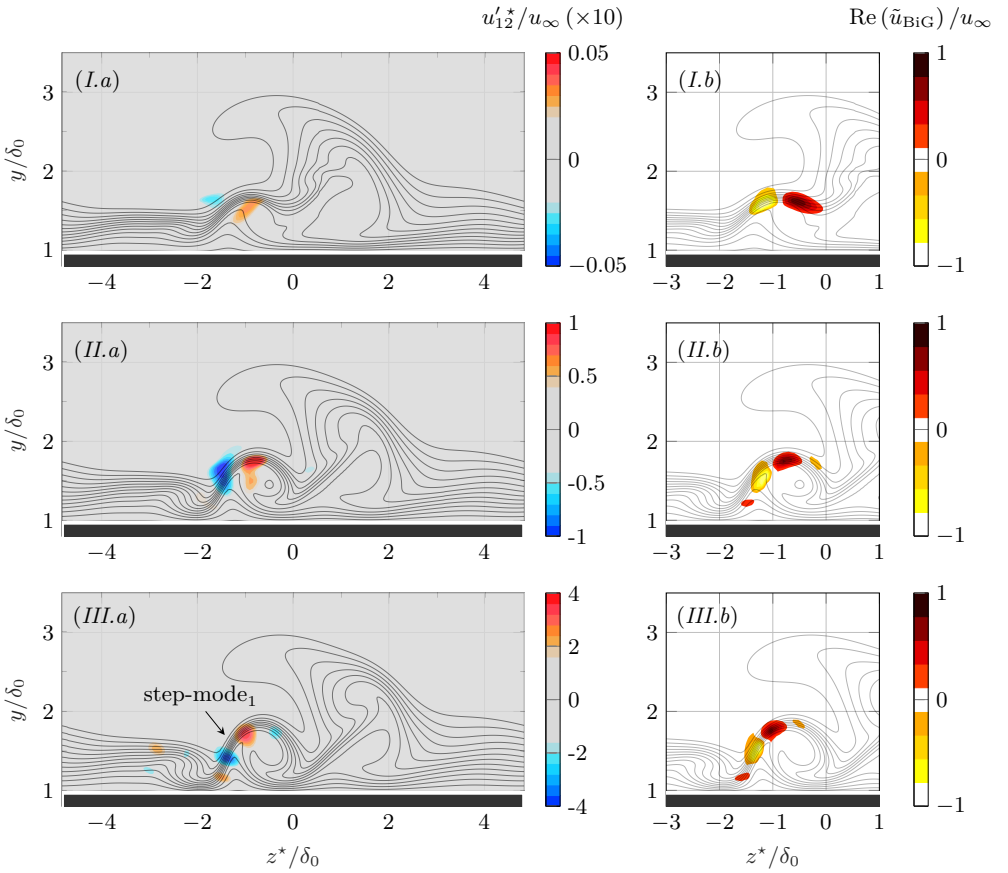

Figure 8.4: Organisation of the $f = 12$ kHz unsteady perturbation field, where $u'^{\star}_{12} = \sum_{j=-13}^{13} \tilde{u}_{(12,j)} \mathrm{e}^{\mathrm{i}(j\beta_0 z)}/u_\infty + \tilde{u}_{(-12,j)} \mathrm{e}^{\mathrm{i}(j\beta_0 z)}/u_\infty$, in case s.$C$ from DNS (a) and real part of the perturbation shape obtained from the local stability approach (b) at $x_{\mathrm{st}}/\delta_0 \approx 5$ (I), 8 (II), 10 (III). Topology of the steady perturbed flow portrayed as isocontours of u_{DB}/u_∞ (ranging from 0 to $1.5u_\infty$) by solid lines in (a,b).

step modes' growth rates ($-\alpha_{\theta,i}\delta_0 \sec\theta$ in table 8.1) are qualified as explosive upon noting that they are a factor 35 larger than the maximum growth rates achieved by the classic secondary crossflow instabilities reported in table 2.8 in § 2.3.3 for no-step conditions. Table 8.1 furthermore specifies the perturbations' wavelength, λ_{x_θ}, phase speed c_{ph}, and group speed c_{g}, all in the direction of the crossflow vortex (i.e., in the non-orthogonal x_θ-direction), which are defined as

$$\lambda_{x_\theta} = \frac{2\pi}{\alpha_{\theta,r}}, \quad c_{\mathrm{ph}} = \frac{\omega_r}{\alpha_{\theta,r}}, \quad c_{\mathrm{g}} = \left.\frac{\partial \omega_r}{\partial \alpha_{\theta,r}}\right|_{\alpha_{\theta,i}}, \tag{8.2}$$

where the subscripts r and i here denote the real and imaginary parts, respectively.

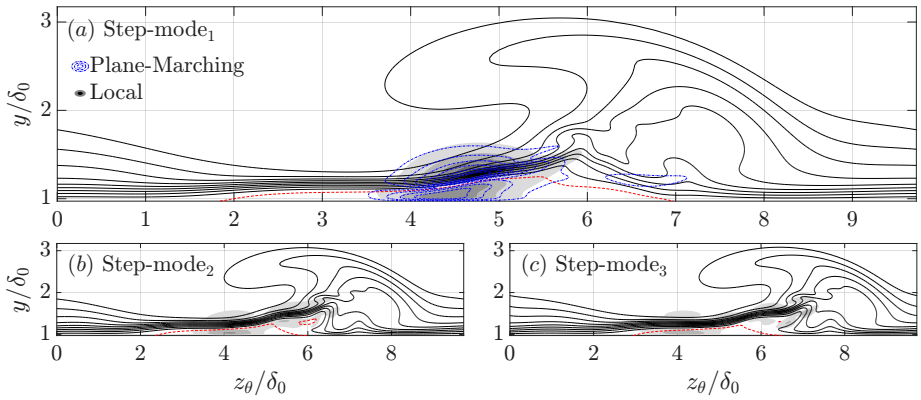

Figure 8.5: Perturbation shape in case s.*C* obtained from the local and plane-marching BiG approaches depicted as $|\tilde{u}_{\mathrm{BiG}}|$-isocontours (1/8, 2/8, ... 7/8 of $\max_{z,y}|\tilde{u}_{\mathrm{BiG}}|$), corresponding to the most unstable instances (x_{st}/δ_0-location corresponding to $\max_x\{-\alpha_{\theta,i}\sec\theta\}$) of CS-modes 1-3 for the frequencies that result in the largest N-factors at $x_{\mathrm{st}}/\delta = 10$ (see details in table 8.1). Isocontours of u_{DB}/u_∞ (solid black: 10%, 20%, ... 90%; dashed red: 0, i.e., flow reversal).

Step-mode	**Method**	f **(kHz)**	$\boldsymbol{x_{\mathrm{st}}/\delta_0}$	$\boldsymbol{-\alpha_{\theta,i}\delta_0\sec\theta}$	$\boldsymbol{\lambda_{x_\theta}/\delta_0}$	$\boldsymbol{c_{\mathrm{ph}}/u_\infty}$	$\boldsymbol{c_{\mathrm{g}}/u_\infty}$
1	BiG local	12	1.19	3.44	1.14	0.70	0.42
1	BiG marching	12	1.19	3.64	1.13	0.69	0.38
2	BiG local	11	2.19	1.78	1.33	0.75	0.58
3	BiG local	9	2.49	1.21	1.74	0.80	0.64

Table 8.1: Most unstable ($\max_x\{-\alpha_{\theta,i}\sec\theta\}$) step mode characteristics for the frequencies that yield the largest N-factors at $x_{\mathrm{st}}/\delta_0 = 10$, obtained using the local or plane-marching BiG approaches (marching step size $s = 0.5\delta_0$, see § B.2 in appendix B) in case s.*C*.

			Step-mode 1			**Step-mode 2**			**Step-mode 3**	
Method	$\boldsymbol{s/\delta_0}$	$\boldsymbol{f}$ (kHz)	11	12	13	9	11	12	9	12
BiG local	–	N	17.35	17.68	17.32	8.79	9.56	9.53	5.64	4.63
	0.5	N	17.01	17.39	16.94					
BiG marching	1.0	N		17.16						
	2.0	N		16.91						

Table 8.2: Linear amplification N-factors at $x_{\mathrm{st}} = 10.38\delta_0$ of unsteady instability eigenmodes using the local or plane-marching BiG approaches in case s.*C*.

Large N-factors are computed for all step modes (table 8.2), at a location upstream of the neutral point of classic *type*-I and *type*-II secondary crossflow instabilities ($x/\delta_0 = 188.4$; plane-marching results for *type*-II, see figure 2.15 in § 2.3.3). How-

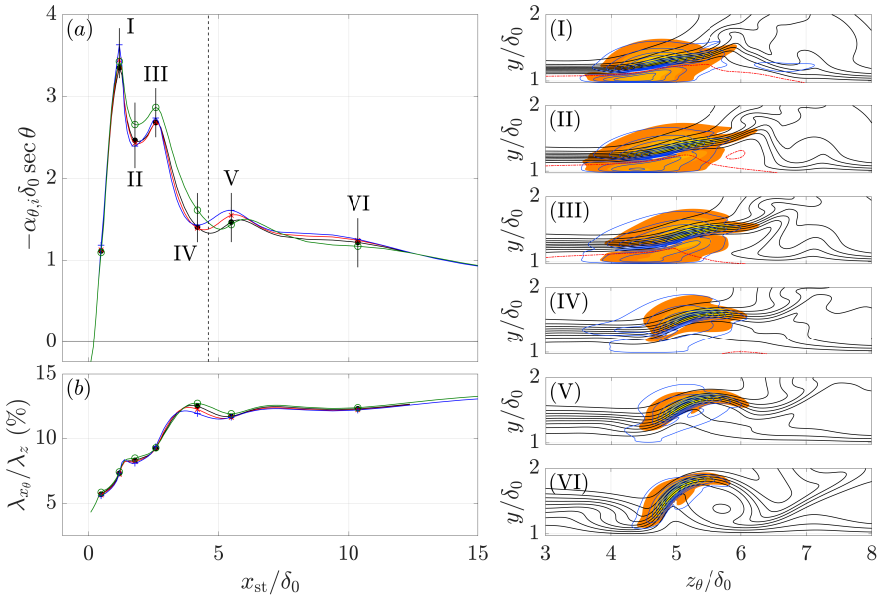

Figure 8.6: Chordwise evolution of the (a) growth rate and (b) wavelength of step-mode$_1$ at 12 kHz as computed with local (green circles) and plane-marching (blue pluses: $s/\delta_0 = 0.5$; red crosses: 1; black dotted: 2) BiG approaches in case s.C. Maximum extent of reverse flow (black dashed line). Panels (I-VI): $|\tilde{u}_{\mathrm{BiG}}|$-isocontours (1/8, 2/8, ... 7/8 of $\max_{z,y}|\tilde{u}_{\mathrm{BiG}}|$) corresponding to step-mode$_1$ at 12 kHz at x-positions indicated in (a,b) as computed with the local (filled contours) and plane-marching (blue isolines: $s/\delta_0 = 0.5$) approach. Isocontours of u_{DB}/u_∞ (solid black: 10%, 20%, ... 90%; dashed red: 0, i.e., reverse flow).

ever, the N-factor achieved by step-mode$_1$ is so much larger than those for step-mode$_2$ (its relative amplitude is $e^{9.53-17.68} = 10^{-3.5}$) and step-mode$_3$ ($e^{4.63-17.68} = 10^{-5.7}$), that the remaining analysis focuses on step-mode$_1$.

The largest amplification factor computed from stability analysis is attained at $f = 12$ kHz (table 8.2). This result is conform with the results from the DNS probe analysis (figure 8.2), which indicates that this frequency component dominates in the DNS at similar x-positions. The shape function of this critical (i.e., most integrally amplified) stability eigenmode, step-mode$_1$ in table 8.2, is ultimately concentrated in x along the shear layers of the streamwise-momentum deficit region that forms downstream of the step (figure 7.1 (f)). This is illustrated in figure 8.4 (b), which compares the chordwise evolution of the eigenmode, as obtained from the local BiG stability approach, with the perturbation field from DNS. The associated growth rates (a) and chordwise perturbation wavelengths (b) of step-mode$_1$ from stability analysis are given in figure 8.6. This provides evidence that step-mode$_1$ is initially significantly destabilised by the local deformation of the shear layer at the upper step corner, where regions of flow recirculation are present (see figure 8.6 (a) in the range $0 \leq x_{\mathrm{st}}/\delta_0 \leq 5$). Further downstream, as it amplifies on the deformed near-wall

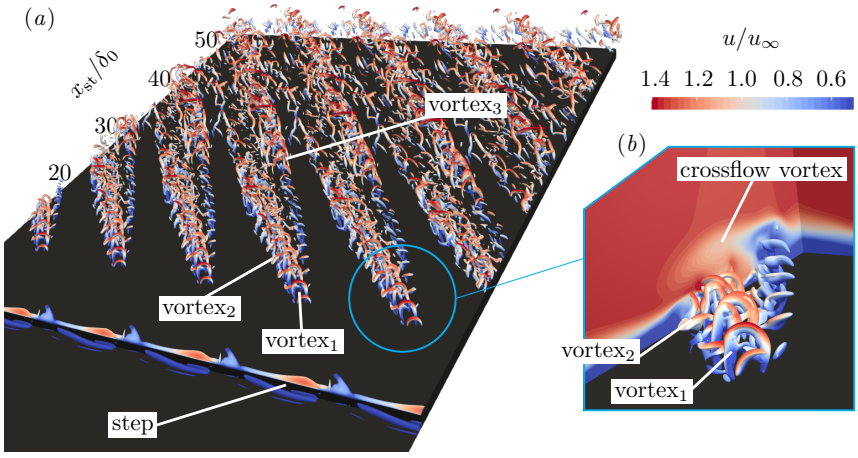

Figure 8.7: Instantaneous flow organisation at the step for case s.C characterised by Q-criterion isosurface ($Q\delta_0/u_\infty = 0.8$) coloured with chordwise velocity (a). Zoom with x-y, y-z planes of chordwise velocity (b). The data are duplicated four times in z for illustration purposes (a).

shear layer, the shape of step-mode$_1$ resembles the perturbation recovered from DNS (figure 8.4 (*III.a*)), albeit notable differences in perturbation shape between DNS and the local stability approach are observed during the early stages of the eigenmode development (figure 8.4 (*I*,*II*)).

8

Instantaneous flow organisation

The spatial amplification of high-frequency instabilities in the deformed near-wall shear layer downstream of the step precedes the onset of large-scale vortex shedding. Unsteady vortical structures are observed directly at the step only in case s.C, while in case s.B, no significant unsteadiness is present. In case s.C, the onset of laminar-turbulent transition is marked by spanwise-periodic wedges of unsteady contamination inclined along the crossflow-vortex direction. This is illustrated in figures 8.7 and 8.8, which depict isosurfaces of Q-criterion (Hunt et al., 1988) at the step.

Three main families of unsteady vortical structures are identified in the instantaneous flow. First, large-scale hairpin vortices shed from the streamwise-momentum deficit region, labelled vortex$_1$ in figure 8.7. Specifically, the inception region of vortex$_1$ spatially correlates with the *shape* of the critical unsteady perturbation –namely, step-mode$_1$ at $f = 12$ kHz– on the deficit region, as computed by linear stability analysis. Second, vortical structures of a rather *amorphous* shape emerge from the shear layer adjacent to the streamwise-momentum deficit region on the left side, developing spatially very close to the wall. These are labelled vortex$_2$ in figure 8.7. Third, a second family of large-scale hairpin vortices form along the shear layer of the distorted *base* (see figure 7.1 (f)) of the stationary crossflow vortex. These are labelled vortex$_3$ in figure 8.7. The fully developed form of vortex$_3$ appears significantly farther downstream ($x_{st}/\delta_0 > 20$) compared to vortex$_1$ ($x_{st}/\delta_0 \approx 10$) as

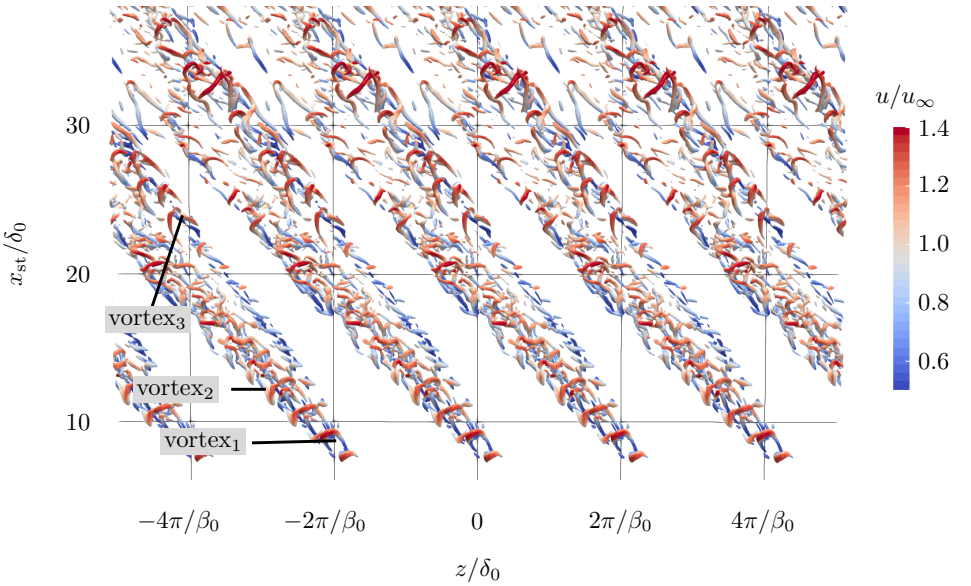

Figure 8.8: Instantaneous flow organisation at the step for case s.C characterised by Q-criterion isosurface ($Q\delta_0/u_\infty = 0.8$) coloured with chordwise velocity The data are duplicated four times in z for illustration purposes.

shown in figures 8.7 and 8.8.

The rapid upward shift of vortex$_1$ and vortex$_3$ in x is a key feature of the vortical evolution at the step. This is elaborated as follows: the primary hairpin vortices induced at the streamwise-momentum deficit region, vortex$_1$, ascend in x towards the upper shear layer of the stationary crossflow vortex. Under reference (no-step) conditions, this upper region is typically associated with the *type*-II secondary crossflow instability (Malik et al., 1999). Similarly, for $x_{st}/\delta_0 > 40$, the secondary hairpin vortices, vortex$_3$, shift upward in x and become immersed in the upper inclined shear layer within the upwelling region of the stationary crossflow vortex (see region labelled as *shoulder* in figure 7.1 (f)). This shear layer typically feeds growth to the *type*-I secondary crossflow instability, see § 2.3.3. This effect provides a plausible explanation for the significant unsteady activity measured by Rius-Vidales and Kotsonis (2021) in the boundary-layer region traditionally linked to the classic *type*-I secondary crossflow instability, albeit the *type*-I mechanism does not appear in the transitional flow from DNS in this x-region.

The power spectral density of temporal probe signals from DNS flattens, signifying turbulence inception, from approximately $x_{st}/\delta_0 = 15$. This trend is quantified in probe measurements taken near the interaction between vortex$_1$ and vortex$_2$, to which the inception of turbulence is attributed in the first place. Probe measurements near vortex$_3$ exhibit spectral flattening at a more downstream location. Therefore, both the DNS and experimental work (Rius-Vidales and Kotsonis, 2022) indicate that

laminar-turbulent transition under supercritical step conditions originates from the *inner side* of the crossflow vortex; that is, the side of the vortex adjacent to the streamwise-momentum deficit region.

Discussion on the laminar-turbulent transition path

The classic routes to turbulence in reference wall conditions (i.e., without surface features) are summarised in the well-known diagram of Morkovin et al. (1994) (see figure 8.9 (*a*)). More recently, Crouch (2022) presented an analogous diagram of transition routes for non-ideal walls (i.e., with surface features), shown in figure 8.9 (*b*) with adaptations: a low-disturbance environment is assumed, and the level of surface-induced flow distortion is introduced as main control parameter. Crouch (2022) redefines the classic path "A" of Morkovin et al. (1994) by sub-dividing it into "A_1", which characterises surface receptivity effects, and "A_2", which accounts for the influence of surface-induced modifications on the growth of existing primary eigenmodes. Furthermore, the diagram in figure 8.9 (*b*) proposes that, in the presence of surface features, the transition route switches directly from "A_1" or "A_2" to "E", since *transient*-growth (or, *non-modal*) effects may occur, but do not alter the transition route (Crouch, 2022). The results of this thesis appear to challenge this claim, as discussed below.

The deformation of the near-wall shear layer downstream of the step arises from the combined effect of (1) the growth of locally formed non-modal perturbation streaks very close to the wall and (2) the destabilisation of high-order harmonic modes of the incoming CFI through an inflectional mechanism farther from the wall (§ 7.3). The analysis in the present chapter has shown that the shear layers adjacent to the crossflow vortex on its inner side (i.e., beneath its crest) support the spatial amplification of secondary unsteady instability eigenmodes that originate from the reverse-flow region. Furthermore, it is demonstrated that the vortex-shedding mechanism leading to transition to turbulence develops if, and only if, the primary incoming CFI has sufficient amplitude (for fixed step height). Consequently, two flow cases with identical surface-step geometry and free-stream receptivity conditions, but differing only in the amplitude of the incoming CFI, may exhibit fundamentally different transition scenarios. This is demonstrated by case s.B (no supercritical transition) *versus* s.C (supercritical transition).

The sequence of physical processes described in the previous paragraph highlights the key role played by non-modal growth in enabling supercritical transition induced by the step. Here, *non-modal growth* refers to the mechanisms responsible for generating the near-wall perturbation streaks at the step, as described in chapter 6 and § 7.2. It bears emphasising the role of these near-wall perturbation streaks. As discussed in § 7.3, the deformation of the near-wall shear layer is a feature of the *total* flow (i.e., base flow plus perturbation) that supports the growth and breakdown of secondary unsteady instabilities. The near-wall streaks, in contrast, belong to the stationary perturbation field and partly underlie the deformation of the near-wall shear layer.

As such, the transition path discussed here exhibits a distinctive twofold character. First, the non-modal growth, manifesting as the perturbation streaks at the

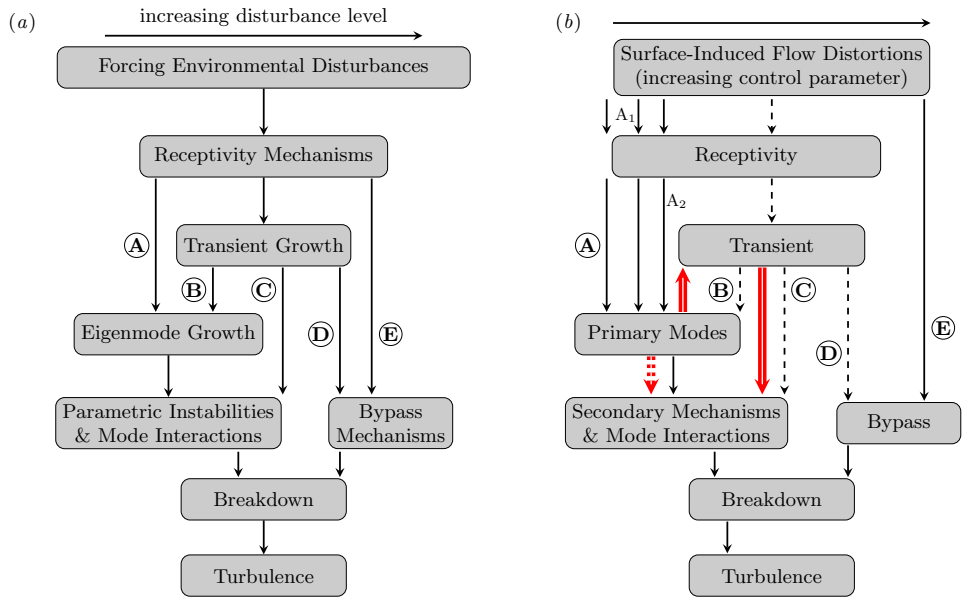

Figure 8.9: Paths to turbulence in boundary-layer flow as a function of: (*a*) the external disturbance level (Morkovin et al., 1994) and (*b*) the surface-induced flow distortion in a low-disturbance environment (Crouch, 2022). Thick (dotted and solid) red arrows in (*b*) indicate the model of supercritical transition due to the step proposed in this thesis. Diagrams reproduced after (*a*) Morkovin et al. (1994) and (*b*) Crouch (2022). The dashed arrows in (*b*) for routes "B", "C", and "D" indicate the original claim by Crouch (2022) that transient-growth effects do not alter the transition route.

step, partially sets the conditions for secondary instability growth. Second, this non-modal growth originates from the growth of primary eigenmodes, namely the incoming CFI. This contribution is represented by the red solid arrows in figure 8.9 (*b*). At the same time, the growth of non-modal streaks contributes only partially to establishing the conditions for breakdown; the local destabilisation, through an inflectional mechanism, of the high-order harmonic modes accompanying the fundamental CFI also plays a role in this process (§ 7.3). The dual contribution to the secondary mechanisms is represented by the red dotted arrow in figure 8.9 (*b*).

With the advent of non-modal stability theory, the flow stability community debated how to reconcile classic concepts of non-linearity and secondary instability mechanisms with *moderate*-amplitude non-modal perturbations (see, for instance, Henningson et al. (1990), Breuer and Landahl (1990), and Henningson et al. (1993)). For further discussion on the *transient* role of stationary perturbations induced by the surface feature itself, the reader is referred to White et al. (2005). Building on the insights from chapter 6 and § 7.3, a parallel can be drawn between supercritical transition due to the step and the description of localised perturbations in boundary-layer flow by Breuer and Landahl (1990): "even a modest spanwise structure [here the cross-stream pattern of the incoming CFI, characterised by $\boldsymbol{v}_n$ in equa-

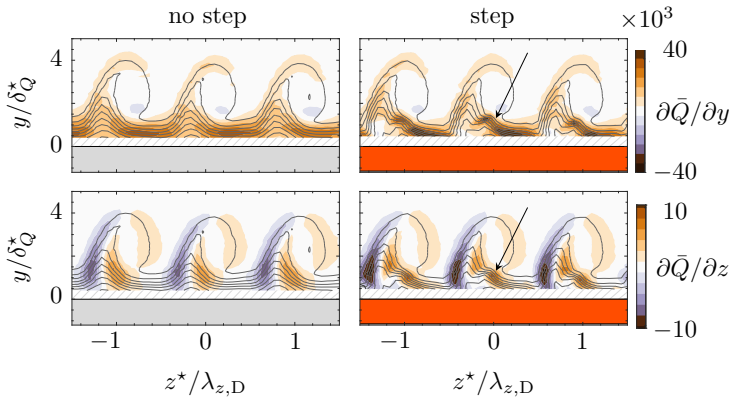

Figure 8.10: Wind tunnel measurements of crossflow vortices in reference no-step conditions (*left*) and step conditions (*right*) at the same location of wing chord downstream of the step. Colour contours of wall-normal (*top*) and spanwise (*bottom*) gradients of time-averaged velocity, $\bar{Q}$, and isolines of $\bar{Q}$, where Q indicates velocity measured through a hot wire probe. The $z^\star$ is the direction of wing span, $\delta^\star_Q$ is a metric of displacement thickness, and $\lambda_{z,\mathrm{D}}$ is the wavelength of CFI. Solid grey and orange areas respectively depict the surface without and with the step present and dashed grey area indicates no data. Arrows indicate the deformation of the near-wall shear layer on the inner side of the crossflow vortex, as identified in the DNS. Adapted from Rius-Vidales and Kotsonis (2022) with permission.

tion (3.12)] can, in the presence of a strong mean shear [here the highly sheared step flow], produce large-amplitude horizontal perturbations [here the near-wall streamwise streaks]. Despite the initial linear character of the disturbance, non-linear effects are quick to establish themselves and we see both the distortion of the 'mean' profile and the growth of secondary instabilities as the disturbance evolves."

Transition advancement due to the step entails a modification of the transition path, relative to the reference (no-step) scenario (figure 8.9 (*b*)). Key elements supporting this alteration of the transition path are consistent with wind-tunnel experiments. First, a pronounced deformation of the near-wall shear layer on the inner side of the crossflow vortex, is confirmed in the time-averaged flow measurements of Rius-Vidales and Kotsonis (2022) (see figure 8.10 adapted from their work). Rius-Vidales and Kotsonis (2022) further note that the pronounced deformation of the near-wall shear layer beneath the crossflow vortex's crest is specific to the set of experiments exhibiting supercritical transition (cf. their figure 5). This observation aligns with the identification that critical unsteady fluctuations –leading to laminar breakdown– develop spatially in this portion of the near-wall shear layer (Rius-Vidales and Kotsonis, 2022). Second, Eppink (2020) attributes laminar breakdown at the step to vortex shedding downstream of the reattachment point of the recirculating-flow region, a mechanism also identified by the DNS (figures 8.7 and 8.8).

Notwithstanding the joint identification of major flow structures between experimental reports and DNS, the nature of the unsteady perturbations that initiate vortex shedding at the step remains an open question. Eppink (2020) attributes the

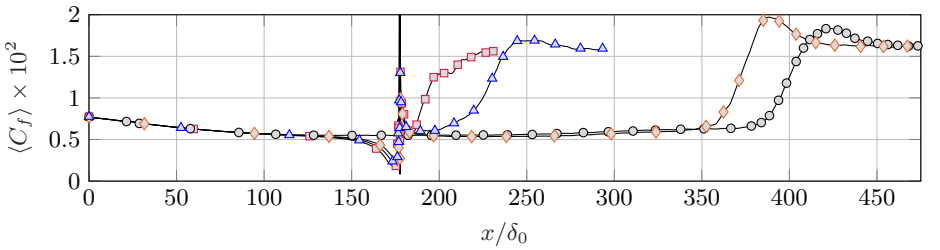

Figure 8.11: Chordwise evolution of the spanwise- and time-averaged skin friction coefficient under *large*-amplitude CFI conditions: reference (no-step) case (black circles), step cases I (orange diamonds), II (blue triangles), and III (red squares). Vertical line indicates the step location.

origin of the higher-frequency perturbations to a shear layer instability, a view supported by the results of this chapter. Moreover, the findings in this chapter further align with the primary observations of Rius-Vidales and Kotsonis (2022) that the frequency content and spatial organisation of critical unsteady fluctuations downstream of the step do not reconcile with those of classic secondary crossflow instabilities. This discrepancy implies the presence of a novel unsteady mechanism introduced by the step, as confirmed by the analysis in this chapter.

8.1.2. Critical transition

Mean skin friction and topology of the steady perturbed flows

Figure 8.11 confirms that the three step heights investigated in this thesis (see table 2.3) induce subcritical ($h/\delta_0 = 0.59$), critical ($h/\delta_0 = 0.76$), and supercritical ($h/\delta_0 = 0.97$) transition, as anticipated. This classification is based on the upstream shift of the transition front, see Rius-Vidales and Kotsonis (2021) for reference, here assessed through the evolution of the mean skin-friction coefficient along the chordwise direction (8.1). Building on the insights from § 8.1.1, it should be emphasised that the regime classification based on step height depends on the selected amplitude of the incoming stationary CFI. The present section focuses on the mechanisms of critical transition under *large*-amplitude CFI conditions (see table 2.6); that is, under the same amplitude conditions as the supercritical case analysed in § 8.1.1.

First, figure 8.12 presents the topology of the steady perturbed flow past the step. In particular, planes of flow at $x_{st}/\delta_0 = 9.4$ are shown, i.e., replicating the layout of figure 7.1 illustrating the supercritical scenario. Data from the subcritical case are also included for reference (figures 8.11 and 8.12), although a detailed analysis of the associated transition mechanisms falls beyond the scope of this section. Overall, figure 8.12 (*a-c*) illustrates the progressive development of the near-wall shear-layer deformation with increasing step height. Ultimately, this deformation attains its most pronounced form in the case with the largest step tested, where the development of a streamwise-momentum deficit region becomes evident (figure 7.1 (*f*)).

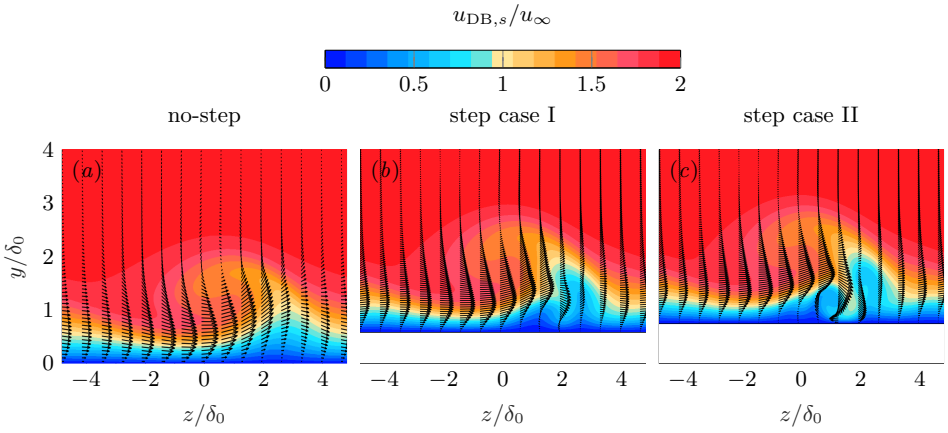

Figure 8.12: Topology of the steady perturbed flow illustrated by z-y planes of velocity $u_{\mathrm{DB},s}$ at $x_{\mathrm{st}}/\delta_0 = 9.4$ considering *large*-amplitude CFI conditions: no-step case (a), step case I (b), step case II (c). The black arrows illustrate the in-plane organisation of the steady perturbed flow ($w_{\mathrm{DB},s}$ and v_{DB}).

Mechanisms of unsteady perturbation at the step

The two-dimensional linear stability analysis introduced in § 8.1.1 to examine the mechanisms of supercritical transition is extended in the present section. Specifically, the stability problem is at present solved using the steady perturbed flow corresponding to the critical step case. The analysis carried out in this section employs the local approach to BiG, see § 2.2.3.

The results of the stability analysis confirm the existence of (at least one) unsteady instability eigenmode, supported by the near-wall shear layer downstream of the step. The behaviour of this eigenmode closely resembles that of step-mode$_1$, previously identified as a main agent driving supercritical transition (see § 8.1.1). Specifically, the eigenmode shape is concentrated within the region of low momentum beneath the crest of the stationary crossflow vortex (figure 8.12 (c)). Furthermore, the eigenmode is qualified as *explosive*, in that it attains a very large N-factor in a short x-distance. Considering the multiple similarities, the newly identified unsteady instability arising under critical step conditions is hereafter also referred to as step-mode$_1$. Following the analysis in § 8.1.1, the subscript '1' denotes the most amplified eigensolution of the local family of *step modes* introduced by the step.

Selected results of the stability analysis are summarised in figure 8.13, which compares the critical and the reference (no-step) cases; results from the subcritical case are additionally included for completeness. In particular, figure 8.13 (a) quantifies the amplification factor of two main families of eigensolutions. Namely, the newly identified step-mode$_1$, represented by the curves concentrated near the step x-location (denoted with closed symbols) and the classic *type*-I secondary crossflow instability, represented by the curves situated farther downstream (denoted with open symbols). For clarity, *type*-II and *type*-III eigenmodes are omitted from figure 8.13, as there is

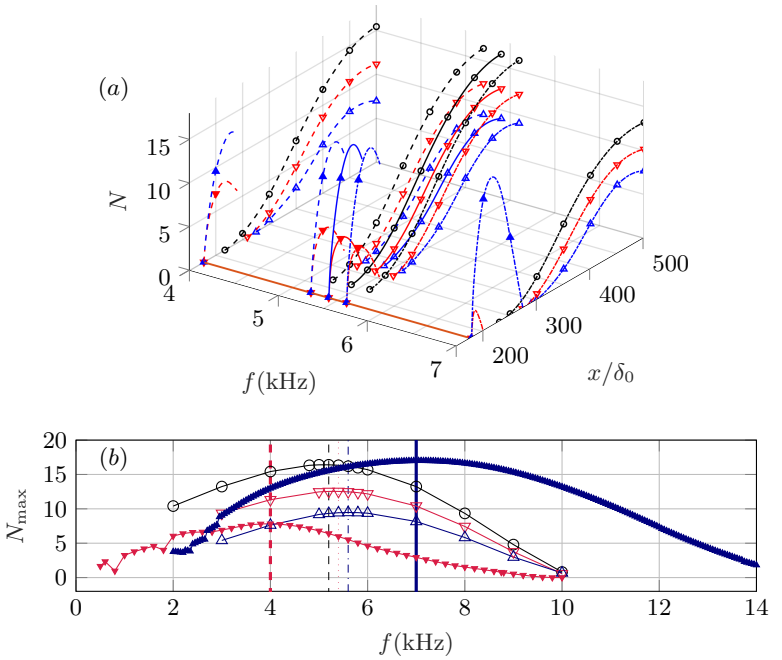

Figure 8.13: (*a*) Amplification factor of the *type*-I instability (curves *far* from the step with open symbols) and the step-mode$_1$ (curves *near* the step with filled symbols) as a function of the perturbation frequency and chordwise position: reference no-step (black circles), subcritical (red downward-pointing triangles), and critical (blue upward-pointing triangles) conditions. *Large*-amplitude CFI conditions are considered (table 2.4). The orange line indicates the step x-location. (*b*) Maximum amplification factor over all x as a function of perturbation frequency for *type*-I (open symbols) and step-mode$_1$ (filled symbols): reference no-step (black circles), subcritical (red downward-pointing triangles), and critical (blue and upward-pointing triangles) conditions. Vertical lines indicate peak locations for *type*-I (thin) and step-mode$_1$ (thick).

no evidence suggesting their significant contribution to the transition process in the critical case.

Under critical conditions, the step-mode$_1$ remains spatially confined to the region immediately downstream of the step (figure 8.13 (*a*)), i.e., it forms an unstable eigensolution exclusively for $x_{st} \leq x \leq 230\delta_0$. It exhibits a very large amplification factor, which is greater than that of subcritical conditions (figure 8.13 (*a*)), but lower than supercritical conditions (§ 8.1.1). Unlike the *type*-I instability, the (maximum) frequency response of the step-mode$_1$ is sensitive to the step height. That is, the largest amplification factor of the step-mode$_1$ shifts from approximately 4 kHz in the subcritical case to around 7 kHz in the critical case. This behaviour is illustrated in figure 8.13 (*b*), which summarises the influence of perturbation frequency on the maximum amplification factor attained (i.e., the peak N-factor across all x-positions).

Finally, figure 8.13 also shows that the *type*-I instability is actually stabilised (in an integral sense) by the presence of the step. This observation forms the basis for

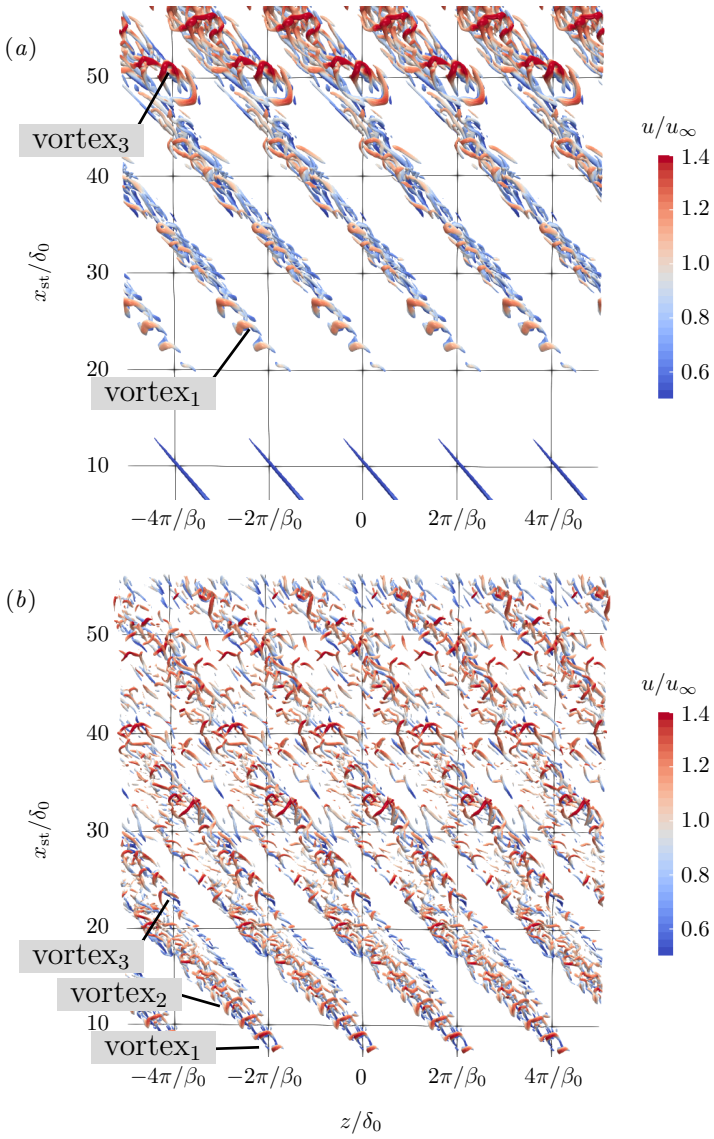

Figure 8.14: Instantaneous flow organisation at the step under *large*-amplitude CFI conditions (table 2.4) characterised by Q-criterion (Q) isosurface, coloured with chordwise velocity in the critical ((*a*), $Q\delta_0/u_\infty = 0.1$) and supercritical ((*b*), $Q\delta_0/u_\infty = 0.8$) cases. The data are duplicated four times in z for illustration purposes. Panel (*b*) here is identically figure 8.8 above.

the discussion in § 8.2, which explores transition delay induced by the step.

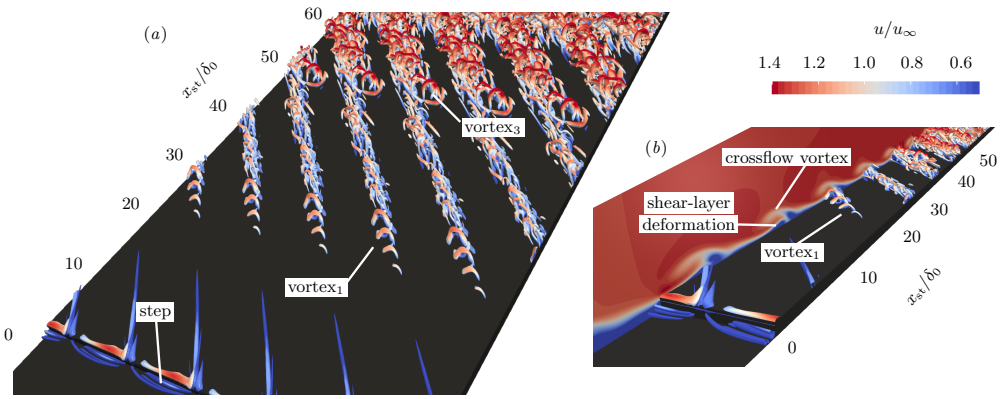

Figure 8.15: Instantaneous flow organisation at the step characterised by Q-criterion isosurface ($Q\delta_0/u_\infty = 0.1$) coloured with chordwise velocity (a). Zoom with x-y plane of chordwise velocity (b). *Large*-amplitude CFI conditions are considered. The data are duplicated four times in z for illustration purposes (a).

Discussion on the laminar-turbulent transition path

In the reference (no-step) case at *large*-amplitude CFI conditions, transition is driven by the amplification of the *type*-I secondary crossflow instability (see § 2.3.3). Under supercritical step conditions, the growth of classic secondary crossflow eigenmodes is *bypassed* by the novel unsteady mechanism originating at the step (§ 8.1.1). The present DNS results reveal that the critical and supercritical scenarios essentially follow the same transition path. Nonetheless, the spatial growth rate of the key perturbation structures is reduced in the critical case, which effectively results in a downstream shift of the turbulence onset region, compared to the supercritical case.

The comparative features of the critical and supercritical cases are elaborated as follows: in the supercritical case, the pronounced deformation of the near-wall shear layer sustains the amplification of secondary instability eigenmodes developing locally at the step. Following the stage of linear eigenmode growth and the subsequent vortex shedding, turbulence inception is first observed near the interaction of two dominant vortical structures: the vortex$_1$ and vortex$_2$ (see figures 8.7 and 8.8). In the critical case, a near-wall deformation of the shear layer –structurally resembling that of the supercritical case introduced in chapter 7– also emerges (figure 8.12 (c)). However, it exhibits smaller spatial extent, relative to the supercritical case; consequently, the stability analysis finds that step-mode$_1$ is less unstable in the critical case. In the DNS, the vortex$_1$ is still identifiable in the instantaneous organisation of the critical step flow, but its formation is delayed compared to the supercritical case, and its spatial development spans a broader chordwise region (figure 8.15).

In addition, vortex$_2$ is either absent or significantly weakened under critical conditions. Correspondingly, inspection of the instantaneous flow organisation reveals that, in contrast to the supercritical case, the pronounced spanwise spreading of the unsteady contamination wedges forming downstream of the step does not origi-

nate from the inner side of the stationary crossflow vortex; i.e., the z-location where vortex_1 and vortex_2 interact. Instead, the significant spanwise spreading of unsteady contamination in the critical case is preceded by the interaction between vortex_1 and vortex_3 (see figure 8.15 (a)).

The vortex_3 –which originates on the crossflow vortex and was previously linked to the deformation of its *base* (see figure 7.1 (f) and the analysis in chapter 7)– emerges downstream of the point of inception of vortex_1 and vortex_2 in both the critical and supercritical cases. Due to the combination of these effects, transition in the critical case is delayed relative to the supercritical case, yet still occurs upstream of the *type*-I-driven transition observed in the reference (no-step) configuration.

8.2. Transition delay by the step

The analysis presented thus far has addressed the two main research questions of this thesis, which concern the mechanisms of stationary interaction at the step and the advancement of laminar-turbulent transition. This section now turns to design strategies for preserving laminar flow when a step is present (§ 1.4). In this regard, a series of findings established throughout this thesis (primarily concerning chapters 4 and 5) have motivated a numerical experiment to explore transition delay.

8.2.1. Observations and hypothesis

The proposed numerical experiment is grounded in the following observations:

- **(*i*)** The interaction between the incoming stationary CFI and the step is locally stabilising under certain conditions; i.e., it can be conditioned to induced a spatial decay of perturbation kinetic energy over a short chordwise region (see §§ 5.1 and 5.3).

- **(*ii*)** In the scenario where process **(*i*)** occurs, the *growth characteristics* of the incoming instability are modified downstream of the region of energy decay. Specifically, the perturbation growth rate does not immediately returns towards that of the reference (no-step) case; instead, it remains reduced over an extended chordwise region downstream of the step. It is noted that observation **(*ii*)** has been reported subsequent to process **(*i*)**; however there is no basis to assume that process **(*ii*)** is exclusively contingent upon the occurrence of **(*i*)**.

- **(*iii*)** The mechanisms responsible for either a moderate (critical) or an abrupt (supercritical) advancement of the transition front are primarily supported by a flow feature structurally independent of the stationary CFI, namely the pronounded deformation of the near-wall shear layer (§ 7.1). This (stationary) shear-layer deformation at the step is, in the first instance, driven by linear perturbation effects (see chapter 6 and § 7.3).

Building on these observations, the following hypothesis is formulated: it is possible to **hinder** the amplification of high-frequency secondary crossflow instabilities, and thus to **passively delay transition**, by inhibiting the growth of the stationary crossflow vortex through its interaction with the step. Transition delay, in this

framework, is contingent upon preventing the adverse effects associated with the amplification of secondary instability eigenmodes in the downstream vicinity of the step, as elaborated throughout this thesis. The development of these eigenmodes forming at the step may be **prevented** if the step interacts with a stationary crossflow vortex of **sufficiently small amplitude**, since the stationary deformation of the near-wall shear layer at the step is driven initially by linear perturbation effects.

8.2.2. Formulation of the numerical experiment

The previous hypothesis is tested through a dedicated numerical experiment, namely a Direct Numerical Simulation of a step case. The numerical methodology employed in this thesis to investigate the mechanisms of transition advancement is adopted here without modification. However, the step height and its chordwise location (see table 2.6) are adjusted to produce a flow environment adjusted to the hypothesised delay of transition. To maintain consistency with the transition analysis carried out throughout this thesis, the initial amplitude assigned to the crossflow eigenmode is kept constant and reproducing *large*-amplitude CFI conditions (see table 2.4).

The step is placed at $x/\delta_0 = 73.90$, within the region of linear CFI growth (see figure 2.11 (c)), and its height is set to $h/\delta_0 = 0.76$. These parameters yield approximately matching conditions in terms of both the amplitude of the fundamental CFI at the step location and the step-to-boundary-layer-thickness ratio, $h/\delta_{99,h} = 0.54$, relative to the configuration analysed in chapter 5, which reported inhibited CFI growth following a significant modification of the perturbation organisation at the step. The current setup results in a roughness Reynolds number of $Re_{hh} = 563.08$, see table 2.3 for a comparison with the main cases analysed in this thesis.

8.2.3. Results

A summary of the key results obtained from the numerical experiment is presented in figure 8.16. A detailed discussion of these results, along with their engineering implications, will be addressed in § 9.2, in the context of the outlook of this thesis.

First, figure 8.16 (a) confirms that the fundamental CFI exhibits a reduced spatial growth rate, compared to the reference (no-step) case, as a result of its interaction with the step. This behaviour is measured over a chordwise extent of $176\delta_0$, that is, approximately 15% of the chord of the reference wing model (§ 2.1.1). Figure 8.16 (b-g) shows a corresponding reduction in the strength of the spanwise shear layer of the stationary crossflow vortex far downstream of the step.

On reproducing the analysis of chapter 5, it is observed that the distortion of the perturbation organisation at the step –setting the conditions for the subsequent inhibition of CFI growth– alters the behaviour of the production mechanism, but it occurs without explicitly reversing the sign of the production term. In this regard, the reverse lift-up effect identified in this thesis (§ 5.3) is a limiting case of significant perturbation distortion at the step, one that results in a local decay of perturbation kinetic energy, but is not a necessary condition for the inhibited downstream growth of the CFI observed here.

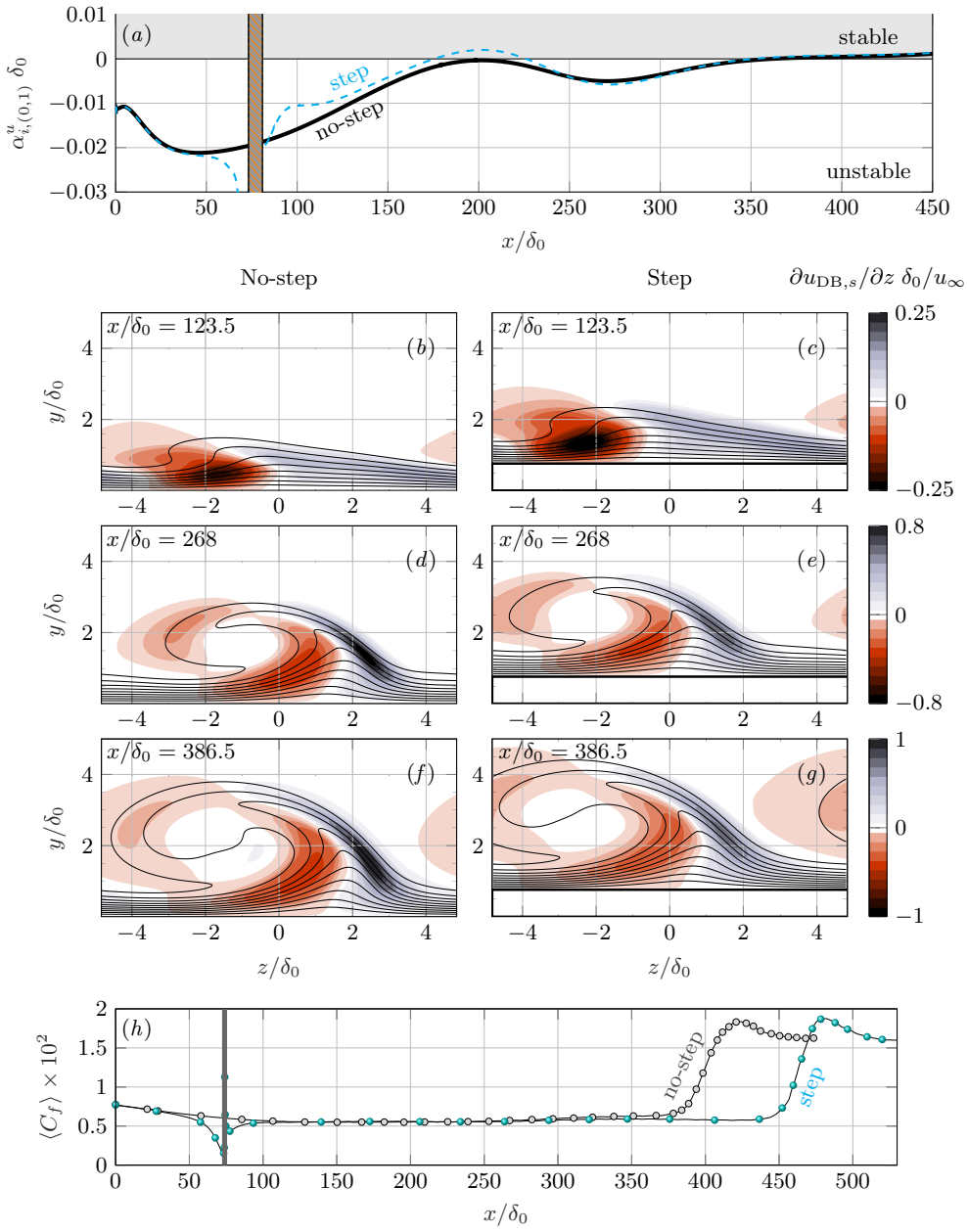

Figure 8.16: Metrics of the transition delay case in *large*-amplitude CFI conditions: (*a*) chordwise evolution of the growth rate of the fundamental CFI in step (dashed cyan) and no-step (solid black) cases. Dashed orange area indicates the x-range dominated by the near-wall streaks at the step. (*b*-*g*) Topology of the stationary crossflow vortex characterised by isolines of $u_{\mathrm{DB},s}$ ranging from $0.2u_\infty$ to $1.4u_\infty$ (solid black) with colour contours indicating the spanwise gradient of velocity $u_{\mathrm{DB},s}$ in the step (right) and no-step (left) cases at $x/\delta_0 = 123.5$ (*b*,*c*), 268 (*d*,*e*), and 386.5 (*f*,*g*). (*h*) Chordwise evolution of the spanwise- and time-averaged skin friction coefficient in the step (cyan spheres) and no-step (black circles) cases. Vertical line indicates the step location.

Transition is ultimately driven by the amplification of the *type*-I secondary crossflow instability, indicating that, in this context, the transition path remains unaltered by the presence of the step. At the same time, the weakening of the spanwise shear layer of the stationary crossflow vortex is postulated to shift the neutral point downstream and/or reduce the spatial amplification factor of the *type*-I secondary instability eigenmode. As a results, a measurable transition delay is observed, corresponding to 5% of the chord of the reference wing model (figure 8.16 (*h*)).

III

Epilogue

9

Conclusions and outlook

9.1. Conclusions

9.1.1. Stationary interaction between a forward-facing step and a pre-existing stationary crossflow instability

This thesis first examined the purely stationary interaction between a forward-facing step and the stationary crossflow instability (CFI) of laminar, incompressible swept-wing boundary-layer flow by performing steady-state Direct Numerical Simulations (DNS). Specifically, it qualitatively and quantitatively assessed the salient flow structures and mechanisms supporting and conditioning the regimes of CFI growth and decay upstream and downstream of the step. The tested steps reached approximately 30 to 50% of the undisturbed boundary-layer thickness, corresponding to roughness Reynolds numbers (Re_{hh}) ranging from 368 to 832. To gain physical insight, the stationary perturbation field was Fourier analysed in the leading-edge-parallel (spanwise) direction and decomposed into spanwise modes.

Mathematical and physical frameworks

This thesis advocated analysing the behaviour of stationary perturbations by decomposing the perturbation field relative to the base-flow orientation rather than relative to the wall. Correspondingly, a theoretical framework was introduced, in which the perturbation field representing the fundamental (i.e., primary-wavelength) CFI was decomposed into a component aligned with the local base-flow streamline (i.e., in the local streamwise direction) and a complementary cross-stream component normal to it (§ 3.2). The streamwise-aligned perturbation component manifested structurally as regions of velocity excess and deficit, while the cross-stream perturbation component typically formed a weaker pattern in the flow, appearing as streamwise-vortical structures that were efficient in redistributing momentum. Several advantages of this decomposition were discussed. These included improved structural coherence of perturbation representation in regions of highly deformed base flow, the ability to assess non-modal growth using metrics inspired by Marxen et al. (2009) (§§ 4.2.3 and 6.2.3), and the identification of the (linear) mechanisms of kinetic-energy transfer between the base flow and the perturbations (chapters 5 and 6), thereby reconciling with classic perturbation effects reported in the literature (§ 5.2).

Perturbation organisation at the step

The topology of the laminar unperturbed base flow at the step included recirculating flow immediately upstream and downstream of all steps studied. However, contrary to the model previously conjectured by Tufts et al. (2017), the main body of the incoming CFI was found to pass over the step sufficiently far from the wall, with no apparent explicit interaction with the regions of flow recirculation. Instead, the CFI developed spatially very close to an additional perturbation structure that formed locally at the upper step corner and was located between the wall and the CFI. This additional structure manifested as stationary perturbation streaks, i.e., regions of streamwise-velocity excess and deficit distributed along the step-edge direction (§ 4.2 and chapter 6). The isolation of the streaks in a structural sense was consistent with several reports of significant stationary-perturbation amplification at the upper step corner (Tufts et al., 2017; Eppink, 2020; Rius-Vidales and Kotsonis, 2021).

The origin of the streaks at the step was attributed to a linear non-modal growth mechanism driven by the lift-up effect (§ 6.2.1). Specifically, it was found that the cross-stream pattern of the incoming CFI mode *lifted-up* and pushed down low- and high-momentum fluid, respectively, in adjacent regions of the strongly sheared step flow. Under this principle, the lift-up effect gave rise to rapidly amplified streamwise streaks near the wall, which inherently adopted the spanwise wavelength of the incoming CFI mode. Therefore, this thesis supported the conclusions of Wilhelm et al. (2003) and Lanzerstorfer and Kuhlmann (2012), who similarly ascribed a linear character and origin for streaks developing in unswept forward-facing-step flows. Furthermore, evidence was provided that the streaks were not a manifestation of additional crossflow instability of the step-flow profiles, as suggested by other studies.

Overall, this thesis proposed that stationary perturbation streaks are a universal feature of three-dimensional laminar forward-facing-step flows, provided that three-dimensional stationary perturbations are present in the incoming boundary layer (chapter 6).

Mechanisms of perturbation growth and decay at the step

Upstream of the step, the fundamental CFI was gradually amplified as it approached the step in the chordwise direction, x, compared with reference (no-step) conditions. A close match between the DNS results and linear Parabolised Stability Equations (PSE) solutions in this region revealed linear perturbation growth driven purely by the modification of the unperturbed base flow by the step. The amplification factor immediately upstream of the step was proportional to the step height (§ 4.2.2).

Immediately downstream of most of the steps studied, the fundamental CFI maintained an amplification trend; that is, its kinetic perturbation energy grew in space. However, in the specific case involving the largest step tested, the fundamental CFI was found to be locally damped (i.e., its kinetic perturbation energy decayed in space) before amplifying again further downstream (§ 4.2.3). This local stabilising effect stood in contrast to the dominant view in the published literature, which suggested that a forward-facing step universally amplifies the incoming CFI upon interaction (Tufts et al., 2017; Cooke et al., 2019; Eppink, 2020).

Specifically, Tufts et al. (2017) described that *sufficiently large* steps (i.e., those influencing transition) are associated with a sudden growth of the incoming CFI, and Eppink (2020) reported initial CFI amplification in the downstream vicinity of the step, driven by a linear perturbation effect. The amplitude of the near-wall perturbation streaks inherently forming in forward-facing-step flows (chapter 6) scaled with the step height (§ 4.2.1), and the steps investigated by Eppink (2020) extend relatively high into the boundary layer; the apparent discrepancy between this thesis and previous studies may therefore have been a mere artefact of including the near-wall streaks in the estimation of instability amplitude, thereby overshadowing the incoming-instability response. Accordingly, this thesis concludes that a forward-facing step does not universally amplify the fundamental CFI on interaction, a finding that is also supported experimentally by Rius-Vidales and Kotsonis (2021).

The underlying mechanism supporting the stabilisation (i.e., amplitude decay) of the CFI at the step was the proposed *reverse lift-up effect* (chapter 5). This novel concept was elaborated as follows: the *classic* lift-up effect (Moffatt, 1967; Ellingsen and

Palm, 1975; Landahl, 1975, 1980) entails a three-dimensional cross-stream perturbation interacting with a shear layer which, by redistributing low- and high-momentum fluid, induces inherently flow-aligned (i.e., streamwise-tangent) regions of momentum deficit and excess. However, if a flow instability pre-exists and carries stream-tangent perturbations, the momentum redistribution by the cross-stream perturbation component may be altered locally (e.g., via a rapid variation of surface geometry) in such a way that it acts by quenching the pre-existing regions of streamwise-momentum deficit and excess. As such, when the *reverse lift-up effect* is active, high-momentum fluid is transported towards an incoming low-speed streak and low-momentum fluid is transported towards an incoming high-speed streak. Thus, the streak system as a whole is attenuated, and the flow exhibits a tendency towards returning to its original (unperturbed) laminar state.

In short, the lift-up effect involves the superposition of perturbation streaks and streamwise-vortical structures (cross-stream rolls). In the classic sense, their interaction with the shear layer amplifies the streaks. However, for certain spanwise phase shifts between the streaks and vortical structures, the same interaction with the shear layer produces a stabilising response. The existence of the reverse lift-up effect, which follows naturally from the original model of lift-up (Ellingsen and Palm, 1975) (§ 5.2.5), was demonstrated through canonical flow examples in this thesis (§§ 5.2.2 and 5.2.4). In conclusion, the lift-up effect governed the behaviour of the fundamental CFI immediately downstream of the step; whether the classic (i.e., destabilising) or the reverse (i.e., stabilising) lift-up effect applied depended, at least, on the step height and the free-stream-flow evolution.

Finally, previous studies (Eppink, 2020) attributed CFI growth locally at the step to the destabilising influence of step-induced inflection points in the crossflow profile. In this thesis, no apparent evidence supporting this effect on the fundamental CFI was found; however, strong evidence was reported for the high-order harmonic (i.e., smaller-wavelength) spanwise CFI modes (§ 4.3). Consistently, significant growth of these high-order harmonic modes was observed immediately downstream of the step in the DNS, in agreement with experimental findings (Eppink, 2020; Rius-Vidales and Kotsonis, 2021).

Effects of incoming perturbation amplitude

The discussion in the conclusions above considered a pre-existing CFI undergoing linear perturbation evolution up to approximately the virtual step location under reference (no-step) conditions. Subsequently, this thesis assessed the effects of CFI amplitude on the salient flow features at the step (chapter 7). In this context, energy-balance equations were developed for the stationary spanwise perturbation modes, individually (§ 3.1). This formulation allowed the examination and segregation of the linear and non-linear mechanisms governing the behaviour of each mode at the step, effectively extending the classic Reynolds-Orr framework.

Downstream of the step, the spatial evolution of the stationary perturbations described above deformed the near-wall shear layer of the steady perturbed flow; that is, flow resulting from the superposition of the laminar unperturbed base flow and the stationary perturbations, without unsteady perturbations present. For the

largest tested values in this thesis of both the initial CFI amplitude (i.e., when the CFI behaves non-linearly already upstream of the step) and the step height, this shear-layer deformation effectively gave rise to an additional flow structure: a streamwise-momentum deficit region located beneath the crest of the incoming crossflow vortex (§ 7.1). The existence of this streamwise-momentum deficit region was confirmed by time-averaged experimental flow measurements (Rius-Vidales and Kotsonis, 2022).

By virtue of the Reynolds-Orr type framework introduced above, the pronounced deformation of the near-wall shear layer in the largest-amplitude CFI case was proposed to have originated from a set of high-order harmonic perturbation modes spatially amplified at the step through two key mechanisms: (1) a linear destabilising effect induced by the inflectional step-flow profiles (as previously described) and (2) a non-linear interaction between spanwise perturbation modes (§ 7.3). The former took place farther from the wall, i.e., in the region dominated by the incoming CFI, whereas the latter developed very close to the wall, i.e., in the region dominated by the perturbation streaks that were initially generated at the step. The latter mechanism was unique to the case with the largest tested CFI amplitude and appeared to spatially sustain some of the streaky structures that otherwise decayed downstream of the step when the amplitude of the incoming CFI was reduced (§ 7.2).

Overall, the stationary deformation of the shear layer downstream of the step (and, by extension, the streamwise-momentum deficit region) diminished as the initial amplitude of the incoming CFI was reduced.

9.1.2. Mechanisms of laminar-turbulent transition advancement induced by a forward-facing step

This thesis subsequently elucidated the mechanisms by which the step induced laminar-turbulent transition advancement. The analysis focused exclusively on the case with the largest initial CFI amplitude tested in this thesis. Unsteady perturbations in the DNS were introduced by applying unsteady wall forcing near the inflow, superimposed on the pre-computed steady perturbed flow. The results from the DNS were complemented by linear stability analysis performed using both the local and plane-marching formulations of the two-dimensional parabolised stability approach.

This thesis concludes that transition advancement due to the forward-facing step stemmed from an unsteady instability mechanism originating at the step (chapter 8). Transition advancement is not attributed to the growth of classic secondary crossflow instabilities on the stationary crossflow vortex –the mechanism typically dominant under reference (no-step) conditions– but rather to an instability of the deformed shear layer downstream of the step. As described above, this shear-layer deformation arose from the interaction between the stationary crossflow vortex and the step flow.

Specifically, in the supercritical scenario (i.e., characterised by an abrupt upstream shift of the transition front near the step), transition developed as follows: the stationary deformation of the near-wall shear layer downstream of the step supported the exponential amplification of a set of high-frequency instability eigenmodes. That is, these eigenmodes appeared at frequencies higher than those of the classic *type*-III secondary instability mechanism, which also develops close to the wall. These high-frequency eigenmodes were fully related to the step, i.e., they did not manifest in the

reference (no-step) case. The linear two-dimensional stability analysis identified that the eigenmode exhibiting the largest amplification factor originated from the shear layers surrounding the localised patches of recirculating flow at the upper step corner. Further downstream, the near-wall deformation of the shear layer –which grew in x and eventually developed into the streamwise-momentum deficit region mentioned above– continued to support the spatial growth of this eigenmode (§ 8.1.1).

The evolution of this critical instability eigenmode spatially correlated with the development of a hairpin vortex-shedding mechanism, emerging from the shear layers surrounding the streamwise-momentum deficit region. The interaction between these primary hairpin vortices and a secondary family of unsteady vortices, which also arose downstream of the step and on the side of the streamwise-momentum deficit region, preceded the onset of turbulence (§ 8.1.1). Consequently, this thesis supported the main conclusions of Rius-Vidales and Kotsonis (2022), who attributed supercritical transition to an unsteady mechanism at the step whose behaviour did not reconcile with that of classic secondary crossflow instabilities. This thesis also supported the main conclusions of Eppink (2020), who linked transition to vortex shedding past the region of recirculating flow. Furthermore, Eppink (2020) reported the key role played by the incoming CFI amplitude in setting early transition conditions. Consistently, this thesis showed that supercritical transition occurred only in the case of the largest CFI amplitude considered (for fixed step height), implying that the transition regime due the step cannot be categorised exclusively based on Reynolds number and wavelength.

In line with previous experimental studies (Rius-Vidales and Kotsonis, 2021, 2022), a decrease in the step height (for a fixed CFI amplitude) shifted the transition regime from the supercritical to the critical scenario (i.e., characterised by a moderate upstream shift of the transition front). However, this thesis did not support the conclusions of Rius-Vidales and Kotsonis (2022), which attributed transition in the critical scenario to the growth of the *type*-I and *type*-II secondary crossflow instabilities on the stationary crossflow vortex, allegedly amplified –referring to the vortex– by the interaction with the step. Instead, evidence was presented in this thesis supporting that the supercritical and critical scenarios essentially follow the same transition path, albeit the main processes described above are spatially more relaxed in the critical case (§ 8.1.2). As a consequence, the birth of key transitional-flow structures is delayed spatially in the critical case, thereby positioning the transition front between that of the supercritical and reference (no-step) cases.

The elucidation of transition mechanisms revealed that significant transition advancement due to the step entailed a modification of the transition path, relative to the reference (no-step) scenario. This proposition, which was made within the context of the transition diagram proposed by Morkovin et al. (1994), concerned and in turn challenged the role of transient growth in that diagram. When manifesting, transient growth typically either bypasses or conditions primary eigenmode growth (Reshotko, 2001). In contrast, in the case of transition induced by the step, the transient growth of perturbation streaks at the step –structures that partially set the conditions for secondary instability and breakdown– was itself preceded and conditioned by pre-existing primary (crossflow) eigenmode growth.

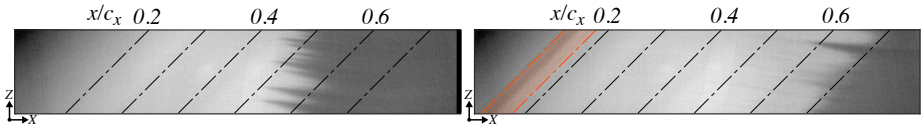

Figure 9.1: Thermal maps demonstrating transition delay of swept-wing flow using a surface hump (right) compared to the reference wing without the hump (left), reproduced from Rius-Vidales et al. (2025). Flow moves from left to right: bright regions indicate laminar flow, dark regions indicate turbulent flow. The solid orange line and shaded orange region mark the hump apex and its width. Here, x is the coordinate orthogonal to the leading edge (with wing chord $c_x = 0.9$ m), while X and Z denote coordinates aligned with the wind-tunnel walls.

9.2. Outlook: potential for passive flow control

This thesis primarily focused on examining the instability mechanisms inducing early transition when a forward-facing step is present. However, a series of unexpected findings revealed that, under certain conditions, the step passively controls the incoming CFI (chapters 4 and 5); as a consequence, transition delay may potentially be achieved. With few exceptions (Fransson et al., 2006; Fujii, 2006; Saric et al., 2011), the dominant view among fluid dynamicists holds that rapid spatial variations in surface geometry advance laminar-turbulent transition. The results of this thesis, however, support a possible exception in the context of low-speed flows dominated by the stationary CFI, thereby challenging the universality of this proposition. The objective of this section is to strengthen this view and propose future research directions for exploring passive flow-control strategies.

The numerical and theoretical findings of this thesis are supported by experimental evidence of transition delay induced by a forward-facing step (Rius-Vidales and Kotsonis, 2021). Transition delay is also reported when using a surface relief composed of surface strips (Ustinov and Ivanov, 2018; Ivanov and Mischenko, 2019). In addition, the author of this thesis is a co-author of related research conducted within the same group at Delft University of Technology (TU Delft), which demonstrates the potential of a smooth surface hump for passive flow control. Specifically, experimental results (see figure 9.1) show that a surface hump delays CFI-driven transition under certain conditions (Rius-Vidales et al., 2025), with its effectiveness being contingent upon the incoming CFI amplitude (Westerbeek et al., 2025). This body of work on transition delay using a smooth surface hump has materialised into an international patent application (Kotsonis et al., 2024).

The growing variety of surface-feature geometries integrated into swept wings that have recently demonstrated transition delay under subsonic flow conditions suggests that these are not isolated exceptions, but indications of an unexplored design space. Specifically, it appears feasible to passively control the stationary CFI of swept-wing flow through a surface relief, provided it matches the relevant instability specifications, i.e., Reynolds number or receptivity conditions, in order to prevent transition advancement. Accordingly, this thesis concludes by proposing Surface Methods for Aerodynamic Relief Technology (SMART) flow control. Two preliminary design

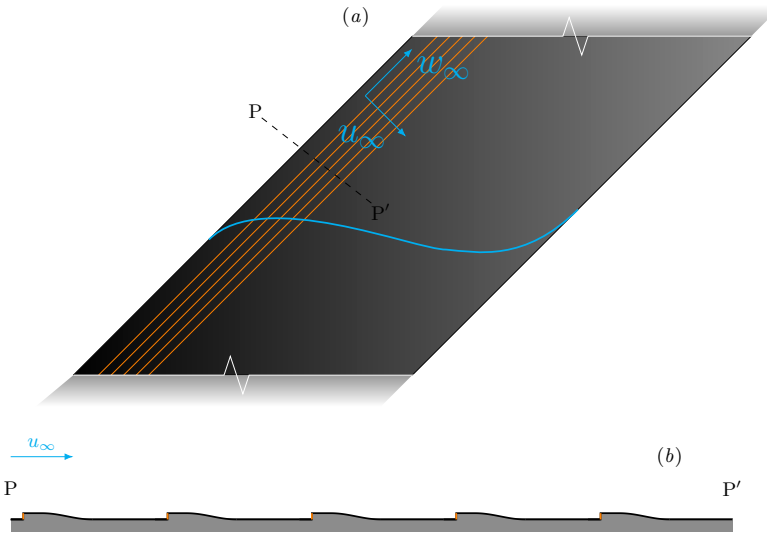

Figure 9.2: Sketch of the physical model of swept-wing flow adapted from figure 2.1, illustrating the flow control method denoted as destructive wave-like interaction. (*a*) Wing model with orange lines indicating the orientation of the surface relief features. (*b*) Cross-sectional view of the surface relief along the direction orthogonal to the leading edge.

strategies can be envisioned, which are outlined next.

9

SMART flow control through destructive wave-like interaction
This method builds upon the identification of the reverse lift-up effect presented in this thesis. As described above (chapter 5), this effect is of the (linear inviscid) algebraic-growth type and has the potential to induce a local decay of perturbation kinetic energy, either in space or in time. Two main considerations associated with the present surface method are summarised as follows:

- **Theoretical foundation**

  In contrast to the main working principles proposed in this thesis, Ustinov and Ivanov (2018) attribute CFI stabilisation induced by surface strips to a reduction in the crossflow velocity within the boundary layer, thereby decreasing the CFI amplification factor in an Orr-Sommerfeld sense. However, the validity of linear local stability methods near sharp surface features remains questionable, particularly since this thesis suggests that confined non-modal-growth mechanisms may dominate in this context. Future research should examine the conditions under which either modal or non-modal effects dominate the interaction between surface features and pre-existing boundary-layer perturbations.

- **Design**

  The perturbation stabilisation associated with the reverse lift-up effect does not require prior knowledge of the wavelength or the perturbation phase upstream

of the surface feature. Therefore, it is applicable potentially successively along an aerodynamic surface for an overall enhancement of the underlying benefit without need for active phase calibration.

The analysis presented in this thesis suggests that the spatial organisation of the cross-stream perturbation field (i.e., the component characterised as $\boldsymbol{v}_n$ in equation (3.12), which is primarily responsible for redistributing base-flow momentum) is sensitive to rapid spatial variations in the base-flow topology (chapters 5 and 6). Accordingly, a surface relief may be designed to manipulate the cross-stream perturbation field; for instance, to locally induce a *destructive* wave-like interaction with (i.e., attenuating) the incoming regions of streamwise-velocity excess and deficit that constitute the fundamental CFI.

An example of such a surface relief is proposed in figure 9.2. Each individual surface feature includes a leading edge that emulates the step to induce a reverse lift-up effect, although alternative shapes may ultimately prove more effective. Downstream of it, the feature gradually merges with the wall, thereby preconditioning the CFI for interaction with the next feature in the relief. This gradual geometric adaptation also aims to suppress or minimise flow separation. Sharp trailing edges, as observed in backward-facing step studies (Krochak et al., 2022), are known to promote flow separation.

SMART flow control through instability *hysteresis*

Refocusing on the main step-CFI analysis presented in this thesis, an ongoing debate in the literature concerns whether the enhanced stationary harmonic activity of CFI at the step induces non-linear growth of the fundamental CFI, or vice-versa (Eppink, 2020; Rius-Vidales and Kotsonis, 2021). This thesis shows that, in the largest step case, the amplitude evolution of the fundamental CFI from DNS reasonably matches the solution of linear PSE, when the PSE is initialised close downstream of (but not at) the step, and the DNS perturbation profile is used as initial condition. This agreement implies that the fundamental CFI evolves following linear mechanisms downstream of the largest step tested. In contrast, for the smaller steps, the CFI behaviour downstream of the step is non-linearly dominated (i.e., it matches the solution to non-linear PSE), suggesting that the nature of the perturbation mechanisms is a function of, at least, the step height (§ 4.3).

Despite the complex interplay between the fundamental CFI and its associated high-order harmonic modes downstream of the step, this thesis isolates a distinctive effect with potential for flow control. Specifically, when the step-CFI interaction occurs in the region of linear perturbation growth, it can lead to a broad area of reduced growth rate of the fundamental CFI, compared to the reference (no-step) case. This behaviour was first identified following the reverse lift-up (§§ 5.1 and 5.3), possibly due to the strong distortion imposed on the perturbation shape. However, the numerical experiment discussed in § 8.2 shows that this reduced growth rate of the CFI past the step is also achieved in the absence of the reverse lift-up effect, which may represent a limiting situation.

Accordingly, two main considerations associated with the present surface method are summarised as follows:

- **Theoretical foundation**

  A qualitatively similar effect, namely reduced growth rate of the CFI, has been reported downstream of a smooth surface hump within the scope of collaborative work (Westerbeek et al., 2025). The unperturbed base flow relaxes spatially towards the reference (no-hump) organisation over a relatively short chordwise distance downstream of the hump. However, this rapid relaxation does not apply to the fundamental CFI, see Westerbeek et al. (2025, figure 6). Future research should investigate how specific surface features convert the incoming CFI into a "less unstable structure" (Westerbeek et al., 2025) and scrutinise the associated spatial *hysteresis* or, perturbation adaptation process, towards the classic Orr-Sommerfeld type of growth.

  This stabilising effect is linked by Westerbeek et al. (2025) to the inhibition of the mechanisms of production (as characterised by P_{β_0} in this thesis, see §§ 4.2.4 and 5.1). In the context of Görtler instability, Sescu and Afsar (2018) similarly argue that passive instability control via wall deformations is possible, and attribute it to a "weakening the effect of lift up".

- **Design**

  In contrast to the first surface method discussed above, the present method falls within the category of flow control based on a single –or a limited number of– surface features. Building on the findings presented in § 8.2 regarding the step, as well as the preliminary investigations by Rius-Vidales et al. (2025) and Westerbeek et al. (2025) on the hump, an optimisation procedure may be carried out to design a surface feature that maximally decreases the amplification factor of an incoming boundary-layer perturbation.

This thesis aims to make a significant contribution to the understanding of flow instability and laminar-turbulent transition. The theoretical and numerical findings presented challenge the classic paradigm in fluid mechanics that surface features are universally detrimental to laminar flow. Instead, under specific conditions, surface features can delay transition and thereby reduce skin-friction drag. This proposition is grounded in the observed ability of a forward-facing step, suitably designed, to stabilise the pre-existing stationary crossflow vortices of a swept-wing boundary layer. The mathematical and physical frameworks developed herein –which are potentially applicable to other instability classes– lay the foundation for exploring and optimising novel strategies for passive laminar swept-wing flow control via surface shaping, while also elucidating the conditions under which transition may conversely be advanced.

Nomenclature

MARKERS

B	Unperturbed base flow.
DB	Steady perturbed flow.
†	Complex conjugate.
e	External (outer) flow.
exp	Experimentally measured.
$\hat{\boldsymbol{v}}$	Pseudo-free-stream.
in	Domain inlet.
n	Perturbation normal to the base flow.
$\prime$	Perturbation quantity.
s	Orientation relative to the inviscid streamline.
str	Amplitude measured at the lower perturbation peak.
$\tilde{\boldsymbol{v}}$	Amplitude (Fourier) coefficient.
tun	Wind-tunnel section, upstream of the wing model.
top	Amplitude measured at the upper perturbation peak.
t	Perturbation tangential to the base flow.
u, v, w	Components of velocity in the chordwise, wall-normal, and spanwise directions.
$\underline{\boldsymbol{v}}$	Non-dimensional variable.

ACRONYMS

AHLNS	Adaptive Harmonic Linearised Navier-Stokes.
BiG	BiGlobal (linear stability analysis).
BS	Blowing-Suction.
CFI	Crossflow Instability.
CFL	Courant Friedrichs Lewy.
DeHNSSo	Delft Harmonic Navier-Stokes Solver.
DRE	Discrete Roughness Elements.
FV	Finite Volume.
FSC	Falkner Skan Cooke.
HLFC	Hybrid Laminar Flow Control.
HNS	Harmonic Navier-Stokes Solver.
IM	Inflow Mode.
KH	Kelvin Helmholtz.
LFC	Laminar Flow Control.
LPSE	Linear Parabolised Stability Equations.
LST	Linear Stability Theory.
NLF	Natural Laminar Flow.
NPSE	Non-linear Parabolised Stability Equations.
OS	Orr Sommerfeld.
PSE	Parabolised Stability Equations.
PPE	Pressure Poisson Equation.
RHS	Right Hand Side.
TS	Tollmien Schlichting.

SYMBOLS

α_i^{OS}	rad/m	Spatial growth rate from Orr-Sommerfeld analysis.
$\alpha^q_{i,(k,j)}$	rad/m	Spatial growth rate from DNS (for a perturbation quantity q with temporal periodicity k and spanwise periodicity j).
$A^q_{(k,j)}$	m/s	Amplitude (for a perturbation quantity q with temporal periodicity k and spanwise periodicity j).
A_0	m/s	Amplitude of the stationary CFI at the inlet.
β_0	rad/m	Fundamental spanwise wavenumber.
β_H	-	Hartree parameter.
c_x	m	Wing chord in the direction orthogonal to the leading edge.
c_X	m	Wing chord in the direction parallel to the incoming stream.
C_p	-	Pressure coefficient.
δ_{99}	m	Boundary layer 99% thickness.
$\delta_{99,h}$	m	Boundary layer 99% thickness at the (virtual) step apex.
δ_0	m	Boundary layer 99% thickness at the inlet.
$\delta^\star$	m	Displacement thickness.
f_0	Hz	Fundamental temporal frequency.
h	m	Step height.
λ_z	m	Spanwise perturbation wavelength.
Λ	rad	Sweep angle.
η	m/s	Perturbation component normal to the base flow.
ψ	m/s	*Total* perturbation (i.e., associated to its modulus).
φ	rad	Perturbation phase.
$\boldsymbol{q}$	-	Vector of state variables.
$\boldsymbol{Q}_\infty^{\mathrm{tun}}$	m/s	Velocity vector in the wind-tunnel section.
ρ	kg/m^3	Density.
S^{exp}	m	Arc length of the aerofoil.
τ	m/s	Perturbation component tangential to the base flow.
Tu	-	Turbulence intensity.
u	m/s	Chordwise velocity.
u_∞	m/s	Free-stream chordwise velocity at the inlet.
u_h	m/s	Chordwise velocity at the (virtual) step apex.
$\boldsymbol{v}$	m/s	Velocity vector.
v	m/s	Wall-normal velocity.
ν	m^2/s	Kinematic viscosity.
w	m/s	Spanwise velocity.
ω_0	rad/s	Fundamental angular temporal frequency.
$\boldsymbol{x}$	m	Cartesian coordinate system.
x	m	Leading-edge-orthogonal (or, chordwise) direction.
x_{st}	m	Chordwise position relative to the step: $x_{\mathrm{st}} = x - 177.62\delta_0$.
y	m	Wall-normal direction.
$\tilde{y}^q_{(0,j)}$	m	Wall-normal location at which the amplitude of perturbation quantity q is measured.
z	m	Leading-edge-parallel (or, spanwise) direction.

Bibliography

Åkervik, E., Brandt, L., Henningson, D. S., Hoepffner, J., Marxen, O., and Schlatter, P. (2006). Steady solutions of the Navier-Stokes equations by selective frequency damping. *Phys. Fluids*, 18:068102.

Alam, M. and Sandham, N. (2000). Direct numerical simulation of 'short' laminar separation bubbles with turbulent reattachment. *J. Fluid Mech.*, 410:1–28.

Albensoeder, S., Kuhlmann, H. C., and Rath, H. J. (2001). Three-dimensional centrifugal-flow instabilities in the lid-driven-cavity problem. *Phys. Fluids*, 13(1).

Allison, E., Kroo, I., Sturdza, P., Suzuki, Y., and Martins-Rivas, H. (2010). Aircraft conceptual design with natural laminar flow. In *27th Congress of the International Council of the Aeronautical Sciences (ICAS)*.

Andersson, P., Berggren, M., and Henningson, D. S. (1999). Optimal disturbances and bypass transition in boundary layers. *Phys. Fluids*, 11:134–150.

Andersson, P., Brandt, L., Bottaro, A., and Henningson, D. S. (2001). On the breakdown of boundary layer streaks. *J. Fluid Mech.*, 428:29–60.

Andersson, P., Henningson, D., and Hanifi, A. (1998). On a stabilization procedure for the parabolic stability equations. *Journal of Engineering Mathematics*, 33:311–332.

Ando, T. and Shakouchi, T. (2004). Flow characteristics over forward facing step and through abrupt contraction pipe and drag reduction. *Res. Rep. Fac. Eng. Mie Univ*, 29:1–8.

Antkowiak, A. and Brancher, P. (2007). On vortex rings around vortices: an optimal mechanism. *J. Fluid Mech.*, 578:295–304.

Appel, T. (2021). *Boundary layer instabilities due to surface irregularities: a harmonic Navier-Stokes approach*. Doctoral dissertation, Imperial College London. Imperial College London. https://doi.org/10.25560/88722.

Armfield, S. and Street, R. (1999). The fractional-step method for the Navier–Stokes equations on staggered grids: the accuracy of three variations. *J. Comput. Phys.*, 153(2):660–665.

Arnal, D. (1994). *Boundary Layer transition: predictions based on linear theory*. AGARD R-793.

Asai, M., Minagawa, M., and Nishioka, M. (2002). The instability and breakdown of a near-wall low-speed streak. *J. Fluid Mech.*, 455:289–314.

Bertolotti, F. P. (1996). On the birth and evolution of disturbances in three-dimensional boundary layers. *Nonlinear Instability and Transition in Three-Dimensional Boundary Layers (ed. P. W.Duck & P. Hall)*, pages 115–132.

Bertolotti, F. P., Herbert, T., and Spalart, P. R. (1992). Linear and nonlinear stability of the blasius boundary layer. *J. Fluid Mech.*, 242:441–474.

Bippes, H. (1991). *Experiments on transition in three-dimensional accelerated boundary layer flows.* Proc. R.A.S. Boundary Layer Transition and Control, Cambridge.

Bippes, H. (1999). Basic experiments on transition in the three-dimensional boundary layers dominated by crossflow instability. *Prog. Aerosp. Sci.*, 35:363–412.

Bonfigli, G. and Kloker, M. (2007). Secondary instability of crossflow vortices: validation of the stability theory by direct numerical simulation. *J. Fluid Mech.*, 583:229–272.

Borodulin, V. I., Ivanov, A. V., and Kachanov, Y. S. (2024). Roughness induced transition delay in a swept-wing boundary layer in presence of free stream disturbances, part 1: Tturbulence effects. *Eur. J. Mech. B Fluids*, 103:193–207.

Brandt, L. (2007). Numerical studies of the instability and breakdown of a boundary-layer low-speed streak. *Eur. J. Mech. B Fluids*, 26:64–82.

Brandt, L. (2014). The lift-up effect: the linear mechanism behind transition and turbulence in shear flows. *Eur. J. Mech. B Fluids*, 47:80–96.

Brandt, L., Cossu, C., Chomaz, J.-M., Huerre, P., and Henningson, D. S. (2003). On the convectively unstable nature of optimal streaks in boundary layers. *J. Fluid Mech.*, 485:221–242.

Brandt, L. and Henningson, D. S. (2002). Transition of streamwise streaks in zero-pressure-gradient boundary layers. *J. Fluid Mech.*, 472:229–261.

Brandt, L., Schlatter, P., and Henningson, D. S. (2004). Transition in boundary layers subject to free-stream turbulence. *J. Fluid Mech.*, 517:167–198.

Braslow, A. L. (1960). *The effect of distributed surface roughness on boundary-layer transition.* AGARD R. 254.

Breuer, K. S. and Kuraishi, T. (1994). Transient growth in two- and three-dimensional boundary layers. *Phys. Fluids*, 6(1983).

Breuer, K. S. and Landahl, M. T. (1990). The evolution of a localized disturbance in a laminar boundary layer. part 2. strong disturbances. *J. Fluid Mech.*, 220:595–621.

Bushnell, D. M. (2003). Aircraft drag reduction—a review. *J. Aerosp. Eng.*, 217(1):1–18.

Butler, K. M. and Farrell, B. F. (1992). Three-dimensional optimal perturbations in viscous shear flow. *Phys. Fluids A*, 14:1426–1441.

Böberg, L. and Brösa, U. (1988). Onset of turbulence in a pipe. *Z. Naturforsch.*, 43a:697–726.

Casacuberta, J., Groot, K. J., Hickel, S., and Kotsonis, M. (2022a). Secondary instabilities in swept-wing boundary layers: Direct Numerical Simulations and Biglobal stability analysis. *AIAA Paper 2022-2330*.

Casacuberta, J., Groot, K. J., Hickel, S., and Kotsonis, M. (2025a). Direct numerical simulation of swept-wing transition induced by forward-facing steps. Under consideration for publication in *J. Fuid Mech.*

Casacuberta, J., Groot, K. J., Tol, H. J., and Hickel, S. (2018). Effectivity and efficiency of selective frequency damping for the computation of unstable steady-state solutions. *J. Comput. Phys.*, 375:481–497.

Casacuberta, J., Groot, K. J., Ye, Q., and Hickel, S. (2020). Transitional flow dynamics behind a micro-ramp. *Flow Turbul. Combust.*, 104:533–552.

Casacuberta, J., Hickel, S., and Kotsonis, M. (2021). Mechanisms of interaction between stationary crossflow instabilities and forward-facing steps. *AIAA Paper 2021-0854*.

Casacuberta, J., Hickel, S., and Kotsonis, M. (2023). Laminar-turbulent transition in swept-wing flows with a supercritical forward-facing step. In *ERCOFTAC Workshop Direct and Large Eddy Simulation, Udine, Italy*, pages 151–156. Springer Nature Switzerland.

Casacuberta, J., Hickel, S., and Kotsonis, M. (2024). Passive stabilization of crossflow instabilities by a reverse lift-up effect. *Phys. Rev. Fluid*, 9:043903.

Casacuberta, J., Hickel, S., Westerbeek, S., and Kotsonis, M. (2022b). Direct numerical simulation of interaction between a stationary crossflow instability and forward-facing steps. *J. Fluid Mech.*, 943:A46.

Casacuberta, J., Westerbeek, S., Sumariva, J. A. F., Groot, K. J., Hickel, S., Hein, S., and Kotsonis, M. (2025b). Streaky perturbations in swept-wing flow over forward-facing step. *Phys. Rev. Fluid*, 10:023902.

Chauvat, G. (2020). *Receptivity, stability and sensitivity analysis of two- and three-dimensional flows*. Doctoral dissertation, KTH Royal Institute of Technology. KTH Publications. https://kth.diva-portal.org/smash/record.jsf?pid=diva2

Chiba, K., Ishida, R., and Nakamura, K. (1995). Mechanism for entry flow instability through a forward-facing step channel. *J. Non-Newtonian Fuid. Mech.*, 57:271–282.

Chorin, A. J. (1968). Numerical solutions of the Navier-Stokes equations. *Math. Comput.*, 22:745–762.

Cooke, E. E., Mughal, S., Sherwin, S. J., Ashworth, R., and Rolston, S. (2019). Destabilization of stationary and traveling crossflow disturbances due to steps over a swept wing. *AIAA Paper 2019-3533*.

Corbett, P. and Bottaro, A. (2001). Optimal linear growth in swept boundary layers. *J. Fluid Mech.*, 435:1–23.

Crawford, B. K., Duncan Jr., G. T., Tufts, M. W., Saric, W. S., and Reed, H. L. (2015). Effects of step-excrescence location on swept-wing transition. *AIAA Paper 2015-1233*.

Crouch, J. (2022). Predicting laminar-turbulent transition influenced by surface-induced flow distortions. In *IUTAM Symposium on Laminar-Turbulent Transition: 9th IUTAM Symposium, London, UK, September 2–6, 2019*, pages 19–32. Springer.

Crouch, J., Kosorygin, V., and Ng, L. (2006). Modeling the effects of steps on boundary-layer transition. In *IUTAM Symposium on Laminar-Turbulent Transition*, pages 37–44. Springer.

Cumpsty, N. A. and Head, M. R. (1969). The calculation of the three-dimensional turbulent boundary layer. Part III. Comparison of attachment-line calculations with experiment. *Aeronaut. Q.*, 20(2):99–113.

D'Alessandro, V., Binci, L., Montelpare, S., and Ricci, R. (2018). On the development of OpenFOAM solvers based on explicit and implicit high-order Runge-Kutta schemes for incompressible flows with heat transfer. *Comput. Phys. Commun.*, 222:14–30.

De Tullio, N., Paredes, P., Sandham, N. D., and Theofilis, V. (2013). Laminar-turbulent transition induced by a discrete roughness element in a supersonic boundary layer. *J. Fluid Mech.*, 735:613–646.

Deyhle, H. and Bippes, H. (1996). Disturbance growth in an unstable three-dimensional boundary layer and its dependence on environmental conditions. *J. Fluid Mech.*, 316:73–113.

Doetsch, H. (1940). Untersuchungen an einigen Profilen mit geringem Widerstand im Bereich kleiner c_a-Werte. Jahrbuch der Deutschen Luftfahrtforschung.

Downs, R. S. and White, E. B. (2013). Free-stream turbulence and the development of cross-flow disturbances. *J. Fluid Mech.*, 735:347–380.

Drake, A., Bender, A., Korntheuer, A., Westphal, R. V., McKeon, B. J., Gerashchenko, S., Rohe, W., , and Dale, G. (2010). Step excrescence effects for manufacturing tolerances on laminar flow wings. *AIAA Paper 2010-375*.

Drake, A., Bender, A. M., and Westphal, R. V. (2008). Transition due to surface steps in the presence of favourable pressure gradients. *AIAA Paper 2008-7334*.

Drake, A., Westphal, R. V., Zuniga, F. A., Jr., R. A. K., and Koga, D. J. (1996). Wing leading edge joint laminar flow tests. In *NASA Technical Memorandum* 4762.

Dryden, H. L. (1953). Review of published data on the effect of roughness on transition from laminar to turbulent flow. *J. Aeronaut. Sci.*, 20:477–482.

Duncan Jr., G. T., Crawford, B. K., Tufts, M. W., Saric, W. S., and Reed, H. L. (2013). Effects of step excrescences on swept-wing transition. *AIAA Paper 2013-2412*.

Duncan Jr., G. T., Crawford, B. K., Tufts, M. W., Saric, W. S., and Reed, H. L. (2014). Effects of step excrescence on a swept wing in a low-disturbance wind tunnel. *AIAA Paper 2014-0910*.

Edelmann, C. and Rist, U. (2014). Impact of forward-facing steps on laminar-turbulent transition in subsonic flows. In *New Results in Numerical and Experimental Fluid Mechanics IX: Contributions to the 18th STAB/DGLR Symposium, Stuttgart, Germany, 2012*, pages 155–162. Springer International Publishing.

Ellingsen, T. and Palm, E. (1975). Stability of linear flow. *Phys. Rev. Fluid*, 18:487–488.

Eppink, J. L. (2018). The effect of forward-facing steps on stationary crossflow instability growth and breakdown. *AIAA Paper 2018-0817*.

Eppink, J. L. (2020). Mechanisms of stationary cross-flow instability growth and breakdown induced by forward-facing steps. *J. Fluid Mech.*, 897:A15.

Eppink, J. L. and Casper, C. (2019). Effects of forward-facing step shape on stationary crossflow instability growth and breakdown. *AIAA Paper 2019-3532*.

Ergin, F. G. and White, E. B. (2006). Unsteady and transitional flows behind roughness elements. *AIAA J.*, 44(11):2504–2514.

Fage, A. and Preston, J. H. (1941). On transition from laminar to turbulent flow in the boundary layer. *Proc. R. Soc. Lond*, 178(973):201–227.

Fasel, H., Bestek, H., and Schefenacker, R. (1977). *Numerical simulation studies of transition phenomena in incompressible, two-dimensional flows*. AGARD CP-224.

Fendt, M. (2017). Airbus BLADE laminar flow wing demonstrator makes first flight. Airbus external communications. Retrieved from `https://https://www.airbus.com/en/newsroom/press-releases/2017-09-airbus-blade-laminar-flow-wing-demonstrator-makes-first-flight`. Accessed: 27 May 2025.

Ferziger, J. H., Milovan, P., and Street, R. L. (2020). *Computational methods for fluid dynamics*. Springer Nature Switzerland AG, fourth edition.

Fischer, T. M. and Dallmann, U. (1991). Primary and secondary stability analysis of a three-dimensional boundary-layer flow. *Phys. Fluids A: Fluid Dynamics*, 3(10):2378–2391.

Floryan, J. M. (1986). Görtler instability of boundary layers over concave and convex walls. *Phys. Fluids*, 29:2380.

Floryan, J. M. and Saric, W. S. (1982). Stability of Görtler vortices in boundary layers. *AIAA J.*, 20(3).

Franco, J. A. and Hein, S. (2018). Adaptive harmonic linearized navier-stokes equations used for boundary-layer instability analysis in the presence of large streamwise gradients. *AIAA Paper 2018-1548*.

Fransson, J. H. M., Talamelli, A., Brandt, L., and Cossu, C. (2006). Delaying transition to turbulence by a passive mechanism. *Phys. Rev. Lett*, 96:064501.

Fujii, K. (2006). Experiment of the two-dimensional roughness effect on hypersonic boundary-layer transition. *J. Spacecr. Rockets*, 43(4):731–738.

Fujino, M., Yoshizaki, Y., and Kawamura, Y. (2003). Natural-Laminar-Flow airfoil development for a lightweight business jet. *J. Aircr.*, 40:609–615.

Gaster, M. (1967). On the flow along swept leading edges. *Aeronaut. Q.*, 18(2):165–184.

Gaster, M. (2000). On the growth of waves in boundary layers: a non-parallel correction. *J. Fluid Mech.*, 424:367–377.

Gibson, T., Soucheleau, B., and Rogers, N. (2021). BLADE - Natural Laminar Flow Flight Testing. In *32nd Congress of the International Council of the Aeronautical Sciences (ICAS)*.

Goldstein, M. E. (1985). Scattering of acoustic waves into Tollmien-Schlichting waves by small streamwise variations in surface geometry. *J. Fluid Mech.*, 154:509–529.

Goold, I. (2018). Flight tests to resume on Airbus BLADE project. AIN Media Group. Retrieved from `https://www.ainonline.com/aviation-news/air-transport/2018-02-04/flight-tests-resume-airbus-blade-project`. Accessed: 24 November 2023.

Gratzer, L. B. (1986). Laminar Flow Control Airfoil. United States Patent No. US 1986/4575030. Filed 11nd March 1986.

Gray, W. (1952). *The nature of the boundary layer flow at the nose of a swept wing*. RAE.

Gregory, N., Stuart, J. T., and Walker, W. S. (1955). On the stability of three-dimensional boundary layers with application to the flow due to a rotating disk. *Philos. Trans. R. Soc. A*, 248(943):155–199.

Groot, K., Serpieri, J., Pinna, F., and Kotsonis, M. (2018). Secondary crossflow instability through global analysis of measured base flows. *J. Fluid Mech.*, 846:605–653.

Groot, K. J., Casacuberta, J., Kotsonis, M., and Hickel, S. (2025). Non-orthogonal plane-marching stability equations for secondary instability of crossflow vortices. Accepted for publication in *Comput. Fluids*.

Groot, K. J. and Eppink, J. L. (2021). Stability analysis of the flow over a swept forward-facing step using PIV base flows in a nonorthogonal coordinate system. *AIAA Paper 2021-2908*.

Grosch, C. E. and Salwen, H. (1978). The continuous spectrum of the orr-sommerfeld equation. part 1. the spectrum and the eigenfunctions. *J. Fluid Mech.*, 87(1):33–54.

Gubisch, M. (2017). Airbus readies laminar-winged A340 for test flights. Flight Global. Retrieved from `https://www.flightglobal.com/analysis/analysis-airbus-readies-laminar-winged-a340-for-test-flights/125260.article`. Accessed: 24 November 2023.

Hall, P., Malik, M. R., and Poll, D. I. A. (1984). On the stability of an infinite swept attachment line boundary layer. *Proc. R. Soc. Lond*, 395:229–245.

Harlow, F. H. and Welsh, J. E. (1965). Numerical calculations of time dependent viscous incompressible flow with free surface. *Phys. Fluids*, 8:2182–2189.

Haynes, T. S. and Reed, H. L. (2000). Simulation of swept-wing vortices using nonlinear parabolized stability equations. *J. Fluid Mech.*, 405:325–349.

Henke, R. (1999). Aircraft drag reduction—a review. *Air & Space Europe*, 1(2):76–79.

Henningson, D. S., Johansson, A. V., and Lundbladh, A. (1990). On the evolution of localized disturbances in laminar shear flows. In *In Laminar-Turbulent Transition: IUTAM Symposium, Toulouse, France, September 11–15, 1989*, pages 279–284. Springer.

Henningson, D. S., Lundbladh, A., and Johansson, A. V. (1993). A mechanism for bypass transition from localized disturbances in wall-bounded shear flow. *J. Fluid Mech.*, 250:169–207.

Hepperle, M. (2008). MDO of forward swept wings. KATnet II Workshop, 28-29 January 2008, Braunschweig.

Herbert, T. (1993). *Parabolized Stability Equations*. AGARD R-793.

Herbert, T. (1997). Parabolized stability equations. *Annu. Rev. Fluid Mech.*, 29:245–283.

Hetsch, T. and Rist, U. (2009). Accuracy of local and nonlocal linear stability theory in swept separation bubbles. *AIAA J.*, 47(5).

Hickel, S. (2008). *Implicit Turbulence Modeling for Large-Eddy Simulation.* Doctoral dissertation, TUM School of Engineering and Design. TUM Repository. https://mediatum.ub.tum.de/654921.

Hickel, S. and Adams, N. A. (2008). Implicit LES applied to zero-pressure-gradient and adverse-pressure-gradient boundary-layer turbulence. *Int. J. Heat Fluid Fl.*, 29:626–639.

HLFC–WIN consortium (2023). A new wing design for the world's skies. Retrieved from `https://www.hlfc-win.eu`. Accessed: 22 November 2023.

Hosseinverdi, S. and Fasel, H. F. (2016). Direct Numerical Simulations of laminar-to-turbulent transition in laminar separation bubbles in three-dimensional boundary-layer. *AIAA Paper 2016-3793.*

Huerre, P. and Monkewitz, P. A. (1990). Local and global instabilities in spatially developing flows. *Annu. Rev. Fluid Mech.*, 22:473–537.

Hultgren, L. and Gustavsson, L. (1981). Algebraic growth of disturbances in a laminar boundary. *Phys. Rev. Fluid*, 24.

Hunt, J., Wray, A., and Moin, P. (1988). Eddies, streams, and convergence zones in turbulent flows. Report CTR-S88, center for turbulence research.

Högberg, M. and Henningson, D. (1998). Secondary instability of cross-flow vortices in falkner-skan-cooke boundary layers. *J. Fluid Mech.*, 368:339–357.

Ivanov, A. V. and Mischenko, D. A. (2019). Delay of laminar-turbulent transition on swept-wing with help of sweeping surface relief. AIP Conference Proceedings 2125.

Iyer, V., Bertram, O., and Seibel, O. (2017). Review of hybrid laminar flow control systems. *Prog. Aerosp. Sci.*, 93(1160):24–52.

Jacobs, R. G. and Durbin, P. A. (2001). Simulations of bypass transition. *J. Fluid Mech.*, 482:185–212.

Janke, E. and Balakumar, P. (2000). On the secondary instability of three-dimensional boundary layers. *Theor. Comput. Fluid Dyn.*, 14:167–194.

Jin, B., Symon, S., and Illingworth, S. J. (2021). Energy transfer mechanisms and resolvent analysis in the cylinder wake. *Phys. Rev. Fluid*, 6.

Jones, B. M. (1938). The boundary layer in flight: some recent flight experiments on the transition from laminar to turbulent flow. *Aircr. Eng. Aerosp. Technol.*, 10(5):135–141.

Jordi, B. E., Cotter, C. J., and Sherwin, S. J. (2014). Encapsulated formulation of the selective frequency damping method. *Phys. Fluids*, 26(3):034101.

Joslin, R. D. (1998a). Aircraft laminar flow control. *Annu. Rev. Fluid Mech.*, 30:1–29.

Joslin, R. D. (1998b). Overview of laminar flow control. In *NASA/TP*-1998-208705.

Kachanov, Y. and Tararykin, O. (1990). The experimental investigation of stability and receptivity on a swept wing flow. IUTAM Symp. "Laminar Turbulent Transition".

Karp, M. and Hack, M. J. P. (2018). Transition to turbulence over convex surfaces. *J. Fluid Mech.*, 855:1208–1237.

Kendall, J. M. (1985). Experimental study of disturbances produced in a pretransitional laminar boundary layer by weak free-stream turbulence. *AIAA Paper*, 85(1695).

Kierbel, D., Farouz-Fouquet, M., and Malard, L. (2019). Method for manufacturing an aicraft leading edge panel that allows extensive laminar flow to be obtained, and leading edge comprising at least one panel obtained using the said method. United States Patent No. US 2019/0061908 A1. Filed 22nd August 2018.

Klebanoff, P. S. (1971). Effect of free-stream turbulence on the laminar boundary layer. *Bull. Am. Phys. Soc.*, 16(11):1323.

Klebanoff, P. S. and Tidstrom, K. D. (1972). Mechanism by which a two-dimensional roughness element induces boundary-layer transition. *Phys. Fluids*, 15(7):1173–1188.

Koch, W., Bertolloti, F. P., Stolte, A., and Hein, S. (2000). Nonlinear equilibrium solutions in a three-dimensional boundary layer and their secondary instability. *J. Fluid Mech.*, 406:131–174.

Kohama, Y., Saric, W. S., and Hoos, J. A. (1991). A high frequency secondary instability of crossflow vortices that leads to transition. Proc. R. Aeronaut. Soc. Conf on Boundary Layer Transition & Control.

Konishi, Y. and Asai, M. (2004). Experimental investigation of the instability of spanwise-periodic low-speed streaks. *Fluid Dyn. Res.*, 34:299–315.

Kotsonis, M., Rius-Vidales, A. F., Zoppini, G., Casacuberta, J., Michelis, T., and Westerbeek, S. (2024). Aircraft surface. International application published under the patent cooperation treat (PCT) No. WO 2024/151166 A1. Filed 15th January 2024.

Krochak, O., Casacuberta, J., Hickel, S., and Kotsonis, M. (2022). Mechanisms of interaction between a stationary crossflow instability and backward-facing steps. In *12th International Symposium on Turbulence and Shear Flow Phenomena, TSFP 2022*.

Landahl, M. T. (1975). Wave breakdown and turbulence. *SIAM J. Appl. Math.*, 28:735–756.

Landahl, M. T. (1980). A note on an algebraic instability of inviscid parallel shear flows. *J. Fluid Mech.*, 98:243–251.

Lanzerstorfer, D. and Kuhlmann, H. C. (2011). Global stability of the two-dimensional flow over a backward-facing step. *J. Fluid Mech.*, 693:1–27.

Lanzerstorfer, D. and Kuhlmann, H. C. (2012). Three-dimensional instability of the flow over a forward-facing step. *J. Fluid Mech.*, 695:390–404.

Li, F. and Choudhari, M. M. (2011). Spatially developing secondary instabilities in compressible swept airfoil boundary layers. *Theor. Comput. Fluid Dyn.*, 25:65–84.

Li, F., Choudhari, M. M., and Duan, L. (2016). Stationary crossflow breakdown due to mixed mode spectra of secondary instabilities. *AIAA Paper 2016-3789*.

Li, F., Choudhari, M. M., and Duan, L. (2017). Stationary crossflow breakdown due to interaction between secondary instabilities. *AIAA Paper 2017-4302*.

Loiseau, J.-C., Robinet, J.-C., Cherubini, S., and Leriche, E. (2014). Investigation of the roughness-induced transition: global stability analyses and direct numerical simulations. *J. Fluid Mech.*, 760:175–211.

Loiseau, J.-C., Robinet, J.-C., and Leriche, E. (2016). Intermittency and transition to chaos in the cubical lid-driven cavity flow. *Fluid Dyn. Res.*, 48.

Luchini, P. (2000). Reynolds-number-independent instability of the boundary layer over a flat surface: optimal perturbation. *J. Fluid Mech.*, 404:289–309.

Lundell, F. and Alfredsson, P. H. (2003). Experiments on control of streamwise streaks. *Eur. J. Mech. B Fluids*, 22:279–290.

Mack, L. M. (1977). Transition prediction and linear stability theory. In *AGARD Conf. Proc. nº 224*.

Mack, L. M. (1984). *Boundary layer linear stability theory*. AGARD No. 709.

Malik, M. R., Li, F., and Chang, C.-L. (1994). Crossflow disturbances in three-dimensional boundary layers: nonlinear development, wave interaction and secondary instability. *J. Fluid Mech.*, 268:1–36.

Malik, M. R., Li, F., Choudhari, M. M., and Chang, C.-L. (1999). Secondary instability of crossflow vortices and swept-wing boundary-layer transition. *J. Fluid Mech.*, 399:85–115.

Marino, L. and Luchini, P. (2009). Adjoint analysis of the flow over a forward-facing step. *Theor. Comput. Fluid Dyn.*, 23:37–54.

Marxen, O., Lang, M., Rist, U., Levin, O., and Henningson, D. S. (2009). Mechanisms for spatial steady three-dimensional disturbance growth in a non-parallel and separating boundary layer. *J. Fluid Mech.*, 634:165–189.

Matsubara, M. and Alfredsson, P. H. (2001). Disturbance growth in boundary layers subjected to free-stream turbulence. *J. Fluid Mech.*, 430:149–168.

Moffatt, H. K. (1967). In *Proceedings of the International Colloquium on Atmospheric Turbulence and Radio Wave Propagation, edited by A. M. Yaglom and V. I. Tatarsky (Nauka, Moscow)*, pages 166–188.

Morkovin, M. (1969). *On the many faces of transition*. Springer, Boston, MA.

Morkovin, M. V., Reshotko, E., and Herbert, T. (1994). Transition in open flow systems–A reassessment. *Bull. Am. Phys. Soc.*, 39:1882.

Müller, B. (1990). Experimentelle untersuchung der querströmungsinstabilität im linearen und nichtlinearen bereich des transitiongebietes. DLR-FB 90-09.

NASA Blog (2011). Laminar flow and the Holy Grail. Retrieved from `https://blogs.nasa.gov/armstrong/2011/02/11/post_1296777084480/`. Accessed: 21 November 2023.

NASA social media (2011). Laminar flow is aviation's Holy Grail. Why should you care if we find it? Retrieved from `https://twitter.com/NASA/status/53084562200334336`. Accessed: 21 November 2023.

Nayfeh, A. H. (1992). Influence of two-dimensional imperfections on laminar flow. SAE Technical Paper (No. 921990).

Paredes, P., Hanifi, A., Theofilis, V., and Henningson, D. S. (2015). The nonlinear PSE-3D concept for transition prediction in flows with a single slowly-varying spatial direction. In *IUTAM Symposium on Laminar-Turbulent Transition: 8th IUTAM Symposium, Copacabana Beach Rio de Janeiro, Brazil, September 8–12, 2019*, pages 36–44. Elsevier.

Park, D. and Park, S. O. (2013). Linear and non-linear stability analysis of incompressible boundary layer over a two-dimensional hump. *Comput. Fluids*, 73:80–96.

Perraud, J., Arnal, D., Séraudie, A., and Tran, D. (2004). Laminar-turbulent transition on aerodynamic surfaces with imperfections. Meeting on Enhancement of NATO military flight vehicle performance by management of interacting boundary layer transition and separation.

Perraud, J. and Séraudie, A. (2000). Effects of steps and gaps on 2D and 3D transition. In *European Congress on Computational Methods in Applied Sciences and Engineering*, Barcelona, Spain. ECCOMAS.

Pfenninger, W. (1965). Some results from the x-21 program. Part I. Flow phenomena at the leading edge of swept wings. recent developments. In *Boundary Layer Research, Part IV*. AGARDograph, 97.

Picella, F., Loiseau, J.-C., Lusseyran, F., Robinet, J.-C., Cherubini, S., and Pastur, L. (2018). Successive bifurcations in a fully three-dimensional open cavity flow. *J. Fluid Mech.*, 844:855–877.

Poll, D. I. A. (1977). *Leading edge transition on swept wings.* AGARD CP-224.

Poll, D. I. A. (1985). Some observations of the transition process on the windward face of a long yawed cylinder. *J. Fluid Mech.*, 150:329–356.

Pollard, A., Wakarani, N., and Shawn, J. (1996). Genesis and morphology of erosional shapes associated with turbulent flow over a forward-facing step. Coherent flow structures in open channels.

Radeztsky, R. H., Kosorygin, V. S., and Saric, W. S. (1991). Control of T-S waves with freestream sound and 2-D roughness. *Bull. Am. Phys. Soc.*, 2629.

Radeztsky, R. H., Reibert, M. S., and Saric, W. S. (1999). Effect of isolated micro-sized roughness on transition in swept-wing flows. *AIAA J.*, 37(11):1370–1377.

Rayleigh, L. (1880). On the stability of certain fluid motions. *Proc. Math. Soc. London*, 11(57).

Reddy, S. C. and Henningson, D. S. (1993). Energy growth in viscous channel flows. *J. Fluid Mech.*, 252:209–238.

Redeker, G., Horstmann, K., Koester, H., Thiede, P., and Szodruch, J. (1990). Design for a natural laminar flow glove for a transport aircraft. In *Flight Simulation Technologies Conference and Exhibit*, page 3043.

Reed, H. L. and Saric, W. S. (1996). Linear stability theory applied to boundary layers. *Annu. Rev. Fluid. Mech.*, 28:389–428.

Reibert, M., Saric, W., Carrillo Jr., R., and Chapman, K. (1996). Experiments in nonlinear saturation of stationary crossflow vortices in a swept-wing boundary layer. In *34th Aerospace Sciences Meeting and Exhibit*, page 184.

Rempfer, D. (2006). On boundary conditions for incompressible Navier-Stokes problems. *Appl. Mech. Rev.*, 59:107–125.

Reshotko, E. (2001). Transient growth: A factor in bypass transition. *Phys. Fluids*, 13.

Ricco, P., Luo, J., and Wu, X. (2011). Evolution and instability of unsteady nonlinear streaks generated by free-stream vortical disturbances. *J. Fluid Mech.*, 677:1–38.

Rius-Vidales, A. F. (2022). *Influence of a forward-facing step on crossflow instability and transition: An experimental study in a swept wing boundary-layer.* Doctoral dissertation, Delft University of Technology. TU Delft Repository. https://doi.org/10.4233/uuid:6fd8a152-ab7a-4ecd-a817-61945d431bef.

Rius-Vidales, A. F. and Kotsonis, M. (2020). Influence of a forward-facing step surface irregularity on swept wing transition. *AIAA J.*, 58(12):5243–5253.

Rius-Vidales, A. F. and Kotsonis, M. (2021). Impact of a forward-facing step on the development of crossflow instability. *J. Fluid Mech.*, 924:A34.

Rius-Vidales, A. F. and Kotsonis, M. (2022). Unsteady interaction of crossflow instability with a forward-facing step. *J. Fluid Mech.*, 939:A19.

Rius-Vidales, A. F., Morais, L., Westerbeek, S., Casacuberta, J., Soyler, M., and Kotsonis, M. (2025). Delay of swept-wing transition using a surface hump. *J. Fluid Mech.*, 1014:A35.

Rodríguez, D., Gennaro, E., and Juniper, M. (2013). The two classes of primary modal instability in laminar separation bubbles. *J. Fluid Mech.*, 734:R4.

Rossow, C.-C. (2010). Aerodynamics – A discipline swept away? *Aeronaut. J.*, 114(1160):599–609.

Sanderse, B. and Koren, B. (2012). Accuracy analysis of explicit Runge-Kutta methods applied to the incompressible Navier-Stokes equations. *J. Comput. Phys.*, 231:3041–3063.

Saric, W. S. (1975). Nonparallel stability of boundary-layer flows. *Phys. Fluids*, 18:945–950.

Saric, W. S. (1994). *Physical description of boundary-layer transition: experimental evidence.* AGARD R-793.

Saric, W. S., Carpenter, A. L., and Reed, H. L. (2011). Passive control of transition in three-dimensional boundary layers, with emphasis on discrete roughness elements. *Philos. Trans. R. Soc. A*, 369(1940):1352–1364.

Saric, W. S., Reed, H. L., and Kerschen, E. J. (2002). Boundary-layer receptivity to freestream disturbances. *Annu. Rev. Fluid Mech.*, 34:291–319.

Saric, W. S., Reed, H. L., and White, E. B. (2003). Stability and transition of three-dimensional boundary layers. *Annu. Rev. Fluid Mech.*, 35(1):413–440.

Scharnhorst, K. (2001). Angles in complex vector spaces. *Acta Appl. Math.*, 69:95–103.

Schlichting, H. (1979). *Boundary-layer theory.* McGraw-Hill, seventh edition.

Schmid, P. J. (2007). Nonmodal stability theory. *Annu. Rev. Fluid. Mech.*, 39:129–162.

Schmid, P. J. and Brandt, L. (2014). Analysis of fluid systems: Stability, receptivity, sensitivity: Lecture notes from the FLOW-NORDITA Summer School on Advanced Instability Methods for Complex Flows, Stockholm, Sweden, 2013. *Appl. Mech. Rev.*, 66(2).

Schmid, P. J. and Henningson, D. S. (2001). *Stability and transition in shear flows.* Springer.

Schrauf, G. (2005). Status and perspectives of laminar flow. *Aeronaut. J.*, 109(1102):639–644.

Serpieri, J. and Kotsonis, M. (2016). Three-dimensional organisation of primary and secondary crossflow instability. *J. Fluid Mech.*, 799:200–245.

Serpieri, J., Venkata, S. Y., and Kotsonis, M. (2017). Conditioning of cross-flow instability modes using dielectric barrier discharge plasma actuators. *J. Fluid Mech.*, 833:164–205.

Sescu, A. and Afsar, M. Z. (2018). Hampering Görtler vortices via optimal control in the framework of nonlinear boundary region equations. *J. Fluid Mech.*, 848:5–41.

Shu, C.-W. (1988). Total-variation-diminishing time discretizations. *J. Sci. Stat. Comput.*, 9(6):1073–1084.

Sleijpen, G. L. G., van der Vorst, H. A., and Fokkema, D. R. (1994). BiCGstab(l) and other hybrid Bi-CG methods. *Numer. Algorithms*, 7:75–109.

Smith, A. and Gamberoni, N. (1956). Transition, pressure gradient and stability theory. In *Aircraft Co., Report No. ES 26 388, El Segundo, CA*.

Smith, A. M. O. and Clutter, D. W. (1959). The smallest height of roughness capable of affecting boundary-layer transition. *J. Aerosp. Sci*, 26(4):229–245.

Smith, D. (2000). *Translator's introduction. In F. Nietzsche, The Birth of Tragedy. (Original work published in 1872).* Oxford University Press Inc., New York.

Spalart, P. R. and Strelets, M. K. (2000). Mechanisms of transition and heat transfer in a separation bubble. *J. Fluid Mech.*, 403:329–349.

Stüer, H., Gyr, A., and Kinzelbach, W. (1999). Laminar separation on a forward facing step. *Eur. J. Mech. B Fluids*, 18:675–692.

Swearingen, J. D. and Blackwelder, R. F. (1987). The growth and breakdown of streamwise vortices in the presence of a wall. *J. Fluid Mech.*, 182:255–290.

Tani, I. (1969). Boundary-layer transition. *Annu. Rev. Fluid Mech.*, 1:169–196.

Tempelmann, D., Hanifi, A., and Henningson, D. S. (2010). Spatial optimal growth in three-dimensional boundary layers. *J. Fluid Mech.*, 646:5–37.

Theofilis, V. (2003). Advances in global linear instability analysis of nonparallel and three-dimensional flows. *Prog. Aerosp. Sci.*, 39:249–315.

Trefethen, L. N., Trefethen, A. E., Reddy, S. C., and Driscoll, T. A. (1993). Hydrodynamic stability without eigenvalues. *Science*, 28:578–584.

Tufts, M. W., Reed, H. L., Crawford, B. K., Duncan Jr., G. T., and Saric, W. S. (2017). Computational investigation of step excrescence sensitivity in a swept-wing boundary layer. *J. Aircr.*, 54:602–626.

Ustinov, M. and Ivanov, A. V. (2018). Cross-flow dominated transition control by surface micro-relief. AIP Conference Proceedings 2027.

van der Vorst, H. A. (1992). Bi-CGSTAB: A fast and smoothly converging variant of Bi-CG for the solution of nonsymmetric linear systems. *SIAM J. Sci. Statist. Comput.*, 13:631–644.

Van Ingen, J. L. (1956). A suggested semi-empirical method for the calculation of the boundary layer transition region. Rep. no. VTH-74, Delft University of Technology, The Netherlands.

Wassermann, P. and Kloker, M. (2002). Mechanisms and passive control of crossflow-vortex-induced transition in a three-dimensional boundary layer. *J. Fluid Mech.*, 456:49–84.

Wassermann, P. and Kloker, M. (2005). Transition mechanisms in a three-dimensional boundary-layer flow with pressure-gradient changeover. *J. Fluid Mech.*, 530:265–293.

Westerbeek, S. (2020). Development of a nonlinear parabolized stability equations (NPSE) analysis tool for spanwise invariant boundary layers. Masters thesis, Delft University of Technology. TU Delft Repository. https://repository.tudelft.nl/record/uuid:7fb699e1-3df7-4fcd-8bda-886e7b11aade.

Westerbeek, S., Casacuberta, J., and Kotsonis, M. (2025). Linear and nonlinear interactions between stationary crossflow instabilities and a smooth surface hump. Under consideration for publication in *J. Fuid Mech.*

Westerbeek, S. H. J., Hulshoff, S., Schuttelaars, H., and Kotsonis, M. (2024). DeHNSSo: The Delft Harmonic Navier-Stokes Solver for nonlinear stability problems with complex geometric features. *Comput. Phys. Commun.*, 302:109250.

Westin, A. K. J., Boiko, A. V., Klingmann, B. G. B., Kozlov, V. V., and Alfredsson, P. H. (1994). Experiments in a boundary layer subjected to free stream turbulence. Part 1. Boundary layer structure and receptivity. *J. Fluid Mech.*, 281:193–218.

White, E. B., Rice, J. M., and Ergin, F. G. (2005). Receptivity of stationary transient disturbances to surface roughness. *Phys. Fluids*, 17(6):064109.

Wicke, K., Kruse, K., and Linke, F. (2012). Mission and economic analysis of aircraft with natural laminar flow. In *28th Congress of the International Council of the Aeronautical Sciences (ICAS)*, pages 23–28.

Wilhelm, D., Härtel, C., and Kleiser, L. (2003). Computational analysis of the two-dimensional-three-dimensional transition in forward-facing step flow. *J. Fluid Mech.*, 489:1–27.

Wu, X. and Hogg, L. W. (2006). Acoustic radiation of Tollmien-Schlichting waves as they undergo rapid distortion. *J. Fluid Mech.*, 550:307–347.

Xu, H., Sherwin, S. J., Hall, P., and Wu, X. (2016). The behaviour of Tollmien-Schlichting waves undergoing small-scale localised distortions. *J. Fluid Mech.*, 792:499–525.

Zaki, T. A. and Durbin, P. A. (2005). Mode interaction and the bypass route to transition. *J. Fluid Mech.*, 531:85–111.

Zoppini, G., Michelis, T., Ragni, D., and Kotsonis, M. (2023). The near wake of discrete roughness elements on swept wings. *J. Fluid Mech.*, 960:A11.

A

Appendix: Plots of perturbation evolution at the step

A

This appendix provides additional plots of stationary perturbation organisation at the step with regard to chapter 4 (figures A.1 and A.2) and chapter 6 (figures A.3 and A.4).

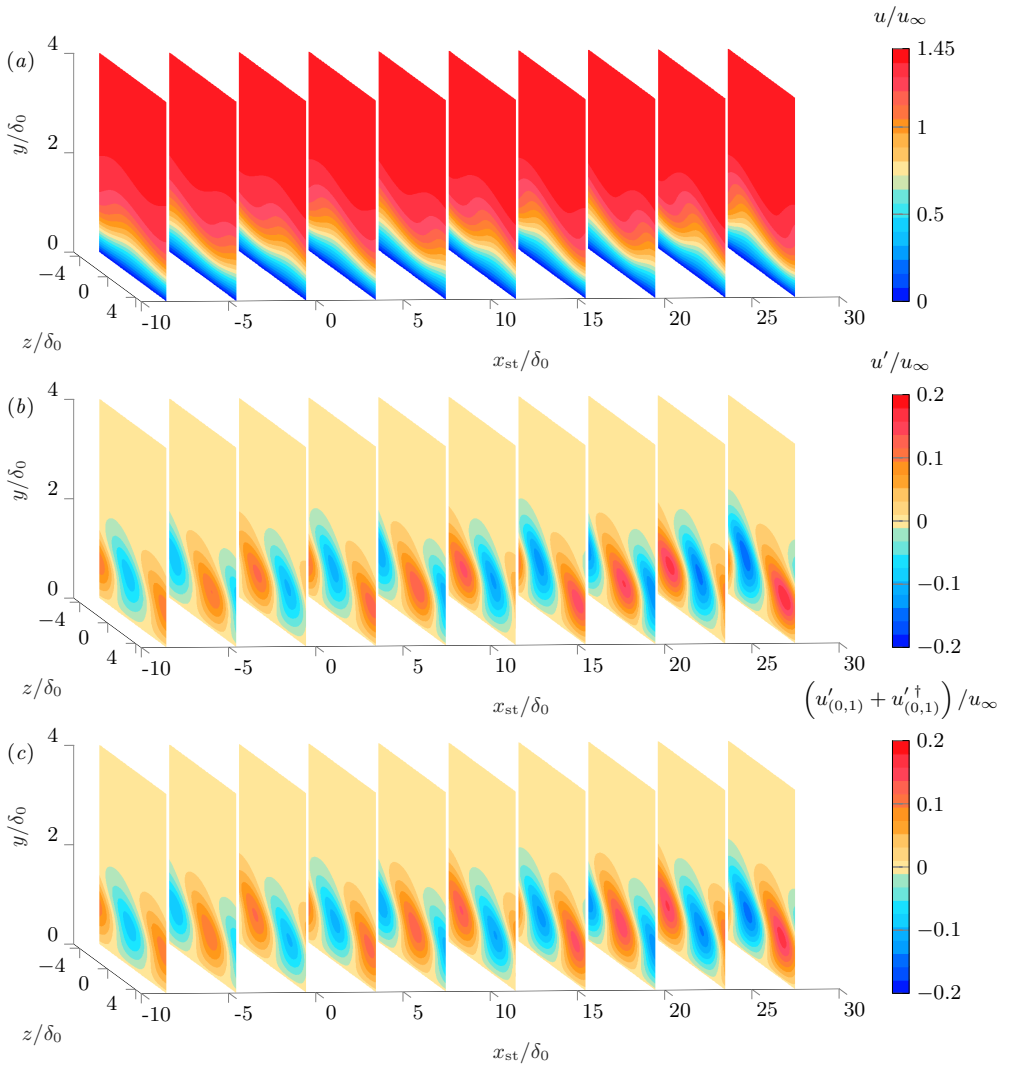

Figure A.1: Organisation of the chordwise velocity of the steady perturbed flow (a), total perturbation field (b), fundamental perturbation field (c) in the reference (no-step) case under *medium*-amplitude CFI conditions.

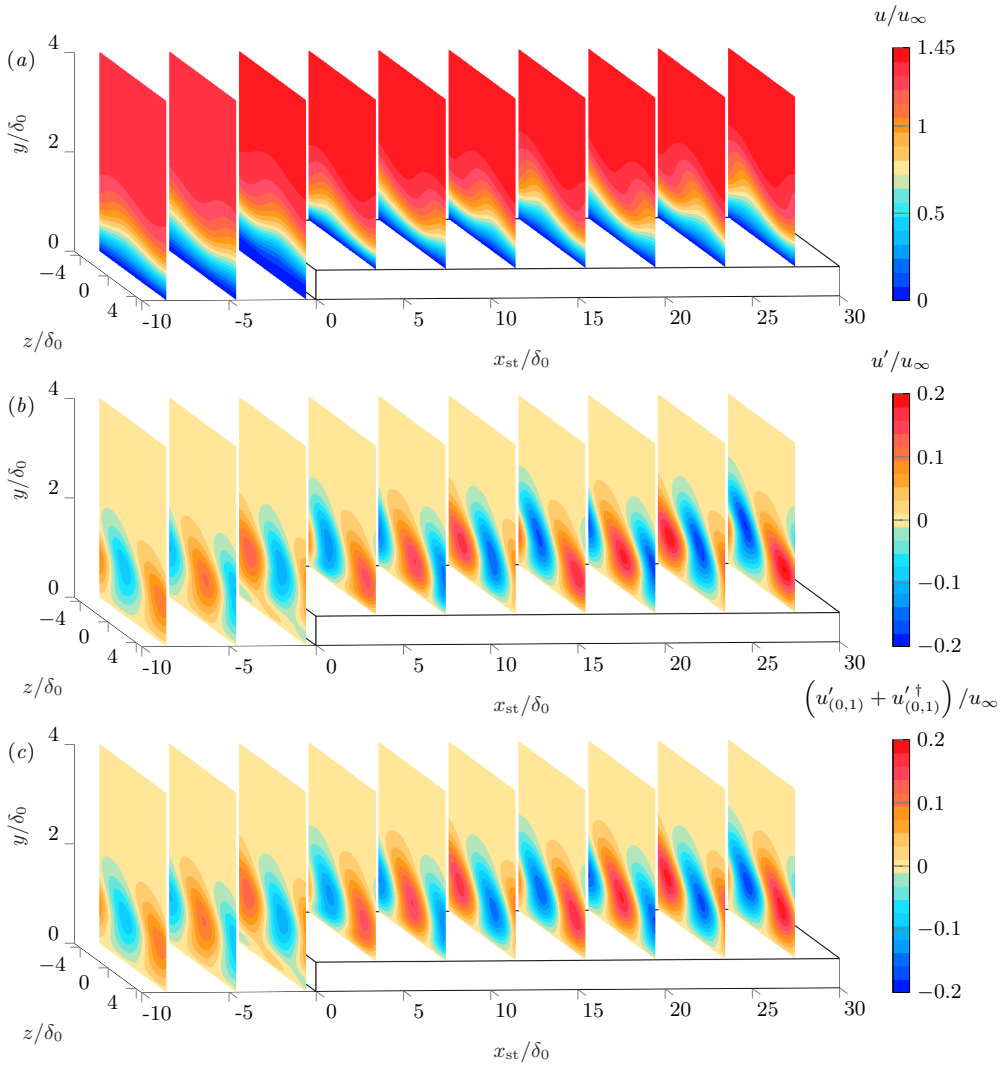

FIGURE A.2: Organisation of the chordwise velocity of the steady perturbed flow (a), total perturbation field (b), fundamental perturbation field (c) in step case I under *medium*-amplitude CFI conditions.

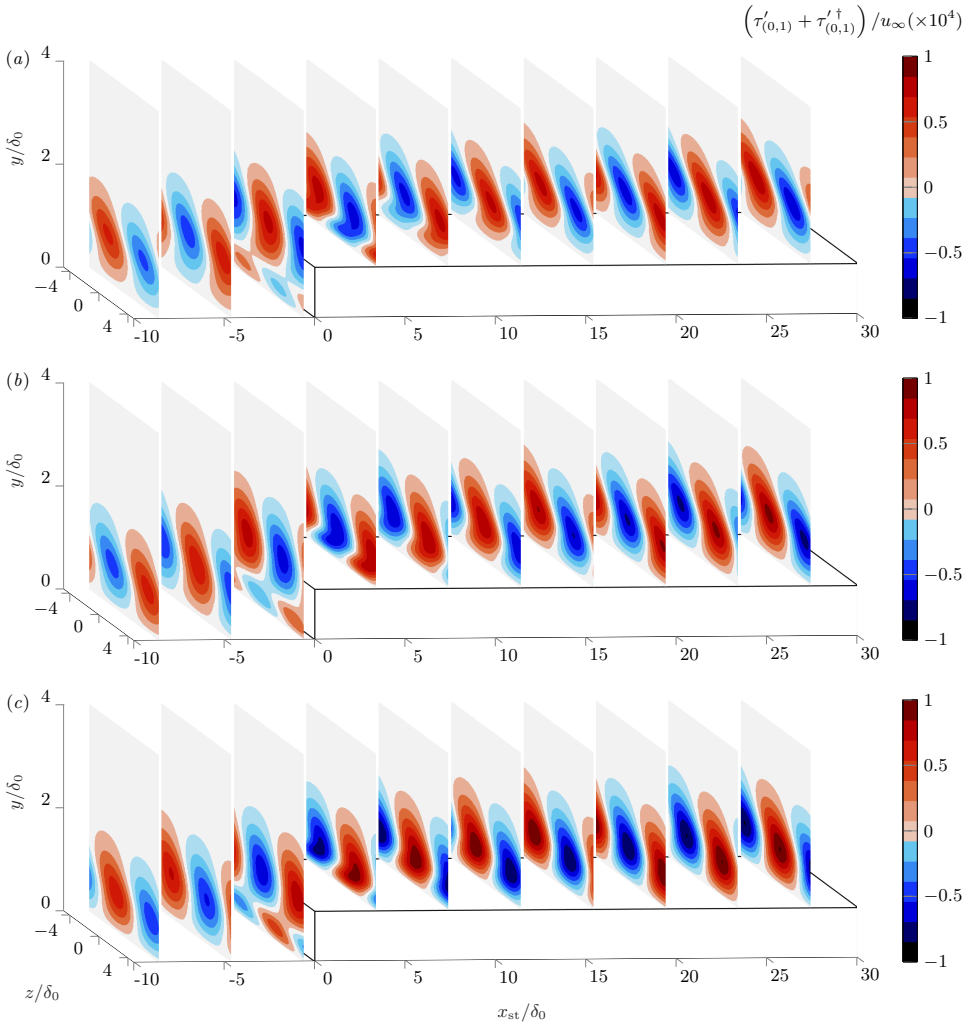

FIGURE A.3: Organisation of the streamwise-velocity perturbation for $\beta = \beta_0$ in cases *Test A* (*a*), *B* (*b*), and *C* (*c*) of table 2.5.

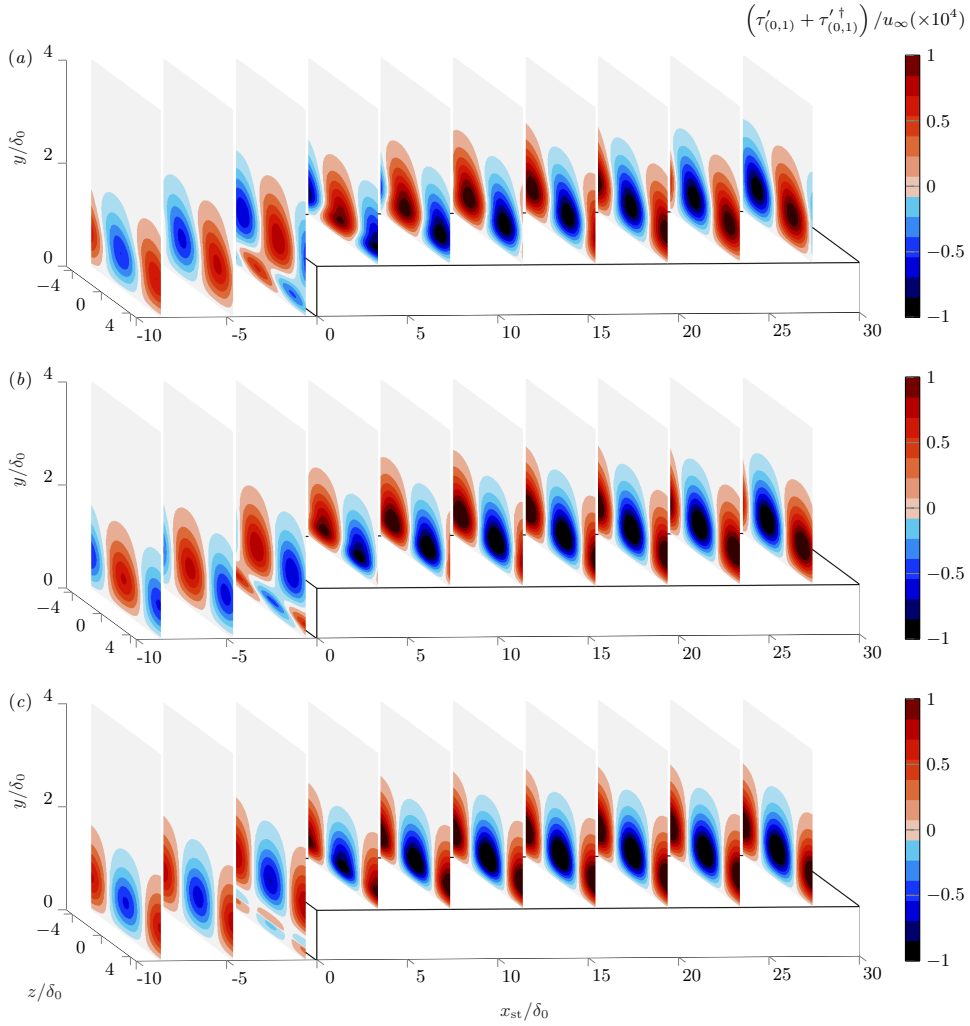

FIGURE A.4: Organisation of the streamwise-velocity perturbation for $\beta = \beta_0$ in cases *Test D* (*a*), *E* (*b*), and *F* (*c*) of table 2.5.

B

Appendix: Setup of stability methods

B.1. Linear and non-linear Parabolised Stability Equations

B

The NPSE are solved on the unperturbed DNS base flow considering a grid containing 500 equispaced streamwise stations and 80 Chebyshev collocation points in the wall-normal direction. The first-order backward Euler scheme is used for the discretisation of chordwise derivatives and eleven stationary spanwise Fourier modes (including the mean-flow distortion) are considered for the representation of perturbations. The simulations are initialised with a stationary crossflow eigenmode obtained from LST on the inflow base-flow profile, to which a finite amplitude is assigned.

The high-order perturbation harmonics are introduced in the chordwise-marching scheme, successively in space, once their *strength* surpasses the threshold of 10^{-8} in units of u_∞; the measure of strength is based on the order of magnitude of the associated non-linear forcing term. When a new harmonic component is added, its amplitude is assumed to be zero in the grid point immediately upstream of it. Strong initial growth is therefore perceived immediately downstream of it. Finally, inherent to the PSE approximations, the complex streamwise wavenumber of each mode is iteratively updated at each streamwise station to a threshold of $10^{-6}/Re$ (where Re is the Reynolds number), ensuring slow chordwise changes in the perturbation shape function. By considering only a single fundamental mode and disabling non-linear interactions, the procedure provides solutions to the Linear Parabolised Stability Equations (LPSE). In this case, the solutions are independent of the initial mode amplitude, which is arbitrarily matched to the NPSE and DNS amplitude at a selected x-position.

B.2. Two-dimensional spanwise BiGlobal

Two-dimensional linear stability analysis is additionally employed in this thesis to assess mechanisms of unsteady instability of the steady perturbed flow downstream of the step[1]. A two-dimensional plane-marching stability approach has been considered, popularly known as PSE-3D (Paredes et al., 2015), which is here formulated using a non-orthogonal coordinate system. The flow case investigated in this thesis requires the use of a non-orthogonal coordinate system because it is periodic in the z-direction, i.e., parallel to the step, while the smallest gradients are encountered in a direction, that is approximately aligned with the crossflow vortex. The latter direction, denoted x_θ, is non-orthogonal versus the y-z plane. The angle between the leading-edge-orthogonal x- and non-orthogonal x_θ-directions is denoted by θ.

The plane-marching stability approach is derived in three steps. First, the Navier-Stokes equations are linearised about the steady perturbed flow, $\boldsymbol{q}_{\mathrm{DB}}$ (2.10). To this end, the instantaneous flow is decomposed into the steady perturbed flow and unsteady perturbations with infinitesimal amplitude, $\boldsymbol{q}'_{\mathrm{BiG}}$. Substituting this decomposition into the Navier-Stokes equations, cancelling the terms that form the governing equations for $\boldsymbol{q}_{\mathrm{DB}}$, and dropping the nonlinear terms in $\boldsymbol{q}'_{\mathrm{BiG}}$ produces

[1] The method description is derived from a publication by the author (see Groot et al. (2025)).

the linearised Navier-Stokes equations. Second, the linearised Navier-Stokes equations are transformed to the non-orthogonal coordinate system. Third, the following stability ansatz, that leverages slow evolution in the x_θ-direction, is imposed:

$$\boldsymbol{q}'_{\mathrm{BiG}}(x_\theta, y, z_\theta, t) = \tilde{\boldsymbol{q}}_{\mathrm{BiG}}(x_\theta, y, z_\theta) \exp\left[\mathrm{i}\left(\int_{x_{\theta,0}}^{x_\theta} \alpha_\theta(\bar{x}_\theta)\, \mathrm{d}\bar{x}_\theta - \omega t\right)\right] + \mathrm{c.c.}, \tag{B.1}$$

where $\tilde{\boldsymbol{q}}_{\mathrm{BiG}} = [\tilde{u}_{\mathrm{BiG}}\ \tilde{v}_{\mathrm{BiG}}\ \tilde{w}_{\mathrm{BiG}}\ \tilde{p}_{\mathrm{BiG}}]^{\mathrm{T}}$ contains the perturbation shape functions, α_θ is the wavenumber in the x_θ-direction, ω is the angular frequency, $x_{\theta,0}$ is initialization location, and $\bar{x}_\theta$ indicates the integration-variable equivalent of x_θ.

Substituting ansatz (B.1) into the linearised Navier-Stokes equations and dropping the second-order x_θ-derivatives of $\tilde{\boldsymbol{q}}_{\mathrm{BiG}}$ yields the plane-marching stability equations. Upon dropping the x_θ-dependence of $\tilde{\boldsymbol{q}}_{\mathrm{BiG}}$ and α_θ, the stability problem reduces to a two-dimensional (i.e., in the $z_{(\theta)}$-y plane) eigenvalue problem, that is referred in this thesis to as the local approach. The reader is referred to Groot et al. (2025) for all relevant details of the non-orthogonal transformation and the full system of stability equations. In the Ω-nomenclature of Groot et al. (2025) that precisely disambiguates the assumptions made in the stability approaches, the plane-marching approach deployed here corresponds to: $\Omega_2 = 0$, $\Omega_1 = \Omega_b = 1$, while the local approach sets: $\Omega_2 = \Omega_1 = 0$ and $\Omega_b = 1$.

The systems of partial differential equations are closed with boundary, initial, and auxiliary conditions. Periodic boundary conditions are imposed at the spanwise boundaries and no-slip conditions are imposed at the wall and free stream boundaries; the y-momentum equation is used as a compatibility condition for the pressure at wall and free-stream boundaries. The local, spatial eigenvalue problem is solved with the Arnoldi algorithm (for complex α_θ, upon specifying a value of ω) in order to obtain the initial condition at a location immediately downstream of the step, namely $x = 178\delta_0$. Ansatz (B.1) in itself does not guarantee that the x_θ-derivative of the perturbation shape functions $\tilde{\boldsymbol{q}}_{\mathrm{BiG}}$ are small; the x_θ-dependence of both α_θ and $\tilde{\boldsymbol{q}}_{\mathrm{BiG}}$ in ansatz (B.1) is leveraged for this purpose. Given a reasonable initial guessed solution for a given x-station, the x_θ-derivative of the shape functions is iteratively minimised by updating α_θ with the following auxiliary condition:

$$\alpha_\theta^{k+1} = \alpha_\theta^{k} - \mathrm{i}\frac{\iint \tilde{\boldsymbol{q}}^{\mathrm{H}}_{\mathrm{BiG}} \mathcal{M} \dfrac{\partial \tilde{\boldsymbol{q}}_{\mathrm{BiG}}}{\partial x_\theta}\, \mathrm{d}y\, \mathrm{d}z_\theta}{\iint \tilde{\boldsymbol{q}}^{\mathrm{H}}_{\mathrm{BiG}} \mathcal{M} \tilde{\boldsymbol{q}}_{\mathrm{BiG}}\, \mathrm{d}y\, \mathrm{d}z_\theta}; \quad \mathcal{M} = \begin{bmatrix} 1 & & & 0 \\ & 1 & & \\ & & 1 & \\ 0 & & & 0 \end{bmatrix}, \tag{B.2}$$

where $\tilde{\boldsymbol{q}}^{\mathrm{H}}_{\mathrm{BiG}} = [\tilde{u}^{\mathrm{H}}_{\mathrm{BiG}}\ \tilde{v}^{\mathrm{H}}_{\mathrm{BiG}}\ \tilde{w}^{\mathrm{H}}_{\mathrm{BiG}}\ \tilde{p}^{\mathrm{H}}_{\mathrm{BiG}}]$ and the superscript H indicates Hermitian transposition. The perturbation-pressure contribution is dropped, because it is directly linked to the velocity perturbations for incompressible conditions. This condition was deemed satisfied when relative α_θ-differences were recorded to drop below a threshold: $|\alpha_\theta^{k+1} - \alpha_\theta^{k}|/|\alpha_\theta^{k+1}| \leq 2.2 \times 10^{-10}$.

Perturbation amplification is quantified with N-factors, calculated as follows:

$$N(x) = -\int_{x_0}^{x} \alpha_{\theta,i}(x_\theta(\bar{x}))\sec\theta(\bar{x})\,\mathrm{d}\bar{x} + \frac{1}{2}\ln\frac{E_{\mathrm{BiG}}(x)}{E_{\mathrm{BiG}}(x_0)}, \tag{B.3}$$

where: $$E_{\mathrm{BiG}}(x) = \iint \left(|\tilde{u}_{\mathrm{BiG}}(x_\theta(x), y, z_\theta)|^2 + |\tilde{v}_{\mathrm{BiG}}|^2 + |\tilde{w}_{\mathrm{BiG}}|^2\right)\mathrm{d}y\,\mathrm{d}z_\theta,$$

$\bar{x}$ is the integration-variable equivalent of the orthogonal x-coordinate, and x_0 is here taken to correspond to the initialisation location near the step.

The stabilisation procedure proposed by Andersson et al. (1998) enables the use of a high resolution in the streamwise direction immediately downstream of the step, without having to drop any potentially relevant terms to eliminate the residual ellipticity (Herbert, 1997). In the Ω-nomenclature of Groot et al. (2025), $\Omega_p = 1$ is set here. A small, constant value of the stabilisation length scale $s = O(\delta_0)$ renders the plane-marching approach effective for the most-amplified perturbation immediately behind the step. Solution convergence is demonstrated as s is reduced (see table 8.2). For more details on the stabilisation approach, see Groot et al. (2025).

The plane-marching BiG equations and boundary conditions are discretised by using finite differences. Central differences are used in z (tenth order) and y (sixth order), while fixing the stencil width and moving the evaluation point for derivatives toward a given boundary when necessary. A BiQuadratic mapping (Groot et al., 2018, § 3.1.4) is used in z to produce an approximately uniform distribution $((z_{i1}, z_{i2})/\lambda_z = (-1, 1)/6$, with $z/\lambda_z \in [-1/2, 1/2])$. Another BiQuadratic mapping is used in y to highly cluster the grid around the shear layer of interest $((y_{i1}, y_{i2}, y_{\max})/\delta_0 = (0.5, 2, 24.92))$.

Upon using a Chebyshev Gauss-Lobatto node-distribution in the computational ξ-domain with $\xi \in [-1, 1]$ (Groot et al., 2018, § 3.1.1), nodes are clustered toward the boundaries to avoid the Runge phenomenon. The wall-normal mapping parameters were chosen to maximise the resolution for the most unstable x-instance of the most amplified mode as computed with the local approach (with maximal $-\alpha_{\theta,i}\sec\theta$ in x for $f = 12$ kHz; $|\Delta\alpha_{\theta,i}/\alpha_{\theta,i}| = 3.0 \times 10^{-7}$ or less, upon reducing the number of nodes by 10% in each direction), see figure B.1 (*a*) for an example grid. The number of nodes ($N_z = 300$, $N_y = 200$) yields an negligible error in $\alpha_{\theta,i}$ (specifically: $|\Delta\alpha_{\theta,i}/\alpha_{\theta,i}| = 8.0 \times 10^{-5}$ or less) at a location where the same mode is less-well resolved based on the mapping setting, see figure B.1 (*b*). Second-order backward differences (backward Euler) are used in x_θ. Steps of $\Delta x/\delta_0 = 0.1$ are taken from the step up to $x_{\mathrm{st}}/\delta_0 = 7.38$, whereafter a larger stride of $\Delta x/\delta_0 = 1$ is used. All integrals over spatial coordinates are computed using numerical approaches with similar or higher orders of accuracy as the finite differences in the corresponding directions.

Finally, the angle $\theta = \theta_{\min}$ which forms between the x_θ-coordinate and the leading-edge-orthogonal x-coordinate in the large-amplitude step case s.*C*, is iteratively found at every considered x-station by minimising the quantity

$$\sqrt{\iint \left\{ \left(\frac{\partial u_{\mathrm{DB}}}{\partial x_\theta}\right)^2 + \left(\frac{\partial v_{\mathrm{DB}}}{\partial x_\theta}\right)^2 + \left(\frac{\partial w_{\mathrm{DB}}}{\partial x_\theta}\right)^2 \right\} \mathrm{d}y\mathrm{d}z}, \tag{B.4}$$

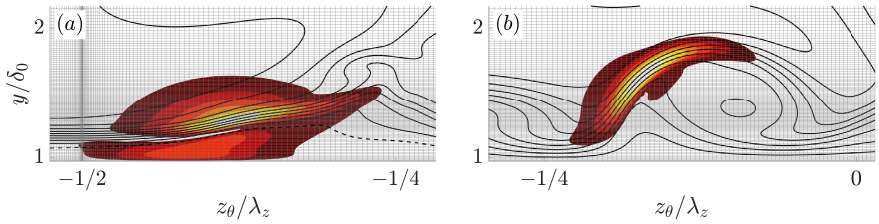

Figure B.1: Grid resolving step-mode$_1$ as computed with the local BiG approach at $x_{st}/\delta_0 = 1.18$ (a) and 10.38 (b) at 12 kHz. Grid (gray lines), isolevels of $|\tilde{u}_{BiG}|$ (filled contours; 1/8, 2/8,... 7/8 of maximum) and u_{DB} (solid lines: 10%, 20%,... 90% of maximum; dashed line: reverse flow).

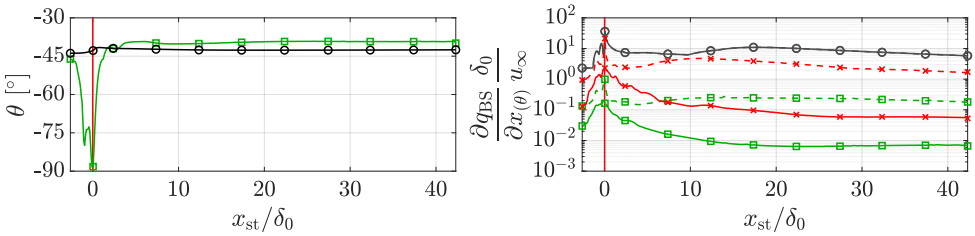

Figure B.2: (a) Chordwise evolution of $\theta = \theta_{min}$ (that minimises expression (B.4), green squares) and the direction of the inviscid streamline (black circles) corresponding to case s.C. (b) Chordwise evolution of the maximum (red lines) and root-mean-square (e.g., equation (B.4); green lines) in the z-y plane of the x- (dashed lines) and x_θ-derivatives (solid lines) and the y-derivative of the velocity in the direction of the inviscid streamline (black line, independent of the choice for θ). The vertical red line indicates the step location.

that is, the root-mean-square of the relevant $\partial \boldsymbol{q}_{DB}/\partial x_\theta$-derivatives in the z-y plane. The angle $\theta = \theta_{min}$ is shown alongside the inviscid streamline angle for case s.C in figure B.2 (a). It is furthermore demonstrated in figure B.2 (b), how the x_θ-derivatives are about an order of magnitude smaller than the x-derivatives (comparing solid coloured versus dashed lines) and how these x_θ-derivatives are more than an order of magnitude smaller than the principal shear associated to the velocity in direction of the inviscid streamline.

Biographical Note

Jordi Casacuberta Puig

By Sílvia Casacuberta Puig

Jordi came into the world as an "Olympic baby", born in Barcelona during the summer of 1992 while the city celebrated the Olympic Games. He grew up between the volcanoes of Olot and the sea of Mallorca, nourished by the love and support of his parents Maria Teresa and Carles, his extended family, and Joke, who hailed from the Netherlands and made him discover the *Stroopwafels* early in his life. I joined the family some years later –I was lucky to be the younger sibling, as it endowed me with the great gift of never having spent a day in my life without having Jordi by my side.

Jordi was always the best student in the class, graduating with honors throughout the school years. He also found time to become a phenomenal basketball player, a passion of his that continues to this day, and to win literary contests that were performed in Barcelona's Opera House (*El Liceu*). His love for fluid mechanics became evident early on: his high school thesis, which earned him numerous awards, studied Gaussian processes on viscous flows. I can still remember Jordi dropping shampoo down a surface of porous volcanic rock with our father in our living room. Jordi enrolled in *Universitat Politècnica de Catalunya* and earned a Bachelors in Aerospace Engineering, where his interest in fluid mechanics solidified. His Bachelors thesis was really two full theses in one: Jordi produced a study of the wall shear stress in the aorta in collaboration with *Hospital Sant Pau* as well as an open access guide to learn OpenFOAM (under the great motto: *let your dreams flow*).

His passion for fluid mechanics brought him to Delft, and in the summer of 2014 we all drove there together from Barcelona to settle Jordi into his new adventure. Jordi completed an MSc in Aerospace Engineering from TU Delft, while also doing an internship in Germany on industrial CFD. Jordi found a home in the research group that he would then stay on for his PhD, joining the dedicated supervision of Prof. Marios Kostonis & Prof. Stefan Hickel. Jordi's research on laminar-turbulent transition has taken him to conferences all around the globe, as well as to the world of entrepreneurship through his aircraft-wing patent (and even to the worlds of Nietzsche and of Greek philosophy).

During his years at Delft, Jordi has also taught and mentored many students, guiding them through the journey of research. I have always admired the spark in his eyes when he tells us about his students over the dinner table, and how clearly he loves sharing his enthusiasm for his field with others. I understand how fortunate these students are –I, too, had Jordi as my role model and teacher growing up. I

still remember how he helped me with my high-school physics homework. He would even calculate the projectile motion of an olive stone under air resistance, then test his results by launching them down our hallway while preparing for Olot's annual longest-throw contest.

Jordi has certainly let his dreams flow, and they have carried him to the enormous milestone of this PhD thesis. In the way, his motion through life –a perfect balance between the patience of laminar order and the spark of turbulence when curiosity takes hold– has touched everyone fortunate enough to share his current.

Curriculum Vitæ

Jordi CASACUBERTA PUIG

29-08-1992 Born in Barcelona, Spain

Education

2010–2014 Bachelors of Science
Polytechnic University of Catalonia, Spain

2014–2018 Master of Science
Delft University of Technology, The Netherlands

2018–2025 PhD in Aerospace Engineering
Delft University of Technology, The Netherlands
Thesis: Instability and transition of swept-wing flow
Promotors: Prof. dr.-ing habil. S. Hickel and Prof. dr. M. Kotsonis

Professional Experience

2015-2016 CFD Intern
EXA Corporation, Germany

2023-2024 Post-doctoral Researcher
Delft University of Technology, The Netherlands

Philosophical Note: laminar-turbulent transition and the striving of the human spirit (back cover)

One of Friedrich Nietzsche's most provocative claims is that "only as an aesthetic phenomenon is existence and the world eternally justified." Building on this proposition, the present essay contends that conducting a PhD thesis in science may be conceived as an artistic practice: one that enacts the tragic aesthetics of Greek culture and thereby constitutes a form of existential justification. At the same time, it warns against the progressive Apollonisation of scientific theses: the privileging of structure and quantifiable deliverables within narrowly defined time horizons at the expense of their Dionysian dimensions, which distorts the balance of scientific-artistic creation. What, then, might Nietzsche's interpretation of classical aesthetics, the dynamics of fluid flows, the form of the scientific thesis, and the striving of the human spirit have in common?

Nietzsche's proposition is situated within the polarity of two artistic drives that, while apparently opposed, are in fact complementary within Greek culture: the Apollonian and the Dionysian. The Apollonian, named after Apollo –the god of light, dream, and prophecy– represents order, structure, clarity, rational knowledge, and moderation. The Dionysian, named after Dionysus –the god of intoxication and ecstasy– embodies chaos, the dissolution of boundaries, formless flux, instinct, and excess (Smith, 2000).

Psychologically, the Apollonian may be understood as the human necessity for conscious control, rational planning, and the maintenance of order (comparable to Freud's ego and superego), while the Dionysian corresponds to unconscious impulses and emotional release. Taken in isolation, the Apollonian reduces life to sterile rationalism; the Dionysian, left unchecked, collapses into destructive excess.

According to Nietzsche, the Greek tragedy of the fifth century BC (exemplified

in the works of Aeschylus and Sophocles) embodies a unique synthesis of the Apollonian and the Dionysian. It unites the Apollonian principle of form, measure, and representation (akin to the plastic arts of sculpture) with the Dionysian principle of rhythm and music, producing an art form that affirms life by reconciling struggle with beauty (Smith, 2000). For Nietzsche, the tragic synthesis shows that difficulty, far from *negating* existence, becomes the medium through which meaning emerges, for it is inseparable from passion and willingness in any genuine *affirmation* of existence.

A central argument of Nietzsche's The Birth of Tragedy is that the rise of Socratic rationalism (mediated into Greek drama above all through the plays of Euripides) signals the decline of Greek tragedy. Socratic culture, with its faith that reason is both the source of virtue and the path to salvation, displaced the tragic worldview by imposing a purely Apollonian foundation masked as morality (Smith, 2000). For Nietzsche, this shift inaugurates the long decline of Western metaphysics: the gradual subordination of life to asceticism, reactive nihilism (see the work of Deleuze), and passive obedience to static objective orders, thereby weakening the existential *Will* (in Schopenhauer's sense) that once enabled individuals to affirm existence and the world by creating, striving, discovering, and self-overcoming.

The tension between the Apollonian and the Dionysian has been invoked in analogies concerning types of researchers. Albert Szent-Györgyi, the recipient of the 1937 Nobel Prize in Physiology or Medicine, observed that "in science the Apollonian tends to develop established lines to perfection, while the Dionysian relies on intuition and is more likely to open new, unexpected alleys for research." He further elaborates: "The Apollonian clearly sees the future lines of his research. Not so the Dionysian, who knows only the direction in which he wants to go out into the unknown and relies, to a great extent, on accidental observations." "A discovery must be, by definition, at variance with existing knowledge [...] A great deal of conscious or subconscious thinking must precede a Dionysian's observations. There is an old saying that a discovery is an accident finding a prepared mind." The Apollonian thus embodies continuity, refinement, and methodological discipline, while the Dionysian embodies rupture, creativity, and openness to chance in discovery.

Concerning a thesis in fluid mechanics, the tension between the Apollonian and the Dionysian manifests itself with particular intensity in both its scientific and metaphysical dimensions. It appears first in the very substance of the natural world: the duality of laminar and turbulent states of fluid motion. Laminar flow –ordered, predictable, and layered– constitutes the epitome of the Apollonian, a dream of clarity and stability. Yet this dream is fragile: at the slightest provocation, it breaks down into turbulence –flow that is disordered, seemingly unpredictable, but inherently containing coherent emergent forms. In between lies instability, the periodic *eternal recurrence* that debates between Apollonian rectitude and Dionysian excess. Because of instability, the fluid flow is never in static order, never granted a final state; its being means always becoming.

Second, the act of conducting a thesis in fluid mechanics mirrors the structure of Greek tragedy: it begins with Apollonian clarity and rational planning, but is inevitably destabilised by Dionysian uncertainty; a necessary tension in the transitioning (or, *becoming*) of the self. As the work progresses, the researcher comes to

realise that the Socratic promise of *poetic justice* through knowledge (with its customary *deus ex machina*[2]) does not apply here. Computer simulations and experiments fail despite rigorous preparation; hypotheses do not yield conclusive results despite accurate execution; articles are rejected despite months of careful labour. The initial Apollonian structure is thus rapidly confronted by one of the two faces[3] of Dionysus, namely, bitterness and destruction. Like Oedipus's fate[4], the Apollonian tragic hero *par excellence*, the researcher does not always hesitate because of moral failing or negligence, but because of what could not be known in advance. Yet it is precisely when the initial plan trembles and the *Will* is embodied, that the second face of Dionysus unexpectedly reveals itself: creativity and joy. Out of the collapse of certainty emerges the possibility of novelty: an affirmation not in spite of the failure, but through it.

A scientific thesis, therefore, cannot be understood without the Dionysian elements that make novelty possible, for a thesis is not only the execution of predefined goals, but also a canvas upon which the researcher expresses himself. Novelty, by definition, lies beyond pre-established objectives; it is never fully contained within the Apollonian plan. In this sense, the discovery at the heart of a thesis is also an aesthetic event: the transfiguration of doubt and failure into the joy of insight through creation and receptivity to the unexpected. Fear not to welcome Dionysus into one's research, and into one's life, for even the *smallest step* may redirect the course of inquiry in unforeseen and beautiful ways.

[2]The expression *deus ex machina* (literally, "god from the machine") originates in classical Greek tragedy, where a god would be lowered onto the stage by a mechanical crane (*mēchanē*) to resolve a seemingly unsolvable plot. In a broader sense, it designates any artificial or improbable intervention that abruptly resolves a dramatic or intellectual problem. Nietzsche criticises this device, insofar as it replaces the tragic confrontation by an Apollonian illusion of resolution.

[3]In Greek mythology, Dionysus embodies a dual nature: he is both the bringer of ecstasy, fertility, and communal joy, and the force of frenzy, destruction, and dissolution. This ambivalence is often analogised to wine, his sacred drink, which can uplift the heart and inspire creativity in moderation, yet intoxicate and ruin when taken to excess.

[4]Oedipus is the mythical king of Thebes in Sophocles' tragedy *Oedipus Tyrannus*. Despite his intelligence and determination to save his city, he fails because he is unaware of his true parentage: in trying to avoid the oracle's prophecy, he unknowingly kills his father and marries his mother. His downfall arises not from moral corruption, but from circumstances hidden from his knowledge.

Acknowledgements

The Greek philosopher Heraclitus famously remarked that *no man ever steps in the same river twice, for it is not the same river and he is not the same man.* In matters of being and becoming, few experiences are as quietly transformative as undertaking a PhD. This section is a gesture of gratitude to those who have guided, accompanied, and inspired me along this journey.

To my promotors

First and foremost, I would like to thank my promotors, Prof. dr. Marios Kotsonis and Prof. dr. Stefan Hickel.

I first met Stefan in 2016 during my MSc thesis, and our scientific collaboration –as well as my admiration for him– has continued throughout this PhD. It was during our early scientific discussions, together with Dr. Koen J. Groot on how to stabilise unstable base flows, that I came to appreciate the true value of working with intelligent, inspiring people who genuinely love what they do. The experience left such a lasting impression in me that, ever since, I have sought to echo that inspiration with my students. For this, I will be forever grateful to Stefan for instilling in me a passion for research, for challenging me with new ideas, and for trusting me when I was at the very beginning of my academic journey. I sincerely wish every student were as fortunate as I have been to work with an advisor who combines scientific brilliance, deep knowledge of fluid mechanics across multiple subfields, international leadership, devotion for education, and genuine warmth, as Stefan does.

In 2018, I met Marios and my life changed forever. When I asked Dr. Koen J. Groot what was his best advice at the beginning of my doctorate, his answer was simple: *learn from Marios.* Unsurprisingly, Koen was right. Marios is one in a million, a scientist and academic advisor who stands as a true role model. Not only for his deep knowledge of fluid mechanics and his restless intellectual curiosity and depth, but also his vision and leadership. Marios leads by example and, in doing so, creates a wake that draws everyone around him towards excellence, determination, and a genuine love for science itself. Yet what one admires most about Marios is his sense of ethics and the methodological approach he brings in the process of scientific creation. I will be eternally grateful to him for his support, for the freedom he has granted me in research, and for trusting me. I have no doubt that the group of Flow Control at TU Delft, under his leadership, will leave its small mark on the history page of fluid mechanics; and I am proud to say that I once worked with Marios.

Whatever you do in life, wherever you are: find your Stefan and Marios.

To the scientific community

I would like to acknowledge the support of the Dutch national e-infrastructure (provided by SURF Cooperative), which was crucial for performing the large Direct Numerical Simulations that underpin the results of this thesis, as well as the European

Research Council for fostering transparent research and innovation across Europe. My gratitude also extends to the anonymous reviewers whose feedback helped improve the scientific articles composing this thesis, as well as to the members of the doctoral committee for their time and dedication to reviewing my work. I would like to thank my colleagues in the flow stability community for the many fruitful interactions: Dr. Juan Alberto Franco Sumariva, Francesco Tocci, and Dr. Stefan Hein from DLR; Dr. Mohammad Moniripiri and Dr. Valerio Lupi from KTH; and Dr. Jenna Eppink from NASA Langley. I also owe special thanks to Olaf W. G. van Campenhout, for the many productive collaborations and discussions, as well as to the professors of the Aerodynamics section at TU Delft, and to all the MSc students I had the pleasure of supervising during my doctorate. Debating with curious and passionate students is, and will always be, a main source of scientific innovation.

To my people

My doctorate would never have been as vibrant, fun, and full of unforgettable moments as it has been without Dr. Luis Laguarda. To Luis –who combines intelligence, elegance, and charisma like no other– I owe the gift of looking back at my years at TU Delft and remembering this academic journey with utmost joy. On the High Speed Laboratory side, this acknowledgement also extends to Dr. Alessandro d'Aguanno –the third *Musketeer*– whom I have always deeply respected, both scientifically and personally, and to Colette Russo. Colette, thank you for your dedication and professionalism, while creating such a joyful atmosphere whenever you are around.

On the Low Speed Laboratory side, together with Dr. Alberto F. Rius-Vidales and Sven Westerbeek, we truly formed a team. Alberto's experimental mastery and Sven's numerical skills greatly contributed to strengthening ideas and propositions developed in this thesis. It has been an absolute pleasure working with you both. Alberto (and Bea), I thank you for our long-lasting friendship, and for your guidance and crossflow expertise; I look forward to elevating our flow-control ideas toward new horizons. Sven, thank you for the most insightful flow-physics discussions over these years; I deeply value the respect and friendship that grew through our collaborations.

Although the scope of this thesis lies on incompressible flow, Marina Barahona's research on compressible flow unexpectedly erupted in the middle of my doctorate –together with Oscar– and I am glad that it did. They both spun my life in ways that I never imagined; I suppose that must be the UPC spirit. Marina, recipient of the Amelia Earhart Fellowship, you possess all the ingredients to become a scientific leader –be one, in a time that needs it. Finally, Ria, thank you for your good vibes every morning, which led to our daily short Dutch practice: *Hartelijk dank!*

I shall now cross the Atlantic Ocean to thank my most prominent co-author, and friend, Dr. Koen J. Groot. Koen is an essential part of the scientist who I am nowadays. Because of his contagious passion for fluid mechanics and for education, his guidance and support over many years, and his habit of challenging me with impossible ideas. Without exception, Koen has always been there when needed, scientifically and also personally. Koen –the man, the legend– you are a role model to many of us. By the way, have you tried *BiGlobal*?

The reader should not forget that my doctorate was partially conduced during the covid-19 pandemic (additional kudos, please). While the idea of pursuing a PhD

under lockdown is, *a priori*, far from ideal, this period unexpectedly became one the happiest. All thanks to my covid-family during lockdown: Franziska, Francesca, and Florine. Your openness, humour, and willingness to dance the covid away at the rythm of *Despacito* were essential in keeping my drive alive through such challenging times. The pandemic was also an inflection point for many of us, changing the lenses through which we perceive friendship and time. Elena, I owe you much of the joy I feel when looking back on my years in the Netherlands; full of unforgettable moments, laughter, festivals, and the pride of so many shared adventures. *¡El ambiente y los temazos han sido realmente espectaculares!*, together with Vicky.

Maya, one my favourite people in this world –though you appeared in my life very unexpectedly, your support was paramount during the final phases of my doctorate. Thank you for the confidence, maturity, and, above all, for vibing at my frequency. I will closely follow your career in public health, for I have no doubt that you will shine with special intensity. The genius of Jen DeNike brushed into my life with great rhizomatic intensity in the final, very intense, stages of this journey, and she became a true *intellectual activator* through our equation: *I will* = *I want* + *I should*! Artemis, thank you for our fun Dionysian conversations and for bringing your genuinely warm personality during the writing stage of this thesis. And last, but not least, thank you to my *laboratory-neighbour* during covid-19, Dr. Theodoros Michelis, whose humour, authenticity, and uniqueness filled the empty, dark rooms with warmth and light.

Throughout my doctoral years, the Low Speed Laboratory grew rapidly, welcoming many new colleagues who created a supportive, enjoyable, and scientifically inspiring atmosphere. Parisa –a true scientist– and my favourite coffee enjoyer; Antonis, my closest Mediterranean soul and thinker, and non-modal ally (I haven't dreamt the lift-up effect, it exists!); Yifu, my main numerical support and favourite Japanese *onsen* enjoyer; Babak, the most lethal board-game liberal of the 1930s; Abdoo, my deepest philosophy and budgets thinker; Giulio, my best spiritual companion during the final stage of the thesis, as well as Pierre, Nick, Srinivas, Martín, Martino, Hendrick, Erica, Saskia, and Marco, whose drive, professionalism, and passion leave the research of the *hump*-transition project in the best possible hands.

These names complement another long list of fantastic colleagues and professional researchers with whom I had the pleasure to share the first part of my doctorate –both inside and outside of the campus– and from whom I learned immensely. Giulia and Kaisheng, my experimental counter-parts; Jane, my favourite existentialist, whose kindness and genuineness should be an example to many; Ata, whose numerical and speaker skills I have always deeply admired; Christoph, one of the most professional researchers I have ever met and certainly the organiser of the best Oktoberfest in Delft; Haris, one of my best students ever, and with whom I shared multiple adventures during covid-19; Gabriel, who rightfully closed Collar's triangle with the best BBQs in Delft; Varun, whose proposition, *Have you heard about the Performance Bar in Rotterdam?*, implicitly marked a before-and-after in my life; Emijl, the best Greek-food companion; Kherlen, whose openness and charisma quickly forged a strong bond during my first (and most likely last) Mongolian heavy metal concert; Tyler, the greatest chef in the group, always cooking the best RANS simulations; Edoardo, the best (or not) companion in *Fiesta Macumba*, Shiaodong, Thomas, Alex,

Constantin, David, and the INCA community; Weibo, and Mohammed.

As an international student in the Netherlands, my emotional map was shaped by a triangle connecting Delft, Mallorca, and Barcelona. It is hard for me to materialise in words why, but this PhD thesis would never have been the same without the small island of Mallorca and three of its inhabitants: Jordi, Guillem, and Juanan. The intensity of a doctorate requires effective outlets, and for that, Mallorca in summer is second to none. My friends, I sincerely value our long-lasting friendship and the countless adventures we have shared during the summer periods encompassed by my doctoral years. When I look back, with you I see only unstoppable laughter, impossible situations, some of the happiest moments of my life, and... *Villa Finca*! What would this PhD thesis be without *Villa Finca*'s summer events? For my gratitude also extends to the colleagues I had the pleasure to meet there more recently: Carlos, Joan, Narcís, Gabri, Pere, and Joaquín.

In Barcelona I have my roots; despite the distance, Dr. Octavi Obiols has been a crucial source of support in this doctorate, and will always remain an essential companion in my life. I look forward to the many adventures we have shared... and the many more we will share. Oriol and David, thank you for always being there throughout this journey, and for exemplifying what friendship truly entails: the same confidence and warm breeze, despite the kilometres and the passing years. The gratitude I owe to Dr. Marc Suñé extends beyond our friendship: he is an example. An academic who lives with love for his passion: pharmaceutical research. Your drive is contagious; I suppose nothing has changed since we studied together in school. I also wish to thank David, Dr. Alejandro Nuñez, Dr. Julià Hinojosa, and Clara for our friendship, and for providing me with the best advise an engineer can receive: *engineers are trained to solve problems and find optimal solutions; yet, not everything in life has a solution, nor does every situation need to be approached optimally.*

To my family

There is one true gift that life has endowed me with, and that is my family: my parents, Maria Teresa and Carles, and my sister, Sílvia. The love and admiration I feel for them are so honest and deep that no written word could ever do justice to this feeling. Their support lies not only in their actions, but above all, in their example: to live life with integrity, honesty, passion, dedication, and love. *Pares, si a alguna cosa aspiro a la vida, és a poder ser per als altres el que vosaltres heu estat per a mi. Sílvia, l'autèntica aventura –ara ho veig– ha estat créixer junts. Continua brillant a la teva manera: pel què, però sobretot pel com; doncs aquí em tindràs sempre, veient-te créixer amb la mateixa admiració i amor de quan érem petits.* This thesis is also dedicated to my grandparents –Maria, Joaquim, Jordi, and Carme– because, while we think about them, they never truly left; and to these generations of women who did not have the chance to study, and of men who endured hardship through intolerance and imposition. May they forever remind us of the value of education, critical thinking, and freedom in the centuries to come.

Jordi Casacuberta Puig
October 19, 2025

Scientific Contributions

Journal articles

9. **J. Casacuberta**, K. J. Groot, S. Hickel, and M. Kotsonis (2025). Direct numerical simulation of swept-wing transition induced by forward-facing steps. First-round review in progress for *J. Fluid Mech.*

8. S. Westerbeek, **J. Casacuberta**, and M. Kotsonis (2025). Linear and nonlinear interactions between stationary crossflow instabilities and a smooth surface hump. Second-round review in progress for *J. Fluid Mech.*

7. K. J. Groot, **J. Casacuberta**, and S. Hickel (2025). Non-orthogonal plane-marching parabolized stability equations for the secondary instability of crossflow vortices. *Comput. Fluids*, Accepted for publication.

6. A. F. Rius-Vidales, L. Morais, S. Westerbeek, **J. Casacuberta**, M. Soyler, and M. Kotsonis (2025). Delay of swept-wing transition using a surface hump. *J. Fluid Mech.*, 1014:A35.

5. **J. Casacuberta**, S. Westerbeek, J. A. Franco, K. J. Groot, S. Hickel, S. Hein, and M. Kotsonis (2025). Streaky perturbations in swept-wing flow over forward-facing step. *Phys. Rev. Fluids*, 10:023902.

4. **J. Casacuberta**, S. Hickel, and M. Kotsonis (2024). Passive stabilization of crossflow instabilities by a reverse lift-up effect, *Phys. Rev. Fluids*, 9:043903.

3. O. W. G. van Campenhout, M. van Nesselrooij, Y. Y. Lin, **J. Casacuberta**, B. W. van Oudheusden, and S. Hickel (2023). Experimental and numerical investigation into the drag performance of dimpled surfaces in a turbulent boundary layer. *Int. J. Heat Fluid Flow*, 100:109110.

2. **J. Casacuberta**, S. Hickel, S. Westerbeek, and M. Kotsonis (2022). Direct numerical simulation of interaction between a stationary crossflow instability and forward-facing steps. *J. Fluid Mech.*, 943:A46.

1. **J. Casacuberta**, K. J. Groot, Q. Ye, and S. Hickel (2020). Transitional flow dynamics behind a micro-ramp. *Flow Turb. Comb.*, 104:533–552.

Patents

1. M. Kotsonis, **J. Casacuberta**, A. F. Rius-Vidales, S. Westerbeek, G. Zoppini, and T. Michelis (equal share) (2024). Aircraft surface. *WO 2024/151166 A1.*

CONFERENCE ARTICLES AND PROCEEDINGS

5. G. Barocco, Y. Chen, M. Barahona, and **J. Casacuberta** (2025). Effect of localised wall heating on crossflow instability in a swept-wing boundary layer. Submitted to the *14th International Symposium on Turbulence and Shear Flow Phenomena, TSFP*.

4. **J. Casacuberta**, S. Hickel, and M. Kotsonis (2023). Laminar-turbulent transition in swept-wing flows with a supercritical forward-facing step. In *ERCOFTAC Workshop Direct and Large Eddy Simulation*, pages 151–156. Cham: Springer Nature.

3. O. Krochak, **J. Casacuberta**, S. Hickel, and M. Kotsonis (2022). Mechanisms of interaction between a stationary crossflow instability and backward-facing steps. In *12th International Symposium on Turbulence and Shear Flow Phenomena, TSFP*.

2. **J. Casacuberta**, K. J. Groot, S. Hickel, and M. Kotsonis (2022). Secondary instabilities in swept-wing boundary layers: DNS and biglobal. *AIAA Paper 2022-2330*.

1. **J. Casacuberta**, S. Hickel, and M. Kotsonis (2021). Mechanisms of interaction between stationary crossflow instabilities and forward-facing steps. *AIAA Paper 2021-0854*.

CONFERENCE PRESENTATIONS

6. **J. Casacuberta**, S. Hickel, A. F. Rius-Vidales, and M. Kotsonis (2024). Numerical investigation of crossflow-driven-transition delay through local sharp surface modification. In *10th IUTAM Symposium on Laminar-Turbulent Transition*.

5. **J. Casacuberta**, K. J. Groot, S. Hickel, and M. Kotsonis (2023). How do forward-facing steps promote laminar-turbulent transition of swept-wing flow? In *14th International ERCOFTAC Symposium*.

4. **J. Casacuberta**, S. Hickel, and M. Kotsonis (2022). Laminar-turbulent transition in supercritical forward-facing steps in crossflow. In *13th Workshop on Direct and Large-Eddy Simulation*.

3. **J. Casacuberta**, S. Hickel, and M. Kotsonis (2022). The reverse lift-up effect in crossflow instabilities over surface irregularities. In *the Joint ERCOFTAC/EU-CTFF European Drag Reduction and Flow Control Meeting*.

2. **J. Casacuberta**, K. J. Groot, S. Hickel, and M. Kotsonis (2022). *Secondary instabilities in swept-wing boundary layers: DNS and biglobal*. In *AIAA Scitech*.

1. **J. Casacuberta**, S. Hickel, and M. Kotsonis (2021). Mechanisms of interaction between stationary crossflow instabilities and forward-facing steps. In *AIAA Scitech*.

AWARDS

1. **J. Casacuberta** (2022). Best speaker at the Burgers Symposium of Fluid Dynamics.

INVITED TALKS

1. **J. Casacuberta** (2023). *Laboratori de Càlcul Numèric (LaCàN)*, UPC BarcelonaTech.

AMINAR

T

RBULENT

TU Delft